

THE STRUCTURE AND REACTIVITY OF HEAVY HYDROCARBONS

James G. Speight,
CD&W Inc., PO Box 1722,
Laramie, WY 82073-1722

KEYWORDS: coal, petroleum, structure

ABSTRACT

The identification of the molecular constituents of coal is an exceptionally formidable, if not impossible, task. And yet, significant advances have been made recently in bringing about an understanding of the molecular nature of coal. As always, there are, and will be, serious questions about the need for such an understanding, relative to the use of coal, but the knowledge gained can often help offset a difficult-to-understand aspect of a processing sequence.

Thus, it can be argued (often successfully with some degree of conviction but not *ad nauseam*) that understanding of the chemical nature of coal constituents is, just like an understanding of the chemical and thermal behavior of coal, a valuable part of projecting the successful use of coal for conversion and/or utilization processes or as a source of chemicals. Thus the derivations of hypothetical and representative models are of some value.

It is, therefore, the purpose of this article to present some indication of the methods that allow coal to be defined in terms of structural entities and also to include an assessment of the various *molecular* structures proposed for coal.

INTRODUCTION

The structure and reactivity of the so-called *heavy hydrocarbons* is a complex field of endeavor. However, before entering this area a definition is necessary.

By definition, *a hydrocarbon contains carbon and hydrogen only* (Morrison and Boyd, 1973; Fessenden and Fessenden, 1990). On the other hand, *if an organic compound contains nitrogen, and/or sulfur, and/or oxygen, and/or metals it is a heteroatomic compound and not a hydrocarbon*. Organic compounds containing heteroelements (elements such as nitrogen, oxygen, and sulfur), in addition to carbon and hydrogen, are defined in terms of the locations of these heteroelements within the molecule and it is the heteroatomic function that determines the chemical and physical reactivity of the heteroatomic compounds (Morrison and Boyd, 1973; Fessenden and Fessenden, 1990). And, the chemical and physical reactivity of the heteroatomic compounds is quite different from the chemical and physical reactivity of the hydrocarbons.

More correctly, coal is a *hydrocarbonaceous* material insofar as it contains carbon and hydrogen but also other elements that add to the complexity of its composition and behavior. In fact, coal is an *organic rock* that is composed of a complex mix of high molecular weight heteroatomic compounds that requires high temperatures for decomposition (through bond rupture) to produce hydrocarbons. It is not a naturally occurring hydrocarbon, although there are small amounts of occluded low molecular weight hydrocarbons that occur within coal as an integral part of coal.

Acceptance of this simple, but correct, scientific premise will assist in the identification of the molecular composition of coal as well as in coal utilization.

The determination of the properties of coal as a means of coal evaluation and with the goal of predicting behavior during utilization is well documented (Hessley, 1990; Berkowitz, 1979; Speight, 1994). However, there is another area of coal characterization that has been at least equally well documented, but perhaps less well recognized as a means of evaluation, which involves studies of the molecular constituents of coal.

In fact, the heterogeneous chemical structures of the wide range of plant chemicals which formed the starting material for coal promise, but do not guarantee, an almost unlimited range of chemical structures within the various types of coal. Thus, it is perhaps best to consider coal as a variety of chemical entities that virtually dictate coal reactivity under specific conditions.

Coal itself (with the exception of the extractable material) may simply be looked upon as a conglomeration of high molecular weight species that may, or may not, be covalently bonded (or, for example, hydrogen-bonded) together to form a complex *macromolecule*. But, in terms of coal science, nothing is simple and the term *macromolecule* is used here very loosely and it is not used with the object of defining any coal as a *single* molecular entity.

A similar line of thinking has been applied to the search for the structures that exist in the higher molecular weight fractions of petroleum that are particularly prone to produce coke and/or reduce catalyst activity during the processing of these materials (Speight, 1999). In the present context, such studies have been more often over the past two decades since coal has, once again, come into increased popularity as a potential source of gaseous and liquid fuels.

It is often argued (often successfully with some degree of conviction but not *ad nauseam*) that understanding of the chemical nature of coal constituents is, just like an understanding of the chemical and thermal behavior of coal, a valuable part of projecting the successful use of coal for

conversion and/or utilization processes or as a source of chemicals. Statements relating to the derivation of hypothetical and representative models are of some value. In fact, the value of any structural model of a complex molecular entity lies in its use as a means of not only understanding process chemistry and physics but also in its use as a means by which processes can be understood and predictions (perhaps tongue-in-cheek and hopefully near to reality) can be made. Of course, such visions are always subject to the willingness of the chemical modeler to learn from experience and also to subject the model to the necessary changes to render it workable (Speight, 1999).

As an aside, but certainly worthy of note, the identification of many of the constituents of petroleum have been achieved as a result of the volatility of these constituents and subsequent application of methods such as gas-liquid chromatography and mass spectroscopy. But in the case of petroleum residua, identification of the individual constituents is much more difficult and heavy reliance has to be put on identification by molecular type (Speight, 1999). The same is essentially true for coal.

Identification of the constituents of complex mixtures (such as petroleum residua and coal) by molecular type may proceed in a variety of ways but generally can be classified into three methods: (1) spectroscopic techniques, (2) chemical techniques, and (3) physical property methods whereby various structural parameters are derived from a particular property by a sequence of mathematical manipulations. It is difficult to completely separate these three methods of structural elucidation and there must, by virtue of need and relationship be some overlap.

The end results of these methods are *indications of the structural types* present in the material (Stadelhofer et al., 1981). However, there is the unfortunate tendency of researchers to then attempt to interrelate these structural types into a so-called *average structure*. But the pronounced heterogeneity of coal makes the construction of *average structures* extremely futile and, perhaps, misleading.

ASSESSMENT OF COAL STRUCTURE

As already noted, the origin of coal dictates that it be a very complex organic material product, having little volatility and containing various molecules which are of different chemical origins and, hence, of different size and chemical structure (Haenel, 1992). Indeed, it must always be emphasized that coal, because of the complexity of its origins, cannot exist as a single molecular entity. Indeed, coal and petroleum, irrespective of their different phases (i.e. solid vs. liquid) might be considered as similar entities, albeit formed from different mixes of the precursors and under different conditions. And no one would ever accuse petroleum of being a single molecular entity and the era of claiming asphaltene (from petroleum) as being single molecular entities is, hopefully, over.

In fact, coal should be considered (on a molecular scale) as a complex heterogeneous organic rock and it is impossible to represent such a material by any single organic structure. What we obtain from oxidation studies (and for that matter from any other of the so-called structural studies) is a series of structural or functional types that occur in coal, subject of course to the above constraint. This must not be construed as a criticism that should bring an end to studies focused on the structural nature of coal but the limitations must be recognized in order to continue meaningful scientific endeavors that will aid in understanding the chemical and physical nature of coal.

Coal structure can be subdivided into two categories (1) the physical structure and (2) the chemical structure. Coal contains extractable smaller molecules that are an integral part of coal and bear a physical and chemical relationship to the non-extractable material. In contrast to many earlier studies of coal *structure*, both are an essential part of any consideration of the structural types in coal and one cannot exist without the other.

Therefore, in terms of physical structure, it is appropriate to note that coal is considered to be a two-component system, a mobile phase and a macromolecular network (Given, 1984a, 1984b; Given et al., 1986) that consists of aromatic ring clusters linked by bridges (Solomon et al., 1992). Thus, lower molecular weight species, the identifiable components of the mobile system, must also be given attention. How they exist in conjunction with the main body of the coal is another issue. They have been variously referred to as *guest molecules* (Redlich et al., 1985), *clathrates* (Given et al., 1986), and (perhaps even less correctly) as *bitumen* (Kreulen, 1948; Grint et al., 1985; Pickel and Gotz, 1991).

Recent work has used the yield of the chloroform extract of coal as an indication of the extent of the mobile phase (Derbyshire et al., 1991). In untreated coals, only a portion of the mobile phase appears to be removable but after *mild* preheating there are sharp increases in the yield of the extract. Perhaps to no one's surprise, that there is an increase in the yield of chloroform-extractable material with treatment temperature. This has been interpreted to mean that there is a gradation in the manner in which the smaller molecules are associated with the network. Thermal studies also tell us that the thermal chemistry of chemical bonds can also vary with temperature.

The results of such work, as mentioned here (and there are many other examples), may provide strong evidence that the *thermal extraction* (perhaps *thermal decomposition* is a more appropriate term) of coal produces evidence for the molecular species that constitute the mobile phase, but, the thermal chemistry of coal is much more complex than these data would suggest! In other words, the pertinent issue relates to the quantity of the mobile phase that exists within coal and under prevailing ambient conditions. In addition, it must also be recognized that a quantity of the mobile phase is generated by the application of thermal conditions that exceed the thermal decomposition threshold of the molecular species in coal. These issues might be resolved by a thorough understanding of the plastic properties of coal (Grimes, 1982).

That coal contains low molecular weight extractable species is a fact. That these species may form a mobile phase within the macromolecular network of coal is effective in explaining some of the many facets of coal behavior, including physical phenomena such as porosity and solvent diffusion (Rodriguez and Marsh, 1987; Hall et al., 1992). However, that the constituents of this network can be extracted (unchanged) by *thermal means* or by solvent treatment after exposure of the coal to high temperatures where the stability of many organic species is suspect and that only the *weak* bonds are broken, is open to question.

In the chemical sense, it should never be forgotten that coal (like petroleum is a natural product and, as such, must be considered to contain vestiges (perhaps somewhat changed from the original!) of the plant material. But to an extent, the nature of the coal must be influenced by the nature of the original material (Given, 1984b; Derbyshire et al., 1989). Studies of the maceral type and content of coal show this to be, at least true in principle but these are physical signs of the coal constitution. Whether these vestiges remain as largely unchanged entities or whether they be completely different from their original form is another question.

An examination of the solubility of coal in a variety of solvents and examination of the infrared spectra of the extracts indicated that coal consists of structures of basically similar chemical type and suggested the coals closely related in rank may be homogeneous in chemical structure. Indeed, there are numerous examples cited in the literature which support this view and it is not surprising that material extracted from coal has been employed as being representative of that particular rank for structural determinations and differences exist predominantly in the molecular weights (i.e. degree of polymerization) of the structural entities.

Caution is advised in interpretations of this nature because the pyridine extracts of coal may, other claims to the contrary because of the complex nature of coal, differ substantially with increasing extraction time and different constituents predominate at different stages of the extractions.

Nevertheless, the major drawback to the investigation of coal structure has been the incomplete solubility of the material, which has in many cases dictated that structural determinations are carried out on extracted material. Even then, the answer may not be complete. For example, coal structure is often considered to analogous to humic acid structure; humic acids are considered to be soluble molecular entities that are produced during the formation of coal. However, humic acid structure is not at all well known and has been, in the past, represented as involving large condensed nuclear systems.

In addition, an aspect of coal science that is often carried in the minds of those whose goal is structural elucidation is the thermal decomposition of coal to coke.

Briefly, it has been assumed, on the basis of the behavior of the thermal decomposition of polynuclear aromatic systems, that coal must also consist of large polynuclear aromatic systems. Be that as it may, such assumptions are highly speculative and, to say the least, somewhat lacking in caution. As an example, similar lines of thinking have been applied to structural assumptions about petroleum asphaltenes when it is known from other pyrolysis studies that smaller, but polar systems, can produce as much thermal coke as the larger nonpolar highly condensed systems (Speight, 1999). Indeed, it is now recognized, on the basis of other studies (Winans et al., 1988) that coal structure (especially the structure of non-anthracitic coals) is not necessarily dominated by polycyclic/polynuclear aromatic species.

Thus, concepts of coal structure must also satisfy any of the relevant data from the variety of chemical manipulations of coal that have been described in a previous section and add positive knowledge about the nature of coal. In addition, a consensus of the aromaticity values reported would be that there appears to be a definite increase with rank.

Indeed, the issue of reality or perception has run amok in recent years in petroleum science where workers have laid claim to be the first with a particular structural postulate when their results were based on (at the time believable but proven and acknowledged since then to be) faulty laboratory techniques which produced erroneous, and essentially fictitious, data! And yet we are asked to believe..... But the ethics of such claims leads to other issues! Back to the present issue.

Obviously, on a molecular basis and because of its complexity coal has been viewed as having many forms, only a few of which are noted here. The argument for any particular structure can sway back and forth but the concept of a *chemical structure* of coal or even a simple, repetitive unit cannot really be justified given the extensive heterogeneity of coals.

Application of computer modeling techniques to the issue of coal structure (Carlson and Granoff, 1991; Carlson, 1992) coupled with the potential of synthesizing a model of acceptable behavioral characteristics (Gunderman et al., 1989) might prove to be quite revealing but it should always be remembered that the computer is not a magician but can only feed upon the data in a somewhat limited (usually non-thinking) form. A sound diet of nutritional data could, however, prove to be quite revealing!

There are also indications that coal may be a system of peri-condensed polymeric structures in contrast to the suggestion of coal being predominantly kata-condensed. The occurrence of anthracene in the thermal products of coal processing has, on many occasions, been cited as evidence for the predominantly condensed nature of the aromatic systems in coal. Be that as it may, and there is some degree of truth to this supposition, there is also the distinct possibility that such anthracene systems in the thermal products are, to a degree, thermal artifacts that are formed by various dehydrocyclization reactions.

On a natural product basis, the occurrence of anthracene-type systems in nature and the occurrence of systems that could conceivably form anthracene are not unknown (Weiss and Edwards, 1980). However, the occurrence of phenanthrene systems (the analogous peri-system to anthracene) is also well documented (Fieser and Fieser, 1949) but has often been ignored in terms of structural entities in coal. On the other hand, the phenanthrene system may be (or, at least, appears to be) prevalent in petroleum (Speight, 1999). Thus, the differences in precursor types and maturation paths notwithstanding, there is the distinct possibility of phenanthrene systems occurring in coal to an extent not previously recognized.

Furthermore, it is somewhat interesting to speculate on the similarity, or dissimilarity, between the structural types that are believed to exist in coal and those found in (or speculated to be in the higher molecular weight fractions of) petroleum.

To date, there have not been any serious efforts to match the two. Nor were there any reasons to do this. Nevertheless, the concept of similarity is intriguing! Perhaps the reasons for the lack of comparison has been the complete differences in character of the two materials as well as the, apparently, overwhelming desire of coal to produce coke on heating. Indeed, the propensity for coal to form high yields of coke in thermal reactions has been a cause of question and puzzlement since the very early days of coal technology.

However, it is the obvious physical differences between coal and petroleum that can raise questions when similarities are considered. Perhaps the most convenient approach is to consider the differences in dimension and space between the two. The properties of coal are very suggestive of a three-dimensional network. This is much less obvious in petroleum (asphaltenes) and may only occur to a very minor extent. Such a difference in spatial arrangement would certainly account for some, if not all, of the differences between the two. Serious consideration of such a proposition would aid physical/chemical/structural studies in both fields. And would, hopefully, induce a more constructive thinking in terms of coal/petroleum behavior.

But more than anything, the structural studies of coal are limited by the continued insistence that one molecule of unlimited size can be constructed which will explain all of the properties of coal. And there appears to be a more distinctive, and recent, trend to the belief that the representation of coal by an *average molecular structure* is inappropriate insofar as it does not reflect the molecular diversity of the components of coal and their is an over riding tendency to ignore the known diversity of coal which is evident from petrographic studies.

An alternate choice is the representation of coal as a two-component system, thereby abandoning the concept of individual structures (Haenel, 1992). Obviously during the use of such a model, the details of any chemical transactions may be missing (but they should always be borne in mind and diminished or ignored) and the model might be convenient to explain many, if not all, of the physicochemical aspects of coal behavior. A very worthy accomplishment, indeed!

The fact that coals are heterogeneous as a group and, indeed, heterogeneous individually does not mean that there cannot be a concept of a macromolecular structure. But such a concept should include a variety of molecular types, perhaps in a manner analogous to the formulation of the structural types in petroleum asphaltenes (Long, 1979; Speight, 1999). There would need to be provisions made for the three-dimensional aspect of coal structure as well as for the presence of the lower molecular weight constituents.

Acceptance of these premises would presumably (or, at least, hopefully) facilitate a better understanding of the concepts of coal behavior in during utilization, such as in beneficiation, combustion, and gasification processes as well as in liquefaction processes.

REFERENCES

- Berkowitz, N. 1979. *An Introduction to Coal Technology*. Academic Press Inc., New York.
Carlson, G.A., and Granoff, B. 1991. In *Coal Science II*. Symposium Series No. 461. H.H. Schobert, K.D. Bartle, and L.J. Lynch (editors). American Chemical Society, Washington, D.C. Chapter 12.

- Derbyshire, F.J., Marzec, A., Schulten, H.-R., Wilson, M.A., Davis, A., Tekely, P., Delpuch, J.J., Jurkiewicz, A., Bronnimann, C.E., Wind, R.A., Maciel, G.E., Narayan, R., Bartle, K.D., Snape, C.E. 1989. *Fuel*. 68: 1091.
- Derbyshire, F.J., Davis, A., and Lin, R. 1991. In *Coal Science II. Symposium Series No. 461*. H.H. Schobert, K.D. Bartle, and L.J. Lynch (editors). American Chemical Society, Washington, D.C. Chapter 7.
- Fessenden, R.J., and Fessenden, J.S. 1990. *Organic Chemistry*. 4th Edition. Brooks/Cole Publishing Co., Pacific Grove, California.
- Fieser, L.F., and Fieser, M. 1949. *Natural Products Related to Phenanthrene*. Reinhold Publishing Corp., New York.
- Given, P.H. 1984a. *Prog. Energy Combust. Sci.* 10: 149.
- Given, P.H. 1984b. In *Coal Science*. M.L. Gorbaty, J.W. Larsen, and I. Wender (editors). 3: 63.
- Given, P.H., Marzec, A., Barton, W.A., Lynch, L.J., and Gerstein, B.C. 1986. *Fuel*. 65: 155.
- Grimes, W.R. 1982. In *Coal Science*. M.L. Gorbaty, J.W. Larsen, and I. Wender (editors). 1: 21.
- Grint, A., Mehani, S., Trehwella, M., and Crook, M.J. 1985. *Fuel*. 64: 1355.
- Gunderman, K.-D., Humke, K., Emrich, E., and Rollwage, U. 1989. *Erdol und Kohle*. 42(2): 59.
- Haenel, M.W. 1992. *Fuel*. 71: 1211.
- Hall, P.J. Mark, T.F., and Marsh, H. 1992. *Fuel*. 71: 1271.
- Hessley, R.K. 1990. In *Fuel Science and Technology Handbook*. J.G. Speight (editor). Marcel Dekker Inc., New York.
- Kreulen, D.J.W. 1948. *Elements of Coal Chemistry*. Nijgh & van Ditmar N.V., Rotterdam, The Netherlands.
- Long, R.B. 1979. *Preprints. Div. Petrol. Chem. Am. Chem. Soc.* 24(4): 891.
- Morrison, R.T., and Boyd, R.N. 1973. *Organic Chemistry*. 3rd Edition. Allyn and Bacon Inc., Boston, MA, USA. p. 40.
- Redlich, P., Jackson, W.R., and Larkins, F.P. 1985. *Fuel*. 64: 1383.
- Rodriguez, N.M., and Marsh, H. 1987. *Fuel*. 66: 1727.
- Solomon, P.R., Best, P.E., Yu, Z.Z., and Charpenay, S. 1992. *Energy & Fuels*. 6: 143.
- Pickel, W., and Gotz, G.K.E. 1991. *Org. Geochem.* 17: 695.
- Speight, J.G. 1994. *The Chemistry and Technology of Coal*. 2nd Edition. Marcel Dekker Inc., New York.
- Speight, J.G. 1999. *The Chemistry and Technology of Petroleum*. 3rd Edition. Marcel Dekker Inc., New York.
- Stadelhofer, J.W., Bartle, K.D., and Matthews, R.S. 1981. *Erdol und Kohle*. 34: 71.
- Weiss, U., and Edwards, J.M. 1980. *The Biosynthesis of Aromatic Compounds*. John Wiley & Sons Inc., New York.
- Winans, R.E., Hayatsu, R., and McBeth, R.L. 1988. *Preprints. Div. Fuel Chem. Am. Chem. Soc.* 33(1): 407.

THROUGH THE LOOKING GLASS: UNRAVELING THE NETWORK STRUCTURE OF COAL

D. M. Gregory, D. F. Stec and R. E. Botto*

Chemistry Division
Argonne National Laboratory
Argonne, IL 60439

ABSTRACT

Numerous swelling parameters measured by magnetic resonance microscopy (MRM) are found to correlate with cross-link density of the polymer network under investigation. Use of these parameters to assess the three-dimensional network structure of coal is discussed.

KEYWORDS: coal, swelling, network structure, magnetic resonance microscopy

INTRODUCTION

Since the original idea by Sanada and Honda¹ of treating coal as a three-dimensional cross-linked network, coal structure has been probed by monitoring ingress of solvents using traditional volumetric or gravimetric methods. However, using these techniques has allowed only an indirect observation of the swelling process. More recently, we have developed magnetic resonance microscopy (MRM) approaches for studying solvent ingress in polymeric systems, about which fundamental aspects of the swelling process can be deduced directly and quantitatively^{2,5}. The aim of our work is to utilize solvent transport and network response parameters obtained from these methods to assess fundamental properties of the system under investigation. Polymer and coal samples have been studied to date.

Previous work in our laboratory^{4,5} had demonstrated that MRM is clearly capable of distinguishing between Fickian and Case II diffusion, which represent two extremes of solvent transport in macromolecular systems. Fickian transport was characterized in rubbery samples as a smooth solvent concentration profile increasing with the square root of time. This process was typical for samples that did not undergo a change in physical state as a result of solvent ingress. By contrast, Case II transport processes were found in glassy polymers and coals that underwent a glass-to-rubber transition during swelling. Transport was characterized by a sharp solvent front moving linearly with time, and network relaxation occurred on a time frame that was fast compared to diffusion of the solvent through the network.

It has long been observed that many polymer systems exhibit what is termed anomalous transport behavior. As in Case II transport, the solvent modifies the physical state of the polymer; however, the transition of state occurs on a time scale comparable to diffusion.

Recent MRM studies have shown direct evidence for the latter process, and has allowed a direct observation of network response with relation to cross link density of the network. To perform these measurements, we took advantage of "contrast" imaging protocols, using protonated and deuterated solvents, and thereby observed physical changes in rubber samples imbibed with solvent. Using contrast-imaging techniques, i.e., employing diffusion weighting or T_2 weighting, we were able to obtain additional information on the polymer network directly. We studied four cross-linked isobutylene/*p*-methylstyrene rubber samples and showed that several NMR parameters correlate directly with cross-link density.

RESULTS AND DISCUSSION

Imaging of Protonated Solvent

Time-resolved MRM experiments monitoring ingress of cyclohexane in several rubbers has suggested anomalous swelling behavior. Consistent with this, the region in the center of the samples was completely devoid of solvent throughout the swelling process. Although the cyclohexane front retained the original object shape throughout, the solvent front was not completely sharp as would be expected for pure Case II behavior.

The velocity of the solvent front correlated well with cross-link density. The velocity of the front was greatest in samples with lower cross-link density. This result is expected in light of the diffusion coefficient measurements, which showed that cyclohexane diffuses faster in samples with a lower cross-link density.

Although we attained reasonably good fits to the data with a linear function of position of the solvent front (x) vs. time (t), this approach is only completely accurate in those cases where swelling is purely Case II. Instead, the data were fit to a generalized function:

$$x = k + v \cdot t^n, \quad (3)$$

where k = constant and v = front velocity. For the entire suite of rubbers, the average value calculated for exponent n ranged from 0.75 - 0.87, which implied the dynamics of swelling are intermediate between Fickian ($n=0.5$) and Case II ($n=1$).

MRM images of cyclohexane swelling of a rubber specimen are shown in Figure 3; a diffusion filter was applied prior to imaging for the images on the right. Because the diffusion coefficient of cyclohexane imbibed in the rubber is substantially less than in the bulk, signal from the faster diffusing bulk solvent is suppressed. In the diffusion-weighted images, however, the intensity of imbibed solvent is greatest immediately behind the solvent front. This is in contrast to the unfiltered images, where the signal intensity is fairly uniform throughout the swollen part of the sample. Thus, there is a direct correlation between intensity of pixels in the diffusion-weighted image and absolute magnitude of the diffusion coefficients. Bright regions indicate solvent with correspondingly lower diffusion coefficients.

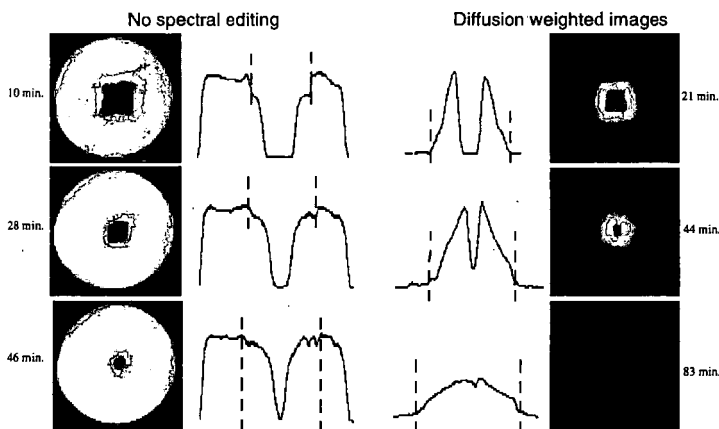


Figure 3. Spin-echo (left) and diffusion-weighted (right) MRM images of rubber specimens.

Moreover, gradations in diffusion coefficients across the swollen samples are perceptible in the filtered images. These effects are most clearly seen and measured in the 1D profiles. Because the diffusion coefficient is a measure of mean free path of a solvent molecule, this distance is shortest for solvent molecules near the solvent front and gradually increases with distance behind the front. This implies that the polymer network continues to expand well after its voids have been filled with solvent.

Imaging in Deuterated Solvent

By acquiring proton images of the rubber samples during a swelling experiment with d_{12} -cyclohexane, we were able to observe changes in the properties of the polymer directly. During swelling, conventional spin-echo MRM indicated that the greatest density of polymer occurs near the solvent front. Behind the front, the density of polymer gradually falls off, consistent with previous results from diffusion-weighted imaging.

Distributional T_2 maps created from the data show a gradation in T_2 values, again with the shortest T_2 's occurring near the solvent front. This parameter reflects changes in polymer chain motion, i.e. the frequency of motion of the polymer chains increases gradually with increasing distance from the solvent front.

We also monitored changes in T_2 vs. swelling time for an area of polymer at a constant distance from the outside edge of the sample. The data fit well to a simple exponential function. The 'rate' of change in T_2 for protons in the polymer correlates with cross-link density of the rubber; the rate is slower for samples with higher cross-link density. Final T_2 values show the same trend; samples with a higher degree of cross linking exhibit a lower final T_2 value.

Relation to Mechanical Models

As we have shown, diffusion coefficients of the solvent and polymer T_2 values parallel one another and reflect the segmental motions of the polymer chains. These changes take place on a time scale comparable to the diffusion process and are characterized by a single rate constant. At this point it is tempting to try to find analogies between the swelling process that we observe and the mechanical processes commonly measured in polymer systems⁴. We draw an analogy between changes in the motional correlation times of the network and strain relaxation in stress-strain experiments.

In a stress-strain experiment, a constant mechanical stress is applied, and the strain required is measured. In a swelling experiment, a constant osmotic stress is exerted by the solvent

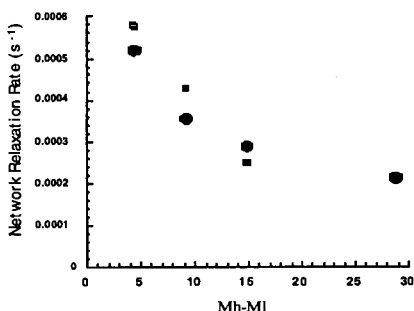


Figure 4. Changes in strain rate from T_1 (circles) and diffusion-weighted (squares) images with cross-link density (Mh-MI) from rheometry torque measurements.

at and beyond the solvent front. In this case, segmental motion of the polymer chains is measured. In both cases, the strain decreases, or relaxes, over time. In the simple Maxwell model, the relaxation rate is given by a single exponential function. As shown in Figure 4, network relaxation rates, as represented by the experimental T_2 relaxation times and solvent diffusion coefficients, decrease with higher cross-link density of the polymer network.

Preliminary Studies on Coal

MRM images depicting *in situ* swelling of a selected specimen of Pittsburgh No. 8 (APCS 4) vitrain with pyridine are shown in Figure 5. The swelling behavior of this coal is highly anisotropic, and is characterized by the solvent moving fastest in a direction perpendicular to the bedding plane. Diffusion of pyridine in this coal is purely Case II: the solvent front is extremely sharp, moves at a constant velocity, is linear with time, and has an exponential factor close to unity. Furthermore, bright regions are not observed near the solvent front in diffusion-weighted images, suggesting that network relaxation occurs on a time scale that is considerably faster than solvent diffusion.



Figure 5. Time-resolved MRM of swelling of Pittsburgh No. 8 vitrain in pyridine.

Back to the Future

It is without question that unraveling the three-dimensional architecture of coal will be key in advancing our understanding of coal behavior and reactivity. In attempts to realize this objective, many researchers in the past have performed systematic swelling studies on coals of different rank. Recently, Suuberg and coworkers⁶ have explored thermodynamic aspects of solvent-coal interactions by monitoring swelling kinetics as a function of solvent type and temperature. Trends in the observed activation energies were consistent with those expected on the basis of size effects of the solvent molecules and by disruption of donor-acceptor and/or hydrogen bonding interactions. Painter and his coworkers^{7,8} also have explored the intricate balance of thermodynamic forces in various hydrogen bonded systems and have developed good mathematical approaches to model the influence of strong intermolecular interactions on polymer properties. There is little question that theoretical treatment of solvent/solute thermodynamics holds the answer to understanding coal behavior, albeit heretofore difficult to realize.

Our previous work⁴ has allowed an estimate of strain rates from solvent front velocities and network relaxation rates, assuming coal/solvent systems exhibit pure Newtonian viscous behavior. To a first-order approximation, the strain rate can be related to the osmotic stress imparted by the solvent, i.e., the chemical potential of the solvent in equilibrium with the polymer. By applying Flory-Rehner (F-R) theory, parameters such as the number-averaged molecular weight between cross links may be estimated.

Assuming stress is purely osmotic in nature, $\sigma = \Pi$, it follows that for a Newtonian fluid the strain rate

$$d\epsilon/dt = RT/v_1\eta \cdot \ln a_s \quad (4)$$

Using classical F-R theory, we can determine Π at v_2^* , by defining the chemical potential of a solvent in equilibrium with the polymer

$$\ln a_s = [\ln(1-v_2) + v_2 + \chi v_2] + \{Z(v_2^{1/3} + v_2/2)\} \quad (5)$$

solvent terms

entropic constraint

where $Z = \rho v_1 / \langle M_c \rangle$, ρ is the dry density of the polymer, v_1 is the molar volume of the solvent, and $\langle M_c \rangle$ is the number-averaged molecular weight between cross links. In the past, numerous simplifying assumptions had to be made in order to apply F-R theory to coal systems, e.g. ignoring the non-Gaussian behavior of dense coal networks, hydrogen bonding effects and changing solvent affinities during swelling.

The problem with applying a statistical mechanics treatment to coals as densely cross-linked networks has now been solved using Painter's recently published approach.⁹ Furthermore, any contributions from hydrogen-bonding equilibria to the chemical potential can be dealt with by considering hydrogen bonding effects globally as part of the interaction enthalpy term, and a resolution of this issue soon will be at hand⁸ for coal systems. Moreover, in order to compute the osmotic pressure at v_2^* , one must assume that solvent χ parameter is independent of concentration. Although this is certainly not true, it is unlikely that χ will vary significantly with concentration (the 3rd term in equation 5).

Moreover, MRM is now capable of providing us with a number of key parameters which can be related to cross-link density of the network. We are able to accurately monitor propagation of the solvent through the network, and can obtain important parameters such as the rate of solvent transport, the kinetic order of transport (from Fickian, through anomalous, to Case II), spatial distributions of the solvent diffusion coefficients, and are capable of determining the concentration profile of the solvent front. We have been able to relate these solvent properties to strain rate. Employing deuterated solvents, we additionally are able to monitor changes of the macromolecular network *in situ* during the swelling process. We are able to observe directly mechanical relaxation of the network on the time scale of the swelling experiment, and to determine concomitant changes in microscopic expansion and mobility of the polymer chains.

There are however several relevant issues that need to be resolved first regarding treatment of the MRM data. Can we infer intrinsic strain rates from swelling experiments, in which the stress forces are exerted by solvent at the front under non-equilibrium solvent-solute conditions? Furthermore, is it possible to derive strict relationships of experimental data that are free of assumption yet adequately define fundamental thermodynamic properties of the system? Can parameters such as the T_g and $T_{1\rho}$ relaxation times and the NMR second moments be used to evaluate cross-link densities directly? Finally, would it be possible to systematically vary solvent and temperature conditions of swelling measurements (cf.

Otake and Suuberg⁶) in such a way that influences the kinetic order of transport, thus allowing a direct observation of network relaxation on a time scale appropriate for imaging?

Although the treatment and analysis of MRM data has until now been only approximate, linking network parameters from MRM with new statistical modeling approaches holds exceptional promise in the future for assessing the three-dimensional structure of coal.

ACKNOWLEDGMENTS

This work was performed under the auspices of the Office of Basic Energy Sciences, Division of Chemical Sciences, Department of Energy, under contract number W-31-109-ENG-38.

REFERENCES

1. Y. Sanada and H. Honda, *Fuel* **1966**, *45*, 295.
2. L. Hou, P. G. Hatcher, and R. E. Botto, *J. Coal Geology* **1996**, *32*, 167.
3. L. Hou, G. D. Cody, D. C. French, R. E. Botto, and P. G. Hatcher, *Energy Fuels* **1995**, *9*, 84.
4. G. D. Cody and R. E. Botto, *Macromolecules* **1994**, *27*, 2607.
5. G. D. Cody and R. E. Botto, *Energy Fuels* **1993**, *7*, 562.
6. Y. Otake and E. M. Suuberg, *Energy Fuels* **1997**, *11*, 1155.
7. M. M. Coleman and P. C. Painter, *Prog. Polym. Sci.*, **1995**, *20*, 1.
8. M. M. Coleman and P. C. Painter, *Macromol. Chem. Phys.*, **1998**, *199*:13-7, 1314.
9. B. Veytsman and P. C. Painter, *Energy Fuels* **1997**, *11*, 1250.

QUANTIFYING FLUIDITY DEVELOPMENT AND MOBILITY IN COALS BY IN-SITU ^1H NMR

Colin E. Snape and Shona C. Martin

University of Strathclyde, Department of Pure and Applied Chemistry,
Thomas Graham Building, 295 Cathedral Street, Glasgow G1 1XL, UK

Keywords: Broadline ^1H NMR, mobile and rigid hydrogen, fluidity, coal tar, polyurethanes.

ABSTRACT

After briefly reviewing the information that has been obtained to date using ^1H NMR to rationalise various phenomena associated with fluidity development, the improvements that can be achieved with various additives for poor coking coals will be described from both a practical and a fundamental standpoint. Trapping neutral oils from coal tar within briquettes prepared with phenolic binders enhances the mobility of the semi-fluid material for poor coking coal without significantly increasing the concentration. In terms of polymer additives, polyurethanes are unique in having a fluidity range that overlaps those of coals. Again, their addition vastly enhances the mobility of the semi-fluid material generated from poor coking coals but, unlike pitches, they do not dissolve any additional coal due to the high volatile losses. However, flexible foams have the ability to act as a plasticiser for much of the macromolecular structure in bituminous coals at relatively low temperatures (200–300°C). For high volatile coking coals, the addition of a petroleum coker feed (vacuum resid) can virtually render them completely fluid which accounts for the high yield of mesophase obtained in the resultant semi-cokes.

INTRODUCTION

In-situ broadline ^1H NMR has proved to be a highly successful technique for investigating the molecular motion in coals and pitches during carbonisation⁽¹⁻¹³⁾. There are usually two contributions to free induction decays of coals arising from mobile (faster relaxing) and rigid (slower relaxing) components that display Lorentzian and Gaussian decays, respectively. Coal, as a cross-linked macromolecular network, gives rise to a substantial inert component that does not soften and this produces a broad Gaussian peak in the NMR spectrum with a much narrower Lorentzian peak from the mobile material superimposed. The peak width is inversely proportional to the spin-spin relaxation time (T_2) of the fluid phase and is highly responsive to changes in mobility and this behaviour can be monitored as a function of temperature. It is fitting to describe recent work at the University of Strathclyde on the use of in-situ ^1H NMR to quantify phenomena associated with fluidity development in carbonisation on two counts. Firstly, Professor Sanada's own pioneering contribution to the development of in-situ ^1H NMR which dates back to the late 1970s⁽¹⁾. Secondly, fluidity development is inexorably linked to the thermal breakdown of the network structures existing in bituminous coals. After summarising the information that has been obtained to date using ^1H NMR to rationalise various phenomena associated with fluidity development, the improvements that can be achieved with additives in the behaviour of poor coking coals will be described from both a practical and a fundamental standpoint.

OVERVIEW OF EARLIER WORK

After the technique was first used by Sanada in the late 70s⁽¹⁾ to identify fluid material from coal and pitch at the early stages of carbonisation, Lynch, Sakurovs and co-workers, from the early 80s onwards⁽³⁻⁹⁾, detected both the rigid and fluid phases using a bench top spectrometer and have referred to their approach as Proton Magnetic Resonance Thermal Analysis (PMRTA). They have used mainly the empirical parameter, M_{2T16} , corresponding to the second moment integration limited at a width of 16 kHz, for gauging the reductions in fluidity as a function of oxidation and solvent extraction and the increases due to pitch/model compound addition. Of particular note is the quantification of interactive effects between different components in blends with both pitch and decacyclene being found to have a much greater effect than predicted on improving fluidity⁽⁷⁾. More recently, the issue of synergism between coals in coking blends has been addressed by Sakurovs⁽⁹⁾. In the majority of the binary coal blends investigated, both positive and negative interactions in terms of fluidity enhancement occurred. Positive interactions were generally greatest for blends of high and low volatile bituminous coals while semi-anthracite merely acted as a diluent to suppress fluidity.

Using both the amount and the T_2 of the mobile hydrogen, work at Strathclyde has established that, at maximum fluidity, the mobile phase accounts for 35-50% of the hydrogen remaining for good coking coals with both its concentration and mobility increasing up to this temperature, T_2 s at maximum fluidity being *ca.* 100 μ s. In contrast, coals that exhibit no softening in the Gieseler generate *ca.* 20% semi-fluid hydrogen with a T_2 of 60-70 μ s⁽¹⁰⁾. Like PMRTA⁽⁶⁾, measurements at Strathclyde have established that some high volatile bituminous coals that display little plasticity development in the Gieseler can generate appreciable fluidity, probably due to volatiles (potential metaplast) escaping at lower temperatures in the Gieseler. Reducing the particle size below *ca.* 150 μ m suppresses plasticity through a reduction in the mobility of the fluid phase with the concentration of rigid material remaining constant. This effect was considerably more pronounced with slow than fast heating (3-4 *cf.* 30°C min⁻¹). In contrast, suppressing the fluidity by mild oxidation reduced primarily the concentration of the fluid phase. Isothermal treatments gave rise to a loss of fluidity due to reductions in both the proportion and mobility of the fluid component. However, the in-situ measurements have confirmed that plasticity development is a reversible phenomenon provided that relatively fast quenching rates (*ca.* 75°C min⁻¹) are used.

As early as 1860, de Marsilly showed that removing solvent extractable material destroys the fluid properties of coking coals⁽¹⁴⁾ as later detected by standard methods, including Gieseler plastometry and dilatation^(15,16). However, it was not possible from standard tests to resolve quantitatively the contributions from the extractable material in coal and the metaplast generated thermally to the overall concentration of fluid material generated. High temperature ¹H NMR measurements were thus carried out on a suite of bituminous coals and their pyridine extracts and residues⁽¹¹⁾. Between one-third and a half of the mobile phase at maximum fluidity is metaplast for good coking coals. Further, taking the separate contributions from the pyridine extracts and residues, the predicted proportions and spin-spin relaxation times of the total hydrogen in the fluid phase at maximum fluidity were in close agreement with those observed for the whole coals. Thus, the pyridine-extractables do not appear to increase the amount of metaplast generated and serve mainly to increase the mobility of the fluid phase.

To help ascertain the contribution semifusinite makes to plasticity development during carbonisation, vitrinite and semifusinite concentrates with purities over 90% were separated by density gradient centrifugation from a medium volatile Australian bituminous coal⁽¹²⁾. For the vitrinite concentrates, the increases in reflectance and the degree of aromatic ring condensation with density correlate with the decreasing mobility of the fluid material. For the coal investigated, the overall contribution of the reactive semifusinite to the fluid phase at maximum fluidity is estimated to be 15 % (*ca.* 4 of the 30 % mobile hydrogen observed). Although interactions between maceral groups may take place in the original coal matrix, mixtures of the vitrinite and semifusinite concentrates did not reveal any synergism.

Hydrogen-donor ability has been ascribed as one of the factors responsible for the stabilisation of the plastic phase during coal carbonisation^(17,18) and to investigate this quantitatively, the interactions of a poor coking bituminous coal with a heat-treated coal tar pitch (CTP) and with a hydrogen-donor pitch (HDP, >450°C residue) obtained from a two-stage coal liquefaction process were compared⁽¹³⁾. When the CTP was added to the coal (25% w/w, 150-250 μ m), the amount of fluid material increased by nearly 20% more than that predicted at maximum fluidity. However, an even larger synergistic effect was observed with the HDP as a result of hydrogen transfer. By 400°C, 90% of the fluid phase concentration observed at 450°C had already been generated, corresponding to an enhancement of 50% over that predicted. However, particle size had a major impact with no enhancement in fluidity was detected below 45 μ m. Other possible approaches to the well-established use of coal tar pitch to enhance fluidity that have been investigated by in-situ ¹H NMR will now be described. The three avenues that have been investigated here are:

- (i) the use of polyurethanes since, in terms of common polymers, these are unique in having a fluidity range that overlaps those of coals;
- (ii) trapping coal tar within briquettes prepared with cold cure phenolic binders prepared from coal tar acids; and
- (iii) the use of a coker feed vacuum resid (VR) to prepare coke rich in mesophase.

EXPERIMENTAL

All the NMR measurements were conducted using a Bruker MSL100 spectrometer equipped with a ¹H high temperature Doty NMR probe, as previously described⁽¹⁰⁻¹³⁾. Approximately 50 mg of sample was packed lightly into a zirconia container and heated with an average heating rate of 4°C min⁻¹ from 25°C up to 550°C in a nitrogen atmosphere. Spectra were obtained at a number of different temperatures and transferred from the spectrometer to a PC for

Fourier transformation and the resultant spectra were fitted to a Lorentzian (narrower peak, fluid material) and a Gaussian (broader peak, rigid material) component.

For the experiments with polyurethane, a rigid and a flexible foam (20% w/w of the foams in the coal blends) were used in co-carbonisation tests with a poor coking coal (the same low volatile bituminous coal (designated AUS-4) as used in the earlier study with pitches⁽¹³⁾). Cold cure briquettes from a similar coal (designated CAN-1) were prepared with a phenolic resole prepared using the acids from low temperature coal tar as described elsewhere⁽¹⁹⁾. However, a resole was also prepared using the whole tar and this also cured successively, effectively trapping the neutral aromatics from the tar within the briquettes. High temperature ¹H NMR experiments were carried out on segments cut from the two types of briquettes and on a physical mixture of the coal with the tar acid resole (85:15 blend). A mass ratio of the VR to Powellton coal of 2:1 was used to replicate the published work of Schobert *et al.*⁽²⁰⁾ where coke with high mesophase content was prepared.

RESULTS AND DISCUSSION

Polyurethane co-carbonisation

Figure 1 shows the ¹H NMR spectra for the 80:20 blends of poor coking coal with the flexible and rigid foams at 450°C. Figures 2 and 3 present the variations with temperature in the proportion and T₂ of the mobile phase, respectively, for the poor coking coal and the blends of this coal with the flexible and rigid foams. The two foams differ in that methyldiisocyanate (MDI) moieties account for 35% of the carbon in the flexible foam compared to 75% in the rigid foam. Further, as well as isocyanate linkages, the rigid foam contains polyisocyanurate (PIR) moieties that confer considerable thermal stability. Thus, whilst the rigid foam is not liquefied fully to temperatures approaching 400°C by which time the volatile losses are high, the flexible foam is liquefied virtually completely by 200°C. This results in approximately 75% of the hydrogen being mobile (Figure 2) which corresponds approximately to 55% of the coal hydrogen, indicating a considerable plasticising effect by the aromatic diamines and diols that result from the cleavage of the isocyanate linkages. This is akin to the effect of polar solvents, such as pyridine, at ambient temperatures^(21,22), although the effect here is larger considering the non-swelling nature of the coal and the related low pyridine extraction yield⁽¹¹⁾. The T₂ of the flexible foam blend at ambient temperatures is high (*ca.* 250 μs, Figure 3) due to the highly flexible chains and it increases to over 500 μs due to the foam being liquefied as the urethane linkages are cleaved. Both the proportion and T₂ of the mobile phase decrease markedly as the flexible foam decomposes until 425°C when the metaplast is generated in significant quantities from the coal⁽¹¹⁾. For the rigid foam, the initial decrease in T₂ can be ascribed to the loss of water. However, as expected, the plasticising effect of the rigid foam is much less pronounced than that of the flexible foam with virtually all the mobile hydrogen below 350°C, which represents the onset of metaplast generation⁽¹¹⁾, being generated from the thermal decomposition of the foam.

By 450°C, the residue yields from both foams are small which means that virtually all of the fluid phase remaining is coal-derived. For this reason, the action of neither of the foams (within experimental error) results in an increase the proportion of mobile hydrogen close to maximum fluidity. However, the rigid foam in particular, for which the residue yield is greater than for the flexible foam, gives rise to a vast increase in T₂ of the mainly coal-derived fluid phase. Thus, the foam residue whilst displaying no appreciable solvent action in terms of increasing the proportion of mobile hydrogen, acts mainly to mobilise the semi-fluid phase to a much greater extent than found for the fluid phase in prime coals (*cf.* T₂ at 450°C of 200 μs for the blend with that of *ca.* 100 μs for good coking coals, albeit the latter contain much more mobile hydrogen). This action is essentially the same as that provided by the pyridine-solubles on the thermally generated metaplast (from the pyridine-insolubles) for good coking coals⁽¹¹⁾.

Coal tar addition to briquettes

It has been found that the enhanced fluidity obtained by trapping the neutral oils from low temperature tar within a cold cure briquette prepared in a laboratory press gives rise to a volumetric increase of 31% for the semi-coke briquette obtained at 600°C compared to only 9% for the normal tar acid resole formulation. Therefore, this initial study suggests that the resole made from whole coal oil can enhance the swelling properties of poor swelling coals considerably. Figures 4 and 5 show the variations with temperature in the proportion and T₂ of the mobile phase hydrogen, respectively, for the whole tar and normal tar acid resole cured briquettes, the green (non-cured) briquette for the whole tar resole and the coal itself. Although for the non-cured briquette, the neutral oils and constituents arising from the thermal decomposition of the binder give rise to an increase in the proportion and the T₂ of the mobile hydrogen at low temperatures, they volatilise below 350°C, resulting in little change in the fluidity characteristics between 400 and 500°C compared to the initial coal (Figures 4 and 5). Above 200-250°C once excess moisture have been removed, such increases in the proportion and

T_2 of the mobile hydrogen have largely been suppressed for the cured resin briquettes, suggesting that, in the case of the whole tar acid resole, the neutral oils have essentially been immobilised. However, for both the cured briquettes, there is an increase in T_2 for the fluid phase hydrogen from 60 to 80-120 μ s between 450 and 500°C (Figure 5), due to the later release of volatiles. The fact that the proportion of fluid hydrogen does not change appreciably indicates that most of the volatiles have been lost from the briquette section used for ^1H NMR and that, unlike CTP, the neutral oils and resin breakdown products are not liquefying the coal. Thus, the swelling action of these constituents in the cured briquettes can be attributed to their ability to mobilise the semi-fluid metaplast generated from the poor coking coal, much in the same way as the rigid polyurethane foam.

Vacuum resid liquefaction

Figure 6 shows the ^1H NMR spectrum obtained at 450°C from the blend of VR and Powellton coal. The rigid phase accounts for less than 4% of the total hydrogen and this proportion corresponds to over 80% of the coal hydrogen being liquefied. This observation, which represents the first full liquefaction experiment conducted by in-situ ^1H NMR, indicates that virtually all of the pre-asphaltenes (THF-insolubles, ca. 40% yield) obtained in the ex-situ liquefaction experiments⁽²⁰⁾ must soften in-situ. Above 450°C, the fluid phase forms semi-coke which, ex-situ, comprises high concentrations of mesophase that can be attributed to the extremely high fluidity observed here. However, unlike petroleum and coal tar pitch where two distinct mesophase types have been resolved with T_{2S} of ca. 20 and 70 μ s with the one having the longer disappearing as more mesophase is formed⁽²³⁾, only one solid phase with the shorter T_2 of 20 μ s is evident here for the VR/coal semi-coke. Thus, the intermediate phase considered to be attributable to gel-like material does not appear to form in significant proportions and the resulting signal is a composite from mesophase spheres and isotropic domains.

CONCLUSIONS

The description of the fluid phase in terms of the concentration and the T_2 of the mobile phase has enabled the effects of various additives during carbonisation to be rationalised in terms of whether they merely solvate the fluid phase as observed for the polyurethanes and the coal tar neutral aromatics within the briquette or, like the VR, dissolve additional coal.

ACKNOWLEDGEMENTS

The authors thank the European Coal & Steel Community for financial support (Contract Nos: 7220-EC/870 and 7220-PR/043) and Dr. H.H. Schobert, Dr. M. Badger and Ms. A. Fickinger at Penn State for providing the vacuum resid and Powellton coal for investigation.

REFERENCES

1. Miyazawa, K., Yokono, T. and Sanada, Y. *Carbon* **1979**, *17*, 223.
2. Lynch L.J., and Webster, D.S. in *Am. Chem.Soc. Symp. Series No. 230* **1983**, 353.
3. Lynch, L.J., Webster, D.S., Sakurovs, R., Barton, W.A. and Maher, T.P. *Fuel* **1988**, *67*, 579.
4. Lynch, L.J., Webster, D.S. and Barton, W.A. *Adv. in Mag. Reson.* **1988**, *12*, 385.
5. Clemens, A.H., Matheson, T.W., Lynch, L.J. and Sakurovs, R. *Fuel* **1989**, *68*, 1162.
6. Sakarovs, R., Lynch, L.J., Webster, D.S. and Maher, T.P. *J. Coal Qual.*, **1991**, *10(1)*, 37.
7. Sakurovs, R., and Lynch, L.J. *Fuel* **1993**, *72*, 743.
8. Lynch, L.J., Sakurovs, R., Webster, D.S. and Redlich, P.J. *Fuel* **1988**, *67*, 1036.
9. Sakurovs, R. *Fuel* **1997**, *76*, 615 and 623.
10. Maroto-Valer, M.M., Andrésen, J.M. and Snape, C.E. *Energy & Fuels* **1997**, *10*, 236.
11. Maroto-Valer, M.M., Andrésen, J.M. and Snape, C.E. *Fuel* **1997**, *76*, 1301.
12. Maroto-Valer, M.M., Taulbee, D.N., Andrésen, J.M., Hower, J.C. and Snape, C.E. *Energy & Fuels* **1998**, *12*, 1040.
13. Maroto-Valer, M.M., Andrésen, J.M. and Snape, C.E. *Fuel* **1997**, *77*, 921.
14. de Marsilly, C. *Ann. Chim. Phys.* **1860**, *3*, 66 and 167.
15. Seki, H., Kumagai, J., Matsuda, M., Ito, O. and Iino, M. *Fuel* **1989**, *68*, 978.
16. Wachowska, H. and Kozłowski, M. *Fuel* **1996**, *75*, 517.
17. Marsh, H. and Neavel, R.C. *Fuel* **1980**, *59*, 511.
18. Seki, H., Kumagai, J., Matsuda, M., Ito, O. and Iino, M. *Fuel* **1990**, *68*, 978.
19. Thoms, L.J., Snape, C.E. and Taylor, D. *Fuel* **1999**, *78*, 1691 and *Proc. 8th Australian Coal Science Conf.* **1998**, 239.
20. Fickinger, A.E., Badger, M.W., Mitchell, G.D., Schobert, H.H. *Prepr. Am. Chem. Soc. Div. Fuel Chem.* **1999**, *44(3)*, 684
21. Barton, W.A., Lynch, L.J. and Webster, D.S. *Fuel* **1984**, *63*, 1262.

22. Kamiński, B., Pruski, M., Gerstein, B.C. and Given, P.H. *Energy & Fuels* **1987**, *1*, 45.
 23. Andrésen, J.M. García, R. Maroto-Valer, M.M. Moineo, S.R. and Snape, C.E. *Prepr. Am. Chem. Soc. Div. Pet. Chem.* **1996**, *41*(3), 621 and *Proc. Carbon '96*, 559.

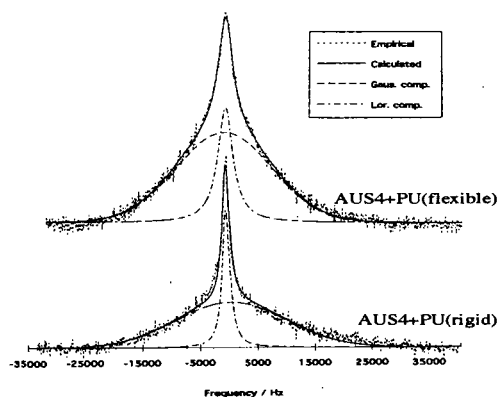


Figure 1 Comparison of ^1H NMR spectra for the blend of poor coking coal with flexible and rigid foams at 450°C

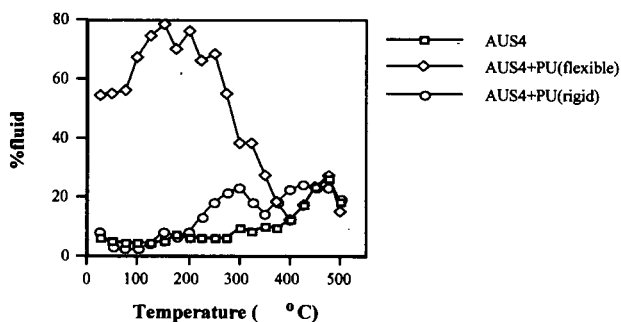


Figure 2 Variation with temperature in the proportion of the mobile phase hydrogen for the poor coking coal and the blends with the flexible and rigid foams (4:1)

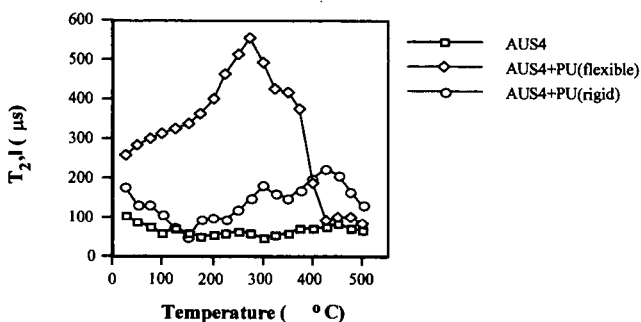


Figure 3 Variation with temperature in the T_2 of the mobile phase hydrogen for the poor coking coal and the blends with the flexible and rigid foams (4:1)

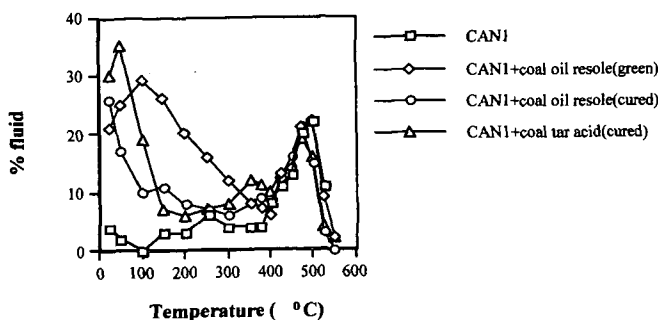


Figure 4 Variation with temperature in the proportion of the mobile phase hydrogen for the normal and neutral oil-containing cold cure briquettes and for the physical mixture of the coal (designated CAN 1) and low temperature coal tar

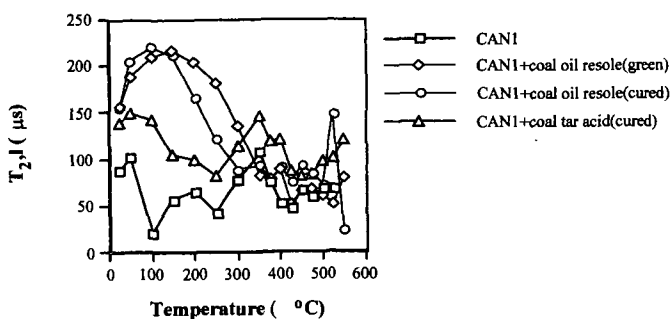


Figure 5 Variation with temperature in the T₂ of the mobile phase hydrogen for the normal and neutral oil-containing cold cure briquettes and for the physical mixture of the coal (designated CAN 1) and low temperature coal tar

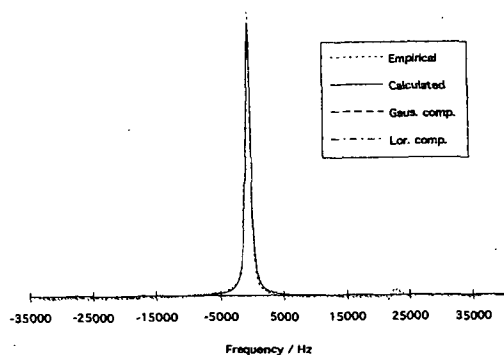


Figure 6 ¹H NMR spectrum obtained at 450°C for the blend of the vacuum resid and Powellton coal (2:1 w/w).

KEROGEN MACROMOLECULAR STRUCTURE

John W. Larsen and Harsh M. Parikh¹, Raymond Michels and Noele Raoult²
and Bernard Pradier³,

¹Department of Chemistry, Lehigh University, Bethlehem, PA 18015

²UMR, 7566 G2R Université Henri Poincaré, BP 23, 54501 Vandœuvre Les Nancy, France

³ELF-EP, CSTJF, Avenue Larribau 64018 Pau, France

Keywords: Kerogen, coal, macromolecular

ABSTRACT

The macromolecular structures of a Bituminous Coal (Illinois No. 6), a Type I kerogen (Green River) and a Type II kerogen (Torcian Shale, Paris Basin) are compared by using solvent swelling measurements. The swelling of Types I and II kerogen roughly follow Regular Solution Theory and show no specific solvent effects. The coal follows Regular Solution Theory for non-polar solvents but shows highly specific interactions with basic molecules. Immature Type I kerogen is much less cross linked than is immature Type II kerogen. Both Type I and Type II kerogen becomes more cross linked during maturation while coals appear to depolymerize during maturation. Only coals are strained. Alkanes dissolve in Types I and II kerogens but not in untreated coals.

RESULTS AND DISCUSSION

Quantitative studies of coal macromolecular structure began with the paper from Sanada and Honda in which they studied the swelling of coals by organic liquids and used the Flory-Rehner equation to calculate the cross-link densities of those coals.¹ The utility of this approach went unappreciated for many years, but it has since become a standard tool of coal science. Coals are Type III kerogens. Types I and II kerogens have long been known to be three dimensionally cross-linked macromolecular solids,² but only recently has systematic study of their macromolecular structure and properties been initiated. It is now possible to compare and contrast some of the macromolecular properties of all three kerogens.

The place to begin is with cross-link densities. All three materials have been studied by solvent swelling and the results are easy to compare. Ironically, the material that was studied first, coal, shows the most complex behavior. Type I kerogen has been selected as the standard to which the others will be compared. Numerous theoretical issues are involved in calculating cross-link densities from swelling measurements.³ Rather than enter the theoretical underbrush, the maximum solvent swelling observed will be taken as a qualitative measure of cross-link density. The solubility parameters of all three kerogens are surprisingly close permitting use of this simplification. The solvent swelling of Green River kerogen is typical of the Type I kerogens so far studied and is shown in Fig. 1. Swelling is reversible and all solvents (non-polar, polar, and hydrogen bonding) fall on the same curve. That curve roughly follows Regular Solution Theory.⁴ The Type II kerogen from Paris Basin Torcian Shale swells much less than does the Type I kerogen and all solvents behave similarly (see Fig. 2). Both kerogens show no specific interactions with the solvents used. The Type II kerogen is much more highly cross linked than Type I. Coals are different (see Fig. 3). First, they swell much more in hydrogen bonding solvents than in non-polar solvents. Two different explanations have been offered for this.^{6,7} For non-polar solvents, the swelling and therefore the cross-link density of pyridine extracted Illinois No. 6 coal is similar to that of the Type I and Type II kerogen used here. The similarity is not general. Green River kerogen swelling varies greatly with its maturation.¹² But there are also some puzzling aspects to coal swelling that have not yet been considered adequately. For example, if one swells untreated Illinois No. 6 coal with aromatic solvents, the swellings are quite small on the order of 10% to 20%. Part of this is because some of the coal is extracted into the solvent lowering the solvent activity and thus decreasing swelling, but this is probably not the major effect. The same coal after exhaustive extraction with pyridine in these same solvents now swells by 40% to 50%. The changes that cause this difference have not yet been adequately explained. The first swelling of coals is irreversible demonstrating that coals are strained.⁸ This behavior seems to be general and has not been observed with either Type I or II kerogen.

Types I and II kerogen are well behaved showing reversible swelling, no specific solvents effects, and roughly following Regular Solution Theory. Type II is highly cross-linked while Type I is not. Coals are very different. Initial swelling are irreversible and basic solvents interact specifically.

The three kerogens differ in the way the macromolecular structure changes during maturation. The single Type I kerogen studied in detail shows a sharp increase in cross-link density early and late in the maturation process, but in the middle a broad region of constant cross-link density (see Fig. 4). The macromolecular structure changes occurring during the maturation of only one Type I kerogen has been studied, and only three samples of that kerogen. The swelling changes are shown in Fig. 2. They show little beyond increasing cross-linking during maturation. The differences in cross-link density between the Type I and II kerogen will translate into greater capacity of immature Type I kerogen for hydrocarbons and more rapid diffusion from the Type I, other things being equal.

A survey of coal swelling reveals confusing dependence of swelling on rank.⁹ An analysis of the amount and molecular weight distribution of coal extracts led to the conclusion that coalification was a net depolymerization.^{10,11} This is opposite to the behavior of the Types I and II kerogen so far studied. Whether the chemical processes are the same or different, they have opposite effects on the cross-link density of the material.

The capacity of the kerogen to dissolve hydrocarbons has a great effect in the expulsion of petroleum from source rocks. A full discussion of this issue is deferred, but some interesting observations are noted here. The capacity of native coals for alkanes is approximately 0. They do not swell in alkanes. Regular Solution Theory predicts that the enthalpy of coal-alkane interactions will be endothermic compared to coal-coal and alkane-alkane interactions. Native coals will not dissolve saturated hydrocarbons. Such hydrocarbons may be diffusionally trapped in coals. Saturated hydrocarbons swell Type I kerogen by as much as 10-15% in spite of unfavorable thermodynamics. We offer a speculative explanation. If the kerogen structure is inhomogeneous and contains regions rich in aliphatic materials, aliphatic liquids might dissolve in these regions. Type II has a very low, but measurable, capacity for alkanes. Perhaps this situation is similar to that of Type I kerogens. These results and conclusions should not be translated to source rocks in petroleum kitchens because pressure effects on polymer structure (e.g. Tg) and mobilities may be significant.

ACKNOWLEDGMENTS

Studies of coals have been supported by the U. S. Dept. of Energy and the Exxon Education Foundation to whom we are grateful. Acknowledgment is made to the Petroleum Research Fund administered by the American Chemical Society for the partial support of this research. We are grateful to Elf for financial support and for the provision of samples.

REFERENCES

1. Sanada, Y.; Honda, H. *Fuel* 1966, 45, 295.
2. Tissot, B. P.; Welte, D. H. *Petroleum formation and occurrence: a new approach to oil and gas exploration* Springer-Verlag, New York: 1978.
3. Faulon, J.-L. *Energy Fuels* 1994, 8, 1020-3 and references therein.
4. Larsen, J. W.; Li, S. *Energy Fuels* 1994, 8, 932-936.
5. Hildebrand, J. H.; Prausnitz, J. M.; Scott, D. L. *Regular and Related Solutions* Van Nostrand Reinhold Co., New York: 1970.
6. Larsen, J. W.; Gurevich, I.; Glass, A. S.; Stevenson, D. S. *Energy Fuels* 1996, 10, 1269-1272.
7. Painter, P. C. *Energy Fuels* 1996, 10, 1273-1275.
8. Larsen, J. W.; Flowers, R. A. II; Hall, P.; Carlson, G. *Energy Fuels* 1997, 11, 998.
9. Quinga, E. M. Y.; Larsen, J. W. in *New Trends in Coal Science*, NATO ASI Series, Y. Yurum Ed., 1991
10. Larsen, J. W.; Mohammadi, M.; Yiginsu, I.; Kovac, J. *Geochim et Cosmochim Acta*. 1984, 48, 135.
11. Larsen, J. W.; Wei, Y. C. *Energy Fuels* 1988, 4, 344.
12. Larsen, J. W.; Green, T. K.; Kovac, J. *J. Org. Chem.* 1985, 50, 4729.
13. Larsen, J. W.; Li, S. *Energy Fuels* 1997, 11, 998.
14. Larsen, J. W.; Li, S. *Organic Geochemistry*, 1997, 5/6, 305-309.

Table 1. The identity of the swelling solvents in the Figures.*

No.	Solvent	$\delta(\text{cal/cm}^3)^{1/2}$			
1.	n-pentane	7.0	16.	acetonitrile	11.9
2.	n-heptane	7.4	17.	nitromethane	12.7
3.	methylcyclohexane	7.8	18.	pyridine	10.7
4.	cyclohexane	8.2	19.	tetrahydrofuran	9.1
5.	o-xylene	8.8	20.	2-propanol	11.5
6.	toluene	8.9	21.	ethanol	12.7
7.	benzene	9.2	22.	acetone	9.9
8.	tetralin	9.5	23.	dimethyl sulfoxide	12.0
9.	chlorobenzene	9.5	24.	o-dichlorobenzene	10.0
10.	1-methylnaphthalene	9.9	25.	chloroacetonitrile	12.6
11.	carbon disulfide	10.0	26.	carbon tetrachloride	8.1
12.	nitrobenzene	10.0	27.	1,2-trichloroethane	9.6
13.	biphenyl	10.6	28.	1,2-dibromoethane	10.4
14.	propionitrile	10.8	29.	methylene chloride	9.9
15.	nitroethane	11.1	30.	1-butanol	11.4
			31.	1-propanol	11.9

*Brandrup, J. and Immergut, E. H., *Polymer Handbook*, 3rd ed. John Wiley & Sons., 1989.

Figure 1. Swelling ratio of Green River kerogen as a function of swelling solvent solubility parameter. (\square) nonpolar solvents, (\blacksquare) polar solvents, (\diamond) H-bonding solvents. The solid line was calculated using the Flory-Rehner equation: assuming $\delta_p=9.75$, $M=242$, and $V_r=95 \text{ cm}^3/\text{mol}$. This figure is from Ref. 14. See Table 1 for solvent identification.

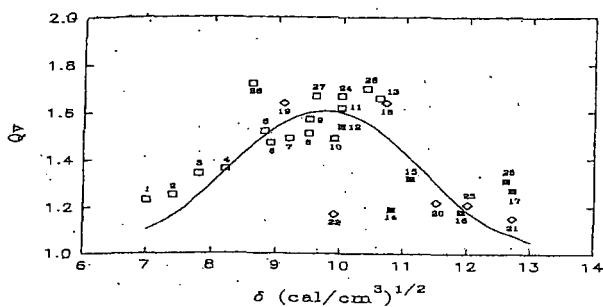


Figure 2. Swelling Ratios of Immature (\square) fully mature (\bullet) Paris Basin Type II kerogen. See Table 1 for solvent identification.

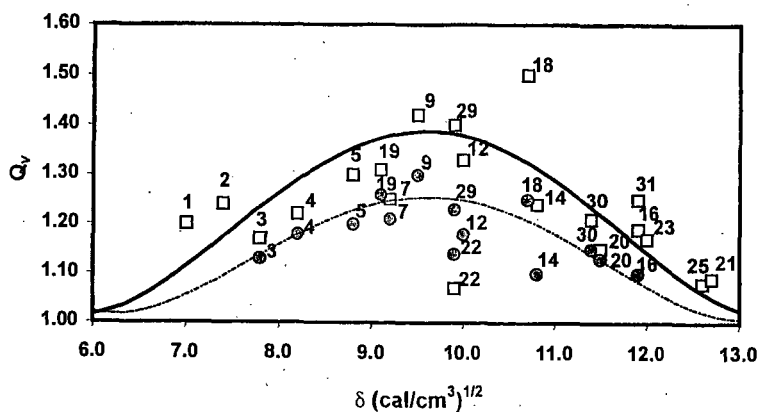


Figure 3. Swelling ratio of Illinois No. 6 coal as a function of swelling solvent solubility parameter (\square) nonpolar solvents, (\blacksquare) polar solvents, (\diamond) H-bonding solvents. See Table 1 for solvent identification. Non-polar solvents are plotted using their non-polar solubility parameters. This figure is from Ref. 12.

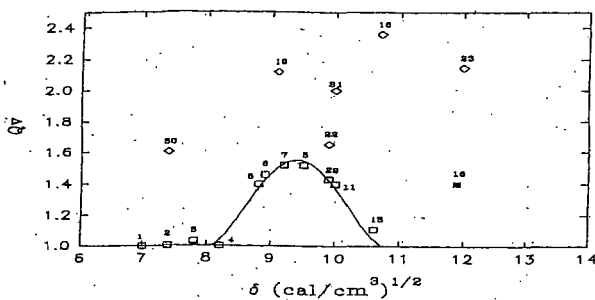
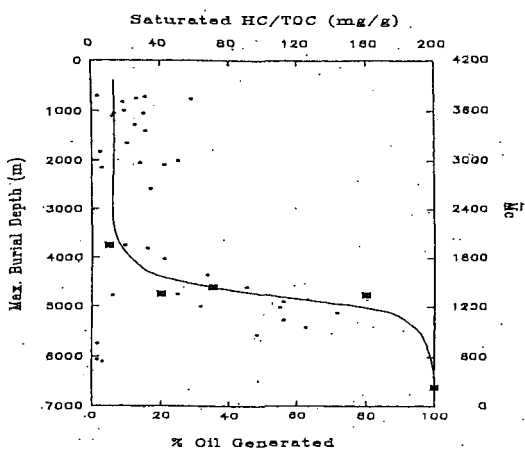


Figure 4. Change in Number Average Molecular Weight Between Cross Links (M_c) as a factor of Maturation for Green River (Type I) kerogen figure from Ref. 13.



MOLECULAR ASSOCIATION AND NETWORK STRUCTURE OF COAL

Yuzo Sanada

Ex-Center for Advanced Research of Energy Technology, Hokkaido University,
Sapporo, 060-8628, Japan

Keywords: coal, network structure, molecular association

Introduction

More than three decades ago, Sanada and Honda have treated coal as a three-dimensional network comprised of macromolecular arrays. Since that time, the concept has been followed by many investigators with various approaches as a gauge of coal macromolecular structure. In this paper, a brief overview of our works on macromolecular network structure of coal has been made.

The recent investigations about molecular and network structure by interactions of coal and electron acceptors have been described.

Hardness, Young's Modulus and Mechanical Properties of Coal [1-3]

The Vickers and Knoop indentation hardness and microstrength of coals of every rank have been determined. The hardness number increases with rank, and reaches a maximum at about 80 per cent carbon content. Hardness then decreases with rank for bituminous coal, shows a minimum at about 90 per cent carbon content, and thereafter suddenly increases again for anthracite as shown in Figure 1. Approximate values of Young's modulus (static) of coals are deduced from the hardness numbers and are order of 10^{9-10} dyne/cm².

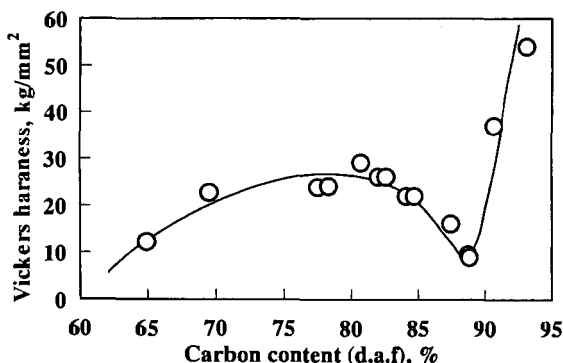


Fig. 1 Relation between Vickers hardness number and rank of coal

The Shore dynamic hardness of coals has also been determined. The relation between Shore hardness and rank of coal shows a maximum at about 80 per cent carbon and a minimum at about 90 per cent carbon content like that static indentation hardness number and rank of coal. The fraction of elasticity and plasticity of coals is deduced from the impact and rebound energies of the free drop indenter. Approximate values of Young's modulus (dynamic) of coals are deduced as well. The calculated dynamic modulus is larger than the static one. The facts imply that coal is one of viscoelastic materials like synthetic high polymer. It is suggested that the mechanical deformation occurred during hardness measurements is mostly governed by non-covalent bonding in the coal structure.

The change of microstrength index versus rank of coal is similar to those of Vickers hardness number and the deduced Young's modulus. The almost similar relationship between the spin-lattice relaxation time derived nuclear magnetic resonance spectroscopy and rank of coal was found as shown in Figure 2.

Temperature Dependence of Knoop Hardness and Glass Transition [4-7]

When amorphous polymers are heated, in general, they show a minimum of indentation hardness,

a maximum of logarithmic decrease of the pendulum, and a change of slope of volume-temperature curve at the glass transition point or zone. We have attempted that the glass transition like phenomena for coal by various measurements, that is, temperature dependence of indentation hardness, decrease of pendulum and volume change method together with wide line NMR at lower temperature range, where there are not occurring any remarkable chemical reactions.

The relation between the Knoop hardness number, H_k , of air-dried coals and temperature is shown in Figure 3. For both brown and bituminous coals, H_k decreases with temperature increase to a minimum at about 50°C and 100°C, respectively and increases with temperature up to 160°C. A small hump is observed at about 80°C for brown coal. The specimens heated to 160°C were allowed to cool in an ordinary atmosphere, then hardness was again measured at room temperature (closed circle in Figure 3). Bituminous coals and anthracite showed almost similar values to the original specimens. This implies the process is reversible step up to 160°C. On the other hand, the H_k value of brown coal became clearly high. The irreversible step is due to moisture release resulting the structure changes. We conclude that the characteristic points thus obtained with the various methods are brought by glass transition of coal.

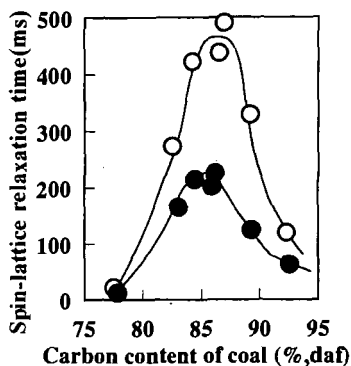


Fig. 2 Relation between ^1H -spin-lattice relaxation time and rank of coal. ● in air; ○ in vacuo

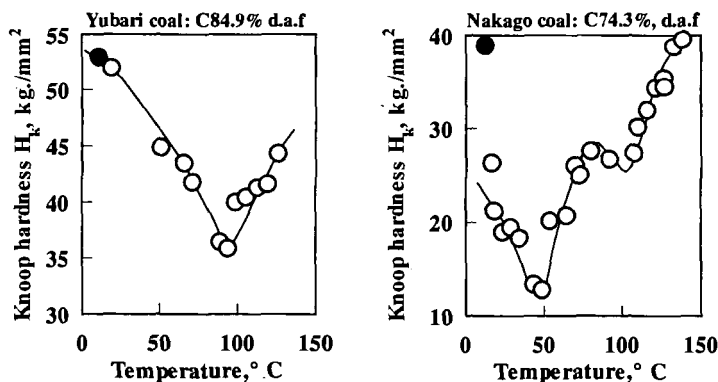


Fig. 3 Temperature dependence of knoop hardness of coals

Swelling Equilibrium and Three-Dimensional Network composed of Macromolecular Arrays [8-10]

Through the investigations above mentioned, a concept is motivated that coal as a three-dimensional network comprised of macromolecular arrays. Since that time, the concept has fostered into the thermodynamics governing solvent swelling as a gauge of coal macromolecules.

The swelling equilibrium of coal by pyridine at 25.0°C was investigated. The molecular weight per crosslinked unit, M_c , of coal was estimated by applying the equation of Flory-Rehner. [Miss calculations were appeared in the original paper. These are corrected by the experiments separately [11, 12]. The results are summarized and shown in Figure 4. The value of M_c of coal over the range 65 to 80 per cent carbon content (d.a.f.) is almost constant. For bituminous coal, M_c increases suddenly with rank to a maximum at about 85 per cent for Japanese coal, then decreases with increase of rank. This relation coincides well with that between maximum fluidity,

measured by Gieseler plastometer, and rank of coal, as shown in Figure 5. It is suggested that the degree of crosslinking is an important factor in determining the thermal properties of coal.

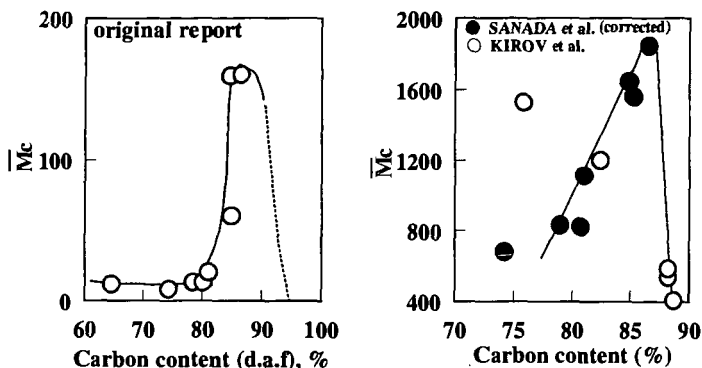


Fig. 4 Relation between molecular weight per crosslinked unit and rank of coal

The equilibrium swelling of coal by various solvents has also been investigated. For brown coal and bituminous coals, the equilibrium swelling degree, Q , increases with increase of the solubility parameter, δ , of the solvent, reaches a maximum at about $\delta = 10.8$, and then decreases with increase of δ as shown in Figure 6. Applying the theory of regular solution, it is estimated that the cohesive energy density of coals over the range from 65 to 87 per cent carbon content is the values between 100 and 140 cal/cm³ ($\delta = 10$ to 12).

In polar solvents the equilibrium swelling degree of coal is almost constant over the range from 65 to 87 per cent carbon content and decreases suddenly with further increase of rank. In non- or slightly- polar solvents, on the other hand, Q increases gradually with increases of rank up to a maximum at about 87 per cent carbon and then decreases. The value of Q for polar solvents increases remarkably with the increase of temperature. Polar solvents form 'coal-solvent' contacts readily by breaking and

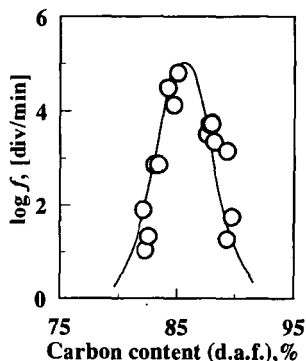


Fig.5 Changes of Gieseler maximum fluidity as a function of coal rank

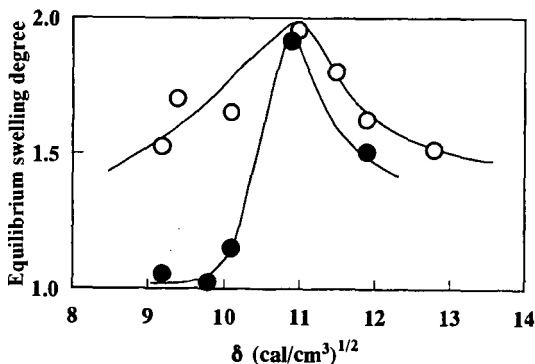


Fig. 6 Relation between equilibrium swelling degree of bituminous coal and solubility parameters of solvents at 25.0°C, ○, (C81.1%); ●, lignite(C65.1%)

/or relaxing the hydrogen bonds in coal. It appears that cohesive forces in coals show a distinct minimum at about 85 to 87 per cent carbon content.

Interactions of coal with various solvents are investigated by means of solvent extraction at the boiling points as well as hardness of solvent-immersed coal. Conclusion obtained is similar to that of swelling measurements.

Molecular Association [12,13]

The thermodynamic behavior of coal is, of course, a macroscopic property. The macroscopic approach examines energy changes in systems with no regard to molecular structure. On the other hand, the microscopic approach examines the molecular structure of coal and related intermolecular interactions.

Interaction energies between molecules are the functions of (1) permanent dipole, (2) induced dipole and (3) dispersion forces. Ionization potential, I , polarizability, α , dipole moment, μ , and distance between the molecules, r , are the most fundamental properties. Figure 7 shows the changes of polarizability and dipole moment together with hydrogen bond energy versus coal rank. Contributions of dipole moment and hydrogen bonding are dominant at the low rank of coal, while polarizability developed by condensed aromatic rings in the structure for high rank coal is important for π - π interactions. The contributions of polarizability, hydrogen bonding and dipole moment for medium rank coal are less important. The relationships between grindability and thermal fluidity of coal and rank are able to explain from the trends with rank as shown in Figure 7.

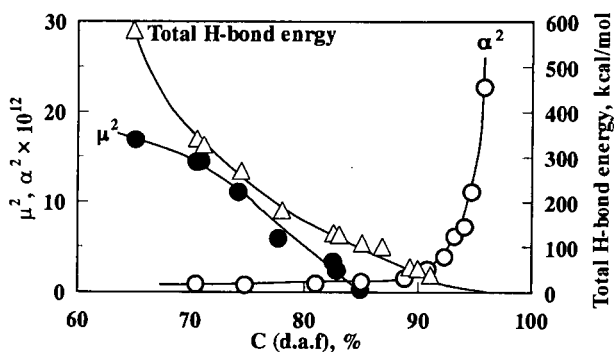


Fig. 7 Relation between molecular association factors and rank of coal

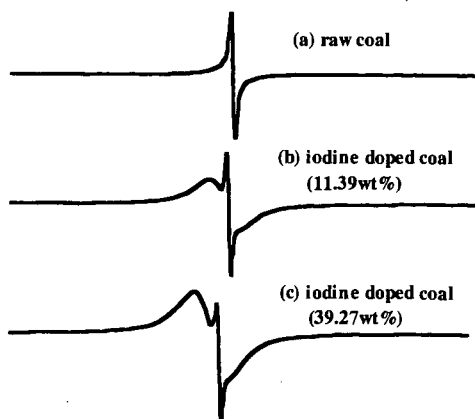


Fig. 8 ESR spectra of raw and iodine doped Upper Freeport(UF) coal

Charge Transfer Complex [15-19]

Coal is consisting with various molecules. It is likely that some of coal molecules behave electron deficient and others sufficient in nature at the solid state. The fact suggests that charge and/or electron transfer are generating between the both. This causes perhaps one of molecular association forces.

Condensed aromatic ring compounds with iodine show a broad e.s.r. signal due to charge transfer. The e.s.r. intensities of them correlate to their ionization potential values. Our investigations for coal have been concentrating the area by means of e.s.r. spectroscopy. Broad e.s.r signal was separated from sharp one by curve deconvolution. Peak intensity of the broad component is increasing with the iodine content as shown in Figures 8 and 9. The intermolecular behaviors of coal have been discussed through the evidences above.

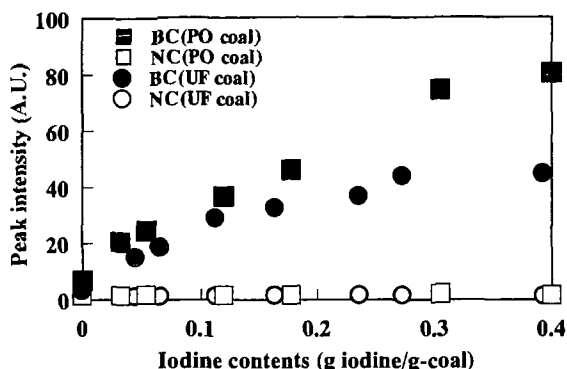


Fig. 9 Changes in peak intensity of iodine doped UF and PO coals ; BC: broad component, NC: narrow component

Acknowledgment

The author wishes to express his sincere thanks to Dr. H. Honda for his supervision at Resources Research Institute. The contributions of my coworkers and former students at RRI and Hokkaido University are most gratefully acknowledged.

References

1. Honda, H., Sanada, Y., *Fuel*, **1956**, 35, 451.
2. Honda, H., Sanada, Y., *Fuel*, **1958**, 37, 141.
3. Yokono, T., Sanada, Y., *Fuel*, **1978** 57, 334.
4. Sanada, Y., Mochida, N., Honda, H., *Bull. Chem. Soc. Jpn.*, **1960**, 33, 1479.
5. Sanada, Y., Honda, H., Nishioka, A., *J. Appl. Polymer Sci.*, **1962**, 6, 94.
6. Sanada, Y., Honda, H., *Fuel*, **1962**, 41, 437.
7. Sanada, Y., Honda, H., *Fuel*, **1963**, 42, 479.
8. Sanada, Y., Honda, H., *Bull. Chem. Soc. Jpn.*, **1962**, 35, 1238 & 1358.
9. Sanada, Y., Honda, H., *Fuel*, **1966**, 45, 295.
10. Sanada, Y., Honda, H., *Fuel*, **1966**, 45, 451.
11. Kielov, N. Y., Oshea, J. M., Sergeant, C. D., *Fuel*, **1968**, 47, 415.
12. Green, T., Kovac, J., Brenner, D., Larsen, J. W., 'Coal Structure', **1982**, R. A., Meyers Ed., Academic Press, p.199.
13. Sanada, Y., *J. Fuel Soc. Jpn.*, **1963**, 42, 238.
14. Sanada, Y., Satou, M., *J. Appl. Coal Petrology, Jpn.*, **1994**, 14, 29.
15. Sasaki, M., Sanada, Y., *J. Jpn. Petrol. Inst.*, **1991**, 34, 218.
16. Sasaki, M., Kumagai, H., Sanada, Y., *Energy & Fuels*, **1992**, 6, 758.
17. Kaneko, T., Sasaki, M., Sanada, Y., 'Magnetic Resonance of Carbonaceous Solids', **1993**, Ed. R. Botto, Y. Sanada, *Advances in Chemistry Series*, 229, ACS, p.529.
18. Sanada, Y., Kumagai, H., Sasaki, M., *Fuel*, **1994**, 73, 840.
19. Sanada, Y., Kumagai, H., Minco, T., Aizawa, S., Chiba, T., to be submitted.

ANALYSIS OF THE REACTION OF CARBON WITH O₂ USING AB INITIO MOLECULAR ORBITAL THEORY

Takashi Kyotani, and Akira Tomita

Institute for Chemical Reaction Science, Tohoku University,

2-1-1 Katahira, Sendai 980-8577 JAPAN.

KEYWORDS: Carbon gasification, O₂ chemisorption, Ab initio MO theory

INTRODUCTION

The mechanism of carbon gasification with oxygen has been widely studied. It is generally accepted that oxygen molecules chemisorb on carbon free sites to form surface oxygen complexes, C(O), which then desorb as CO₂ and/or CO. We attempted to clarify the mechanism of such reaction processes on carbon surface with several experimental techniques such as temperature programmed reaction and step response experiments using isotopically labeled reactants [1, 2]. In addition to these experimental approaches, molecular orbital (MO) theory is very helpful for the understanding of reaction mechanism. The usefulness of MO theory in the analysis of catalyzed and uncatalyzed carbon gasification has been demonstrated by many researchers [3-10]. Recently, using ab initio MO theory Yang *et al.* theoretically investigated desorption behavior of semiquinone, carbonyl and epoxy oxygen as surface oxygen complexes and discussed the mechanism of carbon gasification with oxygen-containing gases [11]. Furthermore, we have found that it is possible to simulate several experimental results of carbon-NO reaction when ab initio MO theory is applied [12]. Here, we attempted to analyze and simulate the chemisorption process of oxygen molecule and the formation of surface oxygen complexes on carbon edge sites using ab initio MO theory.

CALCULATION METHOD

Both the Gaussian 94 [13] and Gaussian 98 [14] packages were used to calculate molecular orbitals of model compounds for carbon-O₂ system. For simplicity, two types of single layer polyaromatic compounds with different sizes were employed as models for carbon. Figure 1 illustrates the structure of the two types of carbon models (models A and B) which have zigzag edge site on the upper side of each model. Some of carbon atoms are numbered for convenience. The edge atoms on the upper side are unsaturated and the rest of them are terminated with hydrogen atoms. A single O₂ molecule was put at a given distance from the zigzag edge in two different ways as shown in Figure 2. For side-on mode, the O₂ bond axis is parallel to the edge line. In the case of vertical mode, the bond axis was perpendicular to the plane of carbon model layer.

In order to investigate how O₂ molecule approaches the zigzag edge site of model A, we attempted to determine potential energy surface for each of the two approach modes (side-on and vertical). For such calculation, a grid for the position of the O₂ molecule was constructed near the edge site as shown in Figure 3, where each grid point was set in Y direction varying from 0.10 to 0.19 nm with an increment of 0.01 nm and in X direction from the right-hand C(1) atom to the most left-hand one with an increment of 0.01 nm. Thus, the shape of the mesh became square. The center of a single O₂ molecule was put on one of the points and then the following Energy calculation was done. First, the whole system including model A and the O₂ molecule was subjected to UHF (unrestricted Hartree-Fock) calculation with the basis set of 3-21G(d) with only O₂ bond distance optimized. Then, density functional method using the B3LYP functional with the basis set of 6-31G(d) was applied for single point energy calculation of the whole system with the optimized O-O distance. This energy calculation was done for all the grid points in Figure 3. For each grid point, the heat of adsorption, ΔH , was determined as a difference between the total energy of the calculated system and the sum of the energies of the corresponding carbon model and O₂ molecule. Since only O₂ bond distance was optimized in this grid calculation, the values of ΔH obtained are always a little larger than these determined by a full optimization calculation.

RESULTS AND DISCUSSION

From the grid calculation mentioned above, potential energy surface of O_2 on carbon zigzag site was determined for both side-on and vertical modes. The resultant surface is shown as two contour plots in Figure 4. The abscissa and the ordinate of each plot were defined as the distance in X direction from the right-hand C(1) atom in model A and the distance in Y direction from C(1) atoms, respectively. The coordinates in the horizontal axis correspond to geometrical position of the model drawn just below each contour plot. Since the potential energy surface was plotted in terms of ΔH , the thermal stability of the whole system can be evaluated from this value, i.e., the larger value the ΔH , the more unstable the system. For the potential energy surface in side-on mode, there are two minima located at the abscissas of 0.13 and 0.37 nm and at the ordinate of 0.14 nm. These two abscissas correspond to the positions of the two C(2) carbon atoms. This finding suggests that the center of O_2 molecule which is approaching model A goes toward either of the two C(2) atoms. Then, the O_2 molecule reaches the minimum at the ordinate of 0.14 nm to form surface oxygen species (model a) as illustrated in Figure 5, where O atoms are chemically bound to the C(1) atoms to form a five-membered ring. On the other hand, the result of the vertical approach was quite different from the side-on case. Since the observed three energy minima (Figure 4) are located at the abscissas corresponding to the positions of the C(1) atoms, the center of O_2 molecule is expected to go toward the C(1) atoms. As the result of such approaching, another surface oxygen species (model b) as shown in Figure 5 is formed at the ordinate of 0.12 nm. The species consists of a three-membered ring and from the energy contour map it can be seen that its thermal stability is lower than that of model a. In both the approach modes, the value of ΔH of each minimum in the contour plots is negative, indicating that the chemisorption of O_2 molecule is an exothermic process. This finding accords with the commonly observed feature for O_2 chemisorption on fresh carbon surface.

We put a single O_2 molecule at a distance of 0.13 nm from the zigzag site of model B in either side-on or vertical mode. Then the whole system including model B and O_2 was subjected to the ab initio calculation with all the geometrical parameters optimized. As a result, oxygen-containing species similar to model a is formed in the case of side-on mode and vertical approach gave model b-like structure. The heat of formation, ΔH , for each fully optimized structure was determined. For side-on and vertical approaches, the values were found to be -490 and -270 kJ/mol, respectively, which are not far from the observed one (-410 kJ/mol).

The process simulated in Figure 4 can be regarded as chemisorption of O_2 on fresh carbon surface without any pre-chemisorbed species. It would be worth elucidating the effect of pre-chemisorbed species on the O_2 chemisorption process. For this purpose, we investigated how the presence of either O or H atom on carbon surface influences the structure and the ΔH of the chemisorbed species on zigzag edge site. As a basic model of the edge site, we employed model B and bound one or two O atoms to the C(1) atoms as a quinone group. In the case of H atom, we terminated one or two zigzag edge carbon atoms by H atom. After the optimization calculation of these pre-chemisorbed models, we put a single O_2 molecule in the side-on mode on the edge sites. The final optimized structures are illustrated in Figure 6. In every case, a five-membered ring species similar to model a is formed upon the O_2 chemisorption. The values of ΔH are tabulated in Table 1, indicating that there is no noticeable change in ΔH , although the presence of a single C(O) increases the ΔH to some extent.

CONCLUSIONS

Potential energy surface of a single O_2 molecule on carbon zigzag site was determined by the ab initio MO calculation. It was concluded from such calculation that the way of how O_2 molecule approaches the zigzag site depends on the relative position of O_2 to the zigzag site, i.e., side-on or vertical mode. Furthermore, the MO theory predicts that the thermal stability of the O_2 -chemisorbed species formed in the side-on mode is higher than that of the vertical case. It was found that the presence of pre-chemisorbed species such as

C(O) or C(H) on zigzag edge site does not influence the structure and the ΔH of O_2 -chemisorbed species.

REFERENCES

- [1] Zhuang, Q.-L.; Kyotani, T.; Tomita, A. *Energy Fuels*, **1995**, 9, 630.
- [2] Zhuang, Q.-L.; Kyotani, T.; Tomita, A. *Energy Fuels*, **1996**, 10, 169.
- [3] Pan, Z. J.; Yang, R. T. *J. Catal.* **1990**, 123, 206.
- [4] Chen, S. G.; Yang, R. T. *J. Catal.* **1993**, 141, 102.
- [5] Chen, S. G.; Yang, R. T.; Kapteijn, F.; Moulijn, J. A. *Ind. Eng. Chem. Res.* **1993**, 32, 2835.
- [6] Janiak, C.; Hoffmann, R.; Sjövall, P.; Kasemo, B. *Langmuir*, **1993**, 9, 3427.
- [7] Kyotani, T.; Ito, K.; Tomita, A.; Radovic, L. R. *AIChE J.* **1996**, 42, 2303.
- [8] Kyotani, T.; Ogasawara, S.; Radovic, L. R.; Tomita, A. *Proc. Carbon'96*, Newcastle upon Tyne, 1996, 276.
- [9] Skokova, K.; Radovic, L. R. *Prepr.-Am. Chem. Soc. Div. Fuel. Chem.* **1996**, 41, 143.
- [10] Chen, S. G.; Yang, R. T. *Energy Fuels* **1997**, 11, 421.
- [11] Chen, N.; Yang, R. T. *J. Phys. Chem. A*, **1998**, 102, 6348.
- [12] Kyotani, T.; Tomita, A. *J. Phys. Chem. B*, **1999**, 103, 3434.
- [13] Frisch M. J. et al. Gaussian 94, Revision E.2, Gaussian, Inc., Pittsburgh PA, 1995.
- [14] Frisch M. J. et al. Gaussian 98, Revision A.7, Gaussian, Inc., Pittsburgh PA, 1998.

Table 1 Heat of adsorption of O_2 -chemisorbed species. (ΔH for model B without any pre-chemisorbed species is -490 kJ/mol.)

Structure	ΔH (kJ/mol)
c	-550
d	-500
e	-480
f	-480

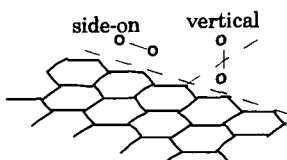


Fig. 2 Two positions of O_2 molecule near carbon edge site

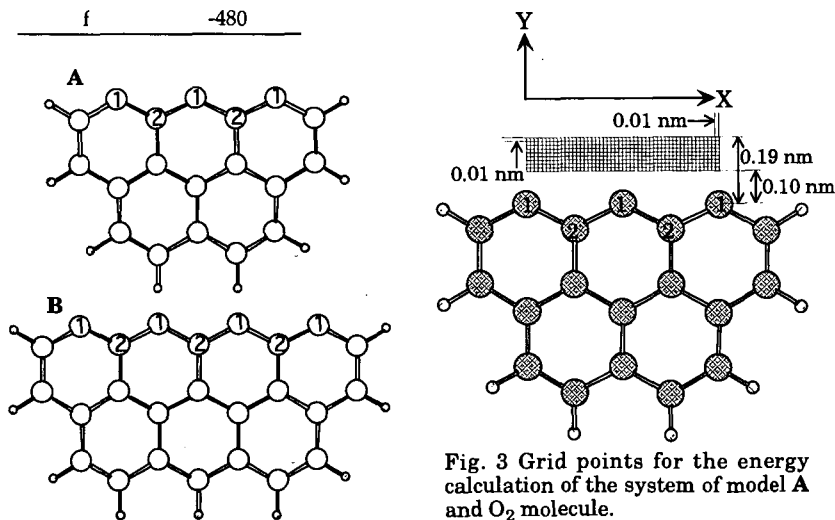


Fig. 3 Grid points for the energy calculation of the system of model A and O_2 molecule.

Fig. 1 Selected models of carbon. Large and small circles stand for carbon and hydrogen atoms, respectively.

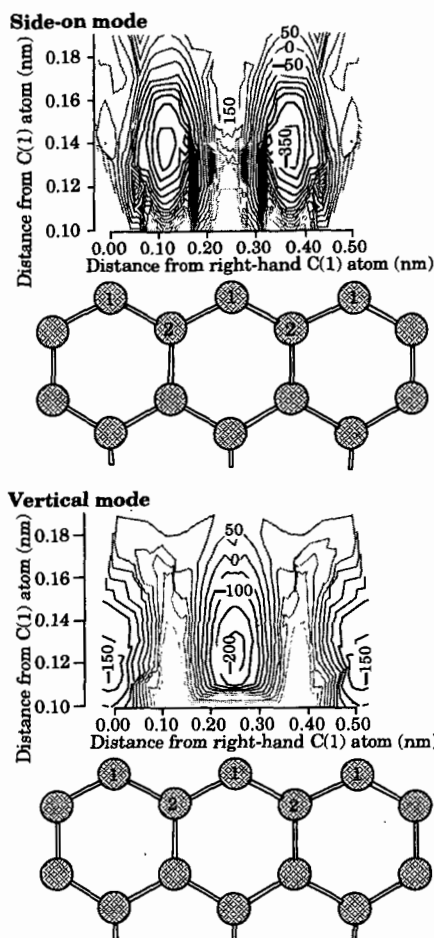


Fig. 4 Energy potential contour map for the carbon-O₂ system. Each contour line corresponds to a heat of reaction for this system and each line is drawn by the step of 50 kJ/mol.

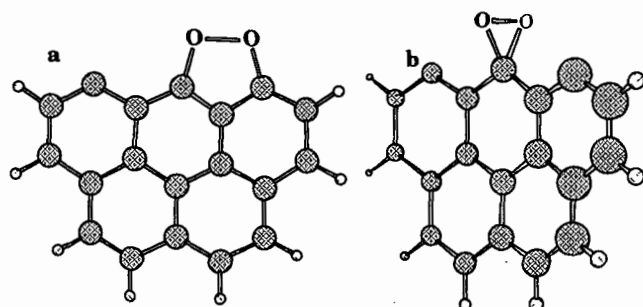


Fig. 5 Surface oxygen complexes formed by O₂ chemisorption on the zigzag site of model A in side-on and vertical modes.

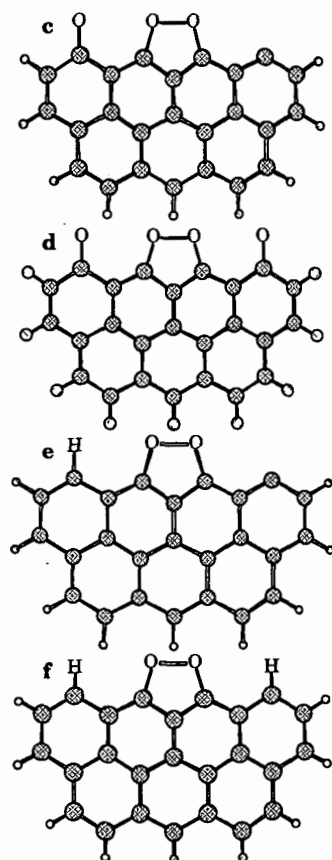


Fig. 6 Surface oxygen complexes formed by O₂ chemisorption on the zigzag site in side-on mode.

ELECTRON DENSITY IN GRAPHENE LAYERS: IMPLICATIONS FOR CARBON REACTIVITY

Ljubisa R. Radovic and Kristina A. Skokova*
Department of Energy and Geo-Environmental Engineering
The Pennsylvania State University, University Park, PA 16802
*BP Amoco Polymers, Alpharetta, GA

KEYWORDS: Molecular modeling, gasification, carbon reactivity

INTRODUCTION

Much has been accomplished in the last few decades to eliminate empiricism from the kinetic treatments of the combustion and gasification of coals, carbons and graphite (1). However, our ability to further quantify the important details of carbon reactivity is now at a critical juncture from both the experimental and the theoretical point of view. The experimental determination of active and reactive surface areas -- typically straightforward but sometimes tedious and complicated by stringent accuracy requirements -- does lead to satisfactory predictions of reactivity as a function of both carbon nature and carbon burnoff. Although not many such results are available in the literature, they do lend support to recent predictions (2,3) that the turnover frequency at the free carbon sites may be burnoff-dependent. In other words, it is not sufficient to know the carbon's total, active and reactive surface areas to understand all the important details of its reactivity behavior; the rate constant normalized with respect to the reactive area may be burnoff-dependent because the dynamics of surface coverage affect not only the number of sites but also their reactivity (3). In such circumstances, experimental complications increase further and mapping the intrinsic reactivity against the important variables (heat-treatment temperature, reaction temperature, pressure, extent of burnoff) remains quite a challenge.

On the other hand, while the *ab initio* molecular modeling of chemical reactions (4) has become possible and is now widely practiced, the extrapolation from either graphite or polyaromatic hydrocarbons to the carbons of interest (e.g., coal chars) is still subject to much uncertainty. In a recent study, Chen and Yang (5) presented a systematic procedure for selecting a suitable calculation level and model structure for the application of the *ab initio* method to the graphite system. They concluded that the use of B3LYP/6-31G(d) model chemistry for molecular properties and of HF/3-21G(d) for stability and geometry optimization, using a seven-ring graphene layer, is the most suitable compromise between accuracy, relevance and computational cost. Thus, for example, they used this approach, coupled with the atoms-in-molecule method (see below), to arrive at the intuitively appealing (and obvious!?) conclusion that a relatively large negative charge exists on the "unbalanced graphite edge sites" which are the "[re]active sites for carbon gasification reactions."

Before attempting to theoretically analyze the interaction between a gaseous molecule (O_2 , NO, CO_2 , H_2O) and the carbon surface (6), it is useful -- and indeed probably necessary -- to evaluate the theory in terms of its consistency with some well known facts about the electronic structure and surface chemistry of graphene layers. At the same time, it is expected that such a theoretical analysis will clarify the details of this electronic structure and thus help in the quantification of gasification reactivity. In particular, the electron density at the edge sites and its changes with the concentration of heteroatoms is of immediate interest. The affinity of the carbon surface for an oxidizing gas is assumed to be dependent on this electron density at the free carbon sites.

The electron density of a molecule is a fundamental property in quantum chemistry, readily amenable to theoretical analysis. The classical Mulliken population analysis, which assigns atomic charges, though arbitrary, is implemented in most commercially available molecular modeling programs. Its results should be viewed with caution, however, because they are known to be dependent on the level of theory and the basis set used. In contrast, the more recent atoms-in-molecule (AIM) approach is claimed not to have this limitation.

In this study a comparison is thus made between the Mulliken population analysis and the AIM approach in their ability to evaluate the electron densities in graphene layers by considering 1-, 2- and 4-ring aromatics. Following the pioneering work of Coulson and coworkers (7), "we can, provisionally, neglect all inter-layer effects and consider only the single layers separately."

COMPUTATIONAL METHODS AND MODEL STRUCTURES

The Gaussian 98W software package (4,8) was used in most calculations. When deemed necessary, it was complemented by Hückel molecular orbital as well as semi-empirical analyses. Figure 1 summarizes the structures that were selected for closer scrutiny. Their selection is based on the following considerations. We agree with Chen and Yang (5) that saturation of the boundaries of these model structures is a crucial step in reactivity calculations for graphite and, especially so, for carbons whose crystallites are much smaller than those in graphite. However, the choice of free edge sites versus hydrogen-saturated sites should not be one of convenience (7); rather, it should attempt to reflect the by now well documented delicate balance between free sites, H-saturated sites and oxygen-saturated sites (9). A comparison of bond orders and charge distributions in structures 1-4 within each series will thus be of interest. Similarly, ever since the pioneering work of Coulson and coworkers (7,10), as well as that of Stein and Brown (11), it has been clear that the size of the graphene layer is an important variable to consider even when edge chemistry is of primary interest. More recent theoretical analyses of carbon gasification (2,3), as well as experimental studies of liquid-phase adsorption on carbons (9), have indeed suggested that the electron density in the basal plane of the graphene layer is affected in an important way by the presence of heteroatoms at the edges, and vice versa. It is thus necessary to assess the dependence of these electronic effects on the size of the graphene layers. A comparison of the bond orders and charge distributions in series B1-N1-P1, B2-N2a-P2a, B3-N3a-N3b-P3a-P3b-P3c, B4-N4a-N4b-P4a-P4b-P4c will make this possible in a first approximation. An additional benefit of analyzing model structures containing few rings is that the results (model structures B1, B3, N1, N3a, N3b, P1, P3a, P3b and P3c) can be readily compared with experiments. Since some "50 carbon atoms" which form a "condensed system with at least two, and preferably three, hexagons in each direction" (7) are thought to be necessary before the model system "may be regarded as graphite and not as a large molecule approximating to graphite" (7), in future work we shall analyze even larger heteroatom-containing graphene layers. For now, we focus on the electron density at the edge carbon atoms, since surprisingly few papers (12,13) have been devoted to this crucial issue for carbon gasification reactivity.

PRELIMINARY RESULTS AND DISCUSSION

Tables 1 and 2 summarize some of our preliminary results. A key unresolved issues is the degree of localization of carbon's π electrons during gasification reactions. In particular, if the localization of π electrons contributes to the stabilization of free edge sites, as has been argued elsewhere (9), then the resultant redistribution of charge density will produce changes in C-C bond lengths, thus affecting CO and/or CO₂ desorption, as well as changes in the affinity of edge sites toward reactant gas chemisorption. Indeed, Wiberg (14) recently used ab initio MO theory to conclude that π electron distribution in condensed aromatic systems is the dominant factor in determining bond lengths.

It is seen in Tables 1a and 2a (note the underlined values) that the presence of carbonyl oxygen produces a consistent increase in the C-C bond lengths adjacent to the C=O group. This in turn supports the concept of induced heterogeneity in carbon gasification kinetics (2,3). It is also interesting to note that the predicted adjacent bond weakening effects of chemisorbed oxygen are sensitive to both the concentration and the exact location of C-O surface complexes. Thus, for example, while bond C8-C9 in structure P3b is weaker than bond C9-C12, as intuitively expected, bond C6-C7 in structure P3a is not weaker than bond C7-C14.

Tables 1b and 2b show that the electron density distribution using the Mulliken population analysis must be subjected to close scrutiny. (The underlined values in Table 2b are the atomic charges on the edge carbon atoms.) While the C atoms adjacent to the carbonyl group are predicted to have a higher affinity for O₂, the electron density at other reactive sites may be lower.

To what extent these trends are affected, in quantitative and perhaps even qualitative terms, when more realistic edge saturation and molecular size effects are introduced, and how this can affect carbon gasification kinetics (15), is the subject of our continued studies.

Table 1a. Comparison of C-C bond lengths (Å) in 2-ring model structures using B3LYP/6-31G(d)//HF/3-21G* with Gaussian 98W.

	1-2	2-3	3-4	4-10	5-10	5-6	6-7	7-8	8-9	1-9
N1	1.357	1.414	1.357	1.419	1.419	1.357	1.414	1.357	1.419	1.419
N3a	1.323	<u>1.475</u>	<u>1.477</u>	1.330	1.466	1.323	<u>1.475</u>	<u>1.477</u>	1.330	1.466
N3b	<u>1.479</u>	<u>1.473</u>	1.326	1.461	1.336	1.459	1.328	<u>1.472</u>	<u>1.495</u>	1.327

Table 1b. Comparison of atomic charges in 2-ring model structures using B3LYP/6-31G(d)//HF/3-21G* with Gaussian 98W.

	C1	C2	C3	C4	C5	C6	C7	C8	C9	C10
N1	-186	-134	-134	-186	-186	-134	-134	-186	.131	.131
N3a	-138	-189	.448	-.305	-.138	-.189	.448	-.305	.182	.182
N3b	-.190	.503	-.271	-.169	-.216	-.219	-.258	.558	-.163	-.078

Table 2a. Comparison of C-C bond lengths (Å) in 4-ring model structures using B3LYP/6-31G(d)//HF/3-21G* with Gaussian 98W.

	1-10	10-12	9-12	8-9	8-14	7-14	6-7
P1	1.382	1.390	1.445	1.338	1.445	1.390	1.382
P3a	1.326	1.464	1.367	1.405	1.363	<u>1.485</u>	<u>1.474</u>
P3b	1.396	1.370	<u>1.475</u>	<u>1.523</u>	<u>1.476</u>	1.370	1.396
P3c	<u>1.470</u>	1.333	1.463	1.325	1.463	1.333	<u>1.470</u>

Table 2b. Comparison of atomic charges in 4-ring model structures using B3LYP/6-31G(d)//HF/3-21G* with Gaussian 98W.

	C1	C10	C12	C9	C8	C14	C7	C6
P1	-0.119	-0.230	0.161	-0.186	-0.186	0.161	-0.230	-0.119
P3a	<u>-0.179</u>	<u>-0.157</u>	0.167	<u>-0.227</u>	<u>-0.185</u>	0.048	0.390	<u>-0.179</u>
P3b	<u>-0.121</u>	<u>-0.190</u>	0.050	0.339	0.339	0.050	<u>-0.190</u>	<u>-0.121</u>
P3c	0.470	<u>-0.343</u>	0.238	<u>-0.171</u>	<u>-0.171</u>	0.238	<u>-0.343</u>	0.470

REFERENCES

1. L. R. Radovic, in *Encyclopedia of Materials: Science and Technology*. K. H. J. Buschow et al., Eds., Pergamon, Amsterdam, 2000, in press.
2. K. Skokova, L. R. Radovic, "On the role of carbon-oxygen surface complexes in the carbon/oxygen reaction mechanism," American Chemical Society, Div. Fuel Chem. Preprints, New Orleans (1996), p. 143.
3. K. A. Skokova, L. R. Radovic, in preparation (2000).
4. J. B. Foresman, A. Frisch, *Exploring Chemistry with Electronic Structure Methods*, Gaussian, Inc., Pittsburgh, 1996.
5. N. Chen, R. T. Yang, *Carbon* **36**, 1061-1070 (1998).
6. T. Kyotani, A. Tomita, *J. Phys. Chem. B* **103**, 3434-3441 (1999).
7. M. Bradburn, C. A. Coulson, G. S. Rushbrooke, *Proc. Royal Soc. Edinburgh A* **62**, 336-349 (1948).
8. M. J. Frisch et al., Gaussian, Inc., 1998.
9. L. R. Radovic, in *Surfaces of Nanoparticles and Porous Materials*. J. A. Schwarz, C. I. Contescu, Eds., Marcel Dekker, New York, 1999, pp. 529-565.
10. C. A. Coulson, L. J. Schaad, L. Burnelle, "Benzene to Graphite-The Change in Electronic Energy Levels," Third Biennial Conference on Carbon, University of Buffalo, Buffalo, NY, Pergamon Press, 1959, p. 27.
11. S. E. Stein, R. L. Brown, *J. Amer. Chem. Soc.* **109**, 3721-3729 (1987).
12. C. A. Coulson, "The electronic structure of the boundary atoms of a graphite layer," Fourth Conference on Carbon, University of Buffalo, Buffalo, NY, Pergamon Press, 1960, p. 215.
13. D. J. Klein, L. Bytautas, *J. Phys. Chem. A* **103**, 5196-5210 (1999).
14. K. B. Wiberg, *J. Org. Chem.* **62**, 5720-5727 (1997).
15. T. Kyotani, K.-I. Ito, A. Tomita, L. R. Radovic, "Monte Carlo Simulation of Carbon Gasification Using Molecular Orbital Theory," *AIChE J.* **42**, 2303-2309 (1996).

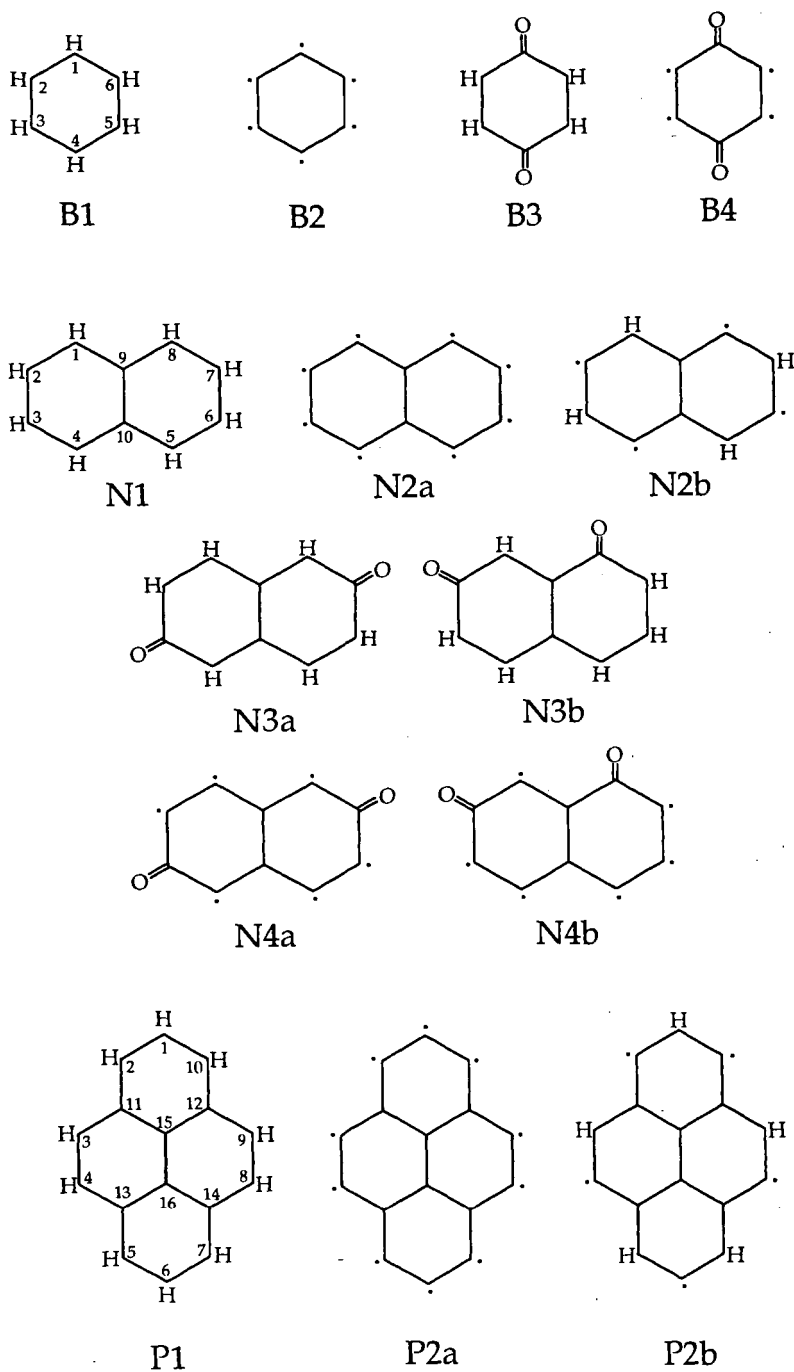


Figure 1. Model structures selected to represent the important surface chemistry effects in carbon gasification kinetics.

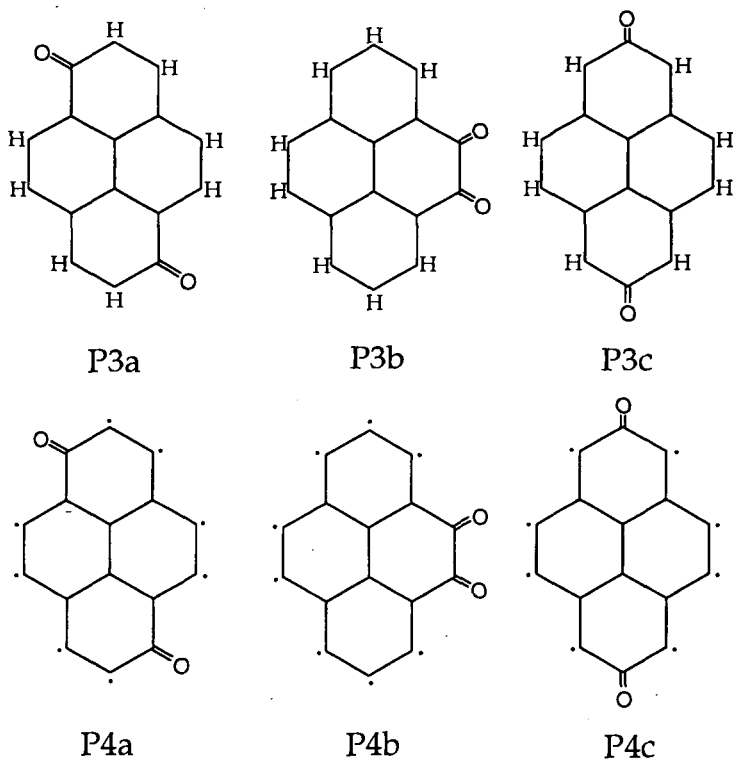


Figure 1 (continued). Model structures selected to represent the important surface chemistry effects in carbon gasification kinetics.

HYDROGENATION MECHANISM OF BENZYL ALCOHOL IN POLAR SOLVENTS ESTIMATED BY MO CALCULATION

Hideyuki Takagi, Takaaki Isoda, Katsuki Kusakabe and Shigeharu Morooka

Department of Materials Physics and Chemistry, Graduate School of Engineering,
Kyushu University, Fukuoka 812-8581, Japan

Key words: MO calculation, hydrogenation of benzyl alcohol in polar solvent,
reaction coordinate

INTRODUCTION

The hydrogenation of aromatic structures is a key reaction in the hydrorefining of heavy oil, asphaltene and coal extracts. In previous studies,^{1,2} we examined the hydrogenation of benzyl alcohol, which was the model compound as the coal extracts from low rank coal, over a ruthenium catalyst at 120°C in a variety of solvents. Our findings showed that the hydrogenation reactivity of benzyl alcohol was related to the relative permittivity of the reaction medium, but the mechanism was not clarified in detail.

Recently, the computer chemistry have been developed, and the structures of intermediates during the chemical reaction can be estimated by molecular orbital (MO) calculation using the personal computer.³ In an earlier study,⁴ we calculated changes in the reaction coordinates during the hydrogenation of benzene and found that the calculated activation energy agreed with that obtained experimentally. A conductor-like screening model (COSMO) assumes that the solvent is a homogeneous medium with a relative permittivity. The reaction coordinate for the hydrogenation of an aromatic compound in a polar solvent can be then analyzed via the application of the COSMO method to the MO calculation.

In the present study, benzyl alcohol was hydrogenated using a ruthenium catalyst at 120°C at a hydrogen pressure of 6 MPa in polar solvents. The reaction coordinate for hydrogenation of benzyl alcohol was estimated by MO calculation, in conjunction with the COSMO method, and the hydrogenation mechanism in polar solvents was discussed.

EXPERIMENTAL SECTION

Benzyl alcohol and ethanol were used as the substrate and the solvent, respectively. An alumina-supported ruthenium catalyst (Ru/Al₂O₃, Wako Chemical) was used as a hydrogenation catalyst. A typical reaction involved the use of 3 g of benzyl alcohol, 0.5 g of catalyst, and 6 g of ethanol. In order to vary the permittivity of the medium, a 3 g portion of formic acid or acetic acid was added. The relative permittivity of a mixed solvent, P_{mix} , can be calculated from the following equation.

$$P_{\text{mix}} = (P_i X_i + P_j X_j) / (X_i + X_j) \quad (1)$$

where P_i and P_j are the relative permittivities of solvent i and solvent j , respectively. X_i and X_j are the mass fractions of solvent i and j , respectively, ($X_i + X_j = 1$). Table 1 shows the relative permittivity of solvents. All reactions were performed in a 50-mL batch autoclave at 120°C for 0-30 min under a hydrogen pressure of 6 MPa. After the reaction, the products were qualitatively and quantitatively analyzed by GC-FID (GC-14A, Shimadzu) and GC-MS (QP-5000, Shimadzu), equipped with a capillary column. Details of the reaction have been reported previously.² Reaction rate constants for the hydrogenation of benzyl alcohol in solvents were then determined from the yields of products.

SIMULATION

Figure 1 shows the pathways for reaction of benzyl alcohol over the Ru/Al₂O₃ catalyst.¹ Hydrogenation of the aromatic ring (route 1) and hydrogenolysis of hydroxy group (route 2) proceed competitively. Cyclohexanecarbaldehyde is produced via route 1, and toluene via route 2. Methylcyclohexane is produced via the hydrogenation of the produced toluene.

A molecular orbital (MO) calculation for hydrogenation of benzyl alcohol was carried out using WinMOPAC Vr.1 (Fujitsu) based on a PM3 Hamiltonian method, and the energy minimization

was defined by an EF method.³ A hydrogen atom was coordinated to an optional atom located on benzyl alcohol or an intermediate molecule. The reaction coordinate between the hydrogen atom and the substrate was then calculated from 3 Å to 1 Å at a step of 0.1-0.2 Å using the COSMO method. The heat of formation was plotted against the reaction coordinate, and the activation energy was calculated as follows:

$$E_c = E_t - E_p \quad (2)$$

where E_c is the activation energy. E_t and E_p are the heat of formation of the transition complex and that of the initial or intermediate compound, respectively.

RESULTS

Hydrogenation via route 1

Figure 2 shows the relationship between the reaction rate constant of route 1 for the hydrogenation of benzyl alcohol at 120°C and the relative permittivity of the medium. The rate constant for route 1 was $8.2 \times 10^{-4} \text{ s}^{-1}$ with no solvent, and $4.5 \times 10^{-4} \text{ s}^{-1}$ in ethanol as the solvent. The addition of acetic acid led to a decrease in the relative permittivity of the medium, and an increase in the rate constant to $8.2 \times 10^{-4} \text{ s}^{-1}$, which was equal to that for the reaction with no solvent. The hydrogenation was completely retarded by the addition of formic acid with a high relative permittivity. This indicates that the rate constant of route 1 can be related to the relative permittivity of the reaction medium.

Figure 3 shows the change in the reaction coordinate for the hydrogenation of benzyl alcohol via route 1. In step 1, the activation energy is 24.6 kcal/mol with no solvent (relative permittivity = 13.1), and 46.6 kcal/mol for the ethanol-formic acid solution (relative permittivity = 30.0). No activation energy is apparent for step 2. In step 3, the activation energy is 12.0 kcal/mol with no solvent, and 26.9 kcal/mol for the ethanol-formic acid solution. In addition, no activation energy is apparent for step 4. A hydrogen atom is not introduced into the double bond of 1-cyclohexanymethanol, based on the MO calculation. This supports the experimental findings that 1-cyclohexanymethanol was converted to cyclohexanecarbaldehyde.^{1,5}

Figure 4 shows the activation energy in route 1 for the hydrogenation of benzyl alcohol as a function of the relative permittivity. The activation energy is determined as the sum of the values of steps 1 and 3. The activation energy is 49.9 kcal/mol for the hydrogenation in ethanol and is decreased to 43.9 kcal/mol by the addition of acetic acid with a low relative permittivity. On the other hand, the activation energy is increased to 73.5 kcal/mol by the addition of formic acid with a high permittivity. In the route for hydrogenation of the aromatic ring in benzyl alcohol, the activation energy, which is estimated from the MO calculation, decreases with decreasing

Table 1. Relative Permittivity of Solvents

system	composition in weight [g] (substrate:solvent:additive)	relative permittivity of mixed solvent
in vacuum		0.0
benzyl alcohol (no solvent)		13.1
ethanol	3 : 6	20.6
ethanol/acetic acid	3 : 6 : 3	17.0
ethanol/formic acid	3 : 6 : 3	30.0

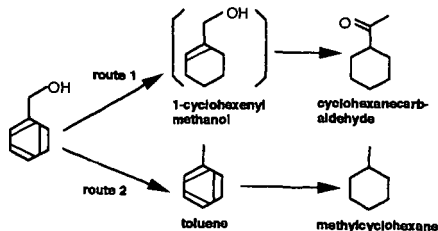


Figure 1. Pathways for reaction of benzyl alcohol over $\text{Ru}/\text{Al}_2\text{O}_3$ catalyst.

relative permittivity of the solution.

Hydrogenolysis via route 2

Table 2 shows the reaction rate constant for hydrogenation of benzyl alcohol via route 2. The rate constant at 120°C was $0.59 \times 10^{-4} \text{ s}^{-1}$ with no solvent, and remained unchanged after the addition of ethanol. The addition of acetic acid in ethanol lead to an increase in the rate constant to $1.57 \times 10^{-4} \text{ s}^{-1}$. Figure 5 shows the hydrogenolysis reaction via route 2, as estimated by the MO calculation. A proton (H^+) is linked to the oxygen atom of the hydroxy group, and intermediate-1 is formed. However, hydrogen atom (H) cannot be attached to the hydroxy group nor the carbon atoms adjacent to the hydroxy group. Intermediate-2 is formed by the attack of a hydrogen atom and then is decomposed, producing toluene and water. This suggests that the hydrogenolysis of the hydroxy group

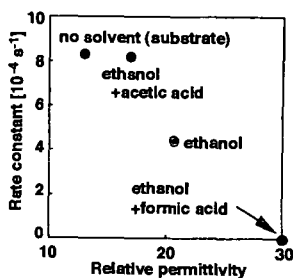


Figure 2. Relationship between reaction rate constant of route 1 for hydrogenation of benzyl alcohol 120°C and relative permittivity of medium.

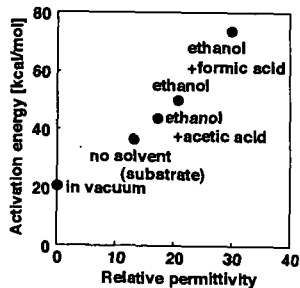


Figure 4. Activation energy in route 1 for hydrogenation of benzyl alcohol as a function of relative permittivity.

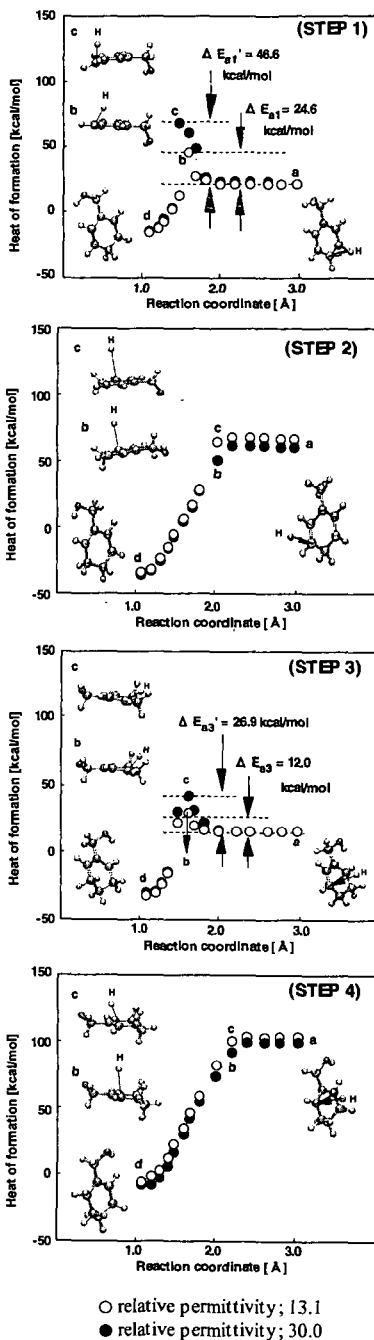


Figure 3. Changes in reaction coordinate for hydrogenation of benzyl alcohol via route 1.

Table 2. Reaction Rate Constant for Hydrogenation of Benzyl Alcohol via Route 2

system	rate constant [10^{-4} s^{-1}]
benzyl alcohol (non-solvent)	0.59
ethanol	0.58
ethanol/acetic acid	1.57
ethanol/formic acid	0.0

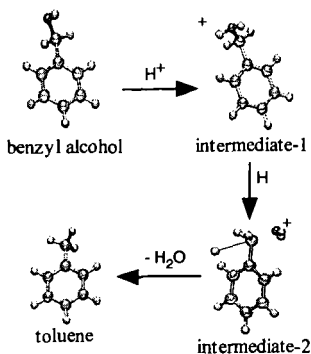


Figure 5. Hydrogenolysis reaction via route 2 estimated by MO calculation.

proceeds via an $\text{S}_{\text{N}}2$ mechanism.

DISCUSSION

The hydrogenation reaction of aromatic compounds with polar substituents, as well as benzyl alcohol, can be divided into two routes; hydrogenation of aromatic ring; and hydrogenolysis of oxygen-containing substituents and bridge bonds. As shown in Figure 2, the rate constant for hydrogenation of the aromatic ring, which was obtained by experimental results, increases with decreasing relative permittivity of the solution. The MO calculation indicates that the heat of formation for the transition state is dependent on the structure, which vary with the relative permittivity of the solution. The heat of formation for the transition state decreases with decreasing relative permittivity of the solution, and, as a result, the activation energy of route 1 decreases. This MO calculation suggests that the value of the heat of formation is related to the reaction rate of route 1. Present study also clarified that the hydrogenolysis of benzyl alcohol is an $\text{S}_{\text{N}}2$ reaction and is promoted by the donation of a proton from the solvent.

CONCLUSIONS

The reaction rate for route 1 increased with decreasing relative permittivity of the solution. The activation energy for hydrogenation of the aromatic ring in benzyl alcohol was estimated by an MO calculation, and decreased with decreasing relative permittivity of the reaction medium. Hydrogenolysis of the OH group in benzyl alcohol was promoted by donating a proton from the solvent, and was consistent with proceeding via an $\text{S}_{\text{N}}2$ reaction. The addition of acetic acid in ethanol enhanced the hydrogenation of the aromatic ring, as well as the hydrogenolysis of benzyl alcohol, but the addition of formic acid inhibited the catalyst activity. This concludes the role of the additives in hydrogenation of aromatic compounds with polar substituents.

ACKNOWLEDGMENT

This work was supported in part of by a "Research for the Future Project" grant from the Japan Society for the Promotion of Science (JSPS), through the 148th Committee on Coal Utilization Technology. Dr. Jerzy M. Rudziski and Ms. Mayumi Matsushita of Fujitsu Kyushu System Engineering Ltd., Japan, supported the computer software used in this study. Useful discussion with Dr. Keiichiro Samejima of Fujitsu Ltd., Japan is deeply acknowledged.

REFERENCES

- (1) Takagi, H.; Isoda, T.; Kusakabe, K.; Morooka, S. *Energy Fuels* **1999**, *13*, in press.
- (2) Takagi, H.; Isoda, T.; Kusakabe, K.; Morooka, S. *Prepr. Pap- Am. Chem. Soc., Div. Fuel Chem.* **1999**, *44*, 1029.
- (3) Isoda, T.; Takase, Y.; Isumi, N.; Kusakabe, K.; Morooka, S. *J. Jpn. Pet. Inst.* **1998**, *41*, 318.
- (4) Takagi, H.; Isoda, T.; Kusakabe, K.; Morooka, S. *Energy Fuels*, to be submitted.
- (5) Nisimura, S.; Hama, M.; *Bull. Chem. Soc. Jpn.* **1966**, *39*, 2467.

Analysis Of Initial Stage Reactions In Coal Pyrolysis By Molecular Orbital Calculation

Takaaki Isoda, Hideyuki Takagi, Katsuki Kusakabe and Shigeharu Morooka

Department of Materials Physics and Chemistry, Graduate School of Engineering,
Kyushu University, Fukuoka 812-8581, Japan

INTRODUCTION

Pyrolysis of coal has been explained based on a chemical percolation and dissociation model [1]. In the early stage of pyrolysis, cross-link structures, which connect aromatic units, as well as peripheral groups, are cleaved, and radical fragments are produced. These radicals are rapidly stabilized to gases, tar and char. The overall pyrolysis reactivity is dependent on the structure of coal.

We recently reported, however, a combination of H_2O_2 oxidation in the presence of alcohols and hydrogenation of the ethanol-extracted samples using a Ru/Al_2O_3 catalyst can alter the coal structure and increase the pyrolysis reactivity. [2] When Yallourn coal was treated by the H_2O_2 oxidation in the presence of alcohols and by the hydrogenation at $120^\circ C$ for 12-72 h at a hydrogen pressure of 10 MPa, the char yield of flash pyrolysis was decreased from 50wt% for the raw coal to 25wt% for the treated coal [2]. Structural analyses of the hydrogenated coal indicated that aromatic rings of the raw coal were partially converted to saturated rings [3]. This indicates that the coal pyrolysis reactivity is also depended on the unit structure in the coal macromolecule.

In this study, pyrolysis reactivities, as well as product distributions, of raw coals was evaluated using a Curie-point pyrolyzer (CPP). The cleaving energies of unit structures of coal were estimated by a reaction coordinate analysis based on molecular orbital calculation. The coal pyrolysis reactivity was then discussed on the basis of the cleaving energy of unit structures.

EXPERIMENTAL SECTION

Pyrolysis; The elemental composition of the coal is summarized in Table I. Yallourn (YL), South Banko (SB), Taiheiyō (TH), Miike (MI), and Hunter Valley (HV) coals were ground to give particles which were 37-74 μm in size, and dried at $70^\circ C$ for 24 h prior to use. A coal sample of 1.5 mg was tightly wrapped with a ferromagnetic foil and pyrolyzed at $386-1040^\circ C$ using a Curie-point pyrolyzer, which could heat the sample at a heating rate of 3000 K/s. Produced gases were analyzed by GC-TCD and GC-FID. Details of the CPP were reported previously [4].

MO Calculation; The decomposition of unit structures of coals was simulated using WinMOPAC V.1 and 2 (Fujitsu), based on a PM3 Hamiltonian and an unrestricted Hartree-Fock method [5]. The unit structure of coal were assumed to be terminated with hydrogen atoms. The molecular weight of the unit structures were 370-398, depending

on coal ranks [6].

RESULTS AND DISCUSSION

Fig.1 shows the snapshots for the detachment of a methoxy group, which is substituted on the unit model structure of a low rank coal (YL). Fig.2 shows the changes in the heat of formation (H.O.F.), corresponding to Fig.1. The distance between the oxygen atom of the methoxy group and the carbon atom of the benzene ring is increased from position with a step of 0.1 Å. The H.O.F., which is E_a at position a, increases with increasing reaction coordinate, and the bond is cleaved at position b. The H.O.F. then approaches to a final value, E_c , when the reaction coordinate is over 2.5 Å [2]. Thus, the energy, which is required to cleave the bond, is calculated from

$$E_{cal} = E_c - E_a \quad (1)$$

where E_c and E_a are the H.O.F. at the excited state (position c) and that at the ground state (position a), respectively. Tables 2-4 show the calculated cleaving energies. The numbers in the tables correspond to those in the unit structure models [6]. As shown in Fig.3, the cleaving energies are similar for the coal unit structure models, because the unit structures are not suffered by the effect of non-covalent bond and steric hindrance in the structure. The C=C double bond requires the largest cleaving energy, 420-470 kJ/mol. The cleavage of single bonds on the benzene ring, such as -OH, -Me, and -H groups, needs cleaving energies of 340-410 kJ/mol. This indicates that the elimination of hydroxy and methyl groups and hydrogen from the benzene ring is rather difficult during pyrolysis. However, the elimination of C-C and C-O bonds requires cleaving energies of 170-300 kJ/mol. The cleaving energy of a carboxy group from the benzene ring of the low rank coal is as low as 159 kJ/mol.

The pyrolysis of raw coals was initiated at 350°C, and the coal conversion increased with increasing temperature in the range of 500-800°C. Fig.4 shows the effect of the reaction temperature on the yields from the flash pyrolysis of the YL coal. The temperature effect can be described by the enthalpy, Q_c , which the coal sample attains during the heating from the initial temperature, T_1 , (50°C) to the reaction temperature, T_2 . Assuming that the heat capacity of the coal sample, C_p , is constant in the temperature range, the enthalpy can be described as follows:

$$Q_c = C_p(T - T_1) \quad (2)$$

where Q_c and C_p are expressed based on the mole of carbon in the raw coal. The enthalpy was 6.3-23.3 kJ/mol-C under the present experimental conditions.

As shown in Fig.4, the yield of CO_2 was increased at $Q_c = 8.9$ kJ/mol-C. This is ascribed to the decomposition of carboxy (C-COOH) and methoxy (O-Me) groups. Methylene cross-links (methylene C-C), C-C and C-H single bonds in naphthenic rings (cyc C-C and cyc C-H) may be cleaved in the range of 10-15 kJ/mol-C. The detachment of hydrogen from methyl groups (H-CH₂-) and that of methyl groups (C-Me) also proceeds in this enthalpy range, and the yields of tar and hydrocarbon gases were increased. Double bonds on the aromatic rings (benzene C=C) were cleaved above 450 kJ/mol on the MO calculation, as well as high temperature, whereas the coal conversion was mostly saturated above 20 kJ/mol-C. The coal is then converted to char, which was stable at high temperatures.

Fig.5 shows the yield of total volatile matter, TVM, from pyrolysis of coals of

different ranks. The TVM from the low-rank and subbituminous coals was increased in the range of $Q_c > 10$ kJ/mol-C, and the pyrolysis reactions are ascribed to the decomposition of carboxy and methoxy groups. However, the TVM from the bituminous coals is increased in the range of 10-17 kJ/mol-C and is mostly composed of tar. In this energy range, cross-links were cleaved, and hydrogen was detached, radicals were effectively stabilized by the hydrogen transfer mechanism, and tar was formed. The above experimental results are in agreement with the order of the calculated cleaving energies shown in Fig.3. The pyrolysis reactivity of coal is decided by parallel radical reactions, of which the activation energies are lower than the cleaving energies. Thus, the activation energies for pyrolysis cannot be directly compared to the cleaving energies calculated by the MO calculation. Under the present pyrolysis conditions, however, the pyrolysis reactions occurred in the range of $Q_c = 7-20$ kJ/mol-C. These values are equivalent to approximately 1/20 of the calculated cleaving energies.

LITERATURE CITED

- [1] Grant, D.M.; Pugmire, R.J.; Fletcher, T.H.; Kerstein, A.R. *Energy Fuels* **1989**, 3, 175.
- [2] Isoda, T.; Takagi, H.; Kusakabe, K.; Morooka, S. *Energy Fuels* **1998**, 12, 503.
- [3] Takagi, H.; Isoda, T.; Kusakabe, K.; Morooka, S. *Int. Conf. Coal Sci.* **1999**, Vol. I, p.255.
- [4] Hayashi, J.-i.; Mizuta, H.; Kusakabe, K.; Morooka, S. *Energy Fuels* **1994**, 8, 1353.
- [5] Hirano, T.; Tanabe, K.; *Mopac Guide Book*, Kaibunshodo, Tokyo, 1991.
- [6] Murata, S.; Miura, M.; Nomura, M.; Takanohashi, T.; Iino, A.; Kumagai, H.; Sanada, Y.; Nakamura, K.; *J. Jpn. Inst. Energy* **1995**, 74, 342.
- [7] Hirano, T.; *Chemical Review*, **1998**, 5, 19.

Acknowledgements. Dr. Jerzy M. Rudziski and Ms. Mayumi Matsushita of Fujitsu Kyushu System Engineering Ltd., Japan, supported the computer software used in this study. Useful discussion with Dr. Keiichiro Samejima of Fujitsu Ltd., Japan is deeply acknowledged.

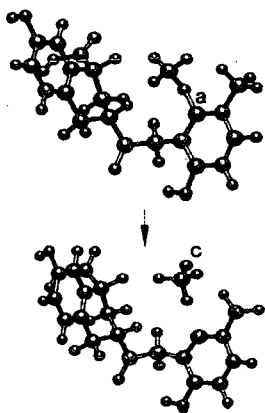


Fig.1 Detachment of a methoxy group from the unit structure model of low rank coal. (Reaction coordinate, a 1.3 Å, c 4.0 Å)

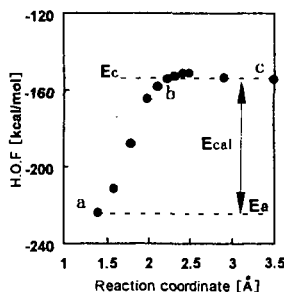


Fig.2 Changes in the heat of formation for detachment of a methoxy group from the unit structure model of low rank coal. Positions a and c correspond to those in Fig.1.

Table 1 Elemental Composition of Coals

coal (abbreviation)	elemental analysis [wt%-daf]				
	C	H	N	(O+S) ^{a)}	ash
Hunter Valley (HV)	80.6	5.5	2.1	11.8	9.5
Miike (MK)	77.9	6.3	1.2	14.6	16.1
Taiheiyō (TH)	73.8	6.6	1.2	18.4	10.9
South Banko (SB)	68.5	5.4	1.2	24.8	2.0
Yalloom (YL)	60.4	5.0	0.5	34.1	1.2

^{a)} determined by reference

Table 2 Cleaving Energies of Bonds in the Unit Structure Model of Low Rank Coal.

bond	position	cleaving energy [kJ/mol]
C-OMe	1	295
O-Me	2	170
C-Me	3	340
C-OH	4	391 - 394
CO-H	5	395
H-C-H	6	295 - 318
benzene-H	7	386 - 416
CO-OH	8	340
C-COOH	9	159
methyleneC-C	10	163 - 320
cycC-C	11	233 - 291
benzeneC=C	12	422 - 474
cycC-H	13	260-306

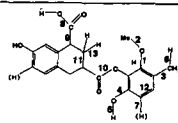


Table 3 Cleaving Energies of Bonds in the Unit Structure Model of Subbituminous Coal.

bond	position	cleaving energy [kJ/mol]
C-Me	1	343
H-CH ₂ -	2	320
C-OH	3	376
H-OC-	4	262
H-CH-	5	257
benzene-H	6	385
C-O	7	189
methyleneC-C	8	227
benzeneC=C	9	448
2benzene-C	10	307
2benzeneC=C	11	469

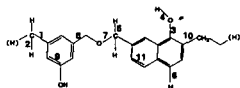


Table 4 Cleaving Energies of Bonds in the Unit Structure Model of Bituminous Coal.

bond	position	cleaving energy [kJ/mol]
C-Me	1	341
C-OH	2	389
H-OC-	3	288
H-CH ₂ -	4	298
benzene-H	5	407
H-CH-	6	279
C-O	7	169
methyleneC-C	8	243
2benzeneC=C	9	457
3benzeneC=C	10	395

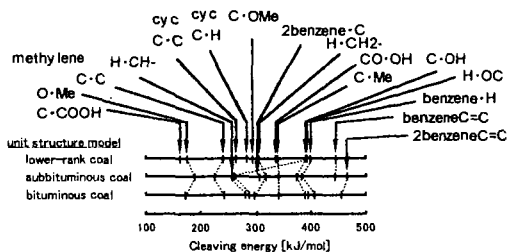
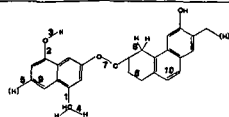


Fig. 3 Cleaving energies for the unit structure models.

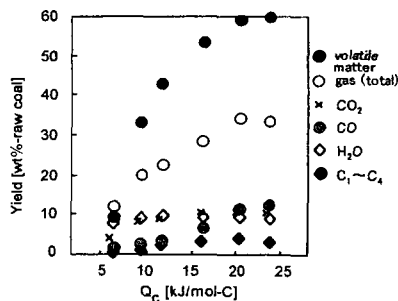


Fig. 4 Effect of enthalpy changes for 1mol of raw coal carbon, Q_c , on product yields by pyrolysis of YL coal.

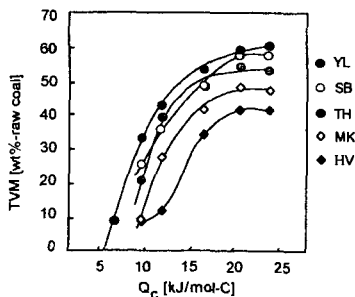


Fig. 5 Effect of enthalpy changes for 1mol of raw coal carbon, Q_c , on the yield of total volatile matter by pyrolysis of coals.

MODELING OF MOLECULAR STRUCTURE OF UPPER FREEPORT COAL BY USING ^{13}C NMR CHEMICAL SHIFT CALCULATION

Toshimasa Takanohashi* and Hiroyuki Kawashima
Energy Resources Department, National Institute for Resources and Environment,
Tsukuba 305-8569, JAPAN

KEYWORDS: coal; model structure; ^{13}C NMR

INTRODUCTION

Many analytical techniques have been widely applied to structural analysis of coal. Solid-state ^{13}C NMR is one of the attractive tools for characterization of coal since coal is hard to dissolve in ordinary organic solvents. Recently, ^{13}C NMR chemical shift prediction software has been used to obtain information of chemical structure of various materials such as polymers. Thomas et al. calculated ^{13}C chemical shift for some substituted pyridines using several NMR prediction programs and showed that the results of the prediction gave good agreement with the experimental values¹.

Several structural models for coal have been based on analytical data obtained with the methods such as pyrolysis GC-MS, ^{13}C NMR measurement²⁻⁴ and hydrogenation HPLC/GC-MS⁵. However, original structures of coals may be broken by pyrolysis and hydrogenation reactions, and only volatile materials of coals may be detectable on the GC techniques. On the other hand, for extract fractions obtained from a room temperature extraction for Upper Freeport coal, the model structures based on the structural parameters obtained from ^1H NMR and ultimate analysis were constructed⁶. Since no significant reaction such as bond breaking seemed to occur during the extractions, model structures based on original chemical structures could be constructed. However, information of types of carbon atom in the extract fractions was insufficient with ^1H NMR, and furthermore the model structure for the extraction residue could not be obtained, since it was insoluble in solvents.

To get directly information of chemical structures of a whole coal including the extraction residue, solid state ^{13}C NMR spectra were measured for several fractions which were obtained from extraction and fractionation at room temperature. The calculated ^{13}C NMR spectra by using an NMR prediction software were determined⁷ for the model structures of the extract fractions that have been suggested by Takanohashi and co-workers⁶. The model structures were improved to fit experimental spectra. In addition, a model structure of the extraction residue was constructed and revised by comparison between its calculated ^{13}C NMR spectrum and the experimental one. Finally, a model structure of Upper Freeport coal including the extraction residue is suggested.

EXPERIMENTAL

Sample Preparation

Upper Freeport coal, which is an Argonne premium coal sample was obtained in ampoules (5 g of -150 μm)⁸. The coal sample was extracted exhaustively with a carbon disulfide / *N*-methyl-2-pyrrolidinone (CS_2 / NMP) mixed solvent at room temperature⁹. The extract obtained was further fractionated by acetone and pyridine into three fractions, acetone-soluble (AS), acetone-insoluble and pyridine soluble (PS), and pyridine-insoluble (PI) fractions, as shown in Figure 1. The PS, PI and residue (the mixed solvent-insoluble (MI) fraction) were washed with acetone, and the AS was washed with acetone - water (1:4 by volume) solutions. All fractions were dried in a vacuum oven at 80 $^\circ\text{C}$ for 12 hr.

NMR measurements

Solid state ^{13}C NMR spectra were measured by both CP/MAS and SPE/MAS methods using a Chemmagetics CMX-300 NMR spectrometer operating at a ^{13}C frequency of 75.46 MHz. All spectra were acquired employing a ^1H 90 $^\circ$ pulse length of 4 μs . This was combined with a magic angle spinning rate of 10kHz. Repetition rates of 4s (CP/MAS) and 60s (SPE/MAS) were used

for all samples. For each spectrum, 4000 (CP/MAS) and 2000 (SPE/MAS) scans were accumulated. The contact time of CP/MAS was 1 ms. The chemical shifts were calibrated with respect to tetramethylsilane using the peak of methyl group on hexamethylbenzene at 17.4 ppm as the external standard.

NMR chemical shift calculation

Chemical shift calculations were carried out using a ACD laboratory C NMR predictor software. The software allows treatment of molecules containing up to 256 carbon atoms. The chemical shift of model structure is calculated by searching for similar sub-structural fragment with the corresponding experimental shift value in the database (600,000 chemical shifts of 50,000 compounds) and evaluating the chemical shift value taking into account intramolecular interactions. The calculated ^{13}C NMR spectra of the model structures for the fractions were obtained by considering an adequate line width.

RESULTS AND DISCUSSION

NMR spectra.

The distributions of types of carbon atom obtained by deconvolution of ^{13}C NMR spectra for each fraction are shown in Figures 2. For all spectra, SPE/MAS gave the lower ratios of CH_3 , CH_2 , CH carbon and higher ones of aromatic and $\text{CH}_2\text{-O-}$ carbon than CP/MAS. This is explained by that carbons with low CP efficiency such as non-protonated aromatic ones could be detected by SPE/MAS. Thus, for samples including many inner carbons like coal, SPE/MAS method may give more quantitative spectrum, although there are other problems such as background of spectrum. While, compared among fractions, the lighter fraction gave larger differences between both methods. Furthermore, the SPE/MAS data showed that except for AS fraction that is the lightest of all fractions here, all fractions including the extraction residue gave a similar distribution of carbon types. Nakamura et al. analyzed aromatic structures of several fractions obtained from mild hydrogenation and reported that ring structures for all fractions including an extraction residue were similar⁵. Iino et al. have also found¹⁰ that addition of small amount (1%) of tetracyanoethylene (TCNE) to the CS_2 /NMP mixed solvent enhanced greatly the extraction yield of Upper Freeport coal, i.e., the original MI became part of the PI fraction, and concluded that the effect of TCNE addition is attributed to dissolution of associates of the coal molecules. Therefore, the PS, PI and extraction residue (MI) have similar chemical structures and their difference may be due to the degree of association between coal molecules.

NMR Chemical Shift Calculation.

The model structures for AS, PS and PI fractions based on the structural parameters obtained from ^1H NMR and ultimate analysis have been suggested⁶. The calculated spectra for their model structures were obtained by using the prediction software. Next, the model structures were modified to fit the experimental spectra. Consequently, the modified model structures were obtained as shown in Figure 3. The calculated spectra of the modified models were compared with the experimental ones, which are shown in Figure 4. For all fractions, the calculated spectra were in excellent agreement with the experimentally obtained spectra. Table I shows ultimate analyses and structural parameters of each model, together with their experimental values. For AS fraction, which is the lightest of all fractions, there were differences in ultimate analysis. The model of AS fraction can be too small to express distribution of chemical structures. While, for PS, PI and MI, their ultimate analyses and structural parameters except for aromaticity, f_a were in good agreement with those of model. The f_a values of models except for AS were higher than those estimated from ^{13}C NMR and ^1H NMR measurements. This reason may be attributed to the inner carbons existed in the heavier fractions, which are hard to be relaxed even under SPE/MAS condition.

A Model Structure of Upper Freeport Coal.

Nakamura et al. constructed⁵ three-dimensionally a model structure of Zao Zhuang bituminous coal using computer-aided molecular design (CAMD) by assuming an anisotropic model structure formed from a periodic boundary cell. The same method was used to construct a model structure of Upper Freeport coal here since both coals have similar structural features⁹. The modified model structures for all fractions including the extraction residue were randomly placed in a rectangular cell, as shown in Figure 5. It is not required to connect between the models by covalent bonds, because all fractions were obtained from the room-temperature extraction and fractionation. The calculation procedure has been reported elsewhere⁵. Finally an associated model structure of Upper Freeport coal was suggested. The estimated density for the model structure was in agreement with the observed one.

CONCLUSIONS

Upper Freeport coal was extracted and fractionated at room temperature, and for all fractions including the extraction residue, ^{13}C NMR spectra were measured. The calculated ^{13}C NMR spectra by using an NMR prediction software were determined for the model structures. The model structures were modified to fit experimental spectra. For all fractions, the spectra calculated for the modified models were in excellent agreement with the experimentally obtained spectra. Finally, by using computer-aided molecular design (CAMD), an anisotropic model structure of Upper Freeport coal was suggested.

ACKNOWLEDGMENT

This work has been carried out as one of "Research for the Future" projects of the Japan Society for the Promotion of Science (JSPS) through the 148th committee on coal utilization technology of JSPS.

REFERENCES

- 1) Thomas, S.; Bruhl, I.; Heilman, D.; Kleinpeter, E. *J.Chem.Int.Comput.Sci.* **1997**, *37*, 726.
- 2) Nomura, M.; Matsubayashi, K.; Ida, T.; Murata, S. *Fuel Proc. Tech.* **1992**, *31*, 169.
- 3) Hatcher, P.G.; Faulon, J.-L.; Wenzel, K.A.; Cody, G.D. *Energy Fuels* **1992**, *6*, 813.
- 4) Faulon, J.-L.; Hatcher, P.G.; Carlson, G.A.; Wenzel, K.A. *Fuel Processing Technology* **1993**, *34*, 277.
- 5) Nakamura, K.; Takanohashi, T.; Iino, M.; Kumagai, H.; Satou, M.; Yokoyama, S.; Sanada, Y. *Energy Fuels* **1995**, *9*, 1003.
- 6) Takanohashi, T.; Iino, M.; Nakamura, K. *Energy Fuels* **1998**, *12*, 1168.
- 7) Kawashima, H.; Takanohashi, T. *Prepr.Pap.-Am.Chem.Soc., Div.Fuel Chem.* **1999**, in press.
- 8) Vorres, K.S. *Energy Fuels* **1990**, *4*, 420.
- 9) Iino, M.; Takanohashi, T.; Obara, S.; Tsueta, H.; Sanokawa, Y. *Fuel* **1989**, *68*, 1588.
- 10) Liu, H.-T.; Ishizuka, T.; Takanohashi, T.; Iino, M. *Energy Fuels* **1993**, *7*, 1108.

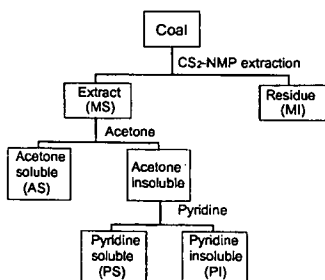


Figure 1 Procedures of Extraction and Fractionation

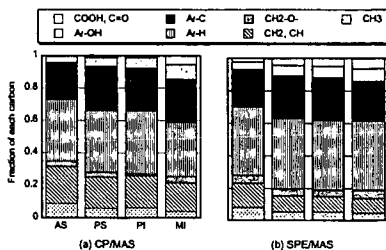


Figure 2 Solid state ^{13}C NMR spectra of the fractions (AS, PS, PI and MI) by CP/MAS (a) and SPE/MAS (b) methods.

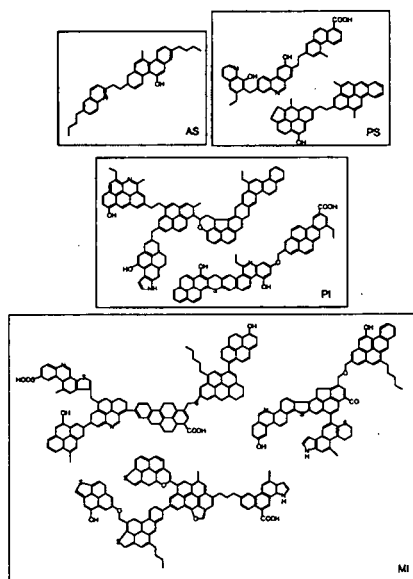


Figure 3 Modified Model Structures of Each Fraction

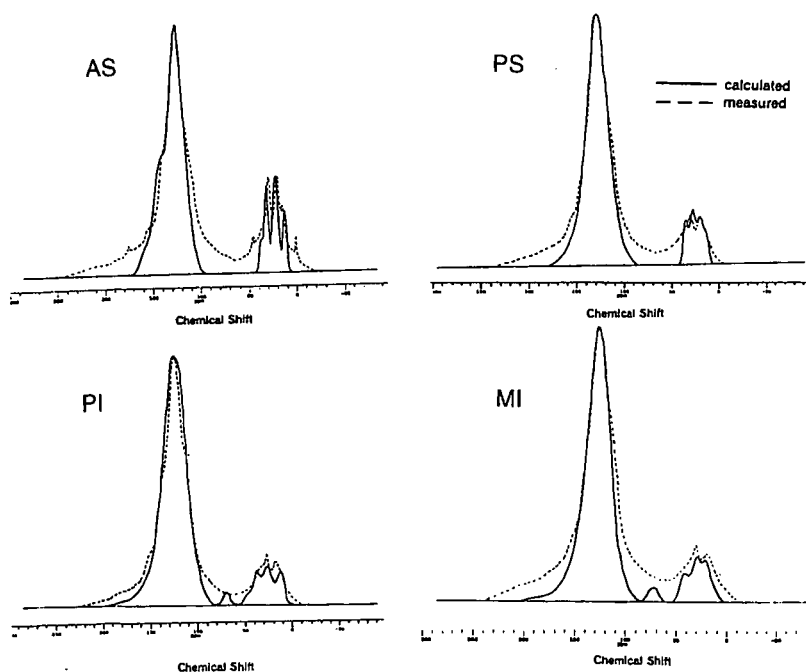


Figure 4 The measured ^{13}C NMR spectra for all fractions, and their calculated spectra.

Table 1 Ultimate Analyses and Structural Parameters for Each Fraction

fraction	C%	H%	N%	S%	O%	H/C	f_a^a
AS, observed	88.5	6.7	1.1	0.5	3.2	0.91	0.72 (0.71)
model	86.9	7.4	2.7	0.0	3.0	1.03	0.71
PS, observed	86.6	5.4	1.8	1.0	5.2	0.75	0.80 (0.78)
model	85.6	5.5	2.3	0.0	6.6	0.77	0.84
PI, observed	85.8	5.0	2.1	1.1	6.0	0.68	0.81 (0.79)
model	85.7	5.0	2.0	1.5	5.9	0.70	0.85
MI, observed	81.7	4.7	1.8	5.5	6.3	0.69	0.81
model	81.8	4.9	1.7	5.4	6.2	0.71	0.85

^aThe values in parenthesis are calculated from ¹H NMR measurement.

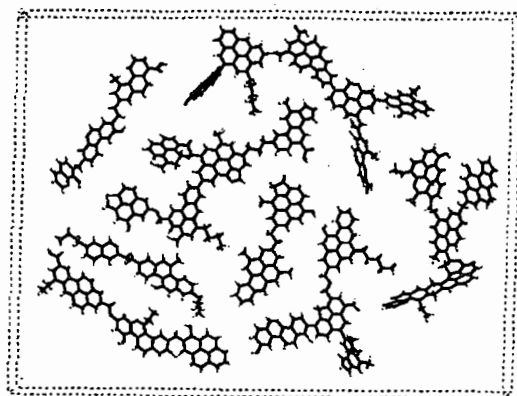


Figure 5 Coal Molecules Put Randomly in a Rectangular Cell.

CHARACTERIZATION OF CHARS FROM PYROLYSIS OF CHLOROGENIC ACID

Ramesh Sharma, Mohammad Hajaligol, Pamela Martoglio-Smith, and Jan Wooten
Philip Morris U.S.A., Research Center, P.O. Box 26583, Richmond, VA 23261

KEYWORDS: char, characterization, chlorogenic acid, combustion, pyrolysis

INTRODUCTION

Chlorogenic acid is a plant material that contains both phenolic and saccharide groups and can be a good representative model compound for biomass. It is one of the components of coffee seeds and tobacco leaves. Commercially, chlorogenic acid is extracted from coffee seeds. When pyrolyzed, chlorogenic acid is reported to undergo a rapid decomposition to form a gaseous product and a solid char. The char then undergoes further reactions to form additional product [1]. A number of studies are reported in the literature on the composition of the gaseous product from chlorogenic acid. Zane and Wender [2] heated a sample of chlorogenic acid in a flask at 600°C for 5 min and observed catechol, 4-methyl catechol, 4-ethyl catechol, benzoic acid, and quinine as the main components. Sakuma *et al.* [1] reported, in addition, phenol and 4-vinyl catechol. Schlottzauer *et al.* [3] pyrolyzed chlorogenic acid at 800°C and observed 5-hydroxymethyl furfural in addition to the above products. These studies indicate that the composition of the gaseous product is dependent on the pyrolysis conditions. Although considerable work has been done on the analysis of the gaseous product, there is no information in the literature on the nature and composition of the product char or the effect of pyrolysis conditions on char characteristics. The nature of the char may govern the extent of secondary reactions.

In this work, the effect of pyrolysis conditions on the yield and nature of chars from chlorogenic acid was studied. The chars were produced at atmospheric pressure under oxidative and non-oxidative (inert) atmospheres and at temperatures ranging from 250° to 750°C. The non-oxidative runs were made with helium as the carrier gas; the oxidative runs with a mixture of 2% oxygen in helium. The concentration of oxygen in the oxidative runs was kept low to prevent a complete combustion of the substrate. The uncondensed gaseous product was analyzed by mass spectrometry. The product char was characterized in terms of its elemental analysis and surface area and by solid-state ¹³C nuclear magnetic resonance (NMR) spectroscopy and Fourier-transform infrared (FTIR) spectroscopy. The surface morphology of char was studied by scanning electron microscopy (SEM). The results of char characterization are discussed in relation to the evolved gases.

EXPERIMENTAL

Chlorogenic acid was obtained from Fisher Scientific. It is predominantly the *trans* isomer with 99% purity. The pyrolysis reactor was a 1/2" diameter quartz tube heated by a 6" long metal-block furnace. The furnace provided about 4" length of uniform temperature profile. The runs were made at atmospheric pressure and temperatures ranging from 250° to 750°C. Up to 300 mg of chlorogenic acid was pyrolyzed in each run which lasted 10 min. The carrier gas was passed continuously over the sample at a flow rate of 220 ml/min. A sample of the uncondensed gaseous product was analyzed on-line by a Balzer QMG511 quadrupole mass spectrometer.

The elemental analysis of the product char was performed at Galbraith Laboratories, Inc. The BET surface area was measured in automated volumetric gas adsorption apparatus (Autosorb 1 from Quantachrome Co.) using nitrogen as an adsorbate. The ¹³C CPMAS NMR spectra were obtained on a Varian Unity 200 spectrometer at a carbon resonance frequency of 50.3 MHz. The MAS spinning speed was ~8100 Hz. The infrared spectra were recorded on a Spectra-Tech IR-Plan microscope interfaced to a Nicolet Magna 560 FTIR spectrometer. The sample was mounted between two KBr plates held in a micro-compression cell. For the SEM analysis, a Topcon SM720 Field Emission Scanning Electron Microscope was used.

RESULTS AND DISCUSSION

Char Yield

Figure 1 shows the effect of temperature on the yield of the solid product, *i.e.* char yield, from chlorogenic acid. In non-oxidative runs, the yield decreases with increase in temperature from 80% at 250°C to 20% above 600°C. The oxidative runs (with 2% oxygen in helium) result in char yields which, at low temperatures, are virtually identical to those from the non-oxidative pyrolysis but are lower (than in non-oxidative runs) at high temperatures. Above 550°C, virtually all the char was converted to gaseous product in the oxidative runs. Interestingly, the char yields are not dependent on the mass of chlorogenic acid pyrolyzed. This indicates that the pyrolysis reactions may not be transport-limited under the pyrolysis conditions used in this study. A preliminary analysis of the data indicated activation energy of 40 kJ/mol for the non-oxidative pyrolysis and 300 kJ/mol for the oxidative pyrolysis. The activation energy for non-oxidative

pyrolysis is rather low. On the other hand, the activation energy for oxidative pyrolysis is typical of that associated with the char oxidation. The gaseous product consisted mainly of phenol, catechol, benzene, and benzoic acid in addition to water, CO and CO₂. Similar products are reported in the literature [2,3]. Above 600°C, in this study, the gaseous product also contained significant hydrogen.

Char Characterization

The product char was obtained as a volcano-like cone having a smooth and 'glassy' external surface. This indicates that the chlorogenic acid forms a melt at relatively low temperature, which is consistent with its melting point (208°C). SEM analysis of chars indicated that the decomposition of chlorogenic acid was accompanied by the formation of bubbles in the melt. The bubbles grew as the reaction proceeded until they broke allowing the gaseous products to escape. The formation, growth, and breaking of bubbles and, in turn, the evolution of the gaseous product and char, were controlled by the pyrolysis conditions. At low temperatures, the char particles were of irregular appearance with a few bubbles inside. At higher temperatures, the particles became more rounded and the bubbles grew larger and, in some cases, the bubble film was broken probably by the escaping gases which may have been released into another closed bubble or to outside. The surface of the melt became increasingly rough due to the growth of globular, rod-like, and platelet structures which decomposed further to leave a carbonized frame of bubbles and pores. Figure 2 shows a typical SEM micrograph of the surface of the char at 650°C. Some of the bubbles are seen to be intact. The char is almost completely carbonized at this temperature. In the presence of oxygen, these carbonized structures were oxidized completely above 550°C.

The hydrogen/carbon (H/C) and oxygen/carbon (O/C) ratios for the chars at different temperatures are plotted in Figure 3. Both the ratios decrease sharply with increase in the pyrolysis temperature indicating that the char becomes increasingly more carbonaceous in nature at high temperatures. Further, the H/C ratio decreases almost linearly with the decrease in the O/C ratio until about 650°C. The major reactions at these temperatures appear to be the dehydration and decarboxylation reactions. However, above 650°C, the H/C ratio drops dramatically relative to O/C ratio indicating a direct dehydrogenation of the product char. This is consistent with the analysis of the gaseous product. Interestingly, the use of oxidative atmosphere does not alter the H/C and O/C ratios significantly relative to those in the non-oxidative case at the same temperature. This may be due to the low concentration of oxygen in the carrier gas.

The BET surface area measurements indicated that the chars prepared below 550°C had a negligible surface area but that the area increased dramatically to 196 m²/g at 650°C, before decreasing slightly at 750°C. Thus, the use of high temperatures seems beneficial in creating a char with a high surface area. The presence of oxygen also enhanced the surface area to a maximum of 90 m²/g at 450°C. Thus, the presence of oxygen appears to affect the physical characteristics of char.

The solid-state ¹³C CP/MAS NMR spectra of chars are presented in Figure 4. The multiplicities of resonances in the individual groups of peak are due to multiple crystalline modifications and/or multiple molecules in the crystalline lattice. The spectrum for chlorogenic acid (not shown) indicated that the chlorogenic acid is mainly crystalline in nature and contains aliphatic, aromatic, phenolic, carbonyl, and carboxyl structures. The spectra of chars (Figure 4) differ progressively with temperature from that of the chlorogenic acid. At 250°C, the resonance bands tend to be broad indicating an increase in the amorphous nature of the sample compared to chlorogenic acid. Since the resonance bands do not change appreciably in number or intensity, the changes appear to be mostly due to melting and the formation of an amorphous state. Above 250°C, there is a steady loss of oxygen functionality indicated by the loss of carbonyl absorptions. The spectrum for the 350°C char shows that the phenolic, carboxyl and carbonyl groups are still present, although the concentration of the latter two groups is considerably small. It is believed that the aliphatic and oxygen groups create links and loops between aromatic clusters of various sizes [4]. As the temperature is increased further, the char loses its aliphatic character completely and becomes more and more aromatic in nature. The resonance bands corresponding to carbonyl groups disappear mostly. The resonances corresponding to phenolic groups also decrease progressively in intensity until they become almost totally absent in the 650°C char. The oxygen-bonded carbons are no longer distinguishable and only a very small aliphatic peak remains, indicating a complete carbonization of the char. The char at 750°C could not be analyzed due to its high conductivity. Essentially similar observations were made from the NMR analysis of the oxidative chars, suggesting that many of the carbons in the chars that react with oxygen were lost probably by oxidation. These results appear to be at variance from those for chars prepared from cellulose [5] where it was observed that the aliphatic resonance of the char was significantly reduced while the resonance of aromatic carbons bonded to oxygen

increased. The difference could be due to differences in substrates as well as in pyrolysis conditions.

The FTIR results, presented in Figure 5, also suggest large chemical changes in chlorogenic acid above 250°C. Both the hydroxyl and carbonyl groups are gradually lost as the pyrolysis temperature is increased although the loss in hydroxyl groups does not appear to be as rapid as that in the carbonyl groups. The aliphatic character of char also decreases at high temperatures. On the other hand, the aromatic character, the C=C and the aromatic ring activities increase and are highest at 650°C. At 750°C, all the bands due to OH, CH, CH₂, and CH₃ stretches have vanished and there is a weak band for C=O. The char is mainly an aromatic polymer of carbon atoms. The spectra show an increasingly large drift in the baseline at high temperatures, which could be due to increase in the carbon black-content of the char as a result of increased carbonization. Boon *et al.* [6] observed a similar loss of oxygen functionality and an increase in the aromatic character with the cellulose chars at high temperatures. As in NMR analysis, the FTIR analysis showed essentially no effect of oxygen on the char characteristics.

The results of characterization are consistent with the evolution of the gaseous products. As the pyrolysis temperature is increased, the char loses most of its oxygen and hydrogen to the gaseous products such as water, CO, and CO₂, and becomes more carbonaceous in nature and low in crystallinity. The char probably also undergoes a direct dehydrogenation at high temperatures.

CONCLUSIONS

The char yield from chlorogenic acid was enhanced by low heating rates and low temperatures but was independent of the mass of substrate pyrolyzed, at least up to 300 mg. The major components of the gaseous product were catechol, phenol and benzoic acid. The surface area of char increased with temperature to a maximum at 650°C. The oxidative pyrolysis enhanced the surface area but decreased the char yield. The char lost its carbonyl, carboxyl, and aliphatic functionalities completely above 550°C. As a result, the carbonaceous and aromatic character of char increased with temperature and was highest at 750°C.

ACKNOWLEDGEMENTS

The authors are grateful to Philip Morris Management for their support of this research and to Bruce Wymack and Dr. Diane Kellogg for their assistance with mass spectrometer. SEM data were provided by Vicki Baliga.

REFERENCES

1. Sakuma, H., Matsushima, S., Munakta, S., and Sugawara, S. *Agric. Biol. Chem.* 46(5), 1311 (1982).
2. Zane, A. and Wender, S.H. *Tob. Sci.* 7, 21 (1963).
3. Schlotzhauer W.S., Snook, M.E., Chortyk, O.T., and Wilson, R.L. *J. Anal. Appl. Pyrol.* 22, 231 (1992).
4. Fletcher, T.H., Solum, M.S., Grant, D.M., and Pugmir, R.J. *Energy Fuels* 6, 643 (1992).
5. Shafizadeh, F. and Sekiguchi, Y. *Comb. Flame* 55, 171 (1984).
6. Boon, J.P., Pastorova, I., Botto, R.E., and Arisz, P.W. *Biomass Bioenergy* 7, 25 (1994).

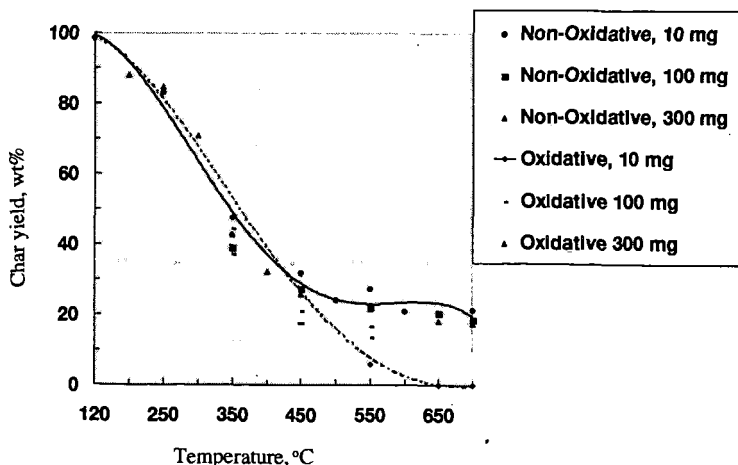


Fig. 1- Effect of temperature on char yield from chlorogenic acid

Char / SEM

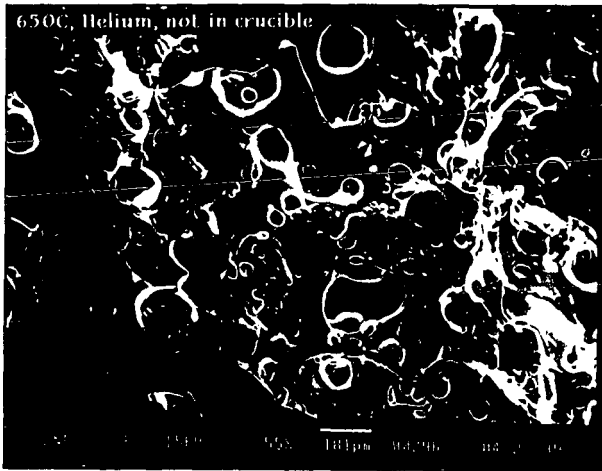


Fig. 2- Surface morphology of the 650°C-char.

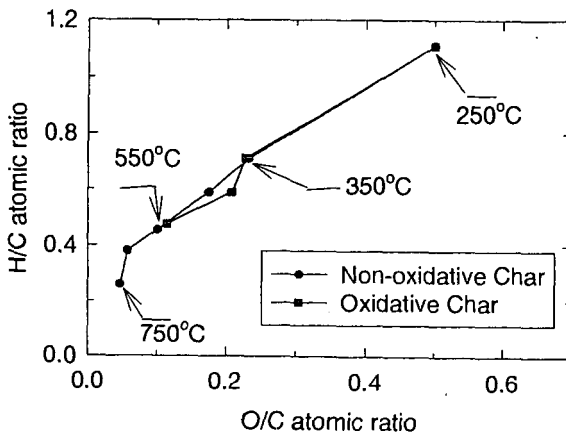


Fig. 3- Relationship between H/C and O/C ratios of chlorogenic acid chars

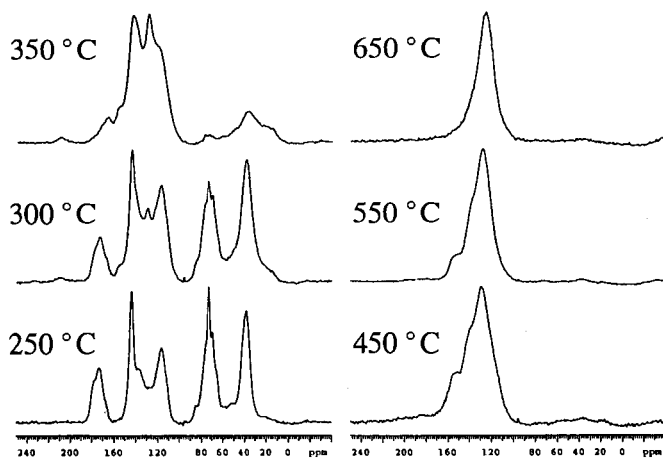


Fig. 4- Solid-state ^{13}C CPMAS NMR spectra of chlorogenic acid chars

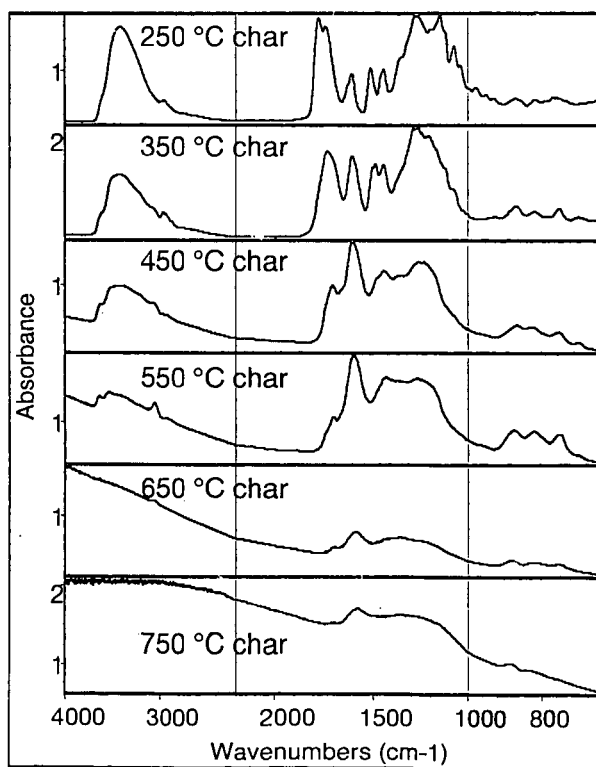


Fig. 5- Fourier-transform infrared (FTIR) spectra of chlorogenic acid chars

EFFECT OF ADDITION OF SALTS ON COAL EXTRACTION IN CS₂/NMP MIXED SOLVENT

Koyo NORINAGA*, Kazuhiro TAKAHASHI, and Masashi IINO
*Institute for Chemical Reaction Science, Tohoku University
Katahira, Aoba-ku, Sendai, 980-8577, Japan*

KEYWORDS: Coal, Extraction, Salts, CS₂/NMP mixed solvent

ABSTRACT

The effect of addition of various salts on the extraction of seven different kinds of coals with carbon disulfide-*N*-methyl-2-pyrrolidinone (CS₂-NMP) mixed solvent (1:1 by volume) was investigated. Addition of some salts considerably increased the extraction yield for several coals. For Upper Freeport coal, in particular, the addition of a very small amount (0.25 mol/kg-coal) of tetrabutylammoniumfluoride increased the extraction yield from 60 to 84%. The effect of a kind of anions on the extraction yield was also examined. It was found that the charge density of anion is responsible for the increase of the extraction yields. The fractionations of the extracts using pyridine indicate that the extracts obtained with the additive contain heavier constituents than those without the additive.

INTRODUCTION

The extraction of bituminous coals with CS₂/NMP mixed solvent (1:1 by volume) was found to give very high extraction yields at room temperature.¹ It was also observed that the addition of a small amount of electron acceptors such as tetracyanoethylene (TCNE) and 7,7,8,8-Tetracyanoquinodimethane (TCNQ) to the mixed solvent increases the extraction yields significantly.^{2,3} For example, the yield of the room temperature extraction of Upper Freeport coal with the 1:1 mixtures of CS₂/NMP increases from 59 to 85 wt% (dry-ash-free basis) by adding only 5 wt% (based on coal) of TCNE to the solvent.² The effects of addition of TCNE are reversible.⁴ Hence the increase of the extraction yield was found to be not due to the breakage of covalent bonds such as ether bonds in coal but due to the suppression of the association between coal macromolecules via non-covalent bonds. Previous studies on the mechanism for enhancing coal solubility have been concentrated on the charge-transfer complex formation between additives and coal. However the correlation between the solubility of coal and the electron acceptability was rather poor. Furthermore EPR studies of Illinois No.6 coal demonstrate that the increase in the spin concentration by the addition of electron acceptors is not due to the formations of new paramagnetic centers, i.e., thermally accessible triplet state arising from charge-transfer interactions.⁵ Thus the formation of the charge transfer complex between the coal and the electron acceptor does not seem to be the plausible mechanism for enhancing coal solubilities. Recently, Chen and Iino proposed another possible explanation for the effect of additives on coal extraction.^{6,7} It was found that TCNE does not exist as a neutral molecule in NMP as well as in the NMP/CS₂ mixed solvent but forms TCNE anion derivative, i.e., NMP 1,1,2,3-pentacyanopropene salt (NPCNP). It has been well known that TCNE easily generate PCNP anion by reacting with aprotic polar solvent such as pyridine⁸ or pyridone^{9,10} in the presence of the proton source like water. They also examined that the effect of addition of NPCNP on the extraction yields of UF coal with CS₂/NMP mixed solvent. The addition of 0.2 mol/kg-coal NPCNP increases the extraction yield from 59 to 72 wt%, which is comparable to the increment by adding the same amount of TCNE. These observations indicate that the anion plays a key role on the enhancement of the coal solubility. However there is little information available on what kinds of anion is effective for the coal extractions. Furthermore, the effect of additives on the solvent properties such as the Gutmanns donor (DN) and acceptor numbers has not been focused yet.

In the present study, the effect of anion on the coal extraction with CS₂/NMP mixed solvent is examined using tetrabutylammonium and lithium salts of various anions systematically. The changes in the bulk property of the solvent with adding salts are also examined based on the solvatochromism of well-characterized probe dye indicators.^{11,12}

EXPERIMENTAL

Solvent extraction. Seven different kinds of coals were used as coal samples. Their particle sizes were finer than 150 μ m. They were dried under vacuum at 353 K for 12 h. The elemental composition of the coal samples are listed in Table 1. 1.0 g of a coal sample was extracted with 60 mL of CS₂/NMP mixed solvent (1:1 by volume) with or without the additive under ultrasonic (38 kHz) irradiation for 30 min at room temperature. The mixtures were subsequently centrifuged under 29000 g for 60 min, and the supernatant was immediately filtered through a membrane paper with a pore size of 0.8 μ m. The residue was repeatedly extracted with the fresh mixed solvent in the same way, until the filtrate become almost colorless. This exhaustive extraction usually needs the repeating of 4-6 times. The residue was thoroughly washed with acetone to remove CS₂ and NMP retained. Extraction yields

were determined on a dry ash free basis from the amount of the residue. The extract, hereafter referred to as MS was further fractionated using acetone and pyridine to yield acetone soluble (AS), pyridine soluble / acetone insoluble (PS), and pyridine insoluble (PI) fractions, respectively. Detailed extraction and fractionation procedures were described in elsewhere.¹ Several kinds of tetrabutylammonium and lithium salts were used as additives. Typical amount of the additive was 0.25 mol/kg coal.

Solvatochromism. The effect of addition of LiCl on the DN of NMP was empirically evaluated by using copper(II)-*N,N,N',N'*-tetramethylethylenediamine-acetylacetonate ($\text{Cu}(\text{tmen})(\text{acac})^+$). The probe dye indicator was dissolved in the NMP/LiCl solvent, and the mixture was subjected immediately to the UV/VIS measurements. The DN was calculated using an empirical equation based on the absorption band of the dye in the solvent.¹²

RESULTS AND DISCUSSION

Effects of addition of the salts on the extraction yields of UF coals are shown in Table 2. The extraction yields varies with the types of salts. TBAF affects the coal extraction most significantly and increased the yield up to 84%. The results for the halogenide salts indicate that a kind of halogenide anions affects the extraction yields. The yields increased in the order, $\text{F}^- > \text{Cl}^- > \text{Br}^- > \text{I}^-$. This indicates that the anions with the small ion radius or large electronegativity are effective for the enhancement of the yield. Lewis acidity or basicity of ions can be categorized reasonably by HASB (Hard and Soft Acids and Bases) principle of Pearson.¹³ He proposed a simple, useful rule, that is, hard acids bind strongly to hard bases and soft acids bind strongly to soft bases. It is convenient to divide bases into two categories, those that are polarizable (low charge density), or "soft," and those that are nonpolarizable (high charge density), or "hard." F^- and Cl^- are categorized into hard base, while Br^- and I^- are soft base. Hard base tends to attract proton strongly. If we use protic solvents, F^- and Cl^- must be strongly solvated and would show little effect on the extraction. Because the CS_2 /NMP mixed solvent is dipolar, aprotic solvent, these anion would be solvated weakly and can interact with some hard acidic sites in coal. Acid-base interaction between coal and anion would be responsible for the enhancement of the extraction yields. On the other hand, soft base such as Br^- and I^- is strongly solvated since the dipolar aprotic solvent such as the mixed solvent can be categorized into soft acid solvent. Hence these soft base can not interact with the coal and have little effect. Non-halogenide anions such as CH_3COO^- , ClO_4^- , and NO_3^- were also used. CH_3COO^- is hard base and increases the extraction yield while others are soft base and the effects are less significant.

Table 3 lists the effect of TBAF addition on the extraction yields of several kinds of coals. Upper Freeport, Lower Kittanning, and Stigler coals are increased their extraction yields with the mixed solvent by the addition of TBAF, but for Pittsburgh No.8, Illinois No.6 coals the yields did not increase. For the addition of TCNE the same tendency of the extraction yields was obtained for the above-mentioned five coals. The results of the fractionation of MS of Upper Freeport coal are shown in Table 4. The increase in the MS yields is mainly due to the increase of the heaviest extract fraction, i.e., PI, and little increase in the lighter fraction of AS and PS. Figure 1 shows the experimental procedure for examination of the reversibility of the effect of additive on the extraction yields of UF coal. The yield of MS obtained from the extraction with LiCl is 78 wt %. The MS was washed exhaustively with acetone/water mixed solvent (1:4 by volume) to remove LiCl retained, and subsequently extracted with the CS_2 -NMP mixed solvent in the absence of LiCl. A portion of MS became again insoluble, i.e., 63 wt % of UF coal is extracted by the mixed solvent. The yield was almost same as the yield of MS obtained without additives. Hence the effects of addition of LiCl seem to be reversible as observed for the addition of TCNE.

Figure 2 shows the effect of LiCl concentration in NMP on the DN of NMP as well as extraction yield with NMP for UF coal. DN of NMP is rapidly increased from 27 to 54 even by the addition of very small amount of LiCl (10 mmol/L) and kept constant value above 10 mmol/L. The extraction yield is also increased by LiCl addition, it increases with increasing the concentration of LiCl up to 120 mmol/L. The increase in the extraction yield is observed even where the DN is almost constant, indicating that the effect of the salt additive on the coal extraction can not be explained only by the change in the bulk property of solvent with salt addition. It is necessary to consider the interaction between coal and anion more in detail.

CONCLUSIONS

The effect of addition of various salts on the extraction of seven different kinds of coals with carbon disulfide-*N*-methyl-2-pyrrolidinone (CS_2 -NMP) mixed solvent (1:1 by volume) was investigated. Addition of some salts considerably increased the extraction yield for several coals. For Upper Freeport coal, in particular, the addition of a very small amount, 0.25 mol/kg-coal of tetrabutylammoniumfluoride increased the extraction yield from 60 to 84%. The effect of a kind of anions on the extraction yield was also examined. It was found that the charge density of anion seems to be responsible for the increase in the

extraction yields. The fractionations of the extracts using pyridine indicate that the extracts obtained with the additive contain heavier constituents than those without the additive.

ACKNOWLEDGMENT. This work was supported in part by a "Research for the Future Project" grant from the Japan Society for the Promotion of Science (JSPS), through the 148th Committee on Coal Utilization Technology.

REFERENCES

- (1) Iino, M.; Takanohashi, T.; Osuga, H.; Toda, K. *Fuel* **1988**, *67*, 1639.
- (2) Liu, H.; Ishizuka, T.; Takanohashi, T.; Iino, M. *Energy Fuels* **1993**, *7*, 1108.
- (3) Ishizuka, T.; Takanohashi, T.; Ito, O.; Iino, M. *Fuel* **1993**, *72*, 579.
- (4) Iino, M.; Liu, H.; Hosaka, N.; Kurose, H.; Takanohashi, T. *Prepr. Pap. Am. Chem. Soc., Div. Fuel. Chem.* **1997**, *42(1)*, 248.
- (5) Thompson, R. T.; Rothenberger, K.S.; Retcofsky, H.L. *Energy Fuels* **1997**, *11*, 739.
- (6) Chen, C.; Kurose, H.; Iino, M. *Energy Fuels* **1999**, *13*, 1180.
- (7) Chen, C.; Iino, M. *Energy Fuels* **1999**, *13*, 1105.
- (8) Middleton, W. J.; Little, E. L.; Coffman, D. D.; Engelhardt, V. A. *J. Am. Chem. Soc.* **1958**, *80*, 2795.
- (9) Thyagarajan, B. S.; Rajagopalan, K.; Gopalakrishnan, P. V. *Chem. Ind.* **1966**, *5*, 1887.
- (10) Thyagarajan, B. S.; Rajagopalan, K.; Gopalakrishnan, P. V. *J. Chem. Soc. (B)* **1968**, 300.
- (11) Reichardt, C. *Chem. Rev.* **1994**, *94*, 2319.
- (12) Spange, S.; Reuter, A.; Vilsmeier, E.; Heinze, T.; Keutel, D.; Linert, W. *J. Polymer Sci. Part A* **1998**, *36*, 1945.
- (13) Pearson, R. G. *J. Am. Chem. Soc.* **1963**, *85*, 3533.

Table 1. Properties of Coal Samples

Coal	Symbol	Ultimate analysis (wt%, daf)				Ash (wt%, db)
		C	H	N	O+S ^{a)}	
Sewell B	SW	88.4	5.3	1.4	4.9	4.6
Upper Freeport	UF	86.2	5.1	1.9	6.8	13.1
Lower Kittanning	LK	84.0	5.6	1.7	8.7	9.0
Lewiston Stockton	LS	82.9	5.4	2.0	9.7	19.6
Pittsburgh No.8	PB	82.6	5.5	2.1	9.8	8.7
Stigler	SG	77.8	4.8	1.5	15.9	11.7
Illinois No.6	IL	76.9	5.5	1.9	15.7	15.0

^{a)} By difference

Table 2. Effect of Salt Types on Extraction Yields ^{a)} of UF Coal

Additive ^{b)}	Extraction yield (wt%, daf)
LiCl	78.1
LiBr ^{c)}	68.7
LiI ^{d)}	60.9
(n-Bu) ₄ N ⁺ F ⁻	83.9
(n-Bu) ₄ N ⁺ Cl ⁻	78.8
(n-Bu) ₄ N ⁺ Br ⁻	61.8
(n-Bu) ₄ N ⁺ I ⁻	59.3
(n-Bu) ₄ N ⁺ OCOCH ₃ ⁻	75.6
(n-Bu) ₄ N ⁺ ClO ₄ ⁻	62.1
(n-Bu) ₄ N ⁺ NO ₃ ⁻	54.0
None	59.8

^{a)} CS₂-NMP mixed solvent (1:1 by volume),
room temperature

^{b)} 0.25 mol/kg-coal ^{c)} 0.95 mol/kg-coal

^{d)} 1.87 mol/kg-coal

Table 3. Effect of TBAF ^{a)} Addition on Extraction Yields ^{b)} of Coals

Coal	C% (dry ash free)	Extraction yield (wt%, daf)	
		None	0.25mol/kg-coal
SW	88.4	33.9	48.0
UF	86.2	59.8	83.9
LK	84.0	38.0	61.6
LS	82.9	25.6	25.8
PB	82.6	37.8	37.4
SG	77.8	26.0	72.2
IL	76.9	24.6	25.5

^{a)} (n-Bu)₄N⁺F⁻^{b)} CS₂-NMP mixed solvent (1:1 by volume), room temperatureTable 4. Effect of TBAF ^{a)} Addition on Extraction Yields ^{b)} of Coals and Fraction Distributions of the Extracts

Coal	TBAF	Extraction yield (wt%, daf)	Fraction distribution (wt%, daf)		
			AS	PS	PI
UF	None	60.1	8.2	25.0	26.9
	0.25mol/kg-coal	82.4	11.5	12.7	58.2
LK	None	38.7	6.3	27.1	5.3
	0.25mol/kg-coal	63.7	9.4	17.9	36.4
PB	None	43.5	12.3	30.0	1.2
	0.25mol/kg-coal	39.9	11.8	23.4	4.7
SG	None	21.2	6.1	14.5	0.6
	0.25mol/kg-coal	62.4	6.4	17.2	38.8
IL	None	27.9	7.8	19.1	1.0
	0.25mol/kg-coal	27.4	10.0	16.8	0.6

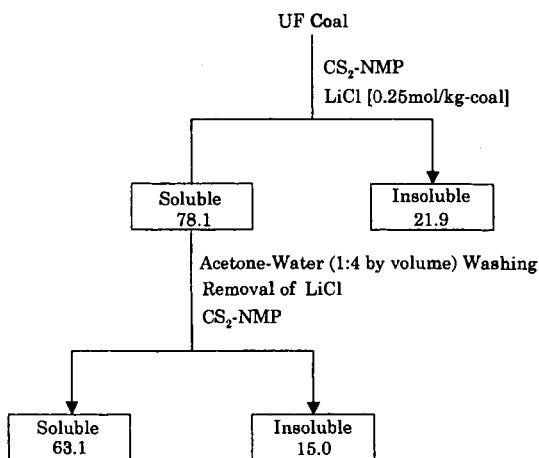
^{a)} (n-Bu)₄N⁺F⁻^{b)} CS₂-NMP mixed solvent (1:1 by volume), room temperature

Fig. 1. Reversibility of the Effect of LiCl Addition on the Extraction Yield

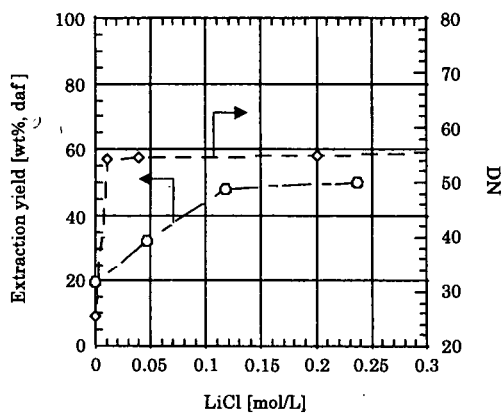


Fig. 2. Effect of LiCl concentration on DN of NMP as well as the Extraction Yield of UF Coal

LOW SEVERITY EXTRACTION OF PITCH FROM COAL AS A PRECURSOR TO VALUE ADDED PRODUCTS - REVISITED.

A.J. Berkovich, C.J. Lafferty and F.J. Derbyshire

Center for Applied Energy Research

University of Kentucky

2540 Research Park Drive, Lexington, KY, USA, 40511.

KEY WORDS: pitch extraction, fibres, anthracene oil.

ABSTRACT: This paper presents preliminary results from a detailed investigation into different methods of extraction of pitch from coal and their affect on the properties of the final pitch product. One such method is the use of cheap and readily available petroleum residues that act as solvents for pitch. Crude anthracene oil, a cheap petroleum residue was shown to extract a reasonable yield of high boiling point material from coal at low temperatures with no over pressure. A series of extractions at temperatures ranging from 200 to 450 °C were performed on coals differing in rank and heteroatom contents. The results indicate that maximum extraction yield occurs between 350 and 400 °C. The extraction capability of recycled anthracene oils recovered from prior extractions was also assessed. Carbon fibres from pitch extracts were produced and their physical properties assessed.

INTRODUCTION: The use of coal derived pitches as precursors for valued added carbon products is well known. As the range of applications for new carbon based products increases the potential exists to tailor precursor properties for specific applications, for example carbon fibres. This paper examines pitch extraction methods and how different extraction conditions effect the properties and performance of pitch derived carbon fibres as a lead into tailoring properties of extracted pitches.

Petroleum residues, such as anthracene oil and petroleum based solvents have been shown to be good solvents for high boiling point liquids from coal (coal derived pitches) [1-4]. However, previous work on coal solvent extraction using such solvents has usually involved pre-hydrogenation of the solvent as well as high gas over pressures during the extraction. Hydrogenation and high pressure extractions adversely affect the economic potential of a solvent extraction process. The aim of this paper was to prepare pitches using mild extraction conditions and assess the potential of these pitches as precursors to value added carbon products.

EXPERIMENTAL: Pitch extractions were performed in 50 mL stainless steel tubing bomb reactors which were heated in a fluidised sand bath while being shaken by a mechanical shaker. Coal samples were crushed to <60 mesh and then slurried in different ratios with the solvent before being placed into the tubing bombs. Two different solvents were used, anthracene oil as well as panasol (a commercially available petroleum derived solvent). The solvents were not hydrogenated nor was any gas over pressure used during the extractions. Extraction temperatures ranged from 250 to 450 °C, with extraction between 10 minutes and 3 hours. After extraction, the reaction mixture was extracted in a Soxhlet apparatus using THF. The THF soluble fraction was then vacuum distilled to 300 °C at 1 mm Hg. The THF insoluble residue was dried in a vacuum oven and its mass used to calculate the yield of extracted material. The softening point of the extraction pitch material was measured. Typically a softening point of 200 to 240 °C was desired for ease of fiber forming and processing. The fiber forming and processing methods have been described elsewhere [5]. Coal samples from Northeast Wyoming's Black Thunder mine and Western Kentucky was used for the extraction experiments. Proximate analyses of the coals showed, Black Thunder contained: 8.89 % moisture; 5.76 % ash; 39.88 % volatile matter; 45.47 % fixed carbon, the Western Kentucky contained: 2.30 % moisture; 8.90 % ash; 34.42 % volatile matter; 53.45 % fixed carbon.

RESULTS and DISCUSSION: Mild condition solvent extractions were performed on Black Thunder coal. The effect of temperature was examined first. Extractions with coal to solvent ratios of 1:2 with anthracene oil and panasol were performed at 200, 250, 300, 350, 400 and 450 °C for 1 hour. Figure 1 compares the effect of temperature on extraction yield for Black Thunder coal using anthracene oil and panasol. Figure 1 shows that anthracene oil produced a higher yield of pitch compared to panasol with the maximum extraction yield occurring at approximately 350 °C for anthracene oil and approximately 450 °C for panasol. The effect of different extraction time was also examined. Again a coal to solvent ratio of 1:2 was used and extraction times of 10 minutes to 3 hours were examined. Figure 2 shows extraction yield versus extraction time. Inspection of Figure 2 shows that 80 % of the extraction yield is attained during the first 20 minutes.

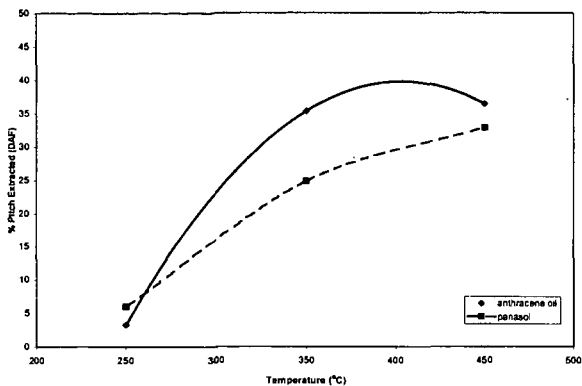


Figure 1 – Effect of temperature on extraction yield for Black Thunder coal.

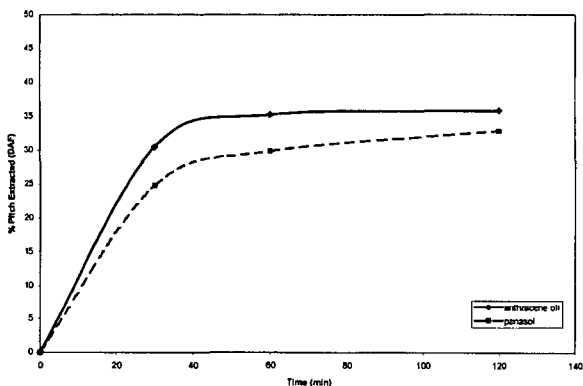


Figure 2 – Effect of time on extraction yield for Black Thunder coal.

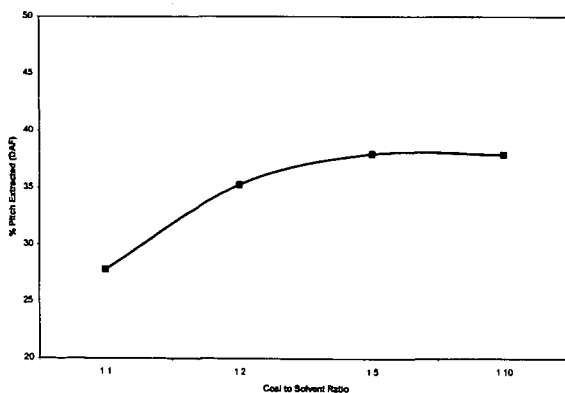


Figure 3 – Effect of increasing solvent concentration on extracted pitch yield

The effect of coal to solvent ratio was also examined, Figure 3 shows a plot of extracted pitch yield versus solvent to coal ratio where anthracene oil was used. Figure 3 shows that using coal to solvent ratios greater than 1:2 did significantly increase the pitch yield. From the results of these preliminary experiments the following extraction parameters were used for subsequent extractions: coal to solvent ratios of 1:2; extraction temperature, 350 °C; extraction time, 60 minutes. The re-use of solvent recovered from distillation was also investigated. Pitch

extractions were performed on Black Thunder coal using recycled solvent as well as mixtures of recycled and fresh solvent. Table 1 shows extracted pitch yields for these experiments. The results showed only a slight decrease in extraction yield for the recycled solvents compared to fresh solvent. The mixtures of fresh and recycled showed almost the same extraction capabilities as the fresh solvent.

Table 1 - Extracted pitch yields for recycled solvents, yields for fresh solvent shown in brackets.

Solvent	% Yield
recycled anthracene oil	28.3 (35.3)
recycled panasol	20.0 (24.82)
1:1 recycled anthracene oil and fresh anthracene oil	35.2
1:1 recycled panasol and fresh panasol	26.8

A summary of pitch extraction conditions and yields is shown on Table 2. The results show that extractions performed on Black Thunder coal under mild conditions have lower extracted pitch yields compared to those using more severe conditions. Tables 2 and 3 contain characterisation data for the extracted pitches. The results show that pitches extracted under mild conditions have very similar characteristics to those extracted under severe conditions. More importantly however, are the characteristics of the fibres formed from the extracted pitches.

Table 2 - Summary of extraction yields and extraction methods.

Coal	Extraction Method	% Yield	Extracted Pitch
Black Thunder	a.oil; 350; 60	35.3	BT1
Western Kentucky	a.oil; 350; 60	90.6	WK1
Black Thunder	pan; 350; 60	24.8	BT2
Western Kentucky	pan; 350; 60	89.2	WK2
Black Thunder	a.oil; 370; 60; H ₂	90.0	BT3

Extraction Method: solvent; temperature (°C); time (min)
a.oil = anthracene oil, pan = panasol

Table 3 - Summary of extracted pitch properties.

Pitch	Softening Point (°C)	Ultimate Analysis (% DAF)				
		C	H	N	O	S
BT1	220	87.6	5.03	1.1	1.6	0.5
WK1	210	91.1	4.5	1.7	1.7	1.0
BT2	220	85.7	5.8	1.4	6.8	0.3
WK2	260	90.2	4.3	1.8	2.5	1.1
BT3	230	87.1	6.0	1.4	5.2	0.3

Carbon fibres formed from the extracted pitches were tested for strength, modulus and resistivity. A summary of these properties is shown in Table 3. Table 3 shows that the physical properties of the carbon fibres formed from pitches extracted under severe and mild conditions are similar.

Table 3 - Summary of properties of pitch derived carbon fibers.

Extracted Pitch	Strength (MPa)	Modulus (GPa)	Resistivity mΩcm ⁻¹
BT1	400	82	8.0
WK1	576	86	47
BT2	319	63	16.7
WK2	347	69	16.3
BT3	380	n/a	27.3

The results show that although extraction yields are lower for the mild condition extractions compared to the severe condition extractions, the properties of the extracted pitches and pitch based fibres are similar. Therefore there is the potential to produce pitch from coal using a low

temperature and low pressure method without sacrificing the performance of the final carbon product.

CONCLUSIONS: Low severity solvent extraction of coal using anthracene oil and panasol were performed to produce a high boiling point liquid, pitch. The pitch extraction yields of the mild condition techniques were compared to those performed under more severe conditions. Although the low severity extractions showed lower yields the chemical characteristics of the extracted pitches were similar to those extracted under more severe conditions. The physical characteristics of carbon fibres formed from pitches extracted under mild and severe conditions were similar.

REFERENCES

1. Oele, A.P., Waterman, H.I., Goedkoop, M.L. and van Krevelen, D.W. *Fuel*, **1951**, *30*, 169.
2. Mishra, S. and Sharma, D. K. *Fuel*, **1990**, *69*, 1377.
3. Rosal, R., Diez, F.V. and Sastre, H. *Ind. Eng. Chem. Res.*, **1992**, *31*, 2407.
4. Cloke, M. and Wang, C. *Energy & Fuels*, **1995**, *9*, 560.
5. Jorro, M. and Ladner, W.R. 4th Int Carbon Con, London, Sept 1974.

CHANGE IN THE PORE SIZE DISTRIBUTION OF BROWN COAL ALONG WITH A PROGRESS OF MOISTURE RELEASE

Haruo Kumagai¹ and Kazuo Nakamura²

¹Center for Advanced Research of Energy Technology, Hokkaido University,
Kita-13, Nishi-8, Kita-ku, Sapporo 060-8628, Japan

²Research and Development Department, Osaka Gas Co., Ltd.,
6-19-9, Torishima, Konohana-ku, Osaka 554-0051, Japan

Keywords : pore, moisture release, macromolecular structure, CAMD

INTRODUCTION

Molecular modeling technique has been employed widely in biological chemistry to provide insight into the conformation, properties and interactions of biomolecules. According to existing development of molecular modeling software, the methodology has allowed treatment of relatively large molecules and has begun to be applied to fuel chemistry by constructing complex heterogeneous macromolecular model. Carlson [1] applied computer-aided molecular design (CAMD) methods to determine three-dimensional minimum-energy conformations for four bituminous coal models. He indicated that nonbonding interactions, in particular, van der Waals and hydrogen bonding interactions, are strong driving forces to form and stabilize the structures of the coal models. Takanohashi and co-workers also determined the minimum-energy conformation of a bituminous coal by a CAMD method and suggested that the coal has a possibility to have an associated structure of constituent molecules in the coal having a continuous distribution of molecular weights [2,3].

Low rank coals such as lignite and brown coal are featured by their high residual moisture contents in the range from 30 to 70wt%. Because of such a high moisture content, moisture removal is the primary and essential step in almost all brown coal utilization processes. Furthermore, the drying step is known to have a significant effect on the physical and chemical characteristics of the dried coal. For example, it has been suggested that drying have negative impact on liquefaction reactivity [4-7] and that in lignite liquefaction the oil yield is higher for dried coal than that for raw or partly dried one [8]. These nominal impacts of drying on the conversion reactivity can be attributed to an irreversible change of pore structure that results in a limitation of accessibility of reacting components [9]. And it is easy to imagine that the pore structure change is brought about by the change in macromolecular structure of coal along with drying.

In a previous paper [10], we investigated the change in conformation for an Australian brown coal with its moisture removal process by means of a CAMD method. The results indicated that change in conformation of the coal simulated by CAMD method is well corresponding to the observed volumetric change, and removal of water molecules results in a drastic conformational change in the final stage of moisture removal. In the present study, conformations of an Australian brown coal are simulated under 3D periodic boundary conditions in order to elucidate the change in the pore distribution along with a progress of moisture release.

CAMD calculation method

The CAMD study was carried out by using an O₂ workstation (Silicon Graphics, Inc.) with Cerius² software (version 3.8, Molecular Simulations Inc.). The software is capable of calculating the most stable structures with the minimum conformational energies using COMPASS, UNIVERSAL and DREIDING force fields. Since our previous study indicated the importance of hydrogen bonding interactions on the stabilization of brown coal conformation,

the DREIDING 2.21 force field was used in this study. Cerius² software allows the use of periodic boundary condition, in which model molecules are placed in a unit cell surrounded by the same cells in all directions. Molecular segments in the cell can interact with others in the neighboring cells as well as in the same cell. If a segment exits on the one surface of the cell, the same one enters from opposite side. The structure of Australian brown coal (Yallourn brown coal ; YL) was modeled by two oligomers, namely a pentamer ($M_w=1892$) and an octamer ($M_w=3074$), of unit structure: The unit structure, which was constructed on the basis of the data from elemental analysis and ¹³C-NMR spectroscopy of the coal [11], is shown in figure 1. Each oligomer was specially arranged so as to have no interaction with others. Simulations of moisture removal process were initiated by generating 413 water molecules (59.95wt%, wet basis) surrounding the model molecule and the **minimum energy conformation (MEC)** for the model with water molecules was calculated based on molecular mechanics and molecular dynamics methods. After MEC was obtained, the volume and density of unit cell and pore distribution were calculated. The pore volume was defined as prove occupiable volume using several size of spherical probe in radius from 0.5Å to 3.0Å. The calculation was repeated decreasing the number of water molecules step by step to 0, and finally MEC for model molecule with 0 water, i.e., completely dried coal was obtained.

RESULTS AND DISCUSSIONS

Change in the volume and in the density of MEC unit cell which contain model molecules of YL and water molecules are shown in figure 2 as a function of the extent of moisture removal (%). During moisture release process, the volume decreases monotonously with moisture removal, and reaches nearly a half of initial volume. Initial density of the cell (1.110 g/cm³) is in a good agreement with experimentally determined raw coal density [12, 13], while density of the cell for completely dried YL (0.929 g/cm³) is slightly higher than mercury density of dried YL (0.873 g/cm³). As shown in figure 2, density of the cell decreases gradually with the extent of moisture removal up to 80%. A significant decrease in density of the cell is observed with the extents higher than 80%. In the previous study [10], we demonstrated that change in the volume for YL model molecules without water molecules proceeds in the final stage of moisture removal at which non-freezable water is removed, and the change in volume corresponds well to the change of non-bonding interaction energies. The significant decrease in density observed in this study is well in harmony with the previous study. Thus, the result indicates that the dense conformation of YL model molecules with water molecules changed to porous one with removal of non-freezable water.

Micropore size distribution is calculated from occupiable volume with spherical probe, V_{occ} , and radius of the probe, R_p . The micropore size distribution curves, dV_{occ}/dR_p vs R_p , are shown in figure 3. The micropore size distribution is little affected with extent of moisture removal at the range from 0% to 65%. As we can expected from change in the cell density, described above, a significant change in the distribution is observed with the extents higher than 80%. The change in micropore size distribution shows the enlargement in pore size that has occurred at the final stage of moisture removal. The total micropore volume increases from 0.15 cm³/g for wet YL (0% moisture removal) to 0.30 cm³/g for completely dried coal, down to a micropore size of 0.5Å. The change corresponded well to the change of density.

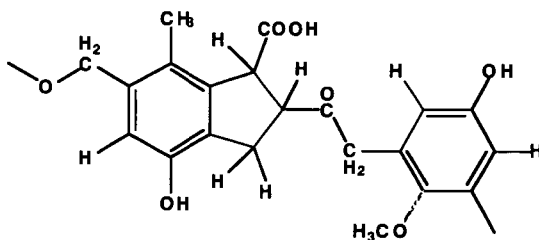
Although techniques are available for the characterization of the micropore structure of dried coal, there are no equivalent procedures to determine the micropore structure of coal in a wet state. Setek and co-workers [14] have applied small angle X-ray scattering (SAXS), and CO₂ sorption technique to determine the microporosity of YL. The micropore volumes for dried YL show reasonable agreement by the two techniques (0.058 cm³/g for CO₂ sorption, 0.060 cm³/g for SAXS) and slightly larger than comparable micropore volume ($R_p > 2.75\text{\AA}$) obtained by CAMD (0.032 cm³/g). The micropore volume for wet YL obtained by SAXS (0.110 cm³/g) is much

larger than that calculated by CAMD ($0.001 \text{ cm}^3/\text{g}$). This probably reflects differences in the size of the structures to determine the microporosity of brown coal.

In summary, the change in volume and density for YL model molecule with its moisture release process could be successfully simulated by using the CAMD method. Although the coal model molecule employed in this study is rather simple and small, the results appear to represent the characteristics of the brown coal, at least change in the density and micropore size distribution along with a progress of moisture release.

REFERENCE

1. Carlson, G.A. *Energy Fuels* 1992, 6, 771.
2. Takanohashi, T.; Iino, M.; Nakamura, K. *Energy Fuels* 1994, 8, 395.
3. Nakamura, K.; Takanohashi, T.; Iino, M.; Kumagai, H.; Sato, M.; Yokoyama, S.; Sanada, Y. *Energy Fuels* 1995, 9, 1003.
4. Gorbaty, M.L. *Fuel* 1978, 57, 796.
5. Atherton, L.E. *Proc. Int. Conf. Coal Sci.* 1985, 553.
6. Neavel, R. *Fuel* 1976, 55, 237.
7. Cronauer, D.C.; Ruberto, R.G.; Silver, R.S.; Jenkins, R.G.; Davis, A.; Hoover, D.S. *Fuel* 1984, 63, 77.
8. Vorres, K.S.; Wertz, D.L.; Malhotra, V.; Dang, Y.; Joseph, J.T.; Fisher, R. *Fuel* 1992, 71, 1047.
9. Vorres, K.S.; Kolman, R.; Griswold, T. *Prepr. Pap. Am. Chem. Soc., Div. Fuel Chem.* 1988, 33 (2), 333.
10. Kumagai, H.; Chiba, T.; Nakamura, K. *Prepr. Pap. Am. Chem. Soc., Div. Fuel Chem.* 1999,
11. Yoshida, T.; Narita, Y.; Yoshida, R.; Ueda, S.; Kanda, N.; Maekawa, Y. *Fuel* 1982, 61, 824
12. Higgins, R.S.; Kiss, L.T.; Alladice, D.J.; George, A.M.; King, T.N.W. *SECV Research and Development Department Report No. SC/80/17*
13. Higgins, R.S.; Kiss, L.T.; George, A.M.; King, T.N.W.; Stacy, W.O. *SECV Research and Development Department Report No. SC/81/28*
14. Setek, M.; Wagerfeld, H.K.; Stacy, W.O.; Kiss, L.T. *Fuel* 1983, 62, 480



C:65.6, H:5.2, O:29.2 wt%

Mw:384.37

H-bond acceptor:7, H-bond donor:3

Figure 1. Unit structure assumed for YL model molecule.

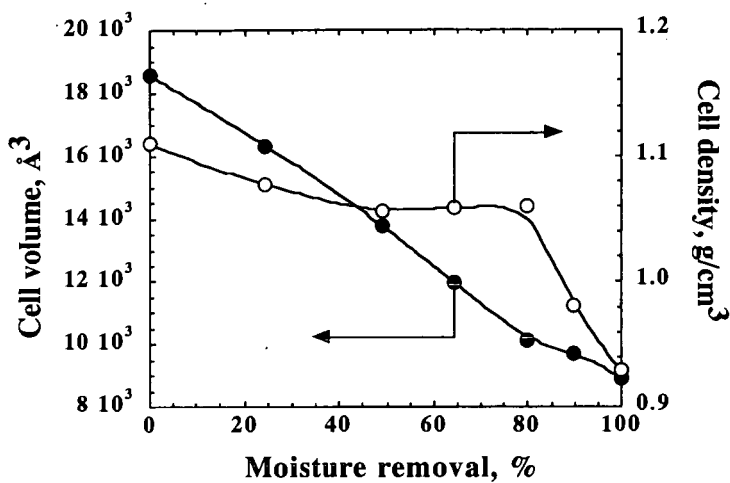


Figure 2. Change in the cell volume and density with extent of moisture removal.

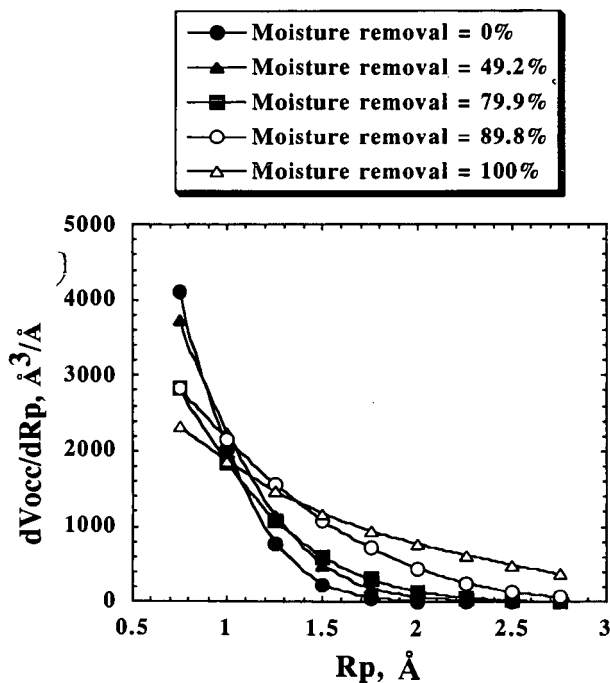


Figure 3. Micropore size distribution curves.

CLUSTER GEOMETRY OF SUPERCRITICAL Xe CONFINED IN CARBON MICROPORES.

M. Aoshima, T. Suzuki, and K. Kaneko

Materials Science, Graduate School of Science and Technology, Chiba University

Yayoi 1-33, Inage, Chiba, 263-8522 Japan

KEYWORDS: Xe adsorption, Cluster structure, Activated carbon

INTRODUCTION

Recently various kinds of porous carbon materials have been developed and their properties and structures have been gathering great concerns in science. There are two types of pores of intraparticle pores and interparticle ones¹. The carbon nanotube of which pore wall is composed of graphitic sheets has crystalline intraparticle pores², when their caps are removed. Activated carbons of the most popular adsorbents are obtained by the activation reaction of carbon materials using H₂O or CO₂. Activated carbon has ill-crystalline intraparticle pores. As activated carbon has excellent adsorptive properties, fine characterization of the pore structure and control of the adsorptive property have been strongly desired. Activated carbon of fiber morphology, so called activated carbon fiber ACF³, is one of hopeful carbon materials. This ACF has considerably uniform slit-shaped micropores without mesopores, showing excellent adsorption properties. The pore size distribution of ACF is very narrow compared with that of traditional granular activated carbon. Consequently, we can understand more an unresolved problem such as adsorption of supercritical gas using ACF as an microporous carbon.

There are many important supercritical gases such as O₂, N₂, CH₄, NO, and H₂ which are deeply associated with energy, environmental, food, and medical technologies. Further understanding of supercritical gas adsorption is requested to support important technologies. Although vapor adsorption on micropores, which is called micropore filling, is considerably understood, micropore filling of a supercritical gas has not been studied sufficiently irrespective of its importance in micropores⁴⁻⁷. We need more fundamental understanding of supercritical gas adsorption. The critical and boiling temperatures of the Xe gas are 289.6K and 165.9K, respectively. The size of a spherical Xe molecule is 0.396nm and the Xe-Xe interaction energy is 217K^{8,9}. Accordingly a considerable amount of Xe can be adsorbed in micropores above the critical temperature only by the dispersion interaction. Xe gas has a potential for important applications such as anesthetic and Xe lamp.

In this work, the relationship between micropore filling of supercritical Xe in micropores of ACF at 300 K and cluster size distribution by cluster analysis is described.^{10,11}

EXPERIMENTAL

Pitch-based ACFs (P5, P10, and P20) were used. The micropore structures of ACFs were determined by the N₂ adsorption isotherm at 77K using the gravimetric method after the pre-evacuation of ACF samples at 383K. The N₂ adsorption isotherm was analyzed by use of the

in Table 1. The average pore width of these ACFs is in the range of 0.75 to 1.05 nm, corresponding to the model graphite pore.

All adsorption isotherms of supercritical Xe at 300K were onvex in the low pressure range, which can be approximated by the Langmuir equation. In particular, the adsorption isotherm of Xe on P5 having the smallest pores was of

Table 1. Micropore parameters of pitch-based ACF samples

	Surface Area m^2g^{-1}	Micropore Volume mlg^{-1}	Pore Width nm
P5	900	0.336	0.75
P10	1435	0.614	0.86
P20	2190	1.136	1.05

the representative Langmuir type. The smaller the pore width, the greater the amount of Xe adsorption in the low pressure region. The absolute amount of Xe adsorption was very great even at 60kPa, being larger than 250 mgg^{-1} regardless of the supercritical conditions. The fractional filling values of Xe adsorption at 60 kPa for P5, P10, and P20 were 0.29, 0.14, and 0.09, respectively. Here, the volume occupied by Xe was calculated by use of the bulk liquid density (3.06 gml^{-1} at 159 K). Then, these ACFs have enough strong molecular field for Xe to be adsorbed even above the critical temperature. In such a case, the DR equation for vapor must be extended to the adsorption of supercritical gas.

Simulated Xe adsorption isotherms

The adsorption isotherms of Xe in the graphite slit pore of $w = 0.90$ to 1.00 nm at 300 K were simulated using the GCMC method. Both simulated isotherms increase with the Xe pressure and bend upward above 50 kPa . In particular, the adsorption isotherm of $w = 0.90 \text{ nm}$ had steeper uptake near 50 kPa than that of $w = 1.00 \text{ nm}$. The upward bending suggests a strong Xe-Xe interaction, accompanying with the cluster formation. Although the simulated isotherms did not agree with experimental one, both results indicate the possibility of the cluster formation upon filling of Xe in the micropore. If there is the cluster formation upon filling in the real ACF system, the further adsorption is blocked near the entrance of slightly wedge-shaped micropores due to the cluster formation; the adsorption isotherm should become Langmurian, as observed.

Xe Cluster size distribution and geometrical cluster structures

We analyzed the snapshots obtained from the GCMC simulation at different pressures for $w = 0.90 \text{ nm}$ system. The cluster analysis evidenced the presence of clusters in the snapshots, giving the cluster size distribution. Before the rising of the isotherm (at 33.7 kPa), 62% of adsorbed Xe molecules are monomers, but we can find 27% of the dimers there; at 50.5 kPa , the percentage of Xe dimers is 30% and even 16% of the trimers are formed. Just after the steep rising at 75.5 kPa , there is the wide distribution of the cluster size; the molecular number in the cluster is in the range up to 12. At 113 kPa the percentage of the monomer drops to 23%, because small Xe clusters merge into greater clusters. Therefore, even above the critical temperature in micropores Xe molecules are associated with each other to form great clusters which can be a precondensed state. This fact supports the idea that predominant adsorption of supercritical gas needs the stable cluster formation between adsorbate molecules.

subtracting pore effect (SPE) method for the α_s -plot with the reference of the standard N_2 adsorption isotherm of nonporous carbon black^{3,12}. The high purify Xe gas was adsorbed on ACF samples at 300K after pre-evacuation of ACF samples at 383K and 1mPa for 2 h. The Xe adsorption isotherm at 300 K was also measured gravimetrically.

GCMC SIMULATION AND CLUSTER ANALYSIS

The established grand canonical Monte Carlo simulation procedure was used. The random movement of molecules makes new configurations and they are accepted according to Metropolis's sampling scheme[13,14]. The pressure P for a chemical potential was directly calculated from the molecular density using GCMC simulation without the wall potential. The radial distribution function (RDF) was calculated. The intensity of RDF at a distance r was obtained from the average number of molecules which are coordinated at the distance between r and $r+\Delta r$ ($\Delta r = 0.01\text{nm}$) for all Xe molecules in 1000 snapshots of the equilibrium state. It was divided by $2\pi r$, because we analyzed only monolayer adsorption region. We used the 12-6 Lennard-Jones potential for the fluid-fluid interaction. The Lennard-Jones parameters of $\epsilon_{\text{ff}}/k = 276.17\text{K}$ and $\sigma_{\text{ff}} = 0.396\text{nm}$ ^{8,15} were used. The interaction potential of a Xe molecule with a single graphite slab was approximated by Steele's 10-4-3 potential function¹⁶. The fitted parameters of the Xe-carbon potential well depth and effective diameter (σ_{w}) were obtained with the use of the Lorentz-Berthelot rules.

We used an established technique of the slit-shaped unit cell in x and y directions^{17,19}. The size of the rectangular cell was $l \times l \times w$, where l and w are the unit cell length and slit width, respectively. The rectangular box is replicated two-dimensionally to form an infinite slit shaped micropore. Here, the w is not equal to the physical width of H , which is defined as the distance between opposite carbon atom layers, but w is the empirical slit width which is the pore width from the molecular adsorption experiment. The w is associated with H by eq. 1²⁰.

$$w = H - (2z_0 - \sigma_{\text{ff}}), \quad z_0 = 0.856\sigma_{\text{ff}} \quad (1)$$

where z_0 is the distance of closest approach. In this work, only model graphite model pore of $w = 0.90$ was calculated.

In the cluster analysis, local molecular configurations of low energy in the equilibrium are presumed to be clusters. The cluster distribution is obtained using the equilibrium snapshots, when the following function $F(\{n_i\})$ is a minimum. We calculated $F(\{n_i\})$ and determined the cluster distribution using the Metropolis method.

$$F(\{n_i\}) = U(\{n_i\}) - TS(\{n_i\}), \quad U(\{n_i\}) = \sum_j U_j, \quad S(\{n_i\}) = k(\ln N! - \sum_j \ln n_j!) \quad (2)$$

Here the number of molecules in the i th cluster is n_i , the total number of molecules N , and the number of ways of allocating N molecules to a given partition $\{n_i\}$. U_j is the cluster formation energy of the cluster j , which consists of n_j molecules; U_j is the sum of each intermolecular potential. $S(\{n_i\})$ is the allocation entropy of partition²¹.

RESULTS AND DISCUSSION

Microporosity and adsorption isotherms of supercritical Xe

The adsorption isotherms of N_2 at 77K on three kinds of ACFs were of Type I, indicating the presence of uniform micropores. The N_2 adsorption isotherm was analyzed by the α_s -plot with the subtracting pore effect (SPE) method¹². Both α_s -plots gave an predominant upward deviation below $\alpha_s=0.5$ due to the enhanced adsorption. The micropore parameters from these α_s -plots for the N_2 adsorption isotherms were determined by use of the SPE method, as given

The intra-cluster radial distribution RDF at 75.5 kPa was calculated. It had a very short peak at 0.44nm corresponding to the dimer at 33.7kPa for both pores. The peak at 0.44 nm indicates the presence of dimers and trimers of regular triangle shape. Also a weak peak at 0.76 nm was observed, suggesting the presence of the complex structure of the regular triangles. Thus, Xe molecules form more and greater clusters having the complex geometrical structure are formed in narrower pores under supercritical conditions.

Acknowledgment

This work was funded by the NEDO project from Japanese Government.

References

1. K. Kaneko, *J. Membrane Sci.*, **96** (1994) 59.
2. S. Iijima, Helical microtubes of graphitic carbon, *Nature*, **354** (1991) 56.
3. Kaneko, C. Ishii, N. Nagai, Y. Hanzawa, N. Setoyama, and T. Suzuki, *Advances Colloid Sci.* **76-77** (1998) 295.
4. K. Kaneko, and Murata, K., *Adsorption*, **3** (1997) 197.
5. K. Kaneko, *Langmuir*, **3**(1987)357.
6. K. Kaneko, *Colloid Surf.*, **37** (1989)115.
7. Z.M.Wang, , T.Suzuki, , N.Uekawa, K.Asakura, and K.Kaneko, *J. Phys. Chem.*, **96** (1992)10917.
8. J.O.Hirschfelder, C.F.Curtiss, R.B.Bird, *Molecular Theory of Gases and Liquids*, Wiley, New York, 1954.
9. A. J.Stone, *The Theory of Intermolecular Forces*, Clarendon press. Oxford, 1996.
10. M. Aoshima, T. Suzuki, and K. Kaneko, *Chem. Phys. Lett.* **310**(1999) 1.
11. M. Aoshima, K. Fukazawa, and K. Kaneko, *J. Colloid Interface Sci.* in press.
12. N. Setoyama, T. Suzuki, and K.Kaneko, *Carbon*, **36**(1998) 1459.
13. N. Metropolis, A. W. Rosenbluth, M. N. Rosenbluth, A. H. Teller, *J. Chem. Phys.* **21** (1953) 1084.
14. M. P. Allen, D. J. Tildesley, *Computer Simulation of Liquids*, Oxford University Press, Oxford, 1987
15. A. J. Marks, J. N. Murrell, A. J. Stace, *J. Chem. Soc. Faraday. trans.*, **87** (1991) 831.
16. W. A. Steele, *Surf. Sci.*, **36** (1973) 317.
17. K. E. Gubbins, *Molecular Simulation*, **2** (1989) 223.
18. R. F. Cracknell, D. Nicholson, N. Quirke, *Mol. Phys.*, **80** (1993) 885.
19. T. Suzuki, K. Kaneko, K. E. Gubbins, *Langmuir*, **13** (1997) 2545.
20. K. Kaneko, R. F. Cracknell, D. Nicholson, *Langmuir*, **10** (1994) 4606.
21. G. N.Coverdale, R. W.Chantrell, G. A. R.Martin, A.Bradbury, A.Hart, and D. A.Parker, *J. Magnet. Magnet. Matter.*, **188** (1988) 41.

LASER-INDUCED INTERACTION OF SILICA WITH METHANE

V. M. Marchenko[†], D. I. Murin[†], and S. V. Lavrishchev[‡]

[†] General Physics Institute of the Russian Academy of Sciences,
38 Vavilov Street, Moscow 117942, Russia;
tel.: +7 (095) 135 3437, facsimile: +7 (095) 135 0270,
e-mail: vmarch@kapella.gpi.ru

[‡] Laser Materials and Technology Research Center of GPI of RAS,
tel.: +7 (095) 132 8393, e-mail: lavr@lst.gpi.ru

KEYWORDS: Silica reduction, laser thermochemistry.

INTRODUCTION

Laser distillation technique advanced by investigations of energy balance in a laser plume formed on the surface of silica (SiO_2) under the action of radiation of the 10.6 mm wavelength was proposed in [1]. The small depth of absorption ($\leq 20 \mu\text{m}$) and the low thermal conductivity resulted in surface heating of silica glass, accompanied by sublimation at $T_s > 1.8 \text{ kK}$. A continuous laser plume appeared at the laser radiation intensities $1 - 6 \text{ kW/cm}^2$ when the target surface was heated to a temperature exceeding the boiling point $T_b \approx 3 \text{ kK}$ [2,3] and the saturated vapor pressure above the surface rose above the atmospheric value. At this laser radiation power the rate of loss of the target material by sublimation of $\sim 3 \text{ mg/s}$ and the specific laser radiation energy of evaporation of silica glass was of 30 kJ/g . A continuous laser plume at the tip of a silica glass rod in air represented a gasdynamic jet of the products of sublimation of SiO_2 at temperatures $T \geq T_b$ escaping into the surrounding atmosphere. According to thermo-chemical analyses [3] at the boiling point T_b thermal decomposition of SiO_2 occurs and composition of the saturated vapor above SiO_2 is governed by equilibrium chemical reaction $\text{SiO}_2 \rightarrow 57.6 \text{ SiO} + 6.6 \text{ O} + 25.8 \text{ O}_2 + 10.0 \text{ SiO}_2$. Cooling of the gaseous products of sublimation by the emission of thermal radiation and by heat exchange with the ambient gas resulted in chemical recombination of these products and condensation of SiO_2 in submicron particles. Deposition of particles on substrates during continuous laser distillation of SiO_2 resulted in synthesis of bulk samples of porous and vitreous structure varied with the temperature of substrates. Laser distillation is useful for rapid synthesis of high-purity and doped samples of silica materials with variable optical properties, including silica nanocomposites [4]. Fluorine-doped silica glasses were synthesized by initiating chemical reactions of the products of pyrolysis in a laser plume with a gas containing freon [5].

Chemical reduction of silica SiO_2 with carbon, hydrogen, and hydrocarbons occurs at high temperatures [6]. Initial stage of the synthesis of Si crystals is smelting of metallurgical silicon in electric furnaces at temperatures $2 - 6 \text{ kK}$ in reactions of reduction of natural silica's with carbon [7]. We investigated experimentally physicochemical processes induced by laser plume on silica glass laser targets streamlined by $\text{CH}_4 - \text{Ar}$ gas flows, composition and microstructure of products of SiO_2 reduction reactions deposited on substrates [8].

EXPERIMENTAL

Experiments were made with laser targets in the form of cylindrical rods of high-purity and technical-grade silica glass of diameters $d \approx 3 \text{ mm}$. Experimental setup is shown in Fig.1. A diverging beam from a cw electric-discharge CO_2 -laser of $\sim 80 \text{ W}$ power was directed on the tip of the rods located behind the focus of an NaCl lens ($F = 27 \text{ cm}$) to enhance the stability of the configuration of the resultant laser plume. The radiation intensity was varied by altering the distance from the focus to the target. The targets were placed inside a silica tube of 25 cm length and inner diameter of 15 mm and streamlined by gas flow directed along the tube opposite to the laser beam and escaped freely into atmosphere. A neutral gas flow surrounding the laser target was provided with Ar, whereas reducing flow consisted of CH_4 or of a $\text{CH}_4 - \text{Ar}$ mixture. The gas flow rate at atmospheric pressure did not exceed 1 liter/min . Silica rods and tubes were used as substrates for the deposition of the laser plume products. The chemical composition of the powder layers deposited on the substrates, sintered or compacted into pellets, was measured with a Camebax SX50 x-ray microanalyser. Microstructure of the laser targets and of the deposited materials was investigated with optical and electron microscopes.

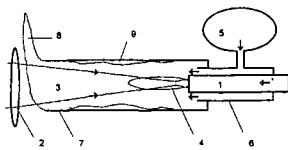


Figure 1. Experimental setup: (1) laser target, (2) NaCl lens, (3) laser beam, (4) laser plume, (5) CH₄ - Ar gaseous mixture, (6) support of the laser target , (7) silica glass tube substrate, (8) flame at the edge of the silica tube, (9) products of the reactions.

RESULTS

At a fixed laser radiation intensity the length of the plume and the spectrum of the emitted radiation depended on the target material. The luminous part of the plume was of ~5 mm length and the emission spectrum was continuous in the visible range when the plume was formed on the surface of high-purity silica glass in an air atmosphere and in Ar. Emission spectra of the plume formed on technical-grade silica glasses included resonance lines of Na and/or K, and the length of the plume increased to ~10 mm. The partly melted and solidified tips of high purity silica glass rods subjected to laser irradiation in atmosphere and Ar had an optically smooth convex shape when the diameter of the laser spot on the end was $d_l > 1/3d$ and a concave shape when d_l was less. Approaching to the focus resulted in a crater formation of ~1 cm deep. The stability of the configuration of targets subjected to laser irradiation was evidently governed by high viscosity of silica glass even at temperature $\sim T_b$.

Radically different results were obtained at the same irradiation geometry when the gas flow around the laser target contained methane. When the gaseous mixture was enriched with methane ($[CH_4] > [Ar]$) irradiation of the tip of rod target resulted in self-ignition of the flowing gas at the exit from the tube at a distance of 20 cm from the target in the region of contact with atmospheric air. Throughout the whole experiment a spontaneous flame was maintained at the tube exit. Ignition of the laser plume inside the tube resulted in additional coloring of the flame at the tube exit, which became yellow or reddish-orange.

Initially stable at fixed radiation intensity convex shape of the target tip changed with time in the presence of CH₄ - Ar flow by the same manner as by approaching of the target to the focus, i.e. by increasing the intensity. The surface of the target tip became concave and after tens of seconds a conical crater with a diameter of ~1.5 mm and up to several millimeters depth was formed.

(Fig. 2a). An analysis of the microstructure of the side surface of a laser target showed that interaction of SiO₂ with CH₄ depended on the distance z from the target tip in accordance with the temperature gradient. There were no changes in the surface structure in the zone with a relatively low temperature ($z > 2$ cm) as after annealing in the flame of a methane burner. Uncolored surface husky islands were observed at higher temperatures ($1 < z < 2$ cm). In the zone with a higher temperature ($0.1 < z < 1$ cm) the side surface of a rod became covered by a specular reflecting black film. In the zone with the highest temperature the surface relief at the tip changed more than during irradiation in air. The tip of a target around the region with removed matter was covered by a black glassy film of 50 - 100 μ m thickness frothed in the high-temperature zone (Fig. 2b) and smooth in the zone where the temperature was lower at the laser spot periphery. Chip of the film revealed nozzle-like channels of the same characteristic size oriented normally to the surface. The smooth region had fine-grained structure.

The frothed film was displaced on the surface of a glass which was completely covered from the inner side by transparent bubbles of 10 - 20 μ m in diameter (Fig. 2c). On the surface of a target irradiated in the high-temperature zone there were hollow spheres with a diameter up to ~100 μ m. The spheres were either transparent or outside coated by a white deposited 'soot' and were easily detached (Figs 2d and 2e). Fig. 2f shows bubbles located on the target surface with characteristic traces of a blowout caused by the escape of internal gases. In the low-temperature zone of the glass at a depth up to ~200 μ m there were also layers saturated with bubbles with typical size of ~25 μ m. Such regions inside some samples contained also whitish-brown formations. After irradiation the bottom of a crater remained transparent, i.e. the products of pyrolysis of SiO₂ were removed from the bottom. Instability of the laser target surface resulting on dependence of the rate of etching of SiO₂ at its boundary on the laser radiation intensity was accompanied by shortening of a plume, its subsequent decay, and a reduction of the rate of target 'combustion'.

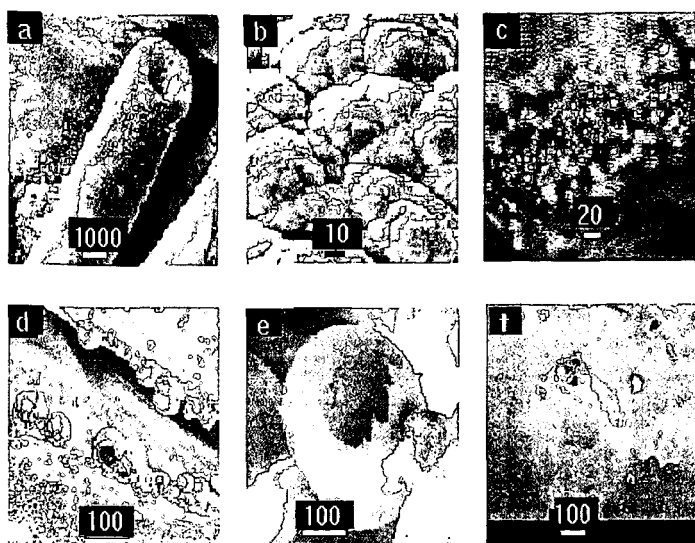


Figure 2. Electron micrographs of laser target (a), boiled and frothed tip of the target (b), bubbles inside (c - photograph) and on surfaces of the targets (d-f).

Vertical convective jet of white smoke emerged from a silica target when the radiation intensity was below the threshold of appearance of a laser plume in an air, $T < T_b$. If the flow of the gas containing CH_4 was repeatedly switched on and off at a constant radiation intensity, a colored plume up to 5 mm length appeared and disappeared in a direction normal to the target tip. This observation indicated that gas-phase reactions took place between the interacting products of a pyrolysis of SiO_2 and CH_4 . Pyrolysis of CH_4 in flowing gaseous mixture interacted with a heated silica rod was indicated by the ejection from the tube of black soot flakes of size up to ~ 1 cm in accordance with the reaction $\text{CH}_4 \rightarrow \text{C} + \text{H}_2$ at a temperature higher of 800 K. The flakes were formed by a network of filaments of ~ 0.1 mm in diameter and a very thin layer of a veil-like net between them. These soot flakes emitted bright radiation inside the tube when they crossed the laser beam. It was difficult to carry out x-ray microanalysis because the electron beam destroyed the filaments. There was no self-ignition of the gas by the laser plume when the partial pressure was in the range $1 > [\text{CH}_4]/[\text{Ar}] > 1/32$ but a self-supporting flame at the tube exit was ignited externally independently on switching the laser plume both on and off. The number of the soot flakes decreased with reducing of CH_4 concentration until they disappeared completely.

Deposition of carried by the flowing gas condensed products on the internal wall of the tube usually lasted the same time as the duration of irradiation of the target (~ 1 min). The deposited layers were cooled and isolated from the atmosphere by continuing the gas flow for ~ 30 s after the irradiation. The elemental composition of the deposited materials depended on the partial pressure of methane in the gas flow and deposition place. In particular, the strongly heated surface of the target itself around the laser spot appeared to be a substrate.

A glass-like black film deposited on the target had the chemical composition of a ternary carbo-silicate system with depended on temperature concentrations of the components. There were measured ratios of components $[\text{Si}] : [\text{O}] : [\text{C}] = 19 : 38 : 42$ and $25 : 59 : 16$ in two points on the external surface adjoining the tip. On a smooth area of the tip surface around the laser spot ratios $[\text{Si}] : [\text{O}] : [\text{C}] = 18 : 21 : 60$ and $20 : 28 : 52$ changed in the direction of a reduction of oxygen and an increase of carbon. This dependence of the composition on the coordinates and, consequently, on the target temperature indicated the reduction reactions occurred on the target.

Black and black-gray layers, mixtures of black and white soot with submicron range microstructure, were deposited on the tube wall when $[\text{CH}_4]/[\text{Ar}] > 1/16$. The layer thickness reached ~ 1 mm and the layer density depended on the actual structure of the flowing gas jets determined by the direction of a plume varied during burning of the target and by the local temperature. When the ratio of concentrations in the similar gas flow around a silica target was $[\text{CH}_4]/[\text{Ar}] < 1/16$ the ejection of matter from the laser target and the rate of deposition decreased

considerably. The color of the coatings on the tube wall changed being at a distance of 0 - 3 cm from the target tip white-brown and yellow and at 3 - 15 cm gray. The elemental composition determined at seven points of a pellet compacted from a yellow-brown layer varied within the range $[Si] : [O] : [C] = (33:1 - 36:8) : (46:6 - 55:6) : (9:6 - 18:3)$. The chemical composition of this layer differed considerably from the stoichiometry of the original silica and was the result of the reduction reactions.

DISCUSSION

The chemical composition of final and intermediate products of induced by laser plume chemical reactions was governed by the chemogasdynamic processes on the laser target and between the gas jets containing the products of pyrolysis of methane and silica. Throughout the investigated range of the concentrations $[CH_4]/[Ar]$ used in experiments flammable gases presented in the flow and chemically reducing conditions were maintained. The observed shape of the laser target surface was qualitatively different from that one in oxidizing or neutral ambient gas. It was attributed by narrowing of the thermal energy flux entering target because of additional heating caused by exothermic surface reactions at the maximum intensity in the laser spot. Laser induced chemical reactions occurred not only in gas phase and on the surface but also in the interior of a target, as indicated by laser-induced surface boiling. The appearance of bubbles inside softened silica was attributed by internal gassing occurred when a target was placed in methane flow. Such gas evolution did not occur when plume combustion was maintained in air and Ar. In a control experiment we introduced inside a silica tube of ~2 mm in diameter a bundle of carbon fibers of 10 μm in diameter. Irradiation of the target smelted the fibers with the glass. The glass-fiber boundary was saturated with bubbles and in some cases surrounded by a white-brown strips.

Boiling of a pure liquid is known to occur because of the appearance of vapor-formation centers, from which bubbles arise inside the liquid, or in a state overheated above the boiling point [9]. The bubbles arise in a liquid if internal pressure $p_i \geq p_a + 2\sigma/r$, where p_a is the atmospheric pressure, σ is the surface tension of silica, r is the bubble radius. In the case under discussion, the quantities σ and r represent the values at the vitrification temperature T_g of silica glass at which the bubble shape becomes frozen. Formation of bubbles from dissolved gases or violent volumetric boiling because of overheating of the liquid phase was not observed in laser targets made of pure silica glass irradiated in atmosphere. Consequently, on the targets streamlined by CH_4 the gas inside the growing bubbles could not consist of the products of pyrolysis of SiO_2 solely because p_i could exceed p_a only at temperatures $T > T_b$. The bubbles appeared at lower temperatures and the boundary of the bubble ensemble was mobile at temperatures $T_g \leq T < T_b$.

The most probable reason of observed phenomenon was gas evolution during exothermic chemical reactions in which silica is reduced by carbon and hydrogen occurred inside softened at high temperatures glass. Carbon and hydrogen were appeared on the surface of the rod by pyrolysis of methane and penetrated in the glass by viscous mixing of the melt and diffusion, as indicated by the characteristic shape of white-brown strips in molten and solidified glass near carbon fibers. Reduction of SiO_2 by carbon $SiO_2 + C \rightarrow Si + SiO + CO$ is used in electrometallurgy for the synthesis of the Si [10]. Silica may be also reduced in the reaction $SiO_2 + H_2 \rightarrow Si + SiO + OH + H_2O$. At temperatures $\sim T_b$ all products of reactions are gaseous because they have lower boiling points. The reactions may cause additional heating of the internal microvolumes of the glass to $T > T_b$ and appearance and growing of microcavities from the gas-formation nuclei filled with gaseous products of the reactions at $p_i > p_a$. A typical shape of the surface at the points of blowout of the bubbles confirmed this hypothesis (Fig.2d). During cooling of the glass the size of the bubbles should decrease and to be frozen at the temperature T_g . This was confirmed by the appearance on a cooled targets of bubbles with concave dents.

The reduction reactions on the surface of a laser target were initiated at temperatures above the temperature of pyrolysis of methane, ~1 kK, and the rate of these reactions increased with increase in temperature up to the boiling point of silica $T_b \sim 3$ kK when a continuous laser plume was formed. The exothermic nature of the reactions was confirmed by lowering of the threshold of formation of a laser plume, when the gas flow contained methane, and supported by increasing of target 'combustion' rate at the maximum intensity in the laser spot as well as by the formation of a crater. The reduction reactions were confirmed also by elemental composition of the laser target surfaces and of the layers of deposited highly disperse products of reactions of white-brown color. Ratio $[Si] : [O] = (79.5 - 46) : (20.5 - 54)$ on the internal surfaces of four split bubbles indicated that the sample became enriched with silicon being higher of its proportion in silicon monoxide SiO . The reduction processes were observed in experiments with carbon fibers so as droplets of deep-brown color inside the bubbles and evidently formed from more refractory Si and/or SiO .

Deposition of particles on the internal wall of a tube from a high-temperature heterogeneous gas flow occurred under the action of thermophoresis forces similar to the MCVD method employed in the fabrication of silica fiber preforms. Droplets observed inside the bubbles, strips on the boundary of carbon fibers and deposited on substrates powder layers all of yellow, white- and deep-brown colors are the products of the disproportion reaction of reduced but unstable condensed silicon oxide $\text{SiO} \rightarrow \text{Si} + \text{SiO}_2$. It was last time determined that gradation of color is connected with microstructure of the samples containing amorphous and microcrystalline silicon.

CONCLUSION

Experimentally were established the experimental conditions, the configuration, and the energy and gasdynamic parameters of initiation by cw laser radiation at the 10.6 mm wavelength of chemical reduction of silica streamlined by gas flow containing methane. The exothermic nature of the reduction reactions was confirmed by decrease of the threshold of appearance of a laser plume and increase in the rate of combustion of the target in the laser spot and formation of a crater so as by an increase in the yield of the reaction products deposited on the tube wall, compared with the yield of the products of pyrolysis of silica in air, and also by a fall of the yield when the concentration of methane in the flowing gas was lowered.

The determined final products of laser-induced reactions of silica with methane are conductive carbo-silicate films on silica surfaces and reduced silicon oxides in gas and condensed phases.

REFERENCES

1. Dianov E M, Koryakovskiy A S, Lebedev V F, Marchenko V M, Prokhorov A M Zh. Tekh. Fiz. 61 (5) 90 (1991) [Sov. Phys. Tech. Phys. 36 551 (1991)]; Sov. Lightwave Commun. 1 223 (1991)
2. Shick H. L. Chem. Rev. 60 331 (1960)
3. Kulikov I. S. Termicheskaya Dissotsiatsiya Soedinenij (Thermal Dissociation of Compounds) (Moscow: Metallurgiya, 1969)
4. Dianov E. M., Lavrishchev S. V., Marchenko V. M., Mashinsky V. M., Prokhorov A. M. Kvantovaya Elektron. (Moscow) 23 1105 (1996) [Quantum Electron. 26 1075 (1996)]
5. Dianov E.M., Koryakovskiy A. S., Marchenko V. M., Lebedev V. F., Pimenov V. G., Prokhorov A M Zh. Tekh. Fiz. 63 (11) 196 (1993) [Tech. Phys. 38 1030 (1993)]
6. Sosman R. B. Phases of Silica (New Brunswick, NJ: Rutgers University Press, 1965)
7. Wolf S., Tauber R. N. Silicon Processing for the VLSI Era (Sunset Beach, CA: Lattice Press, 1996)
8. Lavrishchev S.V., Marchenko V.M., Murin D.I. Quantum Electronics, 28, 920 (1998)
9. Kikoin A. K., Kikoin I. K. Molekulyarnaya Fizika (Molecular Physics) (Moscow: Nauka, 1978)
10. Gel'd P. V., Esin O. A. Protsessy Vysokotemperaturnogo Sintez (Processes in High-Temperature Synthesis) (Sverdlovsk: State Scientific-Research Institute on Ferrous and Nonferrous Metallurgy, 1957)

COMPUTER-AIDED CONSTRUCTION OF COMBUSTION CHEMISTRY MODELS

Oleg A. Mazyar, David M. Matheu, Douglas A. Schwer, and William H. Green, Jr.

*Department of Chemical Engineering, Massachusetts Institute of Technology,
77 Massachusetts Ave., Cambridge, MA 02139*

KEYWORDS: Chemical kinetic models, pressure-dependent rate constants, adaptive chemistry

Introduction

The combustion, oxidation and pyrolysis chemistry of even simple light hydrocarbons can be extremely complex, involving hundreds or thousands of kinetically significant species. Even relatively minor species can play an important role in the formation of undesirable emissions and byproducts. Recently, a number of researchers [1-8] have recognized that the most reasonable way to deal with this complexity is to use a computer not only to numerically solve the kinetic model, but also to construct the model in the first place. We are developing the methods needed to make this feasible, particularly focusing on the need for reliable computer estimates of the pressure-dependent rate constants, rate constants of the reactions with large stereoelectronic effects, and methods for handling situations where the reaction conditions change significantly with time or with spatial position.

We previously devised [8] the first general algorithm for constructing kinetic models appropriate to particular reaction conditions, by numerically testing whether particular species are significant under those conditions. This algorithm can very rapidly and reliably construct rather complex kinetic schemes, testing hundreds of thousands for reactions to find the smaller set which is actually important. It is much less prone to inadvertently omitting an important reaction than other model construction techniques. It has the advantage of clarifying the relationship between the reaction conditions and the kinetic model required. Unfortunately, the existing algorithm is explicitly designed for perfectly mixed, isothermal, isobaric simulations. Relaxing these restrictions raises a number of issues.

Results and Discussion:

A priori rates for combustion reactions

The key issue in constructing any kinetic model, of course, is how to reliably estimate the rate constants required. Many of the important rates for light alkane combustion are known experimentally, though usually over a restricted range of temperatures and pressures (e.g. at room temperature, atmospheric or sub-atmospheric pressure). The highly non-linear combustion process typically involves hundreds of kinetically significant reactive intermediates and even more reactions; it seems unlikely that all the rate constants needed to describe these systems will ever be measured experimentally. What is needed are reliable methods for estimating these reaction rates *a priori*.

Although transition state theory (TST) was proposed more than 60 years ago, and the debate about its microcanonical quantum version known as RRKM has sparked a tremendous amount of effort since the 1960's, this theory was still controversial into the 1990's. It was only over the last decade that conclusive experiments and the elucidation of the connection between TST and quantum scattering decisively established that TST/RRKM is the correct way to calculate most reaction rates. [9-11] Recent advances in computer power and quantum chemistry algorithms have now made it possible to calculate single points on molecular potential energy surfaces (PES's) with something close to "chemical accuracy" of 1-2 kcal/mol. In addition, current DFT technology allows one to calculate rather extensive portions of the PES for even fairly large molecules, albeit with somewhat lower accuracy. [12,13] Several research groups have combined modern quantum chemistry and TST techniques to make *a priori* rate predictions; recent results look very promising. [9,14,15] We have found that in many cases the largest error in *ab initio* rate estimates comes from errors in the calculated barrier height, so one should use high levels of theory for calculating it, but apparently lower levels of theory suffice for estimating the entropic Arrhenius "A" factor (which may be T-dependent). This allows rather accurate rate extrapolations to different temperatures. With some care, complexities such as tunneling, isotope effects, and the large amplitude motions in floppy transition states (TS's) can be modeled accurately *a priori*. [9,14].

Typically rate estimates are made for whole reaction families rather than for individual reactions, an extremely important simplification. The idea is that reaction rates are determined by the functional groups directly involved; the rest of the molecule is more or less a spectator. For example, one would expect that the reactivity of octyl amine and hexyl amine would be very

similar. Usually there are insufficient data to directly verify whether the reaction family idea is valid; but for functional group ideas to work at all it must be at least approximately correct. (For a rare experimental verification see ref. 16).

The Hammond postulate indicates that within a reaction family, the reaction barrier and TS properties should shift with the heat of reaction. These shifts are typically modeled by assuming that the rates follow the simple Arrhenius formula $k(T) = A \exp(-E_a/RT)$, and making linear interpolations between reactions with experimentally determined E_a 's (these interpolations are called "Evans-Polanyi", "LFER", or "Semenov" relations). It is known that the true relationship cannot be linear. Denisov has recently proposed a type of parabolic interpolation. [17] Unfortunately, the experimental data required to make either of these interpolations are often unavailable for the systems of greatest current interest, including many of the reactions important in combustion.

Quantum-chemistry based TST calculations could provide the missing data, but the most accurate quantum techniques are so computationally demanding that only single-point (i.e. fixed geometry) energy calculations are feasible. Much cheaper methods are needed to map out the PES and to determine the vibrational frequencies, etc. required for a TST rate calculations. The method of choice is DFT, which is computationally inexpensive but still fairly accurate in most cases. Unfortunately, current DFT functionals are not reliably enough to be really useful for quantitative kinetics. Current DFT functionals are particularly poor for free-radical oxidations, since they seriously underpredict the strength of peroxidic O-H bonds. [15] We recently developed a method for systematically improving DFT functionals, using as input the results of high-accuracy quantum chemistry calculations. [18] Our approach is based on the fact that the DFT functional determines the electron density as well as the energy; so high-accuracy electron densities provide a strong and very useful constraint on trial functionals.

Many of the components required to make accurate predictions of the chemical kinetics of technologically important processes like combustion already exist. Development and validation of reliable, systematic, quantum/TST-based rate estimation methods would allow us to finally make quantitative predictions about these important chemical processes.

Estimation of pressure-dependent rate constants

For many reactions, pressure-dependent fall-off and chemical-activation effects are very significant. In many cases of importance in combustion chemistry, the initial complex is formed very highly excited, and chemically-activated channels dominate over the thermal pathways. We are currently automating the process of computing pressure-dependent rate constants, so that the computer can do this "on-the-fly" as it constructs the kinetic model. We have devised a general algorithm which constructs every chemically-activated and stabilization reaction pathway, and so can construct and solve the equations which describe the pressure dependence. The required $k(E)$'s and $p(E)$'s can be obtained from the high-pressure limit $k(T)$'s and the group-additivity heat capacities by the inverse Laplace transform technique [19] and the "3-frequency" technique [20] respectively. The pressure dependence can be estimated in many different ways ranging from simple approximations to full-blown time-dependent master equations; we will explore the tradeoffs between accuracy and computational speed.

At least initially, we will use the exponential-down model for energy transfer, and the corresponding Troe $\beta k_\infty[M]$ approximation.[21] For chemically-activated reactions of large molecules, there are a very large number of possible reaction pathways, and some pruning will be necessary. This can be done by setting a criterion for kinetic significance which suppresses the most minor channels. Once one has constructed the pressure-dependence model, it can be solved for a range of pressure and for different initial energy distributions of the activated complex (corresponding to different entrance channels and temperatures). We will test this new tool by computing the pressure dependence of a large number of reactions; in addition to validating the method we expect to find some surprises.

Adaptive complex chemistry for reacting flows

In combustion, the overall rate of reaction is usually controlled as much by mixing as by any rate constant. Conventional reacting-flow simulation techniques can only be used if the chemistry model is very small, since they typically attempt to solve for the concentration of every chemical species in the model at every spatial position at every time point in the simulation. Since the computer can rapidly construct kinetic models adapted to each reaction condition, it should be possible to construct an "adaptive chemistry" reacting flow simulation, where different truncated kinetic models are used at different spatial positions and times. This could dramatically reduce the number of equations which must be solved in the simulation. As a first step towards developing such a simulation, we have been examining how one could in practice develop truncated kinetic schemes known to be reliable over a specific range of reaction conditions. We

will also devise methods for dealing with boundaries between finite elements with different kinetic schemes (involving different numbers of species). For the numerical solution, we will draw heavily on numerical methods for solving differential-algebraic equations with discrete control variables recently developed at MIT. [22] Initially, we will construct the reacting flow simulations by hand, for very simple geometries. Once we demonstrate that the "adaptive chemistry" approach provides a significant advantage over current approaches, we can begin to incorporate the technology developed by others for adaptive gridding [23] that would be required for reacting flows through complex geometries.

References

1. L. Haux, P.-Y. Cunin, M. Griffiths, and G.-M. Come, *J. Chim. Phys.* **1988**, *85*, 739.
2. S.J. Chinnick, D.L. Baulch, and P.B. Ayscough, *Chemom. Intell. Lab. Syst.* **1988**, *5*, 39.
3. E. Ranzi, A. Sogaro, P. Gaffuri, G. Pennati, C.K. Westbrook, and W.J. Pitz, *Combust. Flame* **1994**, *99*, 210.
4. E.S. Blurock, *J. Chem. Inf. Comput. Sci.* **1995**, *35*, 607.
5. L.J. Broadbelt, S.M. Stark, and M.T. Klein, *Comput. Chem. Eng.* **1996**, *20*, 113.
6. M. Nehse, J. Warnatz, and C. Chevalier, *Twenty-Sixth Symposium (International) on Combustion* (The Combustion Institute: Pittsburgh, **1997**).
7. D.J. Klink and L.J. Broadbelt, *A.I.Ch.E. J.* **1997**, *43*, 1828.
8. R.G. Susnow, A.M. Dean, W.H. Green, P. Peczak, & L.J. Broadbelt, *J. Phys. Chem. A* **1997**, *101*, 3731.
9. D.G. Truhlar, B.C. Garrett, and S.J. Klippenstein, *J. Phys. Chem.* **1996**, *100*, 12771.
10. W.H. Miller, *Acc. Chem. Res.* **1993**, *26*, 174.
11. W.H. Green, C.B. Moore, and W.F. Polik, *Ann. Rev. Phys. Chem.* **1992**, *43*, 591.
12. L.A. Curtiss, K. Raghavachari, G.W. Trucks, and J.A. Pople, *J. Chem. Phys.* **1991**, *94*, 7221.
13. A.D. Becke, *J. Chem. Phys.* **1992**, *96*, 2155.
14. See for example (a) S.J. Klippenstein and W.D. Allen, *Ber. Bunsenges. Phys. Chem.* **1997**, *101*, 423; (b) S.J. Klippenstein, A.L.L. East, and W.D. Allen, *J. Chem. Phys.* **1994**, *101*, 9198.
15. W.H. Green, *Int. J. Quantum Chem.* **1994**, *52*, 837.
16. J.B. Koffend and N. Cohen, *Int. J. Chem. Kinet.* **1996**, *28*, 79.
17. E.T. Denisov, *Mendeleev Commun.* **1992**.
18. D.J. Tozer, N.C. Handy, and W.H. Green, *Chem. Phys. Lett.* **1997**, *273*, 183.
19. W. Forst, *J. Phys. Chem.* **1972**, *76*, 342.
20. J.W. Bozzelli, A.Y. Chang, and A.M. Dean, *Int. J. Chem. Kinet.* **1997**, *29*, 161.
21. R.G. Gilbert, K. Luther, and J. Troe, *Ber. Bunsenges. Phys. Chem.* **1983**, *87*, 169.
22. T. Park and P.I. Barton, *ACM Trans. Mod. Computer Sim.* **1996**, *6*, 137.
23. B.A.V. Bennett and M.D. Smooke, *J. Comp. Phys.* **1999**, *151*, 684.

KINETIC MODELING OF THE FORMATION OF POLYCYCLIC AROMATIC HYDROCARBONS

Henning Richter, Timothy G. Benish, Francisco Ayala and Jack B. Howard

Department of Chemical Engineering, Massachusetts Institute of Technology,
77 Massachusetts Avenue, Cambridge, MA 02139-4307, U.S.A.

Keywords: Combustion, PAH, Kinetics

1. INTRODUCTION

Growing evidence of the significant role of polycyclic aromatic hydrocarbons (PAH) in the formation of small particles such as soot in atmospheric aerosols and the known mutagenic or tumorigenic properties of at least some of them^{1,2} necessitate a better understanding of the chemical growth process leading to larger and larger molecules. Combustion represents a major source of PAH and soot particles in the environment, therefore more efficient and cleaner combustion processes would lead to a significant reduction of pollution and to a more economic use of fossil fuels. Kinetic modeling can be expected to be a powerful tool for a better understanding of chemical processes responsible for PAH and ultimately soot formation. A sufficiently developed model will finally allow the assessment of optimized operating conditions for practical combustion devices. In the recent years detailed kinetic models describing the formation of small and medium PAH have been developed and tested against experimental data obtained under well defined laboratory conditions such as shock tube pyrolysis^{3,4} or premixed flames⁵⁻¹¹.

In the present work, two sets of experimental data obtained with different laboratory combustors, fuels and pressures are used in order to improve the reliability and in particular the detailed understanding of elementary reaction steps of a kinetic model developed recently for fuel rich benzene combustion under low pressure conditions¹¹.

2. APPROACH

A nearly sooting low pressure premixed, laminar, one-dimensional benzene/oxygen/argon flame (equivalence ratio $\phi = 1.8$, 30% argon, 50 cm s⁻¹, 2.67 kPa) for which large sets of experimental data^{12,13} are available was modeled using the Premix code¹⁴. This flame has been studied by Bittner and Howard¹² using molecular beam sampling coupled to mass spectrometry (MBMS) to establish concentration profiles for stable species up to 202 amu and radicals up to 91 amu. The temperature profile was determined with a thermocouple taking into account heat losses by radiation. Because the measurements include unstable, often radical, intermediates the data provide valuable insights and have been used for different modeling studies focusing on a better understanding of benzene oxidation chemistry^{3,6,9} and for the assessment of the first reaction steps of PAH growth¹¹. The use of nozzle beam sampling followed by radical scavenging and subsequent analysis by gas chromatography coupled to mass spectrometry, a technique developed and successfully used by Hausmann et al.¹⁵, allowed Benish¹³ to extend the data set to species up to 276 amu in the case of stable species and up to 201 amu for radicals.

The other experimental data used in the present work consist of concentration profiles of light gas species and PAH up to 300 amu measured for fuel rich C₂H₄/O₂/N₂ combustion ($\phi = 2.2$) in a jet-stirred-reactor/plug-flow reactor (JSR/PSR) system by means of gas chromatography operating at atmospheric pressure^{16,17}. The temperature was constant at 1630K in the JSR and 1630 K in the PFR. The outlet of the JSR was coupled to the inlet of the PFR. Kinetic models can be applied easily to both JSR and PFR which allows the comparison of model predictions to experimental data.

The parallel investigation of PAH formation under different conditions at low pressure, atmospheric pressure and different fuels, i. e., benzene and ethylene, is particularly challenging for a kinetic model. The present study is based on a recently published model tested for low pressure conditions¹¹ but with the rate constants of pressure-dependent chemically activated reactions, e. g., for benzene formation via the reaction of acetylene with 1-butadienyl radical²⁰, which have been systematically adapted to 1 atm using the QRRK (Quantum Rice-Ramsperger-Kassel) technique²¹. Thermodynamic data have been critically assessed and updated with available literature data or, in the case of poorly known PAH radicals, computed using *ab initio* techniques. Vibrational analysis performed on the optimized geometries allowed the determination of entropies and heat capacities while enthalpies of formation were determined by means of isodesmic reactions. Rate constants of reactions involved in the growth process have been investigated. The potential energy surfaces, including transition states, of the reactions phenyl + acetylene and of 1-naphthyl + acetylene have been explored. The resulting high pressure rate constants for the different elementary reactions followed by a QRRK treatment allowed the determination of "apparent" rate constants at different pressures and temperatures

c1ccc2ccccc2c1 + C#C \rightleftharpoons c1ccc2ccccc2c1C#C

1-naphthyl + C_2H_2 \rightleftharpoons 1-vinylacetylene

1-vinylacetylene \rightarrow 1-naphthylacetylene + H

1-vinylacetylene \rightarrow acenaphthalene + H

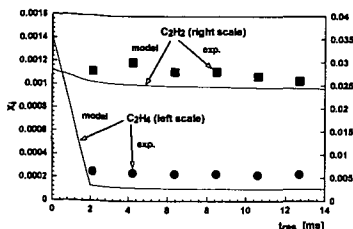


Fig 4. Model predictions and experimental data of ethylene and acetylene in a plug-flow reactor at 1620 K and 1 atm; JSR: $C_2H_4/O_2/N_2$ ($\phi = 2.2$, 71.6% N_2 , 1630K)^{16,17}.

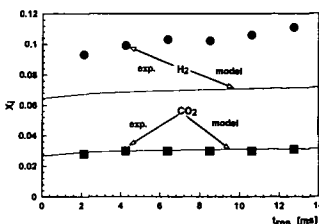


Fig 5. Model predictions and experimental data of H_2 and CO_2 in a plug-flow reactor at 1620 K and 1 atm; JSR: $C_2H_4/O_2/N_2$ ($\phi = 2.2$, 71.6% N_2 , 1630 K, 1 atm)^{16,17}.

b) Beginning of the Growth Process

The formation of polycyclic aromatic hydrocarbons (PAH) and of soot depends mainly on the initial relative concentration of fuel and oxidizer, i. e., the equivalence ratio, reflecting the competition of oxidation with growth reactions. The latter becomes more favorable with increasing equivalence ratio. Assuming an essential role of a subsequent growth process from small to larger and larger PAH, the formation of the first aromatic species is of great interest. The importance of the formation of the first aromatic ring is confirmed by the order of the sooting tendencies: naphthalenes > benzenes > diolefins > monoolefins > paraffins²⁵. Because of the presence of the first aromatic ring in the initial fresh gas mixture in the case of benzene combustion, the formation pathways for benzene will be discussed for ethylene combustion in the jet-stirred/plug-flow reactor system. Different pathways leading to the first aromatic ring, i. e., benzene or phenyl, have been discussed in the past²⁶ and are implemented in the present model. The analysis of the rates of production in the present work showed the reaction between

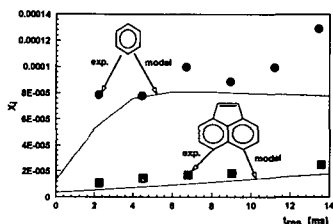


Fig 6. Model predictions and experimental data of benzene and acenaphthalene in a plug-flow reactor at 1620 K and 1 atm; JSR: $C_2H_4/O_2/N_2$ ($\phi = 2.2$, 71.6% N_2 , 1 atm)^{16,17}.

two propargyl (C_3H_3) being the dominant pathway but also the reaction of acetylene with a vinylacetylene radical ($HCCCHCCH$) and of allene (CH_2CCH_2) with a C_3H_2 radical contributed significantly. It should be pointed out that no general conclusions can be drawn from these results because of the likely strong dependence of the relative contributions of the different pathways on experimental conditions such as temperature or fuel type. Nevertheless, the use of different pathways described previously in the literature in the present model allows an at least satisfactory agreement with experimental data as shown in Fig. 6.

c) Formation of the Second Aromatic Ring

Beginning with the first aromatic ring, mainly two pathways may lead to the formation of the next larger fused PAH, naphthalene. First, two subsequent H-abstraction/acetylene-addition steps^{3,10} can lead to 1-naphthyl radicals, stabilized in the next step by recombination with atomic hydrogen. The other possibility consists of the reaction of two cyclopentadienyl radicals^{7,11,27,28}

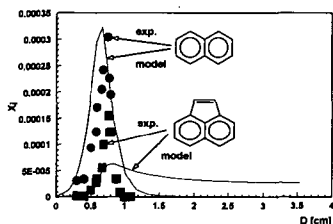


Fig 7. Model predictions and experimental data of naphthalene and acenaphthalene in a nearly sooting premixed benzene/oxygen/argon flame ($\phi = 1.8$, 2.67 kPa)¹³.

benzene flame. Confirming prior results^{7,8,11}, naphthalene formation is dominated by the reaction between two cyclopentadienyl moieties. The comparison of the model prediction with the experimental naphthalene profile measured by Benish shows an excellent agreement (Fig. 7).

Recent measurements of radical concentration profiles in the benzene flame studied in this work¹³ allowed the assessment of the role of hydrogen-abstraction/acetylene-addition pathway under the condition of this flame. In fact, the reaction of the phenylacetylene radical with acetylene to 1-naphthyl (Fig. 8), represents the limiting step for the formation of 1-naphthyl. In contradiction to the good agreement observed for 2-naphthyl radicals (Fig. 10), the 1-naphthyl peak concentration is significantly underpredicted (Fig. 9). As shown in in Fig. 9, the total removal of the hydrogen-abstraction /acetylene addition pathway (Fig. 8) leads to a drastic increase of the 1-naphthyl peak mole fraction, in agreement with the experimental data, while a lack of sufficient consumption in the burnt gases is observed. Based on this observation, completed by tests of the impact of slight adjustments of thermodynamic and kinetic data, it seems likely that the 1-naphthyl concentration, at least under the present conditions, is mainly

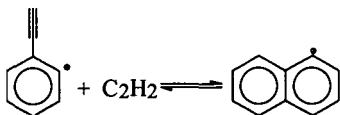


Fig 8. Naphthalene formation via the hydrogen-abstraction/acetylene addition pathway.

governed by the equilibrium of the ring closure reaction (Fig. 8). Also the drastic decrease of the 1-naphthyl mole fraction at the end of the flame front seems to be strongly influenced by the reverse reaction (Fig. 9). Therefore, uncertainties on thermodynamic and kinetic data may be responsible for the underprediction of 1-naphthyl. This hypothesis is consistent with a much better agreement between the model prediction for the 2-

naphthyl radical and the corresponding experimental profile (Fig. 10). 2-naphthyl is formed by hydrogen abstraction from naphthalene and is not directly involved in the above mentioned equilibrium.

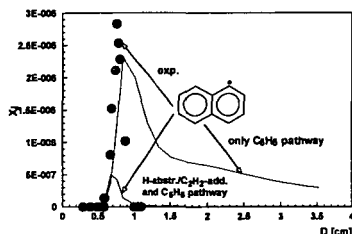


Fig 9. Model predictions and experimental data of 1-naphthyl in a nearly sooting premixed benzene/oxygen/argon flame ($\phi = 1.8, 2.67$ kPa)¹³; use of complete model and after removal of H-abstraction/C₂H₂-addition pathway.

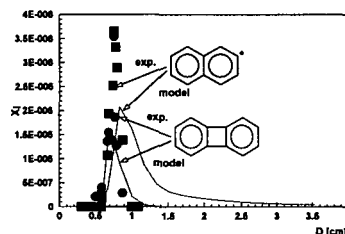
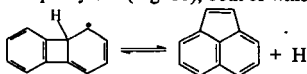


Fig 10. Model predictions and experimental data of 2-naphthyl and biphenylene in a nearly sooting premixed benzene/oxygen/argon flame ($\phi = 1.8, 2.67$ kPa)¹³.

d) Further Growth Process

Acenaphthalene, a PAH containing a five-membered ring, is usually an abundant species in the exhaust of combustion systems generating PAH. The comparison of model prediction with experimental data is shown for ethylene combustion in the JSR/PFR system (Fig. 6) as well as for low pressure benzene combustion (Fig. 7). A particular good agreement could be achieved in the JSR/PFR system, nevertheless also the significant underproduction of naphthalene in this system must be taken into account which leads to the assumption of an even too pronounced acenaphthalene formation. The analysis of the net production rate of acenaphthalene shows a nearly exclusive formation via the reaction of acetylene with 1-naphthyl (Fig. 1), using the rate constant determined for 1 atm by means of the QRRK approach discussed above. A different situation has been observed in the case of low pressure premixed benzene combustion, in agreement with prior work¹¹, where the exclusive use of the reaction between 1-naphthyl and acetylene yields an underprediction of at least 20-fold. This finding confirms the conclusion of Hausmann et al.¹⁵ that another, yet unknown, acenaphthalene formation pathway exists. In the present work an additional acenaphthalene pathway has been suggested and implemented in the model. The isomerization of a biphenylene radical followed by hydrogen loss to acenaphthalene has been assumed and led to a significant improvement in the predictions of acenaphthalene but also biphenylene (Fig. 10), both of which species were measured by Benish¹³.



4. CONCLUSIONS

In conclusion, it can be stated that the kinetic model developed in the present work shows at least encouraging prediction capabilities for the first steps in the growth process to larger and larger polycyclic aromatic hydrocarbons. In particular, its satisfactory performance for two

different fuels and pressures increases its value for potential practical application. In next steps, the model will be extended to larger PAH, including up to eight aromatic rings, and a soot formation model will be implemented.

Acknowledgments

We are grateful to the Division of Chemical Sciences, Office of Basic Energy Sciences, Office of Energy Research, U.S. Department of Energy, under Grant No. DE-FG02-84ER13282 for financial support of the research. The authors thank Prof. J. W. Bozzelli from the New Jersey Institute of Technology for providing software and valuable advice. Prof. W. H. Green and Dr. O. A. Mazzyar from MIT are acknowledged for their contributions to the computational determination of kinetic and thermodynamic data as well as for many helpful discussions.

References

- (1) Durant, J. L.; Busby, W. F.; Lafleur, A. L.; Penman, B. W.; Crespi, C. L. *Mutation Research* **1996**, 371, 123.
- (2) Denissenko, M. F.; Pao, A.; Tang, M.; Pfeifer, G. P. *Science* **1996**, 274, 430.
- (3) Frenklach, M.; Clary, D. W.; Gardiner, W. C.; Stein, S. E. *Twentieth Symposium (International) on Combustion*; The Combustion Institute: Pittsburgh, PA, 1984; p 887.
- (4) Colket, M. B.; Seery, D. J. *Twenty-Fifth Symposium (International) on Combustion*; The Combustion Institute: Pittsburgh, PA, 1994; p 883.
- (5) Lindstedt, R. P.; Skevis, G. *Combust. Flame* **1994**, 99, 551.
- (6) Zhang, H.-Y.; McKinnon, J. Th. *Combust. Sci. and Tech.* **1995**, 107, 261.
- (7) Marinov, N. M.; Pitz, W. J.; Westbrook, C. K.; Castaldi, M. J.; Senkan, S. M. *Combust. Sci. and Tech.* **1996**, 116-117, 211.
- (8) Castaldi, M. J.; Marinov, N. M.; Melius, C. F.; Huang, J.; Senkan, S. M.; Pitz, W. J.; Westbrook, C. K. *Twenty-Sixth Symposium (International) on Combustion*; The Combustion Institute: Pittsburgh, PA, 1996; p. 693.
- (9) Tan, F.; Frank, P., *Twenty-Sixth Symposium (International) on Combustion*; The Combustion Institute: Pittsburgh, PA, 1996; p. 677.
- (10) Wang, H.; Frenklach, M. *Combust. Flame* **1997**, 110, 173.
- (11) Richter, H.; Grieco, W. J.; Howard, J. B. *Combust. Flame* **1999**, 119, 1.
- (12) Bittner, J. D.; Howard, J. B. *Eighteenth Symposium (International) on Combustion*; The Combustion Institute: Pittsburgh, PA, 1981; p 1105.
- (13) Benish, T. G. Ph.D. Thesis, Department of Chemical Engineering, Massachusetts Institute of Technology **1999**, Cambridge, MA, USA.
- (14) Kee, R. J.; Grcar, J. F.; Smooke, M. D.; Miller, J. A. (1997). *A FORTRAN Program for Modeling Steady Laminar One-Dimensional Premixed Flames*. Sandia Rept. SAND85-8240.
- (15) Hausmann, M.; Hebben, P.; Homann, K.-H. *Twenty-Fourth Symposium (International) on Combustion*, The Combustion Institute: Pittsburgh, PA, 1992; p. 793.
- (16) Marr, J. A.; Giovane, L. M.; Longwell, J. P.; Howard, J. B.; Lafleur, A. L. *Combust. Sci. and Tech.* **1994**, 101, 301.
- (17) Marr, J. A. Ph.D. Thesis, Department of Chemical Engineering, Massachusetts Institute of Technology **1993**, Cambridge, MA, USA.
- (18) Glarborg, P.; Kee, R. J.; Grcar, J. F.; Miller, J. A. (1986). *PSR: A FORTRAN Program for Modeling Well-Stirred Reactors*. Sandia Rept. SAND86-8209.
- (19) Lutz, A. E.; Kee, R. J.; Miller, J. A. (1997). *SENKIN: A FORTRAN Program for Predicting Homogeneous Gas Phase Chemical Kinetics with Sensitivity Analysis*. Sandia Rept. SAND87-8248.
- (20) Westmoreland, P. R.; Dean, A. M.; Howard, J. B.; Longwell, J. P. *J. Phys. Chem.* **1989**, 93, 8171.
- (21) Dean, A. M.; Bozzelli, J. W.; Ritter, E. R. *Combust. Sci. and Tech.* **1991**, 80, 63.
- (22) McKinnon, J. T.; Howard, J. B. *Twenty-Fourth Symposium (International) on Combustion*, The Combustion Institute: Pittsburgh, PA, 1992; p. 965.
- (23) Frank, P.; Herzler, J.; Just, T.; Wahl, C. *Twenty-Fifth Symposium (International) on Combustion*, The Combustion Institute: Pittsburgh, PA, 1994; p. 833.
- (24) Alzueta, M. U.; Oliva, M.; Glarborg, P. *Int. J. Chem. Kinet.* **1998**, 30, 683.
- (25) Palmer, H. B.; Cullis, C. F. *The Formation of Carbon from Gases, Chemistry and Physics of Carbon* (editor Walker, P. L.), Vol. 1, p. 265. Marcel Dekker, New York, (1965).
- (26) Miller, J. A.; Melius, C. F. *Combust. Flame* **1992**, 91, 21.
- (27) Dean, A. M. *J. Phys. Chem.* **1990**, 94, 1432.
- (28) Melius, C. F.; Colvin, M. E.; Marinov, N. M.; Pitz, W. J.; Senkan, S. M. *Twenty-Sixth Symposium (International) on Combustion*, The Combustion Institute: Pittsburgh, PA, 1996; p. 685.

NUMERICAL MODELING OF NO REDUCTION USING BIOMASS-BASED MATERIALS AS REBURN FUELS

Sumcet Bhalla and Sama V. Pisupati
Department of Energy and Geo-Environmental Engineering
The Pennsylvania State University
110 Hosler Building
University Park, PA 16802

INTRODUCTION

The role of both homogeneous and heterogeneous reactions in use of solid fuels such as coal for NO_x reduction has been discussed in some previous studies^{1,2,3,4}. However Wendt⁵, and Merceh and Wendt⁶ have discounted heterogeneous reactions showing that they have minor contribution towards reburning. The reduction potential of a fuel depends on its ability to produce CH₄ radicals to react with NO. Assuming only homogeneous gas phase reactions to participate in reduction, a higher volatile matter content of the fuel will enhance the NO_x reduction. In the recent past, the reburning process is reasonably well understood for use of coal and natural gas as reburn fuels^{2, 3, 7, 8, 9, 10,11}. However pyrolysis products of biomass and biomass pyrolysis oils (bio-oils) have also been shown to cause NO_x reduction by mechanisms similar to reburning^{12, 13}. Biomass and biomass based products offer the advantage of not only reduced SO₂, NO_x emissions because of low nitrogen and sulfur content but also reduced green house gases (N₂O and CO₂). However some fundamental questions such as the relative importance of homogeneous gas phase reactions in the process still need to be addressed. In the present study, gas composition from flash pyrolysis of BioLime™ from an earlier study¹⁴ was used to model NO reduction through homogeneous gas phase reactions when BioLime™ is used as a reburn fuel. The numerical predictions were then compared with the NO_x emissions from a down-fired combustor (DFC) to validate the model. A difference in NO_x reduction was observed by using two different BioLime™ samples as reburn fuel under similar operating conditions. This was believed to be due to difference in yield of flash pyrolysis products of the different BioLime™. With this in mind the model was further used to study the relative contribution of each of the pyrolysis gas species in NO reduction through homogeneous reactions. The predictions were then verified by experimental results from the flow reactor.

EXPERIMENTAL

Raw Materials

Two biomass based materials called BioLime™ I and III were obtained from DynaMotive Technologies Corporation. BioLime™ was produced by reacting pyrolysis oils from biomass with air, and lime/water slurry in a stirred. BioLime™ I and III had approximately 7 and 14 wt. % calcium, respectively. Compositional analysis of the samples is shown in Table 1.

	BioLime™ I (As Determined)	BioLime™ III (As Determined)
Carbon (wt. % daf)	48.5	38.7
Hydrogen (wt. % daf)	7.7	8.4
Nitrogen (wt. % daf)	0.23	0.21
Sulfur (wt. % daf)	0.01	0.02
Oxygen (wt. % daf by diff)	43.5	52.6
Ash (wt. % db)	20.9	48.5
Moisture (wt. %)	7.97	4.11

Table 1 Compositional analysis on as determined and dry basis for two BioLime™ samples

Down Fired Combustor

The DFC is 10 ft high with a 20-inch internal diameter rated at a nominal firing rate of 0.5 million Btu/h. Several 4-inch sampling ports are located along the combustor. Sample ports are numbered 1 through 10 starting at the top. BioLime™ is introduced through port 5 into the reburn zone. The reburn zone parameters are shown in Table 2. The flue gases from the heat exchanger pass through a pulse jet baghouse for particulate matter collection. The BioLime™ is prepared, stored in a day tank and pumped to the burner by a Moyno™ progressive cavity pump. The gaseous emissions data during the steady state was averaged.

DFC Reburn zone parameters	Values with the units
Diameter	50.8 cm
Total length	96.52 cm
Volume	195600 cm ³
Pressure	1 atm
Residence time	1.127 seconds
Inlet temperature at the center	1415 K
Inlet temperature at the wall	1426 K

Table 2 Down fired combustor reburn zone parameters

Modeling NO_x Reductions

All numerical calculations were done using a PSR computer code¹⁵, which runs in conjunction with the Chemkin library¹⁶. The reverse rate constants were obtained from the forward rate constants and the thermodynamic data, mainly taken from the Sandia Thermodynamic Database¹⁷. The code computes species concentrations from the balance between the net rate of production of each species by chemical reaction and the difference between the input and output flow rates of species. The model used to predict NO emissions was taken from the studies of Kilpinen *et al.*¹⁸, Glarborg *et al.*¹⁹, and Prada and Miller²⁰. In general the mechanism includes generation of hydrocarbon radicals from C₁ and C₂ parent hydrocarbons, oxidation mechanisms for HCN, and NH₃, together with a subset of the interactions between the hydrocarbon radicals and the nitrogenous species. The nitrogen-hydrocarbon chemistry is essentially an extension of the Miller and Bowman mechanism²¹.

The procedure and assumptions in the above study are:

- (1) Only homogeneous gas phase reactions are responsible for NO reduction. The effect of heterogeneous reactions is neglected. Gases from pyrolysis of BioLime™ react with NO_x in the reburn zone to form N₂ and nitrogenous intermediate species such as HCN and NH₃.
- (2) Gas concentrations are calculated from the yields reported in an earlier study¹⁴.
- (3) Reburn fuel is mixed rapidly and perfectly with the products of combustion from the primary zone. This is achieved by use of high-pressure injection nozzle for feeding the reburn fuel.
- (4) Reburn fuel is pyrolyzed instantly on entering the combustor and therefore pyrolysis kinetics does not control the NO_x reduction kinetics.
- (5) The kinetics of reburning is controlled by the rate constants for the hydrocarbon-NO reaction system. The effect of mass transfer is neglected. This follows from the previous two assumptions.
- (6) An average of the wall and bulk temperature at the point of reburn fuel injection is used as the inlet temperature for the calculations.
- (7) Gas densities are calculated at the reburn zone inlet temperatures.
- (8) The flue gas in reburn zone consists of 14% CO₂, 2.0% O₂, and 497 ppm of CO in nitrogen base. These concentrations of CO₂, O₂, and CO are chosen to be consistent with those of a coal primary flame operated at stoichiometric ratio of 1.0-1.1.
- (9) A residence time of 1.127 seconds is used for the calculations, which is consistent with the residence time in reburn zone of the down-fired combustor.

RESULTS AND DISCUSSION

Predictions of NO_x emissions from the model along with the down-fired combustor data are shown in Table 3. The reburn zone stoichiometry was based on the total amount of fuel and oxidizer that entered the down fired combustor in the first two zones of the combustor divided by the stoichiometric requirement for the primary and reburn fuel⁹. The predictions from model match closely with the DFC data. The results showed a higher NO_x reduction for BioLime™ I than III. However, stoichiometry was different for different runs when BioLime™ I and III are used as reburn fuel. Therefore, to further compare the performance of BioLime™ I and III, NO_x reduction was estimated for both BioLime™ for each run. The results are shown in Figure 1. It can be seen that BioLime™ I produced a higher NO_x reduction than BioLime™ III, and is attributed to the higher yield of total pyrolysis gases for BioLime™ I. These results are in agreement with the studies of Kicherer *et al.*²², who have shown that the main reduction effect is due to the volatiles of the reburning fuel. Therefore, a higher yield of pyrolysis gases will result in a higher NO_x reduction. Different pyrolysis gases can have different NO_x reduction potential. However as seen from Table 3, the relative percentage of pyrolysis gases added was different for different runs. Knowledge of relative contribution of pyrolysis gases in NO_x reduction would help to choose a biomass feedstock that increases the yield of desired species. With this in mind a parametric analysis is done using the model to study the effect of varying concentration of hydrocarbons, CO₂, CO, H₂.

Run (BioLime™)	Stoichiometry	% of Hydrocarbon added	% CO ₂ added	% CO added	% H ₂ added	% NO _x Reduction (DFC)	% NO _x Reduction (Model)
Run 1(I)	0.501	0.13	14.88	0.25	0.23	17.0	16.0
Run 2(I)	0.517	0.14	14.92	0.26	0.24	16.2	16.8
Run 3(III)	0.549	0.09	14.50	0.18	0.20	13.6	11.2
Run 4(III)	0.652	0.04	14.20	0.10	0.08	11.6	4.4
Run 5(III)	0.656	0.05	14.27	0.12	0.11	12.5	7.2
Run 6(III)	0.717	0.05	14.27	0.12	0.11	12.6	6.3

Table 3. Model predictions for percentage NO_x reduction with NO_x reduction from DFC.

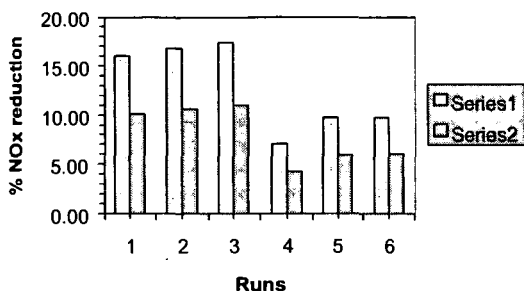
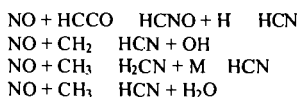


Figure 1. Influence of BioLime™ used on NO_x reduction. The % NO_x reduction is predicted from model for both BioLime™ for each run condition.(Series 1 – BioLime™ I, Series 2 - BioLime™ III)

The results were then verified using the flow reactor. The setup of the flow reactor is discussed in an earlier study⁴. CO₂, CO, and H₂ had very little effect on NO_x reduction. Hydrocarbons were seen to be mainly responsible for causing reduction in emissions of NO_x. Kilpinen *et. al.*²³, Chen *et. al.*²⁴, Merzb and Wondt²⁵ have also shown that for natural gas reburning CO, and H₂ are useable as reburn fuels, even though the rates of reaction for NO reduction by CO and H₂ are significantly slower compared to NO-hydrocarbon reactions. Two main stages are considered to be mainly responsible for nitric oxide reduction. First is the conversion of NO to HCN, through reaction with CH₄ and HCCO.



The second stage is the reaction of HCN with the oxidizing species (O, OH) to form NH₃, N₂, and NO. HCN is first converted to isocyanic acid and HNCO primarily by



and to a lesser extent also through the direct reaction



The HNCO reacts further to NH₂. This occurs primarily by the reaction with H radical



The NH₂ radical depending on the conditions can be converted to N₂, NH₃, or NO.

Burch *et. al.*²⁶ in their study of different fuels (methane, hexane, benzene, and coal) have also shown that NO_x reduction efficiency can also be related to C/H ratio for the fuel. Carbon rich fuels produce more CH₄ fragments, leading to a lower NO_x concentration. BioLime™ I had a C/H ratio of 6.3 whereas BioLime™ III had a C/H ratio of 4.6. Therefore, a BioLime™ with a higher C/H ratio will help to increase the NO_x reduction.

CONCLUSIONS

- 1) Percentage of NO_x reduction using BioLime™ as a reburn fuel was accurately predicted using the homogeneous gas phase reaction model. For most of the conditions, the percentage NO_x reduction predicted from model was well within the allowable variation from the experimental results from down fired combustor and flow reactor. However in some studies like those of Smart and Morgan ²⁷, Chen and Ma ²⁸ have also shown the role of char reactions in NO_x reduction.
- 2) The higher NO_x reduction potential of BioLime™ I over BioLime™ III was attributed to the higher yield of total pyrolysis gases.
- 3) The parametric study from flow reactor showed that the CO , CO_2 , and H_2 have very little effect and hydrocarbon reactions are mainly responsible for NO_x reduction. Hence a fuel with higher C/H ratio will produce more CH_4 fragments, and therefore, result in a better NO_x reduction.

REFERENCES

- ¹ Chen, W.-Y., and Ma, L., "Effect of Heterogeneous Mechanisms During Reburning of Nitrogen Oxide", AIChE Journal, Vol. 42, No. 7, 1996, pp. 1968-1976.
- ² Spliethoff H., Grcul U., Rüdiger, H., and Hein, K. R. G., "Basic effects on NO_x emissions in air staging and reburning at a bench-scale test facility", Fuel, Vol. 75, No.5, 1996, pp. 560-564.
- ³ Liu, H., Hampartsoumian, E., and Gibbs, B. M., "Evaluation of the optimal fuel characteristics for efficient NO reduction by coal reburning", Fuel, Vol. 76, No. 11, 1997, pp. 985-993.
- ⁴ Burch, T. E., Tillman, F. R., Chen, W.-Y., and Lester, T. W., Conway, R. B., and Sterling, A. M., "Partitioning of Nitrogenous Species in the Fuel-Rich Stage of Reburning", Energy and Fuels, Vol. 5, No. 2, 1991, pp.231-237.
- ⁵ Wendt, J. O. L., "Mechanism Governing the Formation and Destruction of NO_x and Other Nitrogenous Species in Low NO_x Coal Combustion Systems", Combustion Science and Technology, Vol. 108, 1995, pp. 323-344.
- ⁶ Merzb, J.B., and Wendt J. O. L., "Air staging and reburning mechanisms for NO_x abatement in a laboratory coal combustor", Fuel, Vol. 73, No. 7, 1994, pp. 1020-1026.
- ⁷ Bilbao, R., Millera, A., Alzueta, M. U., "Influence of the Temperature and Oxygen Concentration on NO_x Reduction in the Natural Gas Reburning Process", Industrial Engineering Chemistry, Vol. 33, 1994, pp. 2846-2852.
- ⁸ Ashworth, B., Sommer, T., Moyeda, D., and Payne, R., "Reburning for Utility Boiler NO_x Control A Comparison of Theory and Practice", Joint Power Generation Conference, Vol. 1, ASME, 1996, pp. 67-76.
- ⁹ Smart, J. P., and Morgan, D. J., "The effectiveness of multi-fuel reburning in an internally fuel-staged burner for NO_x reduction", Fuel, Vol. 73, No. 9, 1994, pp. 1437-1442.
- ¹⁰ Kicherer, A., Spliethoff, H., Maier, H., and Hein, K. R. G., "The effect of different reburning fuels on NO_x -reduction," Fuel, Vol. 73, No. 9, 1994, pp. 1443-1446.
- ¹¹ Burch, T. E., Tillman, F. R., Chen, W.-Y., and Lester, T. W., Conway, R. B., and Sterling, A. M., "Partitioning of Nitrogenous Species in the Fuel-Rich Stage of Reburning", Energy and Fuels, Vol. 5, No. 2, 1991, pp.231-237.
- ¹² Rüdiger, H., Grcul, U., Spliethoff, H., and Hein, K. R. G., "Distribution of fuel nitrogen in pyrolysis products used for reburning", Fuel, Vol. 76, No. 3, 1997, pp. 201-205.
- ¹³ Pisupati, S. V., Simons, G. A., Oehr, K. H., and Zhou, J., "Effect of BioLime™ Atomization Characteristics on Simultaneous NO_x and SO_2 Capture in Coal Combustion Systems", International Pittsburgh Coal Conference, 14th, 1997.
- ¹⁴ Bhalla, S. and Pisupati, S.V., "A Study of Composition and Pyrolysis Behavior of Biomass-Based Materials for NO_x Reduction" Proceedings of The Sixteenth Annual International Pittsburgh Coal Conference, October 11-15, 1999 Pittsburgh, University of Pittsburgh, CD-ROM Paper No. 15-3, 1999
- ¹⁵ Giarborg, P., Kee, R. J., Grcar, J. F., and Miller, J. A., "PSR: A Fortran Program for

Modeling Well-Stirred Reactors", SAND86-8209.UC-4 (1992a), Sandia National Laboratories, Livermore, CA, 1989

¹⁶ Kee, R. J., Rupley, F. M., and Miller, J. A., "Chemkin II: A Fortran Chemical Kinetics Package for the Analysis of Gas-Phase Chemical Kinetics", SAND87-8215, Sandia National Laboratories, Livermore, California, 1989.

¹⁷ Kee, R. J., Rupley, F. M., and Miller, J. A., The Chemkin Thermodynamic Database, Rep. SAND 87—8215, Sandia National Laboratories, Livermore, CA.

¹⁸ Kilpinen, P., Glarborg, P., and Hupa, M., "Reburning Chemistry: A Kinetic Modeling Study", Industrial Engineering Chemistry Research, Vol. 31, 1992, pp.1477-1490.

¹⁹ Glarborg, P., Alzueta, M. U., Dam-Johansen, K., and Miller, J. A., "Kinetic Modeling of Hydrocarbon/Nitric Oxide Interactions in a Flow Reactor", Combustion and Flame, Vol. 115, 1998, pp. 1-27.

²⁰ Prada, L., and Miller, J. A., "Reburning using Several Hydrocarbon Fuels: A Kinetic Modeling Study", Combustion Science and Technology, Vol. 132, pp. 225-250.

²¹ Miller, J. A., and Bowman, C. T., "Mechanism and Modeling of Nitrogen Chemistry in Combustion", Progress Energy Combustion Science, Vol. 15, 1989, pp. 287-338.

²² Kicherer, A., Spliethoff, H., Maier, H., and Hein, K. R. G., "The effect of different reburning fuels on NO_x-reduction," Fuel, Vol. 73, No. 9, 1994, pp. 1443-1446.

²³ Kilpinen, P., Glarborg, P., and Hupa, M., "Reburning Chemistry: A Kinetic Modeling Study", Industrial Engineering Chemistry Research, Vol. 31, 1992, pp.1477-1490.

²⁴ Chen, S. L., McCarthy, J. M., Clark, W. D., Heap, M. P., Seeker, W. R., and Pershing, D.W., "Bench and Pilot Scale Process Evaluation of Reburning for In-Furnace NO_x Reduction", Proceedings of Symposium on Combustion, 1986, Vol. 21, pp. 1159

²⁵ Merzb, J.B., and Wendt J. O. L., "Reburning mechanisms in a pulverized coal combustion", Proceedings of Symposium on Combustion, 1990, Vol 23, pp. 1273

²⁶ Burch, T. E., Tillman, F. R., Chen, W-Y, and Lester, T. W., Conway, R. B., and Sterling, A. M., "Partitioning of Nitrogenous Species in the Fuel-Rich Stage of Reburning", Energy and Fuels, Vol. 5, No. 2, 1991, pp.231-237.

²⁷ Smart, J. P., and Morgan, D. J., "The effectiveness of multi-fuel reburning in an internally fuel-staged burner for NO_x reduction", Fuel, Vol. 73, No. 9, 1994, pp. 1437-1442.

²⁸ Chen, W-Y, and Ma, L., "Effect of Heterogeneous Mechanisms During Reburning of Nitrogen Oxide", AIChE Journal, Vol. 42, No. 7, 1996, pp. 1968-1976.

DIRECT OBSERVATION OF THE CATALYTIC PRODUCTION OF DIMETHYL CARBONATE USING ON-LINE GC/MS

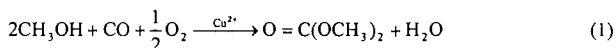
Brian C. Dunn, Jorg Pahnke, Dan Hopkinson, Edward M. Eyring, Department of Chemistry, University of Utah, Salt Lake City, UT 84112.

Genshan Deng, Jacek Dworzanski, Henk L.C. Meuzelaar, Ronald J. Pugmire, Department of Chemical and Fuel Engineering, University of Utah, Salt Lake City, UT 84112.

KEYWORDS: Dimethyl carbonate, fuel oxygenate, on-line GC/MS

INTRODUCTION

Dimethyl carbonate (DMC) has the potential to replace methyl *t*-butyl ether[1,2] (MTBE) as an oxygenate fuel additive for both diesel and gasoline engines.[3] Previous research has shown that the addition of DMC to gasoline or diesel fuel reduces all forms of emissions: hydrocarbons,[3] carbon monoxide,[4] oxides of nitrogen,[4-6] and particulate matter.[7,8] Numerous routes exist for the production of DMC: reaction of methanol with urea with an organotin catalyst,[9] activation of CO₂,[10-12] and the reaction between methyl nitrite and carbon monoxide.[13] A promising route to the industrial production of DMC is the oxidative carbonylation of methanol.[14,15] A drawback of DMC is the lack of knowledge regarding the reaction mechanism that could lead to the efficient industrial production in sufficient quantity to satisfy the enormous demand in the American fuel market. Discovering the reaction mechanism should allow more efficient catalysts for the production of DMC to be developed and could facilitate the widespread adoption of DMC as an oxygen-containing fuel additive. We are investigating the reaction between methanol, carbon monoxide, and oxygen that produces DMC as one product:



In order to obtain detailed information about the underlying reaction mechanisms and kinetics we are using a novel, on-line GC/MS technique developed at the University of Utah Center for Microanalysis and Reaction Chemistry (UUCMARC) that is capable of repetitively recording GC/MS profiles at 1 minute intervals, or less. This method can be used with a variety of chemical reactors and a broad range of reaction conditions[16-18] and enables definitive identification of many volatile or semi-volatile compounds in relatively complex reaction mixtures, while simultaneously producing kinetic profiles of all compounds as a function of time and temperature.

EXPERIMENTAL

The catalysts are prepared by dissolving the appropriate copper and/or palladium salt in methanol, adding the activated carbon support, and refluxing the mixture with vigorous stirring for four hours. The solvent is removed by vacuum distillation and the catalyst is dried under an inert atmosphere until completely free from solvent.

The reaction is studied by placing a mixture of the reactants and a sample of the previously prepared catalyst into a glass-lined stainless steel autoclave. The reaction chamber is suspended in a preheated fluidized sand bath in which the reaction can be carried out under either isothermal or temperature programmed conditions. The autoclave is interfaced to a GC/MS system that allows on-line identification and monitoring of all of the reaction products in real time and the kinetic profile of the reaction is recorded.

A pressure reduction transfer line and a AVS-GC/MS system, where AVS denotes ambient vapor sampling, have been employed for real-time monitoring of the C1 reaction process by on-line analysis of volatile products from a high pressure batch reactor. The pressure reduction line is a 2 m long, 50 μm i.d. fused silica capillary with a volume flow of 0.8 ml/min as a function of the reaction pressure (the initial pressure: 150 psig, the highest pressure: 350 psig at 170 $^\circ\text{C}$). The vapor sampling and GC functions of the system are contained in the Enviroprobe (FemtoScan Corp.), which attaches to a Hewlett-Packard model 5972 MSD (mass selective detector) via a modified, more power efficient version of the standard GC to MSD transfer line interface. The Enviroprobe utilizes an AVS inlet,[19] which performs the repetitive injection of vapor samples into the 10 m long, 250 μm i.d. fused silica capillary column with the temperature of 80 $^\circ\text{C}$. The sampling time is one second and the sampling interval is two and a half minutes.

RESULTS AND DISCUSSION

The on-line GC/MS system was found to perform quite well for this particular reaction process and reactor set-up. Besides providing direct information about the concentrations of organic reactants and products it also proved possible to directly monitor reaction gas components such as oxygen. Since the high partial pressures of these components tend to cause saturation of the molecular ion peak, as well as of the main fragment ion peaks, minor isotope peaks (e.g. $O^{18}O^{16}$ at m/z 34) can be used to monitor the kinetic profiles of these major reaction atmosphere constituents. This proved to be very informative, e.g. by showing that some catalysts cause rapid oxidation of CO to CO_2 at low temperatures, thereby making CO unavailable for the key reaction step with methanol as can be seen from Figure 1.

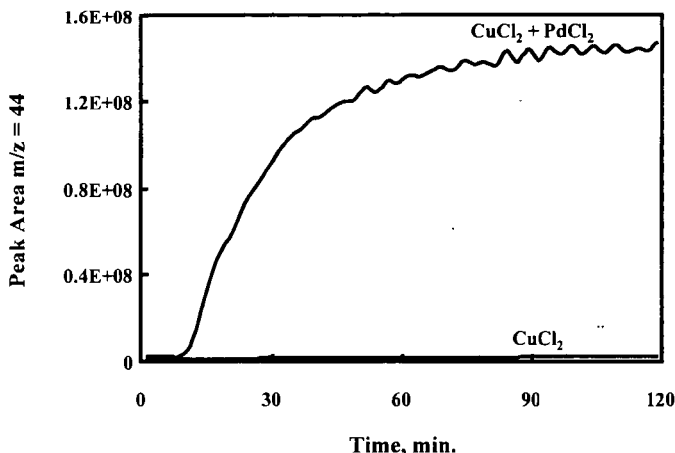


Figure 1. Comparison of CO_2 formation with two different catalysts: $CuCl_2 + PdCl_2$ and $CuCl_2$ only.

The effect of catalyst composition on the overall reaction was studied by preparing a series of catalysts using different metal salts. Six catalysts were prepared: $CuCl_2$, $Cu(Ac)_2$ (copper(II) acetate), $Cu(NO_3)_2$, $CuCl_2 + PdCl_2$, $Cu(Ac)_2 + Pd(Ac)_2$, and $CuCl$. The reactions were conducted under temperature-programmed conditions from 100 °C to 170 °C in order to observe the influence of temperature on the reaction chemistry. In all cases, varying proportions of dimethyl carbonate (DMC), dimethoxy methane (DMM), and methyl formate (MeFOR) were produced. When the acetate salts were employed, a fourth product, methyl acetate (MeAc), was also observed as seen from Figure 2. The product distributions present at the end of each experimental trial are given in Figure 3.

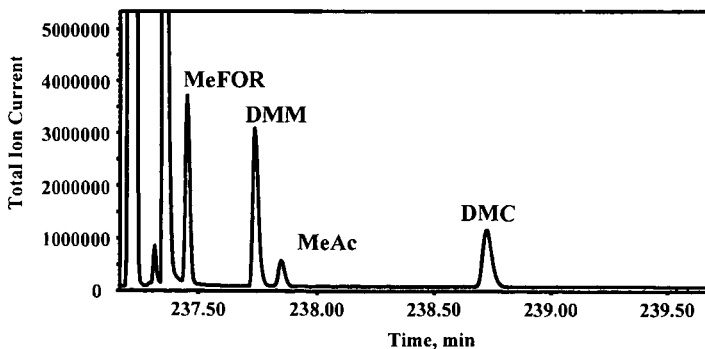


Figure 2. Chromatogram of the products from the following reaction: 0.5 g $CuAc_2$ catalyst, 5.0 g MeOH, 50 psi CO, 100 psi air, 170 °C.

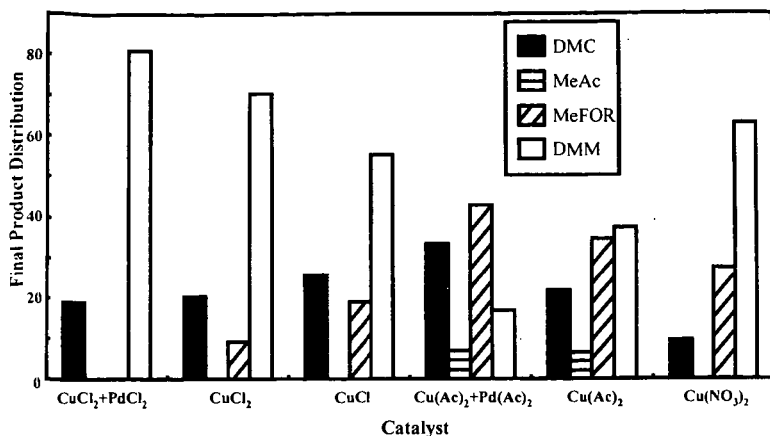


Figure 3. Final product distributions from six different catalysts. All reactions performed under the following conditions: 0.5 g catalyst, 5.0 g MeOH, 50 psi CO, 100 psi air, temperature programmed from 100 °C to 170 °C in 30 min. / 10 °C steps.

Palladium catalyzes the reaction of CO and O_2 to produce a large amount of CO_2 , thereby reducing the amount of CO available for the production of DMC. The catalysts with acetate show significant activity, but because of the formation of a fourth product, methyl acetate, we chose the catalysts based on chloride salts for further study. The $\text{Cu}(\text{NO}_3)_2$ catalyst has the worst selectivity for DMC.

The reactant gas ratio influence was investigated with the CuCl catalyst by using differing amount of CO and air, but maintaining the same total pressure to minimize any pressure effects. Three different gas ratios were used and the product distributions are shown in Figure 4.

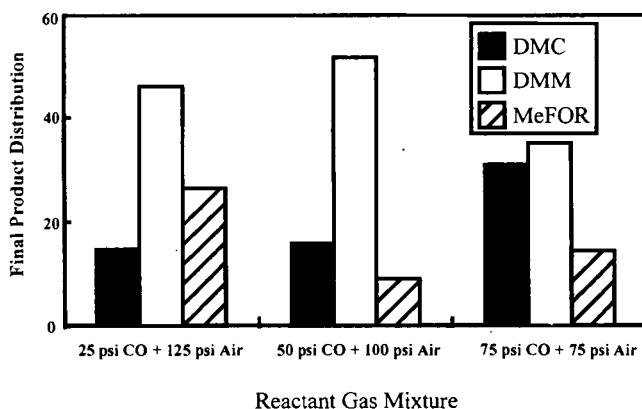


Figure 4. Final product distributions using CuCl catalyst with varying reactant gas ratios.

The influence of the support particle size was examined by using both the CuCl_2 and CuCl catalysts on three different activated carbon support sizes. The final peak areas were normalized by dividing the peak area of each reaction product by the peak area of the internal standard, n-hexane. The Tables 1 and 2 show the results.

Table 1. Final Peak Area Ratios using CuCl_2 Catalysts

Mesh	DMC Area Ratio	DMM Area Ratio	MeFOR Area Ratio
4-14	0.7255	0.3647	0.9506
20-40	0.5784	1.715	0.3207
100	0.6982	0.4843	1.002

Table 2. Final Peak Area Ratios using CuCl Catalysts

Mesh	DMC Area Ratio	DMM Area Ratio	MeFOR Area Ratio
4-14	1.025	0.3724	1.008
20-40	0.8210	1.328	0.7746
100	0.7483	0.3387	0.7420
20-40 crush	0.8629	1.278	0.8092

Because no clear trend was evident from the first six experiments, the final experiment was conducted using the 20-40 mesh CuCl catalyst that had been crushed into a fine powder. The results indicate that using the 20-40 mesh catalyst, in both forms, leads to the production of a much larger amount of DMM than either the larger or the smaller support. This evidence led us to conclude that the 20-40 mesh catalysts were causing the reaction of DMC to form DMM. This hypothesis was tested by loading the reactor with a 10 wt. % solution of pure DMC in methanol. CuCl₂ catalyst on 20-40 mesh support, and oxygen (from air). Figure 5 represents the results from that experiment.

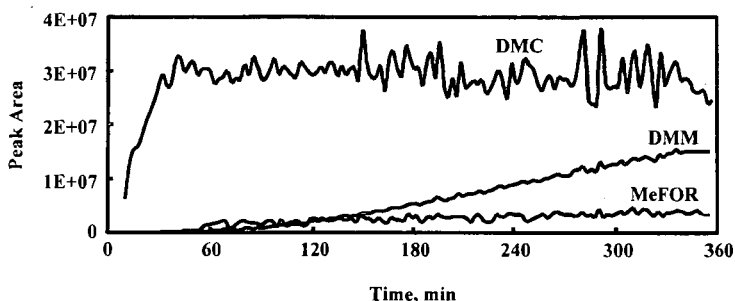


Figure 5. 10 wt. % DMC in methanol and CuCl catalyst.

DMM did gradually appear, but the signal from DMC did not decrease as predicted. The source of the DMM was not the oxidation of DMC, but an independent process. This was tested by charging the autoclave with CuCl₂ catalyst on 20-40 mesh, methanol, and oxygen (from air). No CO was added to inhibit the formation of DMC. Figure 6 is the result from that experiment.

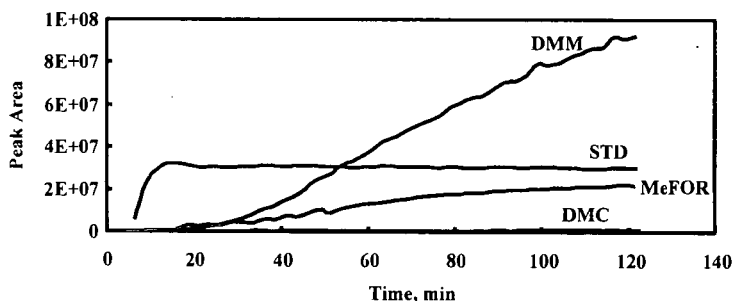


Figure 6. Methanol, CuCl₂ catalyst, and air reacting to form DMM.

Only DMM and MeFOR, the two unwanted products, were formed and at nearly the same rate as in a previous experiment in which CO was added.

CONCLUSIONS

The reaction that forms DMM and MeFOR is independent of the reaction that forms DMC. It should be possible to find a different catalyst that is much more selective for DMC due to these uncoupled reactions. From the Tables, it is clear that CuCl₂ and CuCl give rise to very similar product distributions. This leads us to conclude that the Cu⁺ ion is most likely being oxidized to Cu²⁺ by the O₂ present inside the reactor. Neither the Cu⁺ nor the Cu²⁺ catalyst offers a significant advantage over the other. The relationship between support particle size and reactivity appears to be more complicated than originally expected. This phenomenon is currently under investigation.

ACKNOWLEDGMENTS

Financial support by the U.S. Department of Energy, Fossil Energy Division, through the Consortium for Fossil Fuel Liquefaction Sciences, Contract No. UKRF-462633-99-200, is gratefully acknowledged.

REFERENCES

1. Kirchstetter, T. W.; Singer, B. C.; Harley, R. A.; Kendall, G. R.; Traverse, M. *Environ. Sci. Technol.*, **1999**, *33*, 318-328.
2. Gouli, S.; Lois, E.; Stournas, S. *Energy & Fuels*, **1998**, *12*, 918-924.
3. Pacheco, M. A.; Marshall, C. L. *Energy & Fuels*, **1997**, *11*, 2-29.
4. Japanese Patent 61[1986]-207496; Imoura, S.; Matsushita, D. "Fuel for Internal Combustion Engine": assigned to Toyo Soda Industry; **1986**.
5. Stoner, M.; Litzinger, T. "Effects of Structure and Boiling Point of Oxygenated Blending Compounds in Reducing Diesel Emissions"; SAE Technical Paper Series; **1999**; 1999-01-1475.
6. Murayama, T.; Zheng, M.; Takemi, C.; Oh, Y.; Fujiwara, Y.; Tosaka, S.; Yamashita, M.; Yoshitake, H. "Simultaneous Reductions of Smoke and Nox from a DI Diesel Engine with EGR and Dimethyl Carbonate"; SAE Technical Paper Series; **1995**; 952518.
7. US Patent 4,891,049; Dillon, D. M.; Iwamoto, R. Y. "Hydrocarbon Fuel Composition Containing Carbonate Additive"; assigned to Unocal; **1990**.
8. US Patent 4,904,279; Kanne, D. M.; Iwamoto, R. Y. "Hydrocarbon Fuel Composition Containing Carbonate and Dicarboxylate Additives"; assigned to Union Oil; **1990**.
9. US Patent 5,902,894; Ryu, J. Y. "Process for Making Dialkyl Carbonates"; assigned to Catalytic Distillation Technologies; **1999**.
10. Sakakura, T.; Saito, Y.; Okano, M.; Choi, J.; Sako, T. *J. Org. Chem.*, **1998**, *63*, 7095-7096.
11. Cheong, M.; Kim, S.; Park, J. *New J. Chem.*, **1997**, *21*, 1143-1145.
12. Tomishige, K.; Sakai, T.; Ikeda, Y.; Fujimoto, K. *Cat. Lett.*, **1999**, *58*, 225-229.
13. Matsuzaki, T.; Ohdan, K.; Asano, M.; Tanaka, S.; Nishihira, K.; Chiba, Y. *J. Chem. Soc. Japan*, **1999**, 15-24.
14. Yanji, W.; Xinqiang, Z.; Baoguo, Y.; Bingchang, Z.; Jinsheng, C. *Applied Catalysis, A: General*, **1998**, *171*, 255-260.
15. Tomishige, K.; Sakai, T.; Sakai, S.; Fujimoto, K. *Applied Catalysis, A: General*, **1999**, *181*, 95-102.
16. Meuzelaar, H.L.C. "Comparison of On-line MS Techniques for Complex Reactive Systems," *Proceedings of the Specialists Workshop on Applications of Free-Jet Molecular Beam, Mass Spectrometric Sampling*, October 12-14, Estes Park Center, CO, NTIS, **1994**, NREL-CP-433-7748, 57-64.
17. Meuzelaar, H.L.C.; Liu, K.; Jakab, E. "Development of On-Line Chemical Speciation and Microsimulation Techniques for High Pressure Conversion Reactions in Coals & Waste Materials," *Proceedings of the 1994 U.S. Dept. of Energy Coal Liquefaction and Gas Conversion Contractors' Review Conference*, September 7-8, Pittsburgh, PA, **1994**, 637-649.
18. Nie, X.; McClennen, W.H.; Liu, K.; Meuzelaar, H.L.C. "Development of On-Line GC/MS Monitoring Techniques for High Pressure Fuel Conversion Processes," *ACS Preprints, Division of Fuel Chemistry*, **1993**, *38* (4), 1147-1155.
19. Arnold, N.S.; McClennen, W.H.; Meuzelaar, H.L.C. "Vapor Sampling Device for Rapid Direct Short Column Gas Chromatography/Mass Spectrometry Analyses of Atmospheric Vapors," *Analytical Chemistry*, **1991**, *63*, 299-304.

ISOTOPIC TRACING OF PARTICULATE MATTER FROM A COMPRESSION-IGNITION ENGINE FUELED WITH ETHANOL-IN-DIESEL BLENDS

A. S. (Ed) Cheng¹, Robert W. Dibble¹, Bruce A. Buchholz²

¹Department of Mechanical Engineering, University of California, Berkeley, CA

²Center for Accelerator Mass Spectrometry, LLNL, Livermore, CA

KEYWORDS: diesel particulate matter, oxygenate, isotope tracing, AMS

INTRODUCTION

Environmental and human health concerns over emissions from internal combustion engines continue to bring about increasingly stringent emissions standards and drive research into the use of non-conventional, cleaner-burning fuels. For compression-ignition (diesel) engines, oxygenated fuels have been shown to dramatically reduce particulate matter (PM) while also improving or maintaining acceptable levels of other regulated emissions (NO_x, HC and CO) [1-8]. The mechanisms through which oxygenates reduce PM, however, are not fully understood. In addition to changes in combustion chemistry, the influence of thermophysical properties on fuel injection and fuel-air mixing can play a significant role.

To gain further insight into the effect of oxygenates on diesel engine PM emissions, Accelerator Mass Spectrometry (AMS) was used to investigate the relative contribution to soot (the carbonaceous component of PM) from the ethanol and diesel fractions of blended fuels. AMS counts electrostatically accelerated nuclei (32.5 MeV for ¹⁴C⁴⁺) in a simple particle detector [9]. Molecular isobars are completely disassociated in the charge changing process and any atomic isobars are discriminated in the detector. AMS is particularly efficient in detecting long-lived isotopes ($10\text{ y} < t_{1/2} < 100\text{ My}$). The rarity of long-lived radioisotopes yields a much lower background than that achievable with stable isotopes. For example, the naturally occurring carbon isotopic abundances are: ¹²C (98.9%), ¹³C (1.1%), and ¹⁴C ($1.2 \times 10^{-10}\%$). The natural background of ¹⁴C is 10 orders of magnitude lower than the rare stable isotope ¹³C and AMS achieves limits of quantitation for ¹⁴C below $1 \times 10^{-18}\text{ mol}$ in individual samples ($\text{LOQ} < 1\text{ amol } ^{14}\text{C} / \text{mg C}$). The decrease in background yields much greater sensitivity for ¹⁴C AMS over ¹³C MS. Decay counting long lived isotopes is not efficient; counting 0.1% of the decays of a ¹⁴C sample takes 8.3 years.

MATERIALS AND METHODS

In this study, contemporary grain ethanol (109 amol ¹⁴C/mg C) served as an isotopic tracer in old carbon diesel fuel (0.26 amol ¹⁴C/mg C). The ethanol was manufactured by Midwest Grain Products, Pekin, IL. The diesel was a CARB-certified No. 2 diesel fuel obtained from Golden Gate Petroleum, Hayward, CA. Properties of ethanol and the diesel test fuel are shown in Table 1. Because ethanol is soluble in diesel fuel in only small quantities, either an emulsifier (Span 85, also known as sorbitan trioleate) or a cosolvent (n-butanol) was used to prepare the ethanol-in-diesel blends. An ignition improver, di-tert-butyl peroxide (DTBP), was also used to compensate for the low cetane number of ethanol. The Span 85 and n-butanol were obtained from Spectrum Quality Products, Inc.; the DTBP was obtained from Pfaltz & Bauer. All fuel blend components were converted to AMS samples [10] and ¹⁴C content was measured. The four different ethanol-in-diesel blends investigated are shown in Table 2. A high-speed, high-shear mixer (Greenco Model 1-LV Homomixer) was used to prepare the emulsified blends.

The experimental test engine is a 1993 Cummins B5.9 rated at 175 hp (131 kW). Engine specifications are listed in Table 3. The engine employs a mechanically-governed in-line fuel injection pump capable of injection pressures up to 115 MPa. No modifications were made to the test engine to optimize for operation on the test fuels.

Table 1. Ethanol and diesel fuel properties.

Fuel	Ethanol ^a	Diesel ^b
Density (kg/L)	0.7923	0.8473
Cetane number	<5	49.1
Sulfur (ppm)	-	98
SFC total aromatics (wt. %)	-	16.32
SFC PNA's (wt. %)	-	4.09
Nitrogen	-	< 5 ppm
Boiling point (°C)	78	-
Distillation by D86 (°C)		
IBP	-	173
10%	-	237
50%	-	299
90%	-	336
95%	-	347
EP	-	358
Lower heating value (MJ/L)	21.2	35.4

^a from literature sources^b as determined by fuel analysis

Table 2. Test fuel blends (components listed in percent by volume).

Fuel Blend	Diesel	Ethanol	SPAN 85	n-butanol	DTBP
A	72.0	23.0	4.0	-	1.0
B	70.0	25.0	-	4.0	1.0
C	83.5	11.5	4.0	-	1.0
D	82.5	12.5	-	4.0	1.0

Table 3. Cummins B5.9 engine specifications.

Model year	1993
Displacement	5.88 liters (359 in ³)
Configuration	6-cylinder inline
Bore	102 mm (4.02 in)
Stroke	120 mm (4.72 in)
Compression ratio	17.6:1
Horsepower rating	175 hp @ 2500 rpm
Torque rating	420 ft-lb @ 1600 rpm
Aspiration	turbocharged and aftercooled
Injection timing (fixed)	11.5° BTDC

Prior to beginning any experiments, lab facilities were checked for fixed and aerosol ¹⁴C contamination with AMS analyzed swipes and fullerene aerosol monitors. During the experiments, a steady-state engine speed-load condition of 1600 rpm and 210 ft-lbs (285 N-m) was used and measurements were made for PM, NO_x, HC and CO emissions, as well as for fuel consumption. Gaseous emissions (NO_x, HC and CO) were monitored using Horiba Instruments emissions analyzers and fuel consumption was measured via a load cell mounted under the fuel tank. PM was determined using a mini-dilution tunnel and gravimetric filter paper measurements. The filters (Pallflex Tissuquarz 2500QAT-UP) were conditioned overnight in petri dishes and weighed before and after PM loading on a Mettler UM3 microbalance. Filters were then sealed in plastic bags prior to preparation as AMS samples. Because of the limited quantity of contemporary grain ethanol obtained and time needed to collect sufficient PM mass for AMS analysis (~ 30 min. of engine operation), only one sample was collected for each test fuel.

In preparation for AMS analysis, the filters with collected PM were baked at 900 °C for 2 h prior to use to remove carbon residue and stored in sealed plastic bags after cooling. Filters were cut into 2 or 3 pieces and converted to graphite for AMS measurement of isotope ratios [10]. Isotope ratios were measured to within 1-8%. Relative uncertainties were governed primarily by counting statistics. The samples with very low ^{14}C content had larger uncertainties. AMS measures the isotope concentration of unknown samples relative to those of known standards. In these experiments we normalized to four identically prepared standards of Australian National University Sucrose [11].

RESULTS AND DISCUSSION

Brake-specific emissions and fuel consumption results from the baseline diesel fuel and the four test fuel blends are shown in Table 4. A graphical representation of PM and NO_x emissions is shown in Figure 1. As anticipated, the general trend was towards lower PM emissions with higher levels of oxygenate (note that the cosolvent n-butanol is itself also an oxygenate), although an anomaly exists in that fuel blend C produced a 10% increase in PM. The data also indicates that the homogeneous cosolvent blends are more effective at reducing PM emissions compared to the emulsified blends. NO_x emissions from the ethanol-in-diesel blends were 22% to 27% lower than that of the baseline diesel and did not show large variation across the different blends. Emissions of both HC and CO increased, but remained very low as is typical with diesel engine combustion. Fuel consumption was higher with the test fuel blends due to the lower energy density of ethanol.

Table 4. Brake-specific emissions and fuel consumption results (g/kW-hr).

FUEL	Diesel	Blend A	Blend B	Blend C	Blend D
PM	0.032	0.025	0.012	0.035	0.029
NO_x	6.28	4.58	4.90	4.92	4.88
HC	0.084	0.160	0.172	0.203	0.224
CO	0.312	0.517	0.625	0.358	0.371
bsfc	230	249	270	261	256

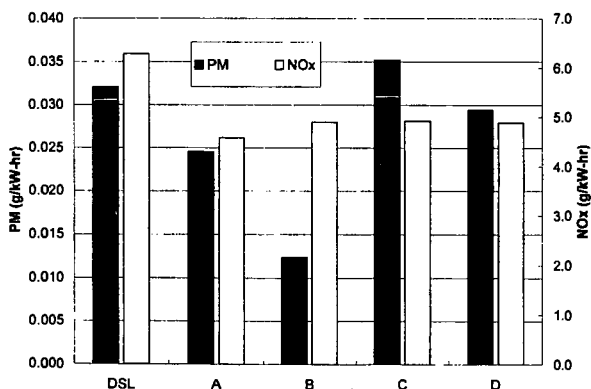


Figure 1. Brake-specific emissions of PM and NO_x .

Isotope ratios of the fuel components are reported in Table 5. The ^{14}C content of the petroleum derived components are low as expected. The emulsifier, Span 85, has a contemporary ^{14}C content, indicating it is derived from biological products.

Table 5. Carbon-14 content of fuel components.

COMPONENT	amol ¹⁴ C / mg C
Diesel	0.26
Ethanol	109
n-butanol	0.31
Span 85	109
DTBP	0.17

Measured isotope ratios (IR) contain contributions from all the components (and possibly more) shown in Eq. 1.

$$IR_{\text{sample}} = \frac{{}^{14}C_{\text{diesel}} + {}^{14}C_{\text{ethanol}} + {}^{14}C_{\text{absorbed}} + {}^{14}C_{\text{emulsifier}} + {}^{14}C_{\text{cosolvent}} + {}^{14}C_{\text{additives}}}{C_{\text{diesel}} + C_{\text{ethanol}} + C_{\text{absorbed}} + C_{\text{emulsifier}} + C_{\text{cosolvent}} + C_{\text{additives}}} \quad (1)$$

In practice we try to reduce the number of terms of this equation by limiting the number of components or rendering some terms negligible through judicious choice of compounds or experimental conditions. Through the use of appropriate controls we determined the contributions of the various components in Eq. 1. Traditional tracer experiments depend on radioactive decay for detection and are usually dominated by a highly labeled tracer with very small mass. In our case, the labeled tracer was not radioactive in the traditional sense and contributed a significant amount of carbon in the measured isotope ratio. We sought to determine the mass of tracer ethanol in the soot and need to consider the products of carbon mass and the isotope ratios. The total carbon mass is expressed in Eq. 2.

$$M_{\text{sample}} = M_{\text{diesel}} + M_{\text{ethanol}} + M_{\text{absorbed}} + M_{\text{emulsifier}} + M_{\text{cosolvent}} + M_{\text{additive}} \quad (2)$$

The product of the isotope ratio and carbon mass of each sample is the sum of the product of each component as described in Eq. 3.

$$IR_{\text{sample}} M_{\text{sample}} = \sum_{i=\text{component}} IR_i M_i \quad (3)$$

Equations 2 and 3 can be solved to determine the mass contributions of each component with knowledge of the isotope ratios of the components and a series of controls adding each component to the fuel mixture.

The isotope ratios of the filter samples loaded with PM from the fuel blends and the associated controls were elevated due to the absorption of atmospheric CO₂ and other carbon compounds on the soot during equilibration. Atmospheric CO₂ has approximately the same ¹⁴C content as ethanol, 109 amol ¹⁴C / mg C. The quantity of absorbed carbon depends on the surface area of the soot and length of time spent equilibrating in the atmosphere. It should scale with the mass of soot deposited on the filters when equilibration times are constant. Separate control blanks were collected for soot samples from fuel blends A and B and from blends C and D. Assuming that all the sorbed carbon was contemporary, the mass of carbon absorbed with the separate sets of filters were 2.4% and 4.2% for blends A and B and blends C and D, respectively. These values for mass fraction of absorbed atmospheric carbon were propagated in the soot samples obtained from the fuel blends and the controls that included emulsifier or cosolvent without the ethanol.

Equations 2 and 3 were used to solve for the fractional mass of carbon in the soot from the emulsifier and ethanol. The mass fraction of carbon in the soot was not measured so all isotope measurements are expressed as fractions of soot carbon rather than absolute numbers. Since the ¹⁴C content of the cosolvent and ignition improver were essentially the same as the diesel fuel,

their contributions to the carbon soot mass could not be determined in our limited experiment. Either n-butanol or DTBP could be traced if desired, but we were not interested in obtaining isotope labeled material for this purpose. Our interest was primarily in tracing the ethanol. The contributions of the ethanol to the carbon mass in the soot is displayed in Table 6. Since the emulsifier is only 4% by volume in blends A and C, its contribution to the carbon mass is not large.

As the data in Table 6 shows, ethanol contributed less to soot than did the diesel in all of the test fuel blends. Results also indicate that the percent of fuel ethanol contributing to soot is higher for the emulsified blends A and C compared to the cosolvent blends B and D. Along with the brake-specific emissions data, this suggests that the chemical mechanisms that inhibit soot formation and/or promote soot oxidation are different depending on the nature in which ethanol is blended with the diesel fuel.

Table 6. Contributions of ethanol to carbon soot mass. Fuel blends A and C used the emulsifier Span 85 while Blends B and D used n-butanol as a cosolvent.

Fuel blend	Ethanol volume % (fuel)	Ethanol carbon mass % (fuel)	Ethanol carbon mass % (soot)
A	23.0	15	8.6
B	25.0	16	6.3
C	11.5	7	4.7
D	12.5	8	3.8

CONCLUSIONS

Gravimetric filter paper measurements and isotopic tracing of PM reveal that ethanol-in-diesel blends reduce PM emissions from compression-ignition engines in a manner which results in a lower ethanol contribution to soot relative to its fraction in the fuel blend. Experimental results also indicate that homogeneous blends of ethanol and diesel behave differently than emulsified blends and yield lower PM emissions.

This study also demonstrated the power of using AMS to perform isotope tracing without using any specially labeled material. No radioactive material was used in any part of these experiments. Therefore, no mixed wastes (radioactive and hazardous) were generated, greatly simplifying disposal [12]. In practice, one could label any fuel additive or component and follow its fate in particulate emissions or exhaust gases. The sub-attomole sensitivity of ^{14}C -AMS can be used to separate components of exhaust gases (e.g., hydrocarbons, CO, CO₂) and quantify fuel stock contributions. Particulate separators can also be used to look at the fate of fuel components in different sized soot emissions.

ACKNOWLEDGEMENTS

Support was provided by a LLNL Center for Accelerator Mass Spectrometry Mini-grant. Work completed at LLNL was supported under DOE contract W-7405-ENG-48.

REFERENCES

1. Cheng, A. S. and R. W. Dibble. "Emissions Performance of Oxygenate-in-Diesel Blends and Fischer-Tropsch Diesel in a Compression Ignition Engine," SAE paper 1999-01-3606, 1999.
2. Wong, G. et al. "Low Soot Emission from a Diesel Engine Fueled with Dimethyl and Diethyl Ether," WSS/CI paper 95F-162, October 1995.

3. Liotta, F. J. and D. M. Montalvo. "The Effect of Oxygenated Fuels on Emissions from a Modern Heavy-Duty Diesel Engine," SAE paper 932734, 1993.
4. Fleisch, T. et al. "A New Clean Diesel Technology: Demonstration of ULEV Emissions on a Navistar Diesel Engine Fueled with Dimethyl Ether," SAE paper 950061, 1995.
5. McCormick, R. L., J. D. Ross and M. S. Graboski. "Effect of Several Oxygenates on Regulated Emissions from Heavy-Duty Diesel Engines," *Environmental Science & Technology*, vol. 31, no. 4, 1997.
6. Bertoli, C., N. Del Giacomo and C. Beatrice. "Diesel Combustion Improvements by the Use of Oxygenated Synthetic Fuels," SAE paper 972972, 1997.
7. Miyamoto, N. et al. "Smokeless, Low NO_x, High Thermal Efficiency, and Low Noise Diesel Combustion with Oxygenated Agents as Main Fuel," SAE paper 980506, 1998.
8. Maricq, M. M. et al. "The Effect of Dimethoxy Methane Additive on Diesel Vehicle Particulate Emissions," SAE paper 982572, 1998.
9. Vogel, J. S., Turteltaub, K. W., Finkel, R., and Nelson, D. E. *Anal. Chem.* 1995, 67, A353-A359.
10. Vogel, J. S. *Radiocarbon* 1992, 34, 344-350.
11. Polach, H. A., In *Proceedings of the 9th International Conference on Radiocarbon*; Berger, R., Suess, H., Eds.; UC Press: Berkeley/Los Angeles, CA, 1979; pp. 115-124.
12. 10 CFR 20.2005 *Fed. Reg.*, 1991, 56, 434.

CHARACTERIZATION OF CHEMICAL COMPOSITION AND SIZE OF DIESEL EXHAUST PARTICULATE MATTER BY LDITOF/MS.

J. Suro*, Q. Chen, I.M. Kennedy, T.A. Cahill and P.B. Kelly

University of California, Davis, California 95616

Key Words: Time of flight mass spectrometry; Diesel soot; Polycyclic aromatic hydrocarbons

Introduction

Diesel engines see extensive use due to their high efficiency and suitable torque characteristics. In general diesel engines have lower carbon monoxide and hydrocarbon emissions than spark-ignition engines. However, they are known to create much larger amounts of particulate matter and polycyclic aromatic hydrocarbons (PAHs) and their derivatives. Contributing factors are higher temperatures and pressures in the combustion process together with larger initial concentrations of aromatics in the diesel fuel.

The presence of the aromatic compounds in the air represents a potential hazard to human health. Several PAHs and nitro-PAHs have been identified as carcinogenic and potentially carcinogenic compounds (Ref. 1). The extent of human exposure to PAHs and their derivatives depends on the partitioning between the gas and particle phases as well as the size distribution of the particle fraction containing the PAHs. There is a much greater potential carcinogenic effect if the PAHs are components of particles that penetrate and deposit into the bronchia and alveoli of the lungs. Studies show that a major fraction of particles that are 1.0 μm or less in diameter might deposit in the air ways and lungs (Ref. 2). Moreover, some recent studies have correlated health effects with the concentration of atmospheric particles, yet have failed to identify the causative agents (Ref. 3). Since the toxicity of particles from different sources varies widely, such studies would be much more valuable if the particles from a source were characterized with respect to size and composition.

Traditional methods for the determination of PAHs and nitrated PAHs are based on gas chromatography/mass spectrometry or liquid chromatography with fluorescence techniques for detection. Both approaches are time consuming, may require solvent extraction and separation, are expensive, and in most cases require multiple runs (Ref. 4). In this study performed on diesel soot, we demonstrate the applicability of Laser Desorption Ionization Time of Flight Mass Spectrometry (LDITOF/MS) as a rapid screening method in the analysis of particulate matter collected and segregated by particle size using a multiple stage portable impactor. LDITOF/MS is capable to generate parent ion dominated spectra with low fragmentation from samples containing particles in a specific size range, which makes LDITOF/MS an excellent technique for the screening for PAHs in complex mixtures without need for solvent extraction and separation.

Experimental

The source of diesel exhaust particulate matter was an experimental direct injection 1 cylinder diesel engine aspirated at normal pressure (no turbocharger was used). Samples were collected with the engine idling warm at 2,000 rpm. Reformulated California grade diesel fuel (low sulfur content) was used for the experiment.

Diesel soot samples were collected using a three stage portable impactor developed by the Delta Group at UC Davis (Ref. 5). The impactor was equipped with aluminum foil strips attached to rotary drums that, during sampling, rotated at a fixed angular speed exposing the attached aluminum strip to an inlet nozzle. The dimensions of the inlet nozzle determined the range of size of particles that hit the surface of the strip. As the drum rotates the segment of aluminum strip exposed to the inlet changed continuously, resulting in a deposition of sample with a time reference. A cyclone pump operating with a flow rate of 22.7 l min⁻¹ allowed for collection of particles less than 2.5 μm in aerodynamic diameter. The 50% cut point of such an impactor has been validated both in extensive field and laboratory studies (Ref. 5 and references there in).

Samples were obtained positioning the impactor at 20 cm from the exhaust of the diesel engine. A Nucleopore® filter at the external inlet prevented coarse matter from entering the impactor. This filter permits particles of diameters smaller than 2.5 μm to penetrate into the impactor.

Particles with aerodynamic diameter between 2.5 μm to 1.15 μm were collected on the first stage of the impactor (denoted stage A). The second stage collected particles within the size range 1.15 μm to 0.24 μm (denoted stage B). The third stage accumulated particles of size 0.24 μm to 0.07 μm (denoted stage C). Particles not trapped on the aluminum strips were collected on a 0.01 μm porous teflon filter at the impactor outlet.

The laser desorption ionization time of flight mass spectrometer used has been described in previous publications (Ref. 6). Ultraviolet radiation of 266 nm produced from the fourth harmonic of a Nd:YAG laser with a 2.5 ns pulse width was used to desorb and ionize the sample. The UV laser beam was focused into the source region through a 250 mm focal length S1-UV quartz lens. The beam was directed incident to the sample surface at 45°. Neutral density optical filters were used to reduce the laser power to 10⁶ W/cm² at the focal point on the sample surface. The beam diameter at the focal point was about 90 μm . A time delay of 250 ns in the application of the extraction potential at the source allowed time for prompt decay of metastable ions and improved overall resolution.

Particulate matter from each stage and from the inlet and outflow filters of the impactor were analyzed using LDITOF/MS. Segments of the aluminum foil from the impactor were attached to the sample probe and loaded into the TOF/MS. Each spectrum recorded was the sum of 240 randomly located laser shots. Blank filters and aluminum foil were checked for contaminants. Both positive and negative mass spectra were collected and analyzed.

Results

Positive ion mass spectra for five diesel particle size ranges matter are shown in Figure 1. Spectrum in *1a*) was obtained from the particles trapped at the external inlet filter with diameters larger than 2.5 μm ; *1b*) shows the spectrum resulting from particles with aerodynamic diameter between 2.5 μm to 1.15 μm , stage A; *1c*) from the size range 1.15 μm to 0.24 μm , stage B; *1d*) was obtained from particles in the stage C whose diameters range between 0.24 μm and 0.07 μm . At the bottom *1e*) display the ion yield obtained from the outlet filter, with particles smaller than 0.07 μm .

Low mass peaks (identified as PAHs), are more abundant in large particles, > 2.5 μm diameter, than small particles, < 0.07 μm diameter. The general trend of the shift of PAH mass, with high mass PAH being associated with the fine particulate is clear in Figures *1a*) through *1e*). Only the smallest particles, 0.07 μm have significant amounts of PAH with mass greater than 400 amu. In contrast, in *1a*) ion yield of mass above 400 Da decreases rapidly.

Two series of PAH ions are observed in all the positive ion spectra in Figure 1. The two series are most apparent in Figure *1e*). The first series is comprised of m/z : 178, 202, 228, 252, 276/278, 302, 326/328, 350/352, 374/376, 398/400/402, and higher masses. The second series has twice the frequency as the first series, with every other peak overlapping (with some exceptions) with the first series. The second series is comprised of m/z 190, 202, 216, 226, 240, 252, 266, 276, 290, 302, 326, 342, 350/352, 366, and higher masses. Both series have been labeled in Figure *1b*). A surprisingly large potassium signal is observed in the smallest particles, Figure *1e*).

Negative ion spectra of the diesel particulate matter are shown in Figure 2. As in the case of the spectra of positive ions, each plot corresponds to a different fraction. From *2a*) to *2e*), spectra were taken from particles larger than 2.5 μm ; from 2.5 μm to 1.15 μm , stage A; from 1.15 μm to 0.24 μm , stage B; ranging from 0.24 μm to 0.07 μm , stage C; and smaller than 0.07 μm . In contrast to positive ion spectra, the highest mass negative ions (m/z : 369, 414, and 447) are associated with the larger particles.

Inorganic ions, OH⁻, Cl⁻, NO₂⁻ and NO₃⁻ are observed for all five particle size range. Very fine particles, < 0.07 μm , show significantly higher HSO₄⁻ than any of the spectra for larger particles.

Discussion

In a recent study by Reilly and collaborators (Ref. 7), organic composition of individual particles of diesel soot are obtained using an excimer laser for ablation ionization. Using this technique they are able to detect known compounds in diesel soot and to establish some differences in

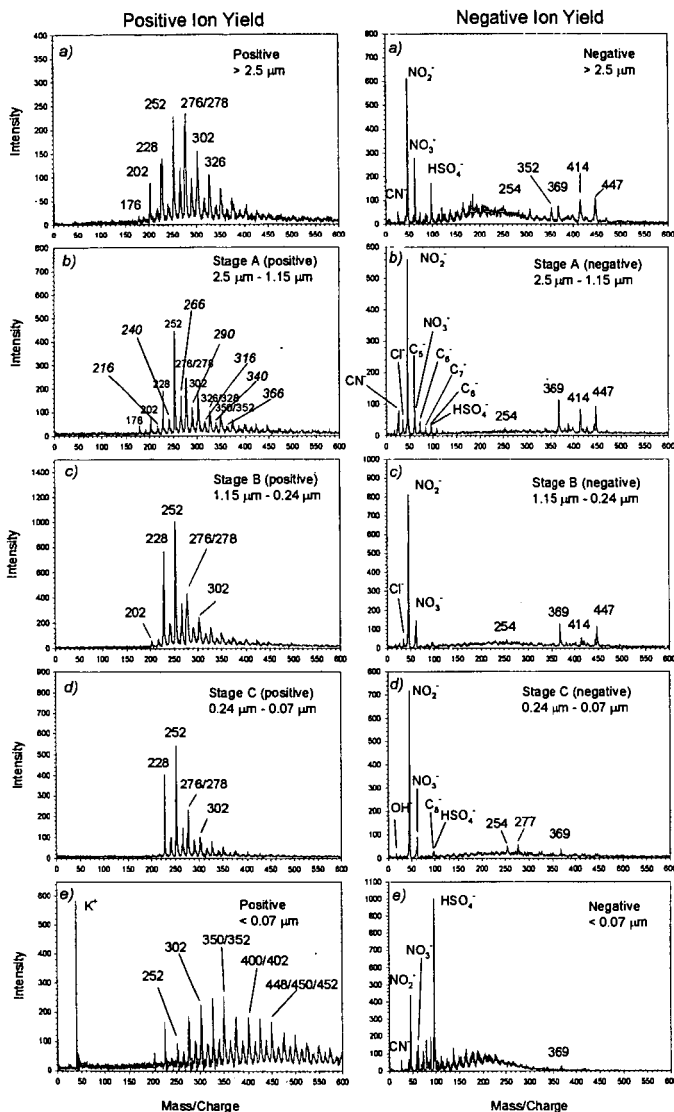


Figure 1. Positive ion mass spectra for five diesel particle size ranges.

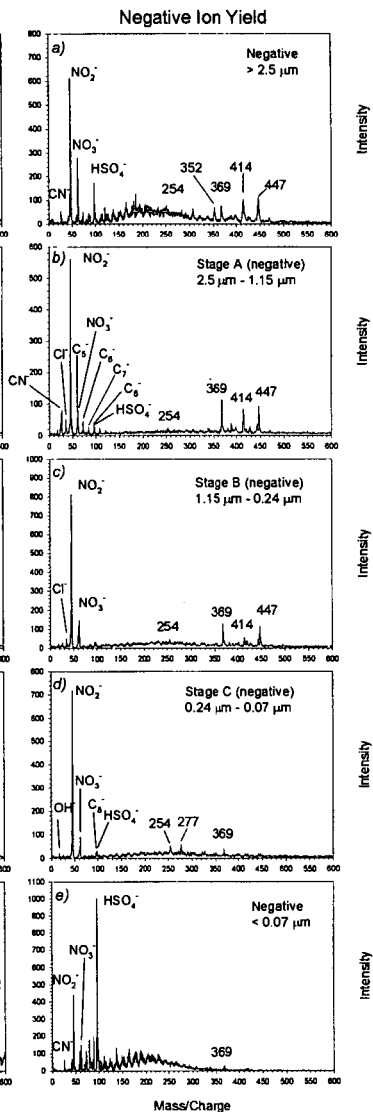


Figure 2. Negative ion mass spectra for five diesel particle size ranges.

chemical composition according to particle size. However their method involves unavoidable fragmentation that obscures their results. On other study, Hankin and John (Ref. 8) examine the chemical composition of individual particles of diesel soot SRM 1650. In their experiment using LDITOF/MS, individual particles fixed to a sample support are subject to microlaser beam that desorbs compounds from the particle, and a second beam ionizes the compounds in the plume of desorbed material. The Hankin and John TOF/MS analysis of SRM 1650 yielded the mass of some certified compounds in their sample as well as some other compounds not certified but

known to be present in such standard such as alkylated PAHs. The Hankin and John study examined only very large particles (~ 20 µm).

In our study we report the first mass spectra of particles that were sized using an impactor. Working with a laser spot of 90 µm of diameter, the signal was derived from many particles at the same time thus obtaining reproducible results that are representative of a particular particle

Table I
PAHs commonly found in diesel soot.

PAH	mass
phenanthrene	178
fluoranthene	202
pyrene	202
benz[a]anthracene	228
chrysene	228
benzo[a]pyrene	252
benzo[e]pyrene	252
benzo[k]fluoranthene	252
perylene	252
benzo[ghi]perylene	276
indeno[123-cd]pyrene	276

size range. In positive ion mode, the most intensive peaks in Figure 1 correspond to PAHs commonly found in diesel exhaust. The spectrum from stage A shows peaks corresponding to the mass of PAHs listed in Table I. Moreover from Figure 1, it is clear that many other PAHs are present in the samples. The first series corresponds to PAHs isomers containing only 6 member rings. The second series, with every other peak overlapping with the first series (with a few exceptions), corresponds to PAHs containing five member rings.

Spectra in Figure 1 shows identifiable peaks up to mass 448; some authors have detected such

mass in environmental samples and have assigned tentatively benz[a]ovalene as the most probable identity of the isomer (Ref. 9). Table II list a few possible assignments to peaks in the second series (Ref. 10).

Soot particles emitted from a diesel engine are usually observed as chain aggregates composed of several tens to hundreds of primary spherical particles. Ishiguro and collaborators (Ref. 11), have found that the structure of such spherical particles consist on an inner core surrounded by an outer shell. The inner core of 0.010 µm are composed of nonplanar molecules. The surrounding

Table II. Few possible mass assignments for peaks in the second series (see text).

Formula	Mass (Da)	Compounds
C ₁₆ H ₁₀	202	Fluoranthene
C ₁₇ H ₁₂	216	Cyclopentaphenanthrene Cyclopentaanthracene Benzofluorene
C ₁₈ H ₁₀	226	Benzo(ghi)fluoranthene
C ₁₉ H ₁₂	240	Cyclopentapyrene Benzofluoranthene Cyclopentachrysene Benzopyrene
C ₂₀ H ₁₂	252	Benzocyclopentantracene
C ₂₁ H ₁₄	266	Benzocyclopentantracene Indenophenanthrene Dibenzofluorene Benzochrysene
C ₂₂ H ₁₂	276	Benzocyclopentapyrene
C ₂₃ H ₁₄	290	Benzocyclopentachrysene Dibenzopyrene
C ₂₄ H ₁₄	302	Cyclopentindenophenanthrene
C ₂₅ H ₁₆	316	Benzinindenophenanthrene
C ₂₆ H ₁₄	326	Indenoperylene
C ₂₇ H ₁₆	340	Tribenzopyrene
C ₂₈ H ₁₄	350	Diindenopyrene
C ₂₉ H ₁₈	366	Dibenzopentacene

outer shell is compose of micro crystallites comprising several polycyclic aromatic hydrocarbon layers oriented concentrically in a soot particle. During shell formation, molecules, radicals, or ions including two to four carbon atoms could contribute the surface reactions promoting the polycyclic growth of the graphitic crystallites. Those observations by Ishiguro and collaborators support the assignment of peaks in Figure 1 as PAHs compounds. The extreme high mass range of PAHs observed for small particles would not be observable by traditional GC/MS.

Diesel soot particles exhibit size ranging (Ref. 12) from 4 µm to 0.04 µm, with a peaking distribution about 0.1 µm. Our study reveal that there are differences in the chemical contents of particles in such range. This information may be relevant in toxicological studies that assess the health hazard imposed by the continuous use of diesel engines. Toxicological assessments, regulation and development of

cleaner running diesel engines(Ref. 13) require development of analytical methods that can examine the exhaust by particle size. Our results may provide a guide for pollutants reduction in the emissions of diesel engines based in a better understanding of the process that generate soot and pollutants.

Conclusions

The ability to use TOFMS to characterize the chemical composition of diesel soot particles captured using an impactor has been demonstrated. The analysis of size segregated particles from the impactor was performed without further preparation loading directly a sample collected on aluminum foil into the MS chamber. Results indicate a variation of the compound contents according to particle size. In general finer particles have high concentration of extremely large PAHs, potassium, and sulfate. The larger particles contain lower mass PAHs. Our data show the presence of many PAHs in diesel soot that have not been fully characterized as compounds found in diesel soot. Our method detected extremely large PAHs not amenable to GC/MS analysis.

Our technique may be useful for the characterization of emissions of different sources according to the size of the particles. Accurate assessment of human health hazards associated with particulate matter requires chemical analysis associated with particle size and source. This information would be very valuable for addressing the question of which are the most important factors on the bioactivity associated with different class of particles.

References

1. R. Bhatia, P. Lopipero and A.H. Smith, Diesel exhaust exposure and lung cancer, *Epidemiology* 1998, **9**, 84.
2. US Environmental Protection Agency, 1996. Air quality Criteria for Particulate Matter, vol. I, EPA/600/P-95/001aP, Washington, DC.
3. Dockery, D.W.; Schwartz, J.; Spengler, J.D. Air pollution and daily mortality – associations with particulates and acid aerosols. *Environ. Res.* 1992, **59**, 362.
4. Scheepers, P.T.J., Velders, D.D., Martens, M.H.J., Noordhoek, J., Bos, R.P. Gas chromatographic-mass spectrometric determination of nitro polycyclic aromatic hydrocarbons in airborne particulate matter from workplace contaminated with diesel exhaust. *J. Chromatogr. A* 1994, **A 677**, 107.
5. Malm, W.C., Sisler, J.F., Huffman, D., Eldred, R.A. and Cahill, T.A. Spatial and seasonal trends in particle concentration and optical extinction in the United States. *J. Geophys. Res.*, 1994, **99**, Sec. D, 1347.
6. Bezabeh, D.Z., Allen, T.M., McCauley, E.M. and Kelly, P.B. Laser desorption ionization time of flight mass spectrometry of nitrated polycyclic aromatic hydrocarbons. *J. Am. Soc. Mass Spect.*, 1997, **8**, 630.
7. Reilly, P.T.A., Gieray, R.A., Whitten, W.B., and Ramsey, J.M. Real time characterization of the organic composition and size of individual diesel engine smoke particles. *Environ. Sci Technol.* 1998, **32**, 2672.
8. Hankin, S.M. and John P. Laser time of flight mass analysis of PAHs on single diesel particles. *Anal. Chem.* 1999, **71**, 1100.
9. Dale, M.J.; Downs, O.H.J.; Costello, K.F.; Wright, S.J.; Langridge-Smith, P.R.R.; Cape, J.N. *Environ. Pollut.* 1995, **89**, 123.
10. Sander, L.C. and Wise, S.A. Polycyclic Aromatic Hydrocarbon Structure Index. NIST Special publication 922. 1997.
11. Ishiguro, T.; Takatori, Y. and Akihama K. Microstructure of diesel soot particles probed by electron microscopy: first observation of inner core and outer shell. *Combustion and Flame*, 1997, **108**, 231.
12. Kerminen, V.M. et. al. Characterization of the particle phase in the exhaust from diesel car. *Environ. Sci. Technol.* 1997, **31**, 1883.
13. Rakopoulos, C.D.; Hountalas, D.T.; Taklis, G.N. and Tzanos, E.I. Analysis of combustion and pollutants formation in a direct injection diesel engine using a multi-zone model. *International Journal of Energy Research*, 1995, **19**, 63.

CO-COKING OF COAL AND PETROLEUM RESID MIXTURES FOR PRODUCTION OF COAL-BASED JET FUEL

Anne E. Fickinger, Mark W. Badger, Gareth D. Mitchell and Harold H. Schobert
The Energy Institute
Coal Utilization Laboratory
The Pennsylvania State University, University Park, PA. 16802

Keywords: Coal/resid co-coking, coal-derived jet fuels, coke formation, delayed coking.

Introduction

The next generation of high Mach aircraft will utilize jet fuel to serve two main purposes. First the fuel will be used as a propellant. The second function of the fuel will be to serve as a heat sink for the aircraft's subsystem. As a result the fuel will be exposed to thermally stressing temperatures that exceed 450 °C, where pyrolytic degradation can occur. If solid deposits form in the fuel as a result of this degradation, plugging of the fuel lines can result. The presently used petroleum-derived jet fuel, JP-8, lacks the necessary hydroaromatic compounds that increase the thermal stability of the fuel. Fuel containing coal-derived components, however, would contain 2-3 ring hydroaromatics that increase the thermal stability of the fuel. However, past methods for obtaining coal-derived liquids are not economical.

There are two main processes for production of coal-derived liquids, coal liquefaction and coal pyrolysis [1,2]. Coal liquefaction produces desired low-boiling aromatic hydrocarbons, which are then upgraded. However the process involves high hydrogen pressures, which pose economic concerns [1]. At the other end of the spectrum, coal pyrolysis is a process that yields coal-derived liquids using mild operating conditions. However, the main products obtained from coal pyrolysis are water, carbon oxides and light hydrocarbon gases while the desired coal-derived liquids are produced in low quantity [2].

In our search for an alternative pathway for producing coal-derived liquids, the desire to incorporate a well-established industrial process became our driving force. Since oil refineries utilize delayed cokers to convert low-valued feedstocks into useful products such as low boiling distillates, it was decided to examine such a process to see if it could be modified to produce coal-derived liquids.

Delayed coking is a commercially used process to obtain quality coke and light hydrocarbon fractions from a low value petroleum resid [3]. This process typically operates in the temperature range of 450-500 °C [3]. For the purpose of this research we decided to incorporate coal into a simulated delayed coking process and termed this novel process co-coking. The intent of this novel process was to obtain liquid products that possess coal-derived structures which, when hydrotreated, would produce a product with higher thermal stability than petroleum-based fuels.

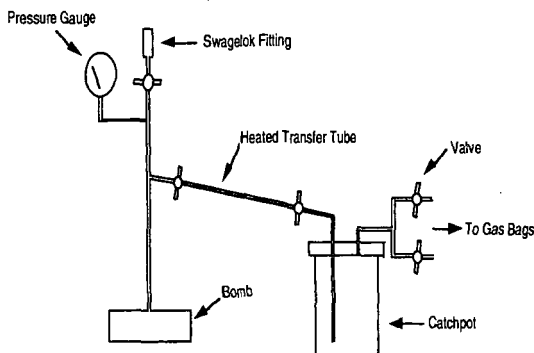
The work presented here focuses on the effects of different feed ratios and reaction length effects for various co-coking reactions. This work represents a continuation of previous studies of co-coking [4,5,6,7].

Experimental

Three coals were originally selected based on their high fluidity, high volatile content and relatively low ash values [7]. This paper, however, will focus on an in-depth study of the Powellton seam coal, to determine effects of reaction conditions, such as feed ratio and reaction length. The trends obtained from this particular coal can then be related to the other two coals based on previous research [6,7]. The coal was ground to a -60 mesh and vacuum dried at 110 °C for 2 hours prior to each experiment to remove excess moisture. Two different petroleum resids were employed. The first was a coker feed supplied by BP America. The second was a decant oil supplied by Marathon Oil Company. Both resids were used as received.

These coking reactions were carried out in a constructed vented reactor system. Figure 1 displays a schematic of reactor system utilized. This system consisted of a modified microautoclave reactor (tubing bomb) that was attached to a catchpot system immersed in an ice bath. The reactor system was developed to model aspects of delayed coking in the laboratory. The bomb portion of the system was intended to model a coking drum, while the catchpot was used to catch volatiles, which were then, re-condense into liquids. Before each reaction, the reactants were placed in the bomb portion of the reactor system in various feed ratios. The bomb portion, piping and catchpot were then purged with nitrogen to remove any air within the reactor system and finally left at ambient pressure. The bomb portion of the reactor system was then placed in a fluidized sand bath at a temperature of 465°C, while the

Figure 1: The vented reactor system



catchpot portion was placed in an ice bath. This temperature proved from previous work [6,7] to produce desirable liquid and solid product yields. Reaction length was varied.

Once the reaction was complete, the reactor system was left to cool. The liquids that accumulated in the catchpot portion of the reactor system were collected and subjected to a hexane extraction to obtain the oil products. The products were then removed from the bomb portion of the reactor system and subjected to a tetrahydrofuran (THF) Soxhlet extraction and finally a hexane extraction to obtain hexane-solubles. The THF-insoluble products were then collected and dried to obtain the coke product on a dry weight basis.

The hexane-soluble fractions from both the catchpot and bomb portion were subject to semi-quantitative analysis using a Shimadzu GC 17A GC-MS, to identify the composition of oils produced, and a HP 5890 II instrument with an FID high temperature simulation distillation GC, to obtain the various boiling cut points. Ultimate analysis and proximate analysis was performed on the coke products using a LECO 600 CHN analyzer and a LECO MAC 400 respectively. Optical microscopy was also performed on the coke products to determine if any interactions were occurring between the coal and petroleum resids.

Results and Discussion

Table 1 shows the overall distribution of the liquid and solid products obtained from co-coking reactions at 465°C for various feed ratios and reaction lengths. We know from previous research that the product distribution from these vented co-coking reactions is unaffected by temperature effects [7]. During the co-coking reactions, partial vaporization and mild thermal cracking, occurs causing both gas and light boiling distillates to flash distillate into the cooled catchpot [8]. The remaining heavy liquids in the bomb portion of the reactor are further subjected to cracking and polymerization reactions, which produce more gas. These gases are also re-condensed in the catchpot [8]. Along with the gases, a solid coke product is formed as a result of cracking reactions. This effect was evident when we examine the product distribution effect versus reaction duration. As the reaction length was increased for a particular feed ratio, the overall liquid yield decreased, while the solid product yield increased. The decrease in overall liquid product yield was mainly a result of the drastic decrease in the THF soluble liquid products as reaction time increased. This occurred because the liquids were exposed to further cracking reactions. The catchpot liquids, however, were unaffected by reaction length, since most of the liquids were flashed off very early in the reaction.

Table 1 also shows the feed ratio effect on the product distribution of co-coking reactions at 465°C. As the amount of petroleum resid was increased in these co-coking reactions for a particular reaction length, the overall liquid products increased, while the overall solid products decreased. Generally the increase in overall liquid product results from an increase in liquid products collected in the catchpot portion of the reactor system. This concurs with logic, since an increase in the amount of paraffinic liquid results in an increase in volatiles, which are easily re-condensed. This present reactor system was not designed to accommodate for adequate gas collection. However, the amount of gas most likely produced from these co-coking reactions, according to mass balances, would be negligible.

The addition of coal from previous studies [6,7] has been shown to decrease the overall liquid product yield when compared to a heat-treated petroleum resid alone. The coal seems to contain highly reactive components that initiate radical reactions that result in retrogressive polymerization reactions.

Overall these liquid and solid yields are comparable to an industrial delayed coking process product distribution of 70% liquids, 10% gas, and 20% coke [3,8]. The product distribution results verify that simplified delayed coking was being simulated by the vented reactor system.

However, our primary goal of this research was to produce low-boiling distillates that can be hydrotreated to produce a thermally stable coal-derived jet fuel. To determine the extent of suitability of the liquid products produced from these co-coking reactions for jet fuel, high temperature simulation distillation GC was performed on the hexane-soluble fractions. For this research, the desired boiling range for the hexane-soluble fraction was 180-330°C. This boiling distribution was defined as the jet fuel range. Figure 2 shows the effect of feed ratio on the liquid yield that fell within the jet fuel boiling range for various co-coking reactions at 465 °C for two hours. The general trend observed was that as more coal was added to these co-coking reactions, the greater the liquid yield, from the catchpot, that distills in the jet fuel boiling range. However, process conditions limit the amount of coal that can be added to a delayed coker. Although the jet fuel boiling yield from the 1:1 ratio of Powellton coal and decant oil in Figure 2 demonstrates a desirable yield of distillates, the ability to process this feed mixture through connective piping in an industrial delayed coker becomes a concern.

Another general trend observed from Figure 2 was that the addition of coal decreases the overall yield of products that distill in the jet fuel boiling range when compared to reaction with heat-treated resid only. The exception that occurred here was with the coker feed. The addition of coal to the coker feed seemed to enhance the yield of jet fuel distillates. This most likely occurred because both the coal and coker feed were acting as hydrogen donors toward the more aromatic components produced in these reactions. This enhancement of the jet fuel boiling distribution yield did not occur when the Powellton coal and decant oil are co-coked, since the decant oil does not appear to act as a hydrogen donor. This explanation was supported by the results obtained when a mixture of the two resids was coked in the presence of the coal. We saw an increase in the yield for the 180-330 °C boiling range when the coker feed was incorporated into the co-coking reactions with decant oil and Powellton coal. The results seem to show that both Powellton coal and the coker feed act as hydrogen donors during these coking reactions, while the decant oil acts as an initiator of radical reactions.

Figure 3 shows the effect of reaction length and feed ratio on the liquid yield from the catchpot that fell within the jet fuel boiling distribution. The general trend observed was that, as reaction length increased, an increase in the jet boiling distribution range occurred. However, an important note was that although the percent yield in the jet fuel range increased as reaction length increased, the overall liquid product being produced decreased. This was mostly likely due to secondary cracking reactions of the heavy liquid, producing more volatiles. Another trend observed involved jet fuel yields from co-coking reactions involving the coker feed, decant oil and the Powellton coal. These yields fell exactly in between the Powellton/coker results and the Powellton/decant results for corresponding reaction lengths and feed ratios.

Ultimate analysis was performed on the hexane-soluble fractions produced from co-coking reactions at 465°C to determine the quality of products being produced. Table 2 shows the H/C ratio for the hexane-soluble products. The results showed the liquid H/C ratio obtained from reactions with a 1:2 feed ratio (coal:resid) in the catchpot were unaffected by reaction length. These results further indicated the liquids obtained in the catchpot had undergone flash pyrolysis. Table 2 also shows that as the feed ratio was increased to 1:4 (coal:resid) there was no real significant effect in the catchpot H/C ratio. While the liquid H/C ratios from the bomb portion showed a decrease in the H/C ratio as reaction length was increased. This occurred because of further liquid decomposition in the bomb portion of the reactor during longer co-coking reactions. When the feed ratio was increased to 1:4 (coal:resid) a higher bomb H/C ratio occurred as a result of the increased concentration of paraffinic compounds.

Ultimate analysis and optical microscopy were performed on the THF-insoluble products to give an indication of the quality of the coke being produced. Figure 4 illustrates that as reaction length was increased, the H/C ratio of the coke product decreased, indicating a more carbon-rich product. This trend was a result of cracking and polymerization reactions that occur in the co-coking reactions. The effect of feed ratio was negligible on the solid H/C ratio.

Optical microscopy indicated enhancement of coal particles when Powellton coal and decant oil was co-coked. However, when the coke products from the coker feed and Powellton coal were examined, no interactions were observed. Varying the feed ratio had no effect on this reaction matrix. Results from co-coking of the three reactants showed that the influence of the decant oil on the coal particles diminished as compared to the coal and decant oil interaction. The influence of the decant oil in this tri-coking proved to be quite variable throughout the

sample. As a result some coal particles were fully enhanced, and some remained unaffected, but most coal particles fell somewhere in between the two extremes.

Conclusions

From work to date we can adequately conclude that we are upgrading these heavy petroleum resids by producing a coke product that is more carbon and liquids with increased H/C ratios. It was found that by increasing the feed ratio to favor the addition of a petroleum resid, the overall liquid product yield increased, but a decrease in the jet fuel boiling distribution yield was observed. While little effect was observed on the H/C ratio of the liquids obtained when the feed ratio was increased, an increase in reaction length resulted in a decrease of the overall liquid products and an increase in the jet fuel boiling distribution yield. In conclusion this process seems to be simulating the delayed coking process on a laboratory scale.

Acknowledgements

The authors would like to express their gratitude to the Department of Defense and Air Force Wright-Patterson Laboratory for the support under contract F33615-98-D2802 delivery order 6.

References

1. Elliot, M.A.(Ed.), in "Chemistry of Coal Utilization Secondary Supplementary Volume", Wiley-Interscience Publication, New York, (1981).
2. Kural, O.(Ed.), in "Coal: Resources, Properties, Utilization, Pollution", Orhan Kural, Turkey, (1994).
3. Speight, J.G.(Ed.) in "The Chemistry and Technology of Petroleum. 2nd Edition", Marcel Dekker Inc., New York, (1991).
4. Martin, S.C., Tomic, J., and Schobert, H.H., ACS Div. Fuel Chem. 42, 3, 121, (1997).
5. Badger, M.W., Fickinger, A.E., Martin, S.C., Mitchell, G.D., and Schobert, H.H., AIE 8th Australian Coal Science Conference Preprints p. 245, December 1998
6. Fickinger, A.E., Badger, M.W., Mitchell, G.D., and Schobert, H.H., ACS Div. Fuel Chem. 44, 1, 106, 1999.
7. Fickinger, A.E., Badger, M.W., Mitchell, G.D., and Schobert, H.H., ACS Div. Fuel Chem. 49, 1, 218, 1999.
8. DeBiase, R., Elliott, J.D., and Hartnett, T.E., *Petroleum Derived Carbons*, ACS Symposium Series No. 303, 156, 1986.

Table 1: Feed ratio and reaction length effects on product yields from co-coking reactions with Powellton coal and the two petroleum resids at 465 °C

RESID	TIME	PRODUCT YIELDS			
		Feed Ratio 1:2		Feed Ratio 1:4	
		Liquid %	Solid %	Liquid %	Solid %
Coker	30 minutes	83.61	24.78	69.19	26.71
Coker	2 hours	38.84	40.74	61.54	30.98
Coker	4 hours	48.71	38.87	55.78	30.20
Decant	30 minutes	73.09	28.57	78.23	13.78
Decant	2 hours	55.47	37.67	56.88	34.03
Decant	4 hours	39.68	43.12	49.24	49.24
Decant/Coker	30 minutes	53.86	30.50	*	*
Decant/Coker	2 hours	44.64	39.88	60.59	26.50
Decant/Coker	4 hours	52.97	40.49	62.01	26.53

* Data Missing

Table 2: Feed ratio and reaction length effects on hexane-soluble product H/C ratios from co-coking reactions with Powellton coal and various petroleum resids at 465 °C

COAL	RESID	TIME	HEXANE SOLUBLE H/C RATIOS			
			Feed Ratio (1:2)		Feed Ratio (1:4)	
			CATCHPOT	BOMB	CATCHPOT	BOMB
Powellton	Coker	30 minutes	2.30	1.64	2.49	2.01
Powellton	Coker	2 hours	1.86	1.36	2.30	1.36
Powellton	Coker	4 hours	2.30	0.87	2.47	1.03
Powellton	Decant	30 minutes	1.30	1.05	1.23	0.90
Powellton	Decant	2 hours	1.40	0.70	1.45	0.82
Powellton	Decant	4 hours	*	0.90	1.59	0.76
Powellton	Decant/Coker	30 minutes	1.60	0.98	*	*
Powellton	Decant/Coker	2 hours	1.51	1.16	1.74	1.46
Powellton	Decant/Coker	4 hours	1.67	1.82	1.78	1.04

* Data missing

Figure 2: Feed ratio effects on the jet fuel boiling distribution (180-330°C) for the hexane-soluble fractions from co-coking reactions at 465°C for two hours

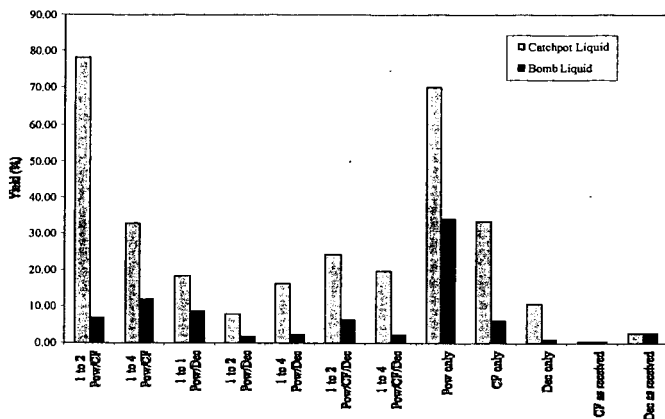


Figure 3: Reaction Length effects and feed ratio effects on the jet fuel boiling distribution of the catchpot hexane-soluble fraction from co-coking experiments at 465 °C.

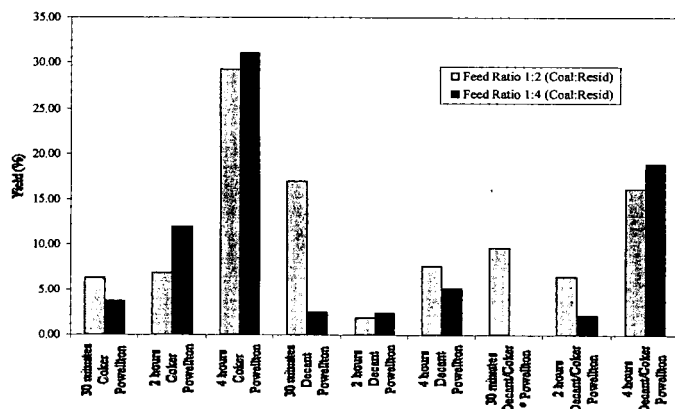
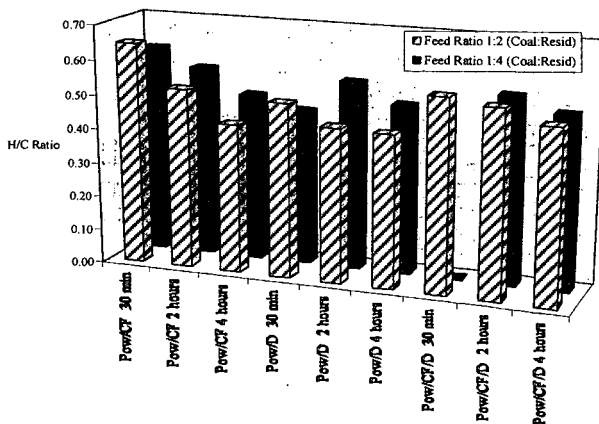


Figure 4: Reaction length and feed ratio effects on the solid coke products formed from co-coking reactions at 465 °C with Powellton coal and the two petroleum resid



COMPARISON OF THE THERMAL STABILITY OF COAL-DERIVED JET FUELS IN THE AUTOXIDATIVE AND PYROLYTIC REGIMES UNDER BATCH AND FLOW CONDITIONS

John M. Andrésen, James J. Strohm and Chunshan Song*
Applied Catalysis in Energy Laboratory, The Energy Institute
The Pennsylvania State University, University Park, PA 16802

KEYWORDS: Pyrolysis, thermal stability, aviation jet fuels.

ABSTRACT

The thermal stability of coal- and petroleum-derived jet fuels and the associated model compounds decahydronaphthalene and n-tetradecane, as they go through the autoxidative and pyrolytic regime both under batch and flow conditions, was studied. Under batch reactor conditions, the decahydronaphthalene showed excellent thermal stability up to 500°C, whereas the n-tetradecane started its cracking process at around 450°C. Flow reactor studies mirrored the thermal decomposition of the model compounds, although the cracking appeared at higher bulk fuel temperatures. The thermal behavior of the experimental jet fuels also confirmed that the paraffinic proportion of the fuels is the main reason for thermal fuel degradation.

INTRODUCTION

Cycloalkane-rich liquids, such as those derived from coal, have great potential as precursors for advanced jet fuels that meet the more stringent thermal stability requirements for the future high-Mach jet aircraft [1]. Currently, commercial planes are utilizing conventional paraffinic based jet fuels that may be exposed to temperatures up to 300°C [2]. However, as the flight speed will be increased to high Mach numbers, the fuel is expected to experience temperatures as high as 482°C (900°F) or above, since the jet fuel also functions as the main coolant for the different electronic and mechanical parts of the aircraft. Even though the residence time at such elevated temperatures is expected to be fairly short (matter of minutes or less), the jet fuels presently used have been shown to form solid deposit that can lead to catastrophic malfunction of the jet aircraft. The current jet fuels are petroleum-derived and consequently rich in linear alkanes, which are highly susceptible to pyrolytic cracking, resulting in coking [3]. The thermal stability of a jet fuel in the pyrolytic regime can be greatly enhanced by utilizing liquids rich in cycloalkanes [4]. This is the case for hydrotreated coal-derived liquids, where the aromatic structures have been transformed over to their corresponding cyclo-alkanes [5]. An additional problem with jet fuels is the presence of dissolved oxygen from air, which reacts with the fuel during the autoxidative regime (150-250°C) before the fuel and its oxygenated reaction products enter the pyrolytic regime (400-500°C) [6]. Accordingly, the present study compares the thermal stability of coal- and petroleum-derived jet fuels and associated model compounds, as they go through the autoxidative and pyrolytic regime, both under batch and flow conditions. Differences in chemical reactivity between linear- and cyclo-alkane model compounds are related to the superior thermal stability of the coal-derived jet-fuels.

EXPERIMENTAL

The samples investigated were the two model compounds tetradecane (TD, Aldrich 99%) and decahydronaphthalene (DHN, Aldrich 98%, a mixture of cis- and trans-decahydronaphthalene), a hydro-treated light cycle oil (DA/HT LCO) and a coal-derived jet fuel named JP8C.

For the batch study, a volume of 5 ml was charged into a microautoclave with a total volume of 25 ml [7]. The system was pressurized with 100 psi of air and heated in a fluidized sandbath. The heating-rate used was approximately 5°C min⁻¹ from room temperature and the microautoclaves were removed upon reaching 250, 350, 450 and 500°C. After reaction, the microautoclaves were rinsed of sand and quenched. When the microautoclaves were cooled to ambient temperature, the gas phase and liquid fraction were removed for analysis. The tube and the stem of the microautoclave were washed in pentane until a clear color was obtained and then dried. The amount of solid deposition was determined from the increase in weight of the tube and stem.

The GC-MS analysis of the liquid products was performed on a Shimadzu GC-174 coupled with a Shimadzu QP-5000 MS detector. The column used was a Restek XT15 column with a coating phase of 5% diphenyl / 95% dimethyl polysiloxane and it was heated from 40 to 290°C with a heating rate of 6°C min⁻¹.

The flow reactor is outlined in Figure 1. The fuel tank was degassed with high-purity N₂ (99.9%) to ensure the absence of oxygen for the pyrolytic study. In addition, the jet fuel was purged with air to compare our autoxidative studies in batch reactors with those of the flow reactor. An HPLC pump was used to pressurize the jet fuel up to 700 psi with a flow rate of 6 ml/min. Within the furnace, a 0.040" (1.02 mm) ID silcosteel tubing was used. This ensured a liquid hourly space velocity (LHSV) of 450. The temperature profile was established by welding thermocouples to the tubing in addition to inserting thermocouples within the tubing and at the

exit of the furnace (the last thermocouple is indicated in Figure 1, where also a silcosteel union tee was used to minimize catalytic jet fuel degradation). The temperature profile is shown in Figure 2 and is somewhat different to that reported in the literature for other flow reactor systems [8]. The GC/MS traces are reported according to the exit temperature of the actual fuel. Immediately after exiting the furnace, the jet fuel is cooled by refrigerated ethylene glycol. The tubing used is also silcosteel to avoid secondary reactions during cooling of the stressed jet fuel. The cooled jet fuel is then filtered to accumulate any solids formed using a 0.8 μm filter. Further, a back pressure valve is used to control the furnace pressure. The cooled jet fuel is then allowed to enter a storage vessel, where the liquid products are separated from the gaseous products.

RESULTS AND DISCUSSION

Batch reactor studies The content of the liquid remaining for n-tetradecane (TD), decahydronaphthalene (DHN) and the coal-derived jet fuel JP8C stressed under the influence of air in the temperature range 250 to 500°C is compared in Figure 3. At low temperatures (250 - 350°C), the formation of gas and solid products is very small. However, as the temperature is increased to 450°C and indeed for the one stressed at 500°C, the content of liquid remaining is reduced. Especially the linear alkane, TD, has a drastic lowering of the liquid phase, reaching a level below 80%. The coal-derived jet-fuel, JP8C, shows an improved thermal stability compared to TD, where above 90% of the liquid remains, while the cycloalkane, DHN, shows the highest ability to resist thermal cracking. The reduction in the liquid produces gas and solids, and although not shown here the linear alkane forms about 0.2 wt% solid residue already at 250°C. The solid deposition is not significantly increased at 350°C, but rises sharply when stressed further to 500°C, following a similar trend to the solid deposition found using flow-reactor studies [8, 9]. The vast difference in liquid yields between liquids rich in linear alkane and those mainly containing cyclo-alkane (including the JP8C and LCO HT/DA) as showed in Figure 2, can be explained further by studying the ability of the different hydrocarbons to resist thermal cracking. Figure 4 shows the variation in the remaining concentration of TD and DHN in the liquid products with temperature, taking into account the formation of gas and solids. In the autoxidative zone the reduction in the concentration of the two compounds is small. However, as the temperature reaches the pyrolytic regime, a great difference in thermal stability of the two compounds is shown. At 500°C only around 35% TD is remaining, while 85% of the DHN has not reacted.

The above differences in thermal stability can be related to the differences in the oxidation chemistry in the autoxidative zone and the thermal stability of the oxygenated compounds from linear- and cyclo-alkanes to remain in the liquid. Figure 5 shows the GC/MS trace of the reaction products from stressing of TD in air up to 250°C. A range of linear alkane products is present as the tallest peaks in the different peak clusters. A row of compounds with oxygen functional groups is associated with each linear alkane, such as acids, aldehydes and ketones. The compounds present at 250°C do not alter when stressed up to 350°C, but a drastic change in the product distribution appears as the temperature is increased to 450°C. At this temperature the concentration of n-alkanes are greatly increased and also 1-alkenes are produced as a result of thermal cracking [10]. Although, some oxygenated compounds still remain in solution, the reactivity of these species clearly adds to the thermal degradation of the linear alkane, TD. The cyclo-alkane, DHN, also experiences some oxidation in the autoxidative zone, as shown in Figure 6. The mixture of trans- and cis-decahydronaphthalene used here (retention time of 14 and 15 minutes, respectively), gave oxygenated products which appear in a narrow retention time range of 18 to 21 minutes. Particularly ketones and alcohols dominate, where compounds such as 2-butyl cyclohexanone and decahydronaphthol are abundant. The presence of alcohols in the products from DHN indicates that oxygenated cyclo-alkane compounds are more stable than their linear equivalents. As the temperature is increased to 450°C only small changes in the product distribution occur, which again confirm the higher stability of cyclo-alkanes derived compounds, where oxygen is captured. By further increasing the stressing up to 500°C, non-oxygenated single ring compounds, such as 1-methyl cyclohexene, appear at lower retention times, but still the oxygenated compounds are present. The development of the hydrogen-donor tetrahydronaphthalene may also further enhance the thermal stability of the liquid.

The changes in the product distribution from the coal derived jet fuel, JP8C, stressed under air at 250 and 500°C are shown by the GC/MS traces in Figure 7. At 250°C, JP8C is rich in one and two ring cyclo-alkanes, and at longer retention times a series of long-chain linear alkanes in the range of C12 to C18 is present. When stressed up to 500°C, only small changes in the cyclo-alkane distribution occur, while the concentration of the linear alkanes has decreased drastically. Based on the study of stressing TD in both the autoxidative zone and further in the pyrolytic regime, the reduction in the linear alkane concentration can be due to the following two reasons. Firstly, the tendency of linear alkanes to react with oxygen and form less stable compounds, and secondly, the lower thermal stability of the linear alkanes themselves in comparison to cyclo-alkanes.

Flow reactor studies

The findings from the batch reactor studies were further correlated with stressing of model compounds under flow conditions both in the absence and presence of oxygen. Silcosteel tubing was used in this work to minimize any metal surface-catalyzed fuel decomposition. Figure 8 shows the concentration of DHN remaining as a function of the exit temperature of the liquid. With a LHSV of 450, DHN presents a similar behavior when stressed under both N₂ and air, where the thermal cracking of the liquid takes place at temperatures above 620°C. Indeed, nearly identical evaluation of the DHN both under N₂ and air supports the findings from the batch reactor studies that the air uptake by DHN is reduced in comparison to linear alkanes such as TD. Flow reactor studies using TD were also carried out. However, the TD generated extensive coke formation resulting in blockage of the 1/16" tubing through the furnace. This was observed under both N₂ and air, where the dotted vertical line in Figure 8 shows the temperature at which the TD under oxidative conditions started coking, while the solid line indicates the same temperature for TD under inert atmosphere. The fact that TD actually cokes at temperatures where DHN is essentially unconverted again supports the previous findings from the batch reactor studies. The difference in the thermal stability of cyclo-alkanes and linear alkanes is also illustrated in Figure 9, showing the GC/MS traces of the LCO derived jet fuel, DA/HT LCO, stressed alone with fuel outlet temperatures of 520 and 620°C. With a LHSV of 450 very little jet fuel degradation takes place when the maximum fuel outlet temperature was 520°C, and the GC/MS trace is virtually identical to those reported on the initial DA/HT LCO fuel [3, 5]. Increasing the temperature to 570 and 590°C (not shown here) there is some pyrolytic cracking of the jet fuel, but it is not before 620°C that the appearance of aromatic compounds starts becoming significant. This scenario is somewhat different to that of the batch reactor studies, where similar changes were observed at a lower temperature for the coal derived jet fuel JP8C (Figure 7). On the other hand, during the batch reactor studies the jet fuel had residence times substantially longer than that of the present flow reactor experiments. However, again there are only slight changes in the cyclo-alkane compounds, and as expected the thermal exposure at 620°C has cracked virtually all the long chain alkanes into lighter compounds and aromatic compounds, opening the possibility for detrimental solid deposition.

CONCLUSIONS

The changes in product distribution for a linear alkane, n-tetradecane (TD), and a bicyclic alkane, decahydronaphthalene (DHN) were related to a cycloalkane-rich coal-derived jet fuel, JP8C, in batch reactors and a light cycle oil-derived jet fuel, DA/HT LCO, under flow conditions. Under batch conditions, the linear TD showed less thermal stability than that of JP8C, and particularly lower than that of DHN when stressed under air. This was associated with the formation of a range of oxygenated compounds from TD such as acids, aldehydes and ketones, which showed lower thermal stability than those oxygenated compounds derived from DHN. The flow reactor studies confirmed the findings under batch conditions, but the temperatures at which cracking occurs were shifted to considerably higher temperatures.

ACKNOWLEDGEMENTS

The authors wish to thank the US Air Force Wright Laboratory and the US AFOSR for their support. We are grateful to Prof. Harold H. Schobert of The Pennsylvania State University for his support and discussions, and to Mr. William Harrison III, Dr. Tim Edwards and Dr. Cindy Obringer of WPAFB for helpful suggestions.

REFERENCES

- (1) Edwards, T., Prep. Am. Chem. Soc.-Div. Petr. Chem., 41(2), 481-487 (1996).
- (2) Yoon, E.M., Selvaraj, L., Song, C., Stallman, J.B and Coleman, M.M., Energy & Fuels, 10, 806-811 (1996).
- (3) Andrésén, J.M., Strohm, J.J. and Song, C, Prep. Am. Chem. Soc.-Div. Petro. Chem., 43(3), 412-414 (1998).
- (4) Andrésén, J.M., Strohm, J.J. and Song, C, Prep. Am. Chem. Soc.-Div. Fuel Chem., 44(1), 199-203 (1999).
- (5) Strohm, J.J., Andrésén, J.M. and Song, C, Prep. Am. Chem. Soc.-Div. Petro. Chem., 44(3), 386-390 (1999).
- (6) Hazlett, R.N., Thermal Oxidative Stability of Aviation Turbine Fuels, ASTM, Philadelphia, PA (1991).
- (7) Song, C., Eser, S., Schobert, H.H. and Hatcher, P.G., Energy & Fuels, 7, 234-243 (1993).
- (8) Minus, D.K. and Corporan, E., Prep. Am. Chem. Soc.-Div. Petro. Chem., 43(3), 360-363 (1998).
- (9) Edwards, T. and Atria, J.V., Prep. Am. Chem. Soc.-Div. Petro. Chem., 40(4), 649-654 (1995).
- (10) Andrésén, J.M., Strohm, J.J. and Song, C, Prep. Am. Chem. Soc.-Div. Fuel Chem., 44(1), 194-198 (1999).

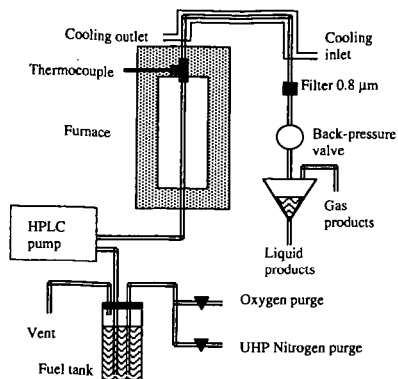


Figure 1. Outline of flow reactor.

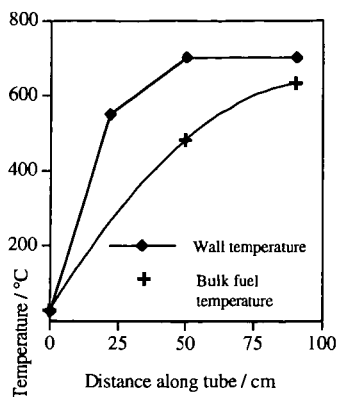


Figure 2. Temperature profile of the flow reactor system, showing correlation between wall and actual bulk fuel temperatures.

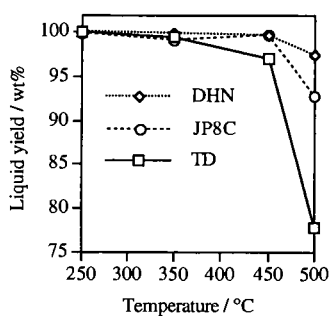


Figure 3. Comparison of liquid remaining for TD, DHN and the coal-derived jet fuel JP8C stressed in batch reactor under the influence of air in the temperature range 250 to 500°C.

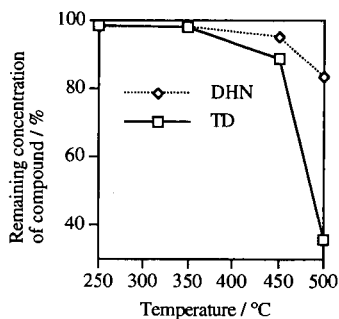


Figure 4. Variation in the remaining concentration of tetradecane and decahydronaphthalene with temperature stressed under 100 psi air in batch reactor.

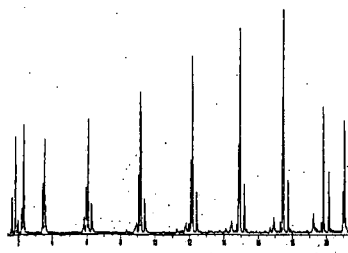


Figure 5. GC/MS trace of the reaction products from stressing TD in batch reactor under 100 psi air up to 250°C.

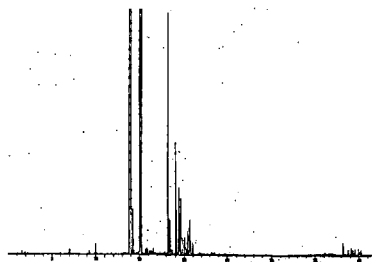


Figure 6. GC/MS trace of the reaction products from stressing DHN in batch reactor under 100 psi air up to 250°C.

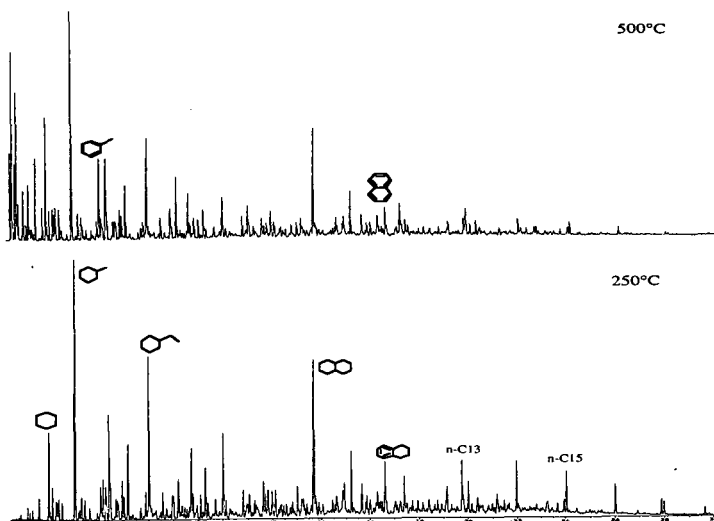


Figure 7. GC/MS traces of the coal derived jet fuel, JP8C, stressed under 100 psi air in batch reactors from room temperature to 250°C (bottom) and 500°C (top).

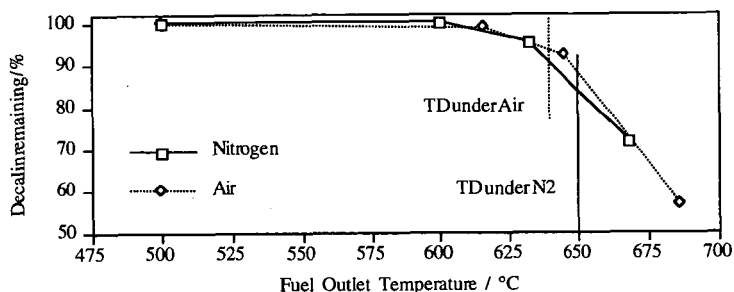


Figure 8. Remaining concentration of DHN with temperature under flow conditions.

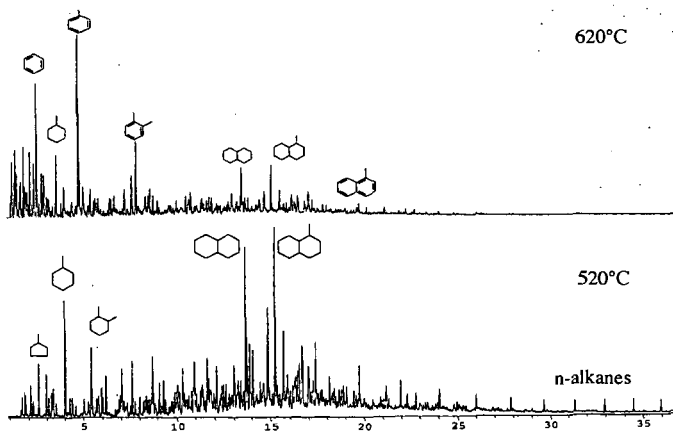


Figure 9. GC/MS traces of the DA/HT LCO jet fuel under flow conditions at fuel outlet temperatures of 520 and 620°C.

TEMPLATE-INDUCED CRYSTAL GROWTH

John W. White, A. Brown, K. Edler, S. Holt, J. Watson, P. Reynolds, J. Ruggles
Research School of Chemistry
The Australian National University
Canberra ACT 0200, Australia

and

L. Iton
Materials Science Division
Argonne National Laboratory
Argonne, USA

KEYWORDS: Biomineralisation, Silicate, Film

ABSTRACT

The process of "mineralisation" in biology leads to a diversity of inorganic structures based on silica or calcium carbonate. Some of these are composite and, at the same time, highly crystalline. In all cases a molecular or self assembled "template" species has been identified as the promoter for the crystallisation of the new structure. In biology these "templates" are the end step in the conveyance of genetic information to the inorganic synthesis and an understanding of how they work is the key to mimicking biomineralisation in the laboratory. The lecture will describe how modern scattering methods, using x-rays and neutrons, have revealed the very first steps in the process from the first association of the inorganic with the "template" in zeolite and mesoporous silicate syntheses in the bulk and at interfaces. We now have some control of the phase diagram at surfactant interfaces and novel nanoscale structures have been produced and quantitative thermodynamic information on the kinetics of growth between 20Å and 1000Å will be discussed. It now seems to be possible also to reproducibly create structure at the micron scale and the lecture will describe some of these developments.

INTRODUCTION

Part of the future of chemical physics is to understand and control the ways in which intermolecular forces give rise to the diversity of structure and dynamics in biological systems. Mimicking phenomena like biomineralisation, in particular the role of molecular templates as a basis for growing inorganic structures, and using modern synchrotron x-ray and neutron scattering shows the way to make a variety of new materials. The structures produced in this way appear on the nanometer scale, the tens of nanometer scale and the micron scale. As the objective of our work is to understand formation mechanisms and to control growth, the combined use of equilibrium thermodynamic properties and kinetic paths to metastable states is of interest.

MOLECULAR TEMPLATES

In nature, molecular or macromolecular templates such as poly l serine have been invoked as the structure directing agents in the organisation of silica to form the beautiful structures observed in diatoms^{1,2} and proteins made by molluscs appear to give rise to the colourful composite "nacre" of shells³. The calcium carbonate here is of almost single crystal quality interspersed with organic matter⁴. An example for the laboratory is the formation of the zeolite, Silicalite or ZSM-5 directed by the tetra n-propyl ammonium ion as template. We have found that the influence of this ion is great, even at the earliest stages of hydrothermal synthesis at room temperature both in the gel phase⁵ and from clear preparations^{6,7}. Homogeneous nucleation around the template ion can thus be followed from the scale of about two nanometres to microns⁷. Figure 1 shows the *in situ* x-ray small angle scattering from a clear solution synthesis mixture as a function of time of heating at 100C.

LIQUID CRYSTAL TEMPLATES - THE TENS OF NANOMETER SCALE

The production⁸ of mesoporous materials with internal structures in the tens of nanometre scale using surfactant liquid crystal mesophases as templates for silicate growth was a major step upward in the scale of structures that could be induced by templates. That the chemistry and structure^{9,10,11} may be optimised by improvements to the synthetic conditions^{12,13} continues to suggest new means of control the structure directing process by modifying the surfactancy, the direction of surfactant phase transitions and by imposing external constraints.

By constraining growth to a surface - the air liquid interface, highly crystalline one and two dimensional structures may be studied^{14,15}. The structural problem is greatly simplified and mesoporous films with considerable potential practical application are produced. The kinetics of this form of growth are admirably studied by the new methods of x-ray and neutron reflectivity.

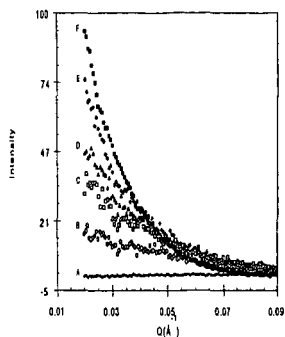


Figure 1. Small angle x-ray scattering patterns of the silicalite solution after heating times of A) 0 min, B) 30 min, C) 60 min, D) 120 min, E) 360 min and F) 840 min.

Films may be grown^{14,16,17} by slowly hydrolysing tetra ethoxy silane in the presence of an aqueous surfactant solution at about ten times the critical micellar concentration. The kinetics show a prolonged induction phase where there is no visible film growth for five to ten hours and then a fairly rapid growth of film to thicknesses of about a few microns. Changing the conditions allows thicker or thinner films to be made. X-ray and neutron reflectivity methods allow these processes to be followed in real time and the subsurface structures to be worked out at each stage. In these methods¹⁸ the intensity of specularly reflected x-rays or neutrons is analysed for reflection angles above the critical angle for external reflection.

Figure 2 shows the x-ray specular reflectivity from the air water interface at which a templated silica film is growing. In the "induction phase" (a,b) the reflectivity is clearly modified from that of water or a surfactant solution of the same strength as that of the cetyl trimethyl ammonium bromide used for the preparation. The bump in the reflectivity shows that there is a surface excess and treatment of the data indicates that this "embryo film" is about 27Å thick. Its growth up to the point where a film can be seen has been followed^{14,15}. The data contain a strongly falling (Q_z^{-4}) Fresnel component which may be removed by multiplying by Q^4 to show the Kiessig fringe - the form factor - of this surface layer. At longer times of reaction (b,c) a clear Bragg peak emerges showing that a highly ordered film structure has been created at the interface.

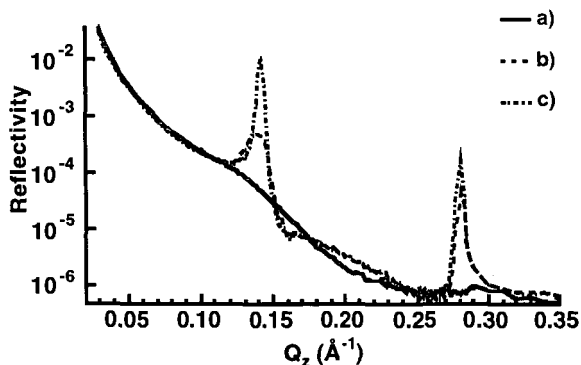


Figure 2. X-ray reflectivity from the air - water interface during the induction period showing the development of the reflectivity profile over time into diffraction peaks. a) 530 minutes, b) 608 minutes, and c) 687 minutes. The quality of the fits is shown.

Using neutron reflectivity and choosing deuterated and non deuterated surfactant against heavy water and air contrast matched water the contrast between the surfactant part and the silicate part of the film layer structure can be systematically varied¹⁵. In combination with the x-ray reflectivity results a complete picture of the development in one dimension, emerges. Figure 3 shows the Fresnel corrected reflectivity functions for several contrasts (left hand side) and the appropriately transformed real space densities at and below the growing surface at various times.

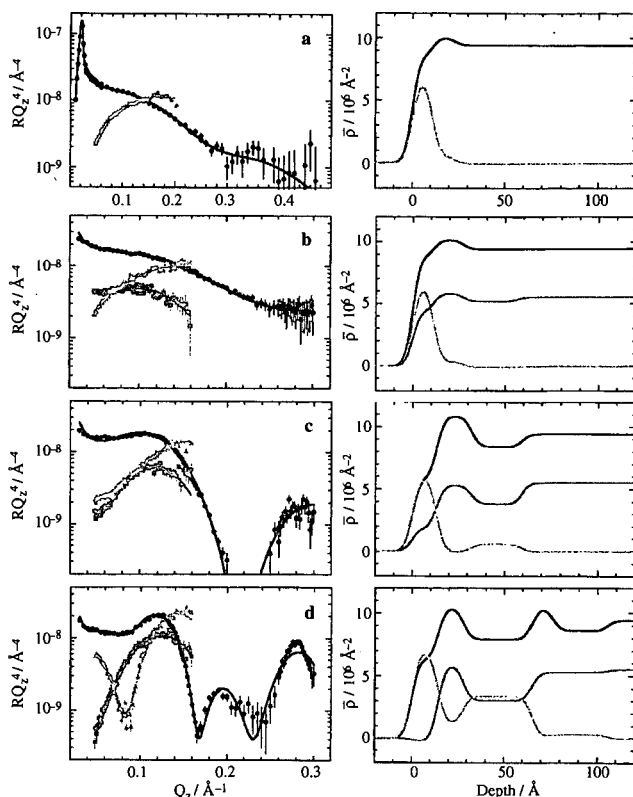


Figure 3. Fresnel corrected reflectivity profiles for both x-rays (black), deuterated surfactant on air contrast matched water (orange), and protonated surfactant on D_2O (blue) with the corresponding real space profiles for a growing silicate film at the air - water interface.

The real space model emerging from these data is of silicated, hexagonally arranged micelles lying parallel to the air-water interface as shown in Figure 4. Another aspect for the future comes from our recent work using x-ray and neutron reflectometry to study the induction phase for film growth and the origin of the hexagonally packed tubular micelle at apparently much lower concentrations of surfactant than would be expected for this phase in the pure surfactant. It now looks as though an anion induced phase transition from a glassy or cubic phase to the hexagonal occurs and that this may be controlled by chemical means¹⁹. A similar phenomenon has been observed by Aksay et al for calcium carbonate films templated by a porphyrin based surfactant²⁰.

MICRON SCALE STRUCTURES AND THE FUTURE

In experiments to improve our understanding of the chemistry behind the growth of three dimensional MCM-41 structures from cetyl trimethyl ammonium templated gels some remarkable structures on the micron scale were observed by transmission electron microscopy²¹ on the underside of the growing films. One of these is shown in Figure 5. Rod like, disc like and worm like structures were also recorded, some resembling the tactoids observed by Bernal and Fankuchen²² in tobacco mosaic virus solutions at concentrations above ca 1.5wt%. We and others^{17, 23} have recorded them frequently in film preparations such as those described above.

We suppose that such structures (particularly the worm-like structures) might be common in surfactant systems but are observable to us because that are "fossilised" by the silicate component and so are durable enough to see in the electron microscope. Clearly there is another length scale operating to form these structures. For example, inside the tactoids one can clearly see the ca 40Å diameter threads of the templated, silicated cylindrical micelles whose scale is determined by the surfactant size and silica coating. The balance of the surface and bulk energy created by such adhesion of tubules to form a tactoid bundle may provide the length scale determining the bundle size. That such structures might also be designed poses one of the fascinating future possibilities for the work described in this lecture.

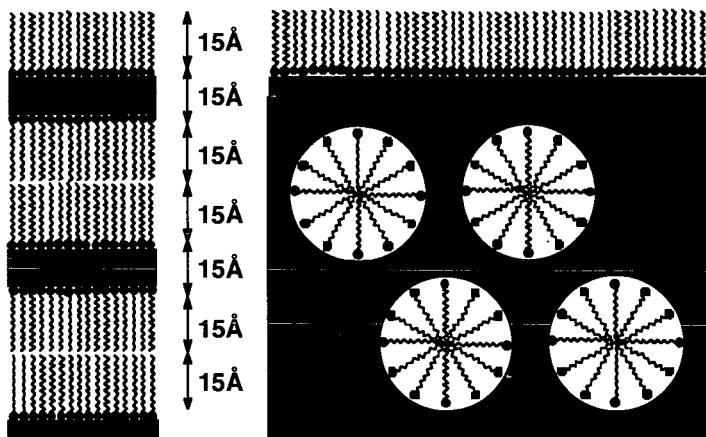


Figure 4. Model of the one dimensional structure at the air-water interface of a growing silicate film templated at 25C by a cetyltrimethyl ammonium template.



Figure 5. Micron scale structure observed on the growing side of a silicate film templated by cetyl trimethyl ammonium bromide.

REFERENCES

1. R.E. Hecky *et al.*, *Marine Biology*, **19**, 326-330, (1973).
2. Chia-Wei Li and B.E. Volcani, *Protoplasma*, **124**, 10-29, (1985).
3. B.L. Smith, *Chemistry and Industry*, 17 August, 649-653 (1998).
4. X. Shen, A.M. Belcher, P.K. Hansma, G.D. Stucky and D.E. Morse, *J. Biol. Chem.*, **272**, 32472-32481, (1997).
5. T.O. Brun, J.E. Epperson, S.J. Henderson, L.E. Iton, F. Trouw and J.W. White *Langmuir*, **8**, 1045-1048, (1992).
6. J.N. Watson and J.W. White, *Chemical Communications*, 2767-2768, (1996).
7. J.N. Watson, L.E. Iton, R.I. Keir, J.C. Thomas, T.L. Dowling and J.W. White *Journal of Physical Chemistry B*, **101**(48), 10094-10104, (1997).
8. Beck, J. S., Vartuli, J. C., Roth, W. J., Leonowicz, M. E., Kresge, C. T., Schmitt, K. D., Chu, C. T.-W., Olson, D. H., Sheppard, E. W., McCullen, S. B.; Higgins, J. B. and Schlenker, J. L., *J. Am. Chem. Soc.*, **114**, 10834, (1992).
9. G.D. Stucky, A. Monnier, F. Schüth, Q. Huo, D. Margolese, D. Kumar, M. Krishnamurty, P. Petroff, A. Firouzi, M. Janicke and B.F. Chmelka, *Mol. Cryst. Liq. Cryst.*, **240**, 187, (1994).
10. K.J. Edler and J.W. White, *J. Chem. Soc., Chem. Commun.*, 155-156 (1995).
11. D. Cookson, K.J. Edler, P.A. Reynolds and J.W. White, *Journal of the Chemical Society, Faraday Transactions*, **93**, 199-202 (1997).
12. R. Ryoo, and J.M. Kim, *J. Chem. Soc., Chem. Commun.*, **711** (1995).
13. K.J. Edler, P.A. Reynolds, D. Cookson and J.W. White, *Chemistry of Materials*, **9**, 1226-1233, (1997).
14. A.S. Brown, S.A. Holt, Thien Dam, M. Trau and J.W. White, *Langmuir*, **13**(24), 6363-6365, (1997).
15. A.S. Brown, S.A. Holt, P.A. Reynolds, J. Penfold and J.W. White, *Langmuir*, **14** (19), 5532-5538, (1998).
16. I.A. Aksay, M. Trau, S. Manne, I. Honma, N. Yao, L. Zhou, P. Fenter, P.M. Eisenberger, S.M. Gruner, *Science*, **273**, 892 (1996).
17. H. Yang, N. Coombs, G.A. Ozin, *Journal of Materials Chemistry*, **8**, 1205 (1998).
18. J. Penfold, R.M. Richardson, A. Zarbakhsh, J.R.P. Webster, D.G. Bucknall, A.R. Rennie, R.A.L. Jones, T. Cosgrove, R.K. Thomas, J.S. Higgins, P.D.I. Fletcher, E. Dickinson, S.J. Roser, I.A. McLure, A.R. Hillman, R.W. Richards, E.J. Staples, A.N. Burgess, E.A. Simister and J.W. White, *J. Chem. Soc., Faraday Trans.*, **93**(22), 3899-3917, (1997).
19. J.L. Ruggles*, S.A. Holt, P.A. Reynolds and J.W. White. Submitted to *Langmuir*, (1999).
20. G. Xu, N. Yao, I.A. Aksay and J.T. Groves, *J. Amer. Chem. Soc.*, **120**, 11977-11985, (1998).
21. K.J. Edler, J. Dougherty, R. Durand, L. Iton, G. Kirton, G. Lockhart, Z. Wang, R. Withers and J.W. White, *Colloids and Surfaces*, **102**, 213-230 (1995).
22. J.D. Bernal and I. Fankuchen, *J. Gen., Physiol.*, **25**, 111, (1941).
23. M. Trau, Private Communication (1998).

APPLICATIONS OF X-RAY AND NEUTRON METHODS TO POROUS MANGANESE OXIDE SYSTEMS

Steven L. Suib¹, Wei Tong¹, Stephanie L. Brock², Jaya Nair², Volker Urban³, and Pappannan Thiagarajan³

¹Department of Chemistry, University of Connecticut, U-60, Storrs, CT 06269-3060,
²Department of Chemistry, Wayne State University, 5101 Cass Avenue, Detroit, MI 48202, ³Intense Pulsed Neutron Source Division, Argonne National Laboratory, 9700 South Cass Avenue, Argonne, Illinois 60439

KEYWORDS: manganese oxides, crystallization, small angle neutron scattering (SANS)

ABSTRACT

This presentation will focus on the use of X-ray and neutron methods for studying various microporous and mesoporous manganese oxide materials. The manganese oxide systems crystallize as either layered or tunnel structure systems. The initial stages of nucleation and structural phase changes that occur during aging and thermal treatment will be discussed. Both diffraction and scattering methods have been used in these systems. Complementary characterization methods include surface area, pore size distribution, scanning electron microscopy, and high resolution electron microscopy experiments.

INTRODUCTION

The synthesis of quantum size¹ porous semiconducting^{2,3} manganese oxides has been accomplished by systematically varying the nature of organic cations which are used as structure directors.⁴ One of the major precursors for preparation of manganese oxide materials is KMnO_4 , which readily reacts with organic cations. This facile set of reactions has inhibited the synthesis of porous manganese oxides that contain organic moieties. We have focused on new synthetic routes to porous manganese oxides in the absence of inorganic cations. Stable colloids of layered manganese oxide materials can be prepared from reduction of tetraalkylammonium (tetramethylammonium, tetraethylammonium, tetrapropylammonium and tetrabutylammonium) permanganate salts. Such systems are interesting because particle size can be controlled, the colloids are extremely stable at room temperature, a variety of crystalline materials can result, and the initially formed phases can be interconverted into other phases. The particle sizes can be controlled from about 15 to 200 Å which allows systematic studies of nanocrystalline phase materials. Several aspects of these materials will be discussed including synthesis, characterization, and potential applications. Other related materials that have been prepared by using surfactants in order to generate mesoporous materials will also be described. The primary methods that have been used to understand these materials are X-ray powder diffraction and small angle neutron scattering methods.

EXPERIMENTAL

Samples were prepared by pipetting small amounts of the colloidal sol onto glass slides with concomitant evaporation of solvent prior to thin film formation, or by spreading thin layers of the sol onto glass slides. A Scintag XDS-2000 diffractometer with CuK_α radiation was used to obtain diffraction data. SANS data were collected on the time-of-flight small-angle diffractometer (SAD) at the Intense Pulsed Neutron Source (IPNS) at Argonne National Laboratory.

RESULTS AND DISCUSSION

X-ray diffraction (XRD) methods were used to study the phases that formed during synthesis of the colloids and subsequent production of gels and heated gels. XRD patterns of various tetraalkylammonium cations reacted with permanganate led to production of well ordered systems after thermal treatment. The mesoporous materials typically produced broad diffraction data so that lattice parameters and structural models were developed with electron diffraction data from transmission electron microscopy methods.

The XRD data clearly show that expanded octahedral layer (OL) synthetic birnessite materials (OL-1) were produced in all cases. The originally formed colloids before heating were quite amorphous whereas thermal treatment even at mild temperatures (such as 70°C) led to production of well ordered phases.

Small angle neutron scattering (SANS) experiments clearly show that small nanoclusters of manganese oxide are formed at initial stages of reaction. We have used this information to stop the growth of such nanoclusters in order to use various size species to prepare other systems. By using SANS data for sols heated and aged to different extents it has been possible to prepare clusters of various sizes. Further support for the varying sizes of such clusters comes from UV-visible spectroscopy where growth of the clusters leads to a red shift in absorbance.

The interlayer structure of these materials shows that about 3 major types of structures can form. One structure involves intercalation of only the tetraalkylammonium cations in between the layers. Another structural type involves incorporation of the tetraalkylammonium cations as well as one layer of water molecules which increases the d-spacing between these layers. A further increase in d-spacing occurs when 2 different water layers are incorporated with the tetraalkylammonium cations in between the layers of OL-1.

The shapes of the colloids can be determined by modeling the SANS data. Several shapes were proposed and the best fit to the data analysis is a layered phase similar to OL-1. These layered disks are believed to be precursors for most of the octahedral molecular sieve (OMS) and octahedral layered materials of porous manganese oxides that have been prepared.⁵ Several other factors are in line with this observation. First of all, the most common mineral of manganese oxide is the layered structure birnessite. Synthetic birnessite with small particle sizes is OL-1, which seems to always form in syntheses of OMS and OL materials. Secondly, calorimetric studies⁶ also suggest that birnessite and OL materials have lower heats of formation than any other porous or nonporous manganese oxide mineral or synthetic material.

The mesoporous manganese oxide systems that have been prepared also seem to grow from this initial layered phase.^{7,8} Certainly other factors are important in such syntheses such as the average oxidation state of manganese, the nature of the surfactant used in the synthesis, and the solvent.

The average manganese oxidation state in these systems is often around 3.6 or 3.7 as determined by titration and X-ray absorption studies. The reduction of Mn^{4+} to Mn^{3+} and Mn^{2+} leads to mixed valency, which in turn gives rise to enhanced conductivity of these materials. The semiconducting nature of these particulates allows experiments where charging problems can occur to be done more readily. Some examples include surface analyses by Auger electron spectroscopy, X-ray photoelectron spectroscopy and morphological studies by scanning and transmission electron microscopy. Such morphological studies have confirmed the generation of layered structures, although at times fibrous structures can be observed.^{4,8}

CONCLUSIONS

XRD and SANS studies have provided a wealth of information about porous manganese oxide materials such as the nature of the size and shape of particulates, stability, thermal effects, and the mechanism of crystal growth. Such studies are in line with the generation of layered nanoclusters of manganese oxide similar to birnessite, which can grow and aggregate into other structures.

REFERENCES

1. Steigerwald, M. L.; Brus, L. E. *Acc. Chem. Res.* **1990**, *23*, 183-188.
2. Zhang, L.; Coffer, J. L.; Xu, W.; Zerda, T. W. *Chem. Mater.* **1997**, *9*, 2249-2251.
3. Counio, G.; Esnouf, S.; Gacoin, T.; Boilot, J.-P. *J. Phys. Chem.* **1996**, *100*, 20021-20026.
4. Brock, S. L.; Sanabria, M.; Suib, S. L.; Urban, Thiagarajan, Potter, D. I., *J. Phys. Chem.*, **1999**, in press.
5. Suib, S. L., *Curr. Op. Sol. State Chem.*, **1998**, *3*, 63-70.
6. Fritsch, S.; Post, J. E.; Suib, S. L.; Navrotsky, A., *Chem. Mater.*, **1998**, *10*, 474-479.
7. Tian, Z. R.; Tong, W.; Wang, J. Y.; Duan, N.; Krishnan, V. V.; Suib, S. L., *Science*, **1997**, *276*, 926-930.
8. Luo, J.; Suib, S. L., *J. Chem. Soc. Chem. Comm.*, **1997**, 1031-1032.

Jerry E. Hunt, Langqiu Xu, Randall E. Winans, and S. Seifert
Chemistry Division
Argonne National Laboratory
9700 South Cass Ave.
Argonne, IL 60439

KEYWORDS: small angle X-ray scattering, sieving, separation, MCM

ABSTRACT

We have studied the temperature stability of M41S class siliceous mesoporous materials loaded with carbonaceous material by temperature programmed small-angle X-ray scattering (TPSAXS) techniques. Results show the thermal structural instability of large pore pure silica sieve material with carbonaceous material (such as coal extracts) occluded within the pores of mesoporous 31 Å M41S materials. Unfilled pore M41S materials do not show thermal-related structural instability.

INTRODUCTION

Mesoporous silicates are attractive candidates for separations and applications in catalysis due to their high surface areas and highly ordered mesoporous (20-100 Å) nature. MCM-41 is one member of a family of highly uniform mesoporous silicate materials introduced by Mobil, whose pore size can be accurately controlled in the range 1.5 Å-10 nm.^{1,2} This recently discovered class of zeolites, more generally called, M41S, should be useful to effect size separation, act as hosts to nanoclusters, and as shape selective separation media, due to their large pore sizes. True molecular sieving on the size range of molecular and cluster types found in aggregating solutions should be possible with M41S materials by tuning the pore size.

The thermal stability is of crucial importance to the practical application of these mesoporous materials. Few reports of the thermal stability of these mesoporous materials are in the literature. Pure silica M41S is stable when heated to 850°C in air or 800°C in air with low water vapor pressure.³ However, the mesoporous structure collapses when mechanically compressed or when exposed to water vapor for long periods at room temperature.⁴ There are enormous efforts devoted to improving the stability of these materials.

In the present investigation, we have synthesized mesoporous silicate materials with a surface area of approximately 1100 m²/g and pore sizes of approximately 25 Å and 31 Å. The subject of this paper is the study of the temperature stability of these pore filled mesoporous materials as measured by small angle X-ray scattering.

EXPERIMENTAL

The SAXS instrument was constructed at ANL and used on the Basic Energy Sciences Synchrotron Radiation Center CAT undulator beamline ID-12 at the Advanced Photon Source.

Monochromatic X-rays (8.5 -23.0 keV) are scattered off the sample and collected on a 19 x 19 cm² position sensitive two-dimensional gas detector. More recent data are taken using a 9-element mosaic CCD detector (15 x 15 cm) with maximum resolution of 3000 x 3000 pixels. An advantage of this new detector is that unlike the wire detector, the full beam for the undulator can be used, which gives a factor of 1000 increase in intensity. The scattering intensity has been corrected for absorption, the empty capillary scattering, and instrument background. The differential scattering cross section has been expressed as function of the scattering vector q , which is defined as $q = (4\pi/\lambda) \sin \theta$, where λ is the wavelength of the X-rays and θ is the scattering half-angle. The value q is proportional to the inverse of the length scale (Å⁻¹). The instrument was operated with a sample-to-detector distance of 68.5 to obtain data at $0.03 < q < 0.7 \text{ Å}^{-1}$.

A quartz capillary heating apparatus was constructed to obtain a controlled heating rate under an inert atmosphere of nitrogen for in situ SAXS measurements. Quartz capillaries (1 mm) were used to sample 1 mg of M41S material. Scattering patterns were obtained as the sample is heated from 25-600 °C under a nitrogen flow system at a rate of approximately 25°/ minute.

Synthesis of MCM-41 was an approach combining the advantages of several literature works.^{2,3,5} Different chain length of surfactants, ranging from dodecyltrimethylammonium to octadecyltrimethylammonium bromide, were used as a template to construct a periodic mesophase. The silica source used was tetramethyl orthosilicate. The synthesis was carried out at room temperature in the solution of methanol and sodium hydroxide mixture. The materials were annealed at 600 °C. Pure silica versions of these zeolites were prepared to alleviate irreversible absorption by aluminum sites.

X-ray diffraction (XRD) analyses were carried out on a Rigaku Miniflex+ instrument using $\text{CuK}\alpha$ radiation, a NaI detector, a 0.05° step size, and a $0.50^\circ/2\text{min}$ scan rate. XRD and SAXS showed pore sizes of 25 Å and 31 Å for the two M41S-class zeolites.

A pyridine extract of mv bituminous Upper Freeport coal (APCS 1) of the Argonne Premium Coal Samples series was divided and stirred for one week in 31 Å and 25 Å M41S material. After filtering, the zeolite material containing the coal was extracted with methylene chloride. Approximately 25% of the coal material was recovered from each zeolite by methylene chloride extraction. Further extraction with chlorobenzene resulted in only a few additional percent of coal.

TGA-DTA (thermal gravimetric analysis and differential thermal analysis) measurements were obtained on a SDT 2960 from TA Instruments. These samples were measured against an alumina standard in a 100 mL/min O_2 flow with a temperature ramp of $10^\circ\text{C}/\text{min}$ to 800°C . The TGA data is also represented in its first-derivative or differential thermal gravimetry (DTG) format. Total organic loss were calculated by measuring the weight loss over the approximate temperature range of 200–600 °C.

RESULTS AND DISCUSSION

Small angle X-ray scattering

A typical plot of the scattering data for the two pore sizes of M41S material is shown in Figure 1. At low q ($< 0.04 \text{ Å}^{-1}$), scattering arises from the whole particle. This scattering can be related to information about the particle size, composition, and, ultimately, surface texture. The Bragg diffraction peaks give information about the internal structure of the particles, defining the nature, and packing dimensions of the channel in the mesoporous materials. The curves clearly show relatively narrow Bragg diffraction peaks associated with the hexagonal lattice. The lattice spacing d is 25 Å and 31 Å for the two materials synthesized. The relatively narrow diffraction peaks indicate good crystalline structure. The acquisition time for each data set was 0.1 sec.

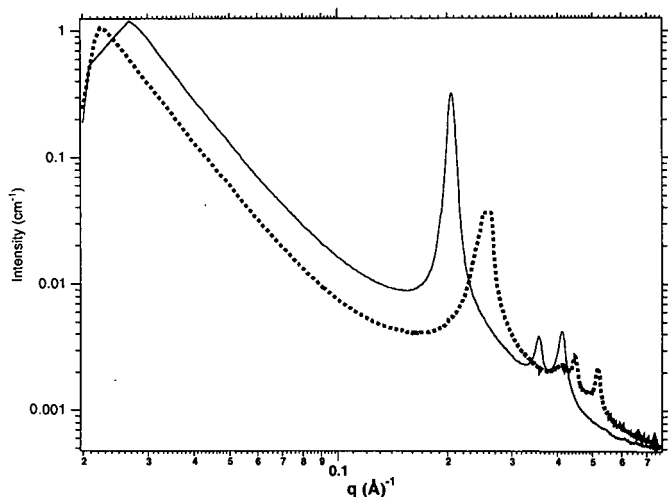


Figure 1. The small-angle X-ray scattering from 25 Å (dotted line) and 31 Å (solid line) M41S mesoporous silicate materials.

In the TPSAXS experiments, the M41S materials retain their structure even at temperatures as high as 650 °C.

When the void spaces in the M41S materials were filled with pyridine extracts from coal, the scattering is quite similar to the unfilled materials. This can be seen in comparing Figure 1 with the room temperature scattering of Figures 2 and 3. The extracts are expected to contain clusters of organic molecules which fill the pores of the M41S materials.

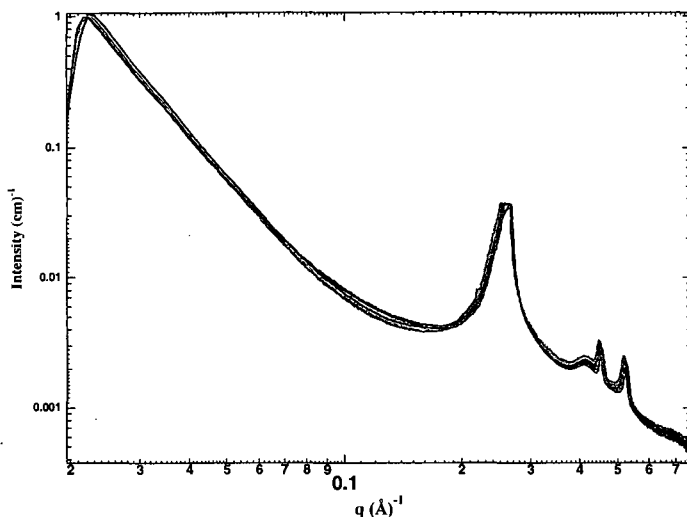


Figure 2. The temperature programmed small-angle X-ray scattering of coal extract imbibed in 25 Å M41S mesoporous material. The temperature range is from 25 °C to 600 °C.

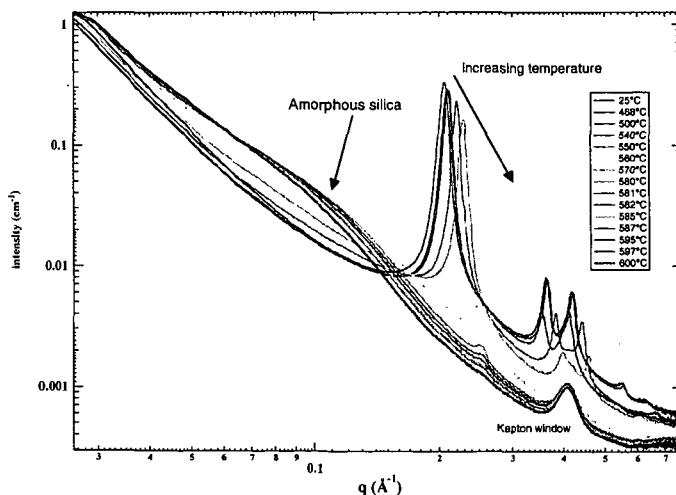


Figure 3. The temperature programmed small-angle X-ray scattering of coal extract imbibed in 31 Å M41S mesoporous material. The temperature range is from 25 °C to 600 °C.

Figure 2 shows that the mesoporous structure for the 25 Å material is maintained throughout the temperature range of 25-600 °C. The scattering is dominated by the mesoporous material and remains essentially unchanged over the entire temperature range. We used TGA to determine the weight loss as a function of temperature. From this data we can determine the total amount of organic material in the mesoporous zeolite. The TGA data shows a weight loss per cent of the total sample weight of 15.6% for the 25 Å material. The TGA indicates that very low molecular weight material is evolved at about 60 °C, which we assign to occluded pyridine. The major part of the organic material begins to come off at roughly 300 °C and peaks at 500 for the 25 Å material. In addition, there is a distinct shoulder at 520 in the 25 Å which may indicate different organic compounds or clusters of compounds.

The TPSAXS data for the 31 Å material is shown in Figure 2. The most striking feature of this data is the clear structure collapse of the mesoporous material. The 31 Å material rapidly collapses beginning around 475 °C as indicated by the decreasing Bragg diffraction peak. At the same time a large hump appears around 0.08 Å⁻¹, which we assign to amorphous silica. The structure collapses completely at 600 °C to what appears to be an amorphous silica phase. The 31 Å pore size material contains a larger amount of coal extract from the pyridine solution 22.6% for the 31 Å material versus 15.6 % for the 25 Å M41S mesoporous material. In the TGA analysis the major part of the organic material begins to come off at roughly 300 °C and peaks at 440 °C for the 31 Å material. In addition, there is a distinct shoulder at 460 in the 31 Å that may correspond to different organic compounds or clusters of compounds. A peak at 675 in the 31 Å material is only 1.5% of the total weight, but may be related to very tightly bound (very polar) organic material on the silica.

Certainly, very polar material from the coal extracts will bind to the silica. For both M41S mesoporous materials, only 25% can be removed from the zeolite by washing. The more nonpolar materials will be preferentially extracted in the washes of coal-infused M41S material leaving more tightly bound polar compounds. Mass spectrometry results show some differences in the nature of organic material in the two M41S materials. The 31 Å material has larger aromatic ring sizes than the 25 Å material.⁶

Clearly, the lower molecular weight materials (such as residual pyridine and other lower boiling point compounds) that are evolved from the M41S materials do not affect the ordered structure. However, at higher temperatures, the 31 Å material begins to decompose, while the 25 Å remains stable. There are two possibilities to consider. First, if the forces associated with thermal decomposition of the organic material are the same, then the larger pore material is less stable than the smaller. Alternatively, because data suggests that there are differences in the organic material structure, quantity, and the decomposition of the organic material, the 31 Å material may experience more stress on the structure than the 25 Å material, resulting in complete destruction of the larger mesoporous material. Further investigation of the surface structure of the mesoporous using TPSAXS is planned.

ACKNOWLEDGMENT

This work was performed under the auspices of the Office of Basic Energy Sciences, Division of Chemical Sciences, U.S. Department of Energy, and use of the Advanced Photon Source was supported by BES-DOE, all under contract number W-31-109-ENG-38. The support of the BESSRC staff is appreciated, especially J. Linton, M. Beno, G. Jennings, and M. Engbretson.

REFERENCES

1. Beck, J. S., U.S. Pat., No. 5,057,296, 1991
2. Beck, J. S.; Vartuli, J. C.; Roth, W. J.; Leonowicz, M. E.; Kresge, C. T.; Schmitt, K. D.; Chu, C. T.-W.; Olson, D. H.; Sheppard, E. W.; McCullen, J. B.; Higgins, J. B.; Schlenker, J. L., *J. Am. Chem. Soc.*, 1992, 114, 10834-43
3. Chen, C. Y.; Li, H. X.; Davis, M.E. *Microporous Mater.* 1993, 2, 17
4. For example, Tatsumi, T.; Koyano, K. A.; Tanaka, Y.; Nakata, S. *Chem. Lett.* 1997, 469.
5. Pinnavaia, T. J.; Thorpe, M. F., *Access in Nanoporous Materials*, Plenum Press: New York, 1995.
6. Hunt, J. E.; Winans, R. E.; Ahrens, M.; and Xu, L. *Prepr. Pap. - Am. Chem. Soc., Div. Fuel Chem.*, 218th ACS National Meeting, New Orleans, Aug. 22-26, 1999, pp. 610-613.

THE CRYSTALLIZATION OF HECTORITE CLAY AS MONITORED BY SMALL ANGLE X-RAY SCATTERING AND NMR

K. A. Carrado*, L. Xu, S. Seifert, D. Gregory, K. Song, R. E. Botto
Chemistry Division 200, Argonne National Laboratory
9700 South Cass Avenue, Argonne, IL 60439

KEYWORDS: clay, crystallization, small angle x-ray scattering (SAXS)

ABSTRACT

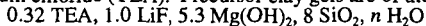
We have probed the 48-hr crystallization of a magnesium silicate clay called hectorite. Small angle x-ray scattering (SAXS) at the Advanced Photon Source using aliquots ex situ has revealed that data is consistent with ex situ XRD, TGA, AFM, and IR data in that all these techniques see clay crystallites beginning to form in the first few hours of reaction. Tetraethylammonium (TEA) ions are used to aid crystallization and become incorporated as the exchange cations within the interlayers. ^{13}C NMR shows that 80% of the final TEA loading is accomplished in the first 10 hrs. ^{29}Si NMR displays a visible clay silicate peak after just 1 hr. In addition, the first in situ study of clay crystallization of any kind was performed by in situ SAXS. Results are consistent with the ex situ data as well as showing the sensitivity of SAXS to sol gel reactions occurring on the order of minutes.

INTRODUCTION

The mechanism of formation of clays is of interest because of the use of synthetic layered silicates as heterogeneous catalyst supports and in various other technological applications. We have probed the crystallization of a magnesium silicate clay called hectorite by several ex situ (samples isolated after progressive crystallization times) techniques. For complete crystallization, heating for 48 hours at 100°C is needed. However, several techniques have revealed that significant clay growth occurs in the first few hours of hydrothermal treatment. Evidence of clay peaks in XRD occurs after just 4 hours of hydrothermal treatment, and $\text{Mg}(\text{OH})_2$ is no longer observable by XRD after 14 hours; observable changes in DTG and IR occur at about 4-6 hours as well [1]. From AFM results [2], Ostwald ripening is apparent in this system in certain time frames. Most noticeably at 4 hours but still at 8 hours, nucleation of the clay crystallites is occurring. Between 8 and 14 hours, the nucleation is complete, as evidenced by the unimodal distribution of lengths and heights in the 14 hour sample. At times longer than 14 hours, particles appear to simply coalesce and form substantially larger aggregate particles. We have now exploited both small angle x-ray scattering (SAXS) and solid state NMR to access different size regimes, length scales, and timeframes, to add information to the overall scenario of a clay crystallization mechanism.

EXPERIMENTAL

The typical method for in situ hydrothermal crystallization of organo-hectorite clays is to create a 2 wt% gel of silica sol, magnesium hydroxide sol, lithium fluoride, and organic in water, and to reflux for 2 days. Complete details can be found elsewhere [1-3]. Reagents were purchased from Aldrich. The organic of choice for crystallization studies is tetraethylammonium chloride (TEA). Precursor clay gels are of the composition:



to correlate with the ideal hectorite composition [4] of $\text{Ex}_{0.66}[\text{Li}_{0.66}\text{Mg}_{5.34}\text{Si}_8(\text{OH},\text{F})_4]$, where Ex = exchangeable cation (Ex = Li, TEA from this gel). A typical (scaled-down) reaction begins by dissolving 0.72 mmol of TEA in water and adding 4.8 mmol LiF with stirring. Separately, 24 mmol $\text{MgCl}_2 \cdot 6\text{H}_2\text{O}$ is dissolved in water and mixed with 32 ml of 2 N NH_4OH to crystallize fresh $\text{Mg}(\text{OH})_2$. Prior to use, this brucite source must be washed several times with water to remove excess ions. It is then added wet to the organic-LiF solution. This slurry is stirred for about 15 minutes before addition of 0.036 mol silica sol (ludox HS-30, Na⁺-stabilized, 30%). This mixture is refluxed for up to 48 hr then centrifuged and the products are washed and air-dried. Small aliquots for ex situ time-resolved studies are removed at various times during the crystallization.

The SAXS instrument was constructed at ANL and used on the Basic Energy Sciences Synchrotron Radiation Center CAT undulator beamline ID-12 at the Advanced Photon Source [5,6]. For ex situ powder studies, the same powders as were used for the NMR analyses were sprinkled onto and sealed in scotch tape "cells". For the ex situ gel studies, wet aliquots were concentrated (via centrifugation) and transferred to 1.5 mm quartz capillaries. The SAXS data were collected in 5 minutes exposures (scans). Controls of pure silica and brucite sols (diluted to appropriate concentrations) were also run in

capillaries. For the in situ study, a small portion of unreacted clay gel was transferred to a 1.5 mm quartz capillary and sealed (the gel was first pre-concentrated by 75%). This capillary was placed in a home-built furnace assembly such that the gel was directly in the beam path. Temperature was computer-controlled; scanning began at 70°C, which took only 3-4 minutes to reach. Within 5 minutes the temperature had reached 100°C and held at $\pm 1^\circ\text{C}$ for the duration of the run. SAXS data were collected in 2 min scans divided by 5 μsec for the first 2 hrs, then as 10 min scans for the remaining 10 hrs. Monochromatic x-rays at 10.0 keV were scattered off the sample and collected on a $19 \times 19 \text{ cm}^2$ position sensitive two-dimensional gas detector. The scattered intensity has been corrected for absorption, scattering from a blank capillary containing only water (or scattering from blank scotch tape for the powder studies), and instrument background. The differential scattering cross section can be expressed as a function of the scattering vector Q , which is defined as: $Q = 4\pi (\sin \theta) / \lambda$, where λ is the wavelength of the x-rays and θ is the scattering half angle. The value of Q is proportional to the inverse of the length scale (\AA^{-1}). The instrument was operated at a sample-to-detector distance of 67.0 cm to obtain data at $0.04 < Q < 0.7 \text{ \AA}^{-1}$. Mylar windows were used because mylar does not have diffraction peaks in this Q range.

NMR data were acquired on a Bruker Advance DSX-200 spectrometer operating at a ^{13}C Larmor frequency of 50.3 MHz. A Bruker 7mm MAS probe and a simple 90° -pulse-acquire experiment was used for all experiments. Sample spinning was maintained at $4000 \pm 2 \text{ Hz}$. Data were acquired in the presence of proton decoupling with proton power set to 80 kHz. The 90° -pulse times were 6.5 and 7.0 μs for ^{13}C and ^{29}Si , respectively. Recycle delays were 3 and 200 sec for ^{13}C and ^{29}Si experiments respectively. The number of transients recorded were 2400 and 128 for ^{13}C and ^{29}Si spectra, respectively. All spectra were referenced to TMS. Hexamethylbenzene was used as a secondary reference for ^{13}C spectra, and TKS was used as a secondary reference for ^{29}Si spectra [7]. All samples were packed to the same level in the rotor. However, because of variations in density, the sample weight varied from 114 to 153 mg. Thus, the data points in Figure 4 were normalized by weight. No attempt was made to normalize the spectra in the stacked plot (Figure 3).

RESULTS AND DISCUSSION

Results from SAXS using aliquots ex situ show, first, that data for both isolated dried powders and the wet gels are consistent with each other. This has implications for SAXS sample preparation in that, for convenience, either form (wet or dry) can be used. Figure 1 shows the data from the gels. Scattering from the starting material silica sol (seen at about 0.08 \AA^{-1}) gradually disappears as the clay crystallizes and scatters in the basal spacing region (0.4 \AA^{-1} , 15 \AA). This phenomenon is visibly evident at about 6 hrs. High background levels in this high- q region that are probably due to brucite scattering (as seen in the control sample that was measured) disappear sooner, between 1 and 4 hrs. This data is consistent with ex situ XRD, TGA, and IR data in that all these techniques see clay crystallites beginning to form after about 4 hrs of reaction.

In addition, the first in situ study of clay crystallization of any kind was performed by in situ SAXS. These data are shown in Figure 2 with only a few representative curves displayed. Results are consistent with the ex situ data. There is background scatter in this high- q basal spacing region well past the 4 hr point in at which it disappears for ex situ samples. It is suspected that this is due to the overall weak intensity of the signal due to a low concentration of clay in the beam (note the low intensity at $q = 0.04 \text{ \AA}^{-1}$, especially as time progresses).

Tetraethylammonium (TEA) ions are used to aid crystallization, and they become incorporated as the exchange cations within the interlayers. Figure 3 displays the ^{13}C NMR plots of several powder aliquots with the methyl and methylene peaks of TEA clearly growing in with time. In fact, this technique is so sensitive that in as little as 30-60 minutes there is enough TEA incorporation to be visible. A plot of the normalized signal (by weight) with reaction time shows that 80% of the final TEA loading is accomplished in the first 10 hrs (see Figure 4), after which the incorporation occurs at a much slower rate. This is in agreement with AFM results [2], where Ostwald ripening is apparent in this system only in certain time frames. Most noticeably at 4 hours but still at 8 hours, nucleation of the clay crystallites is occurring. Between 8 and 14 hours, the nucleation is complete, as evidenced by the unimodal distribution of lengths and heights in the 14 hour sample. At times longer than 14 hours, particles appear to simply coalesce and form substantially larger aggregate particles. ^{29}Si NMR displays a visible clay silicate peak after just 1 hr, which increases as the silica peak decreases up to 48 hrs (figure not shown).

CONCLUSIONS

The ^{13}C NMR data presented here has allowed us to nearly pinpoint the time at which clay crystallites stop nucleating and begin to simply accrete and coalesce. Previous AFM studies had indicated that this occurred between 8 and 14 hours for the hectorite system. After 10 hours, ^{13}C NMR shows that 80% of the TEA has been incorporated in a linear fashion. This may mean that just one mechanism is active during the early stages of nucleation and crystallization. Between 10 and 14 hours there is a clear break in the NMR data of TEA uptake, after which AFM has shown that primarily agglomeration of particles is taking place. The SAXS data are in agreement with all other methods in terms of visible tracking of clay nuclei. The in situ SAXS data, since they are in agreement with ex situ data, confirm that vital information is not lost by isolating aliquots at various times for analysis. In addition, careful analysis of these SAXS curves in the future should yield information on changes occurring on the timescale of minutes.

ACKNOWLEDGEMENTS

R. E. Winans, M. Beno, and J. Linton of ANL are recognized for their help with various SAXS experimental details, as are P. Thiyagarajan and K. Littrell of ANL for devising the SAXS data analysis packages. J. Gregar of ANL sealed the SAXS sample cells for in situ heating. This research was performed under the auspices of the U.S. Dept. of Energy, Office of Basic Energy Sciences, Division of Chemical Sciences under contract number W-31-109-ENG-38, and benefitted from the use of the APS at ANL.

REFERENCES

1. K. A. Carrado, P. Thiyagarajan, K. Song, "A study of organo-hectorite clay crystallization", *Clay Minerals* **1997**, *32*, 29-40.
2. K. A. Carrado, G. W. Zajac, K. Song, J. R. Brenner, "Crystal growth of organo-hectorite clay as revealed by atomic force microscopy", *Langmuir* **1997**, *13*, 2895-2902.
3. K. A. Carrado, "Synthetic organo- and polymer-clays: preparation, characterization, and materials applications", *Applied Clay Science* **1999**, in press.
4. R. E. Grim, *Clay Mineralogy*, 1968. McGraw-Hill: NY, p. 68.
5. R. E. Winans, S. Seifert, P. Thiyagarajan, "Time resolved small angle x-ray scattering reactivity studies on coals, asphaltenes, and polymers", *Am. Chem. Soc. Div. Fuel Chem. Prepr.* **1999**, *44*, 576-580.
6. For a full description of the instrument see <http://www.bessrc.aps.anl>.
7. J. V. Muntean, L. M. Stock, R. E. Botto, "Tetrakis(trimethylsilyl) silane: a suitable standard for solid state NMR spectroscopy", *J. Magn. Reson.* **1988**, *76*, 540-542.

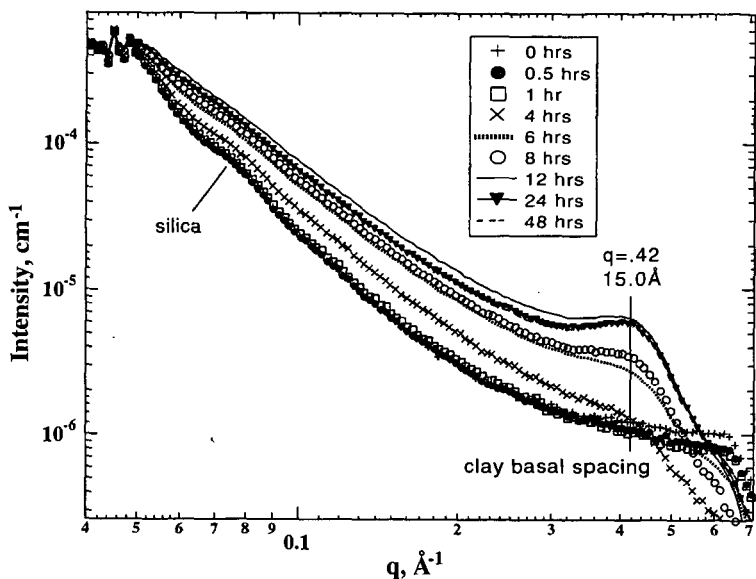


Figure 1. SAXS of ex situ synthetic TEA-hectorite gel aliquots taken at various times indicated in the legend.

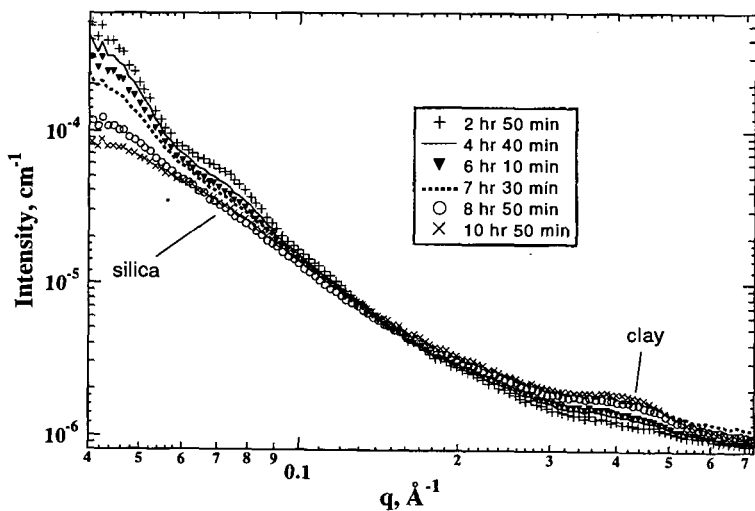


Figure 2. SAXS of in situ TEA-hectorite gel during crystallization at early stages. Only a few selected plots are shown for clarity as detailed in the legend.

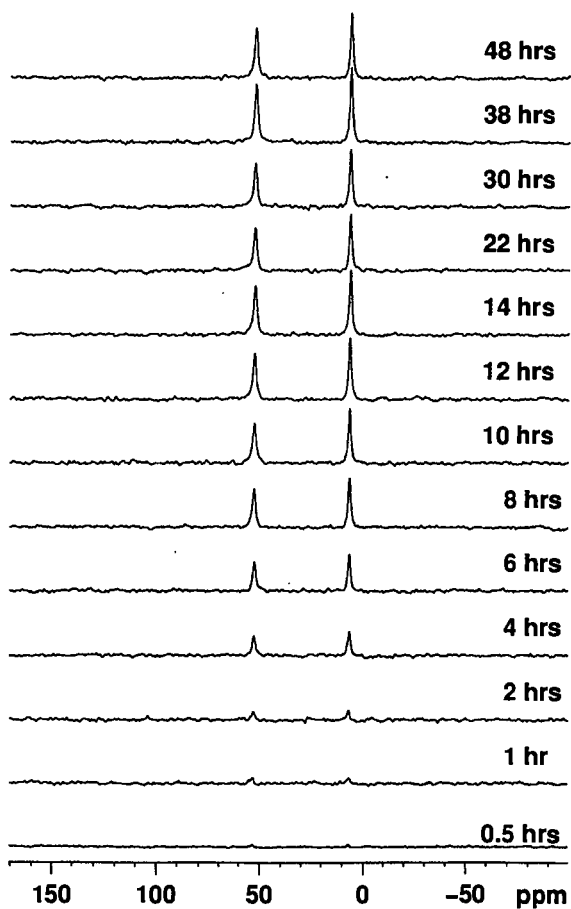


Figure 3. Solid state ^{13}C NMR of the CH_3^- and $-\text{CH}_2^-$ TEA peaks during crystallization of TEA-hectorite (ex situ).

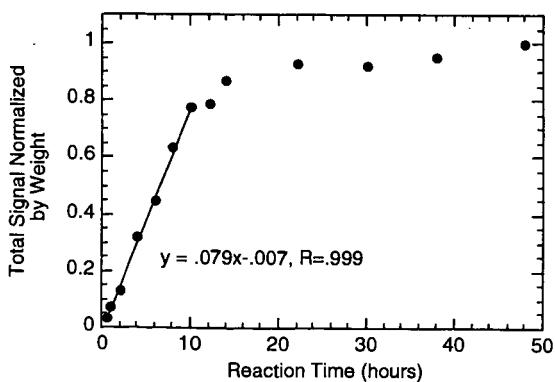


Figure 4. Correlation of TEA ^{13}C NMR signal intensity vs. reaction time during the crystallization of TEA-hectorite.

X-RAY STUDIES OF METAL – SUPPORT INTERACTIONS IN CATALYSTS

J. Lynch, O. Ducreux, D. Uzio, B. Rebours
Institut Français du Pétrole
1 & 4 Avenue de Bois Préau
92852 Reuil Malmaison Cedex
France

KEYWORDS : EXAFS, X-ray diffraction, catalysts

INTRODUCTION

The support plays a number of roles in supported metal heterogeneous catalysts. Besides assuring mechanical integrity of the system it must have an open pore structure providing access to the active phase and may also be an active component through its surface acid properties. The support may also directly affect the properties of the metal phase through what is usually classed as 'metal – support interaction'.

In the case of cobalt catalysts for the Fischer–Tropsch reaction, with metal particles several tens of nanometers in diameter, many supports have been compared. Varying conclusions have been drawn as to the effect of the support on the activity and selectivity of these catalysts. Although in a study by Bartholomew [1] the catalytic activity of supported cobalt varied in the order $\text{Co/TiO}_2 > \text{Co/SiO}_2 > \text{Co/Al}_2\text{O}_3$, Bessel [2] obtained a higher activity for alumina support than for silica while Iglesia et al. [3] found no effect on changing the support. Different activation and operating conditions were however used for these studies. Little information is available on how the support and the activation procedure influences the structure of the cobalt which forms the active phase of this type of catalyst.

The activity of alumina supported palladium catalysts, used for selective hydrogenation reactions, has been shown to reach an optimum for particle sizes of about two nanometers [4]. Although particle sizes below two nanometers would allow an increase in available surface palladium, a decrease in catalytic activity is observed. This has been attributed [5] to the loss of metallic character of the palladium atoms due to an increased effect of the metal–support interaction for small particles. Recent studies in our laboratory show that using palladium nitrite rather than the conventional palladium acetylacetonate as precursor can lead, for palladium particles of the same size, to increased catalytic activity for sub-nanometer particles. It is therefore of interest to determine the possible differences in metal–support interaction induced by changes in the precursor.

One of the major obstacles in obtaining this type of information resides in the fact that the catalysts must be studied in their reduced state. In this study the effect of the metal–support interaction on the structure of the metallic phase has been studied using two in-situ X-ray techniques : X-ray diffraction (XRD) and Extended X-ray Absorption Fine Structure (EXAFS) spectroscopy. The former is well adapted to the case of Fischer–Tropsch catalysts with a large particle size. For the small particles and metal loadings below 1% typical of hydrogenation catalysts no lines due to the metal are observed by XRD. EXAFS is particularly useful in this case as the technique is element specific and no long range order is required.

MATERIALS AND METHODS

Fischer–Tropsch catalysts were prepared by incipient wetness impregnation of TiO_2 , SiO_2 and Al_2O_3 using aqueous solutions of cobalt nitrate. The samples were dried in air and calcined at 573 K before characterisation. XRD showed that the only crystalline form of cobalt present was Co_3O_4 and the corresponding particle sizes were determined by line broadening. Details of cobalt loading, specific surface area and Co_3O_4 particle size are given in table 1.

Catalyst	Co loading (% wt.)	Specific surface area (m^2/g)	Co_3O_4 particle size (nm)
Co/TiO_2	11.3	16	75
Co/SiO_2	13.0	460	14
$\text{Co/Al}_2\text{O}_3$	10.5	180	20

Table 1 : Characteristics of the cobalt catalysts

Supported palladium catalysts with a metal loading of 0.3 % wt. were prepared by incipient wetness impregnation of alumina ($130 \text{ m}^2/\text{g}$) using palladium bis-acetylacetonate in toluene (this solid is referred to as $\text{Pd}[\text{acac}]$) or a mixture of palladium nitrate and sodium nitrite with a 1:4

molar ratio of Pd/NO₂ (referred to as Pd[NO₂]). After drying the solids were calcined at 623K. Transmission electron microscopy studies showed no evidence for particle sizes greater than 1 nm in both cases.

XRD studies of Co/SiO₂ and Co/Al₂O₃ were carried out using Cu (K α) radiation on a Siemens D501 $\Theta - 2\Theta$ powder diffractometer equipped with an Anton Parr reaction chamber adapted to allow Fischer-Tropsch reactions to be carried out [6]. Reduction studies were carried out under hydrogen flow, ramping the temperature up to the desired value at 5K/min then keeping the temperature stable during XRD analysis (4 hrs). CO conversion data was obtained in-situ at 473K using synthesis gas (H₂/CO = 9, 3 bar, 8.5 g.h.l⁻¹). The silica support is amorphous allowing the XRD pattern due to cobalt phases to be clearly identified. For the poorly crystallised alumina sample an XRD pattern of the support without cobalt was subtracted after normalisation. In the case of Co/TiO₂ the presence of many sharp lines from the support (rutile and anatase forms) prevents the cobalt phases from being correctly analysed. This sample was studied using the anomalous diffraction effect at the Laboratoire pour l'Utilisation de Rayonnement Electromagnétique (LURE, Orsay) on the H10 beam line using synchrotron radiation from the DCI storage ring running at 1.85 GeV with an average current of 250 mA. The difference pattern of XRD data recorded at energies far from (7614 eV) and close to (7715 eV) the cobalt K edge allowed the cobalt phases to be isolated.

EXAFS data for the Pd catalysts were obtained on the EXAFS4 beam line at LURE, in transmission mode through a double crystal Si(111) monochromator using two ion chambers as detectors. The EXAFS reactor cell, identical to that designed by Lytle et al. [7], allows *in situ* treatment of samples at temperatures up to 773 K. The sample was reduced under flowing hydrogen using a temperature program (5K/min). The Pd K-edge region was analysed using a standard data analysis package [8]. For analysis of local environment, the EXAFS was first transformed from k space to r space (k³, Hamming windows 2.8, 4.3, 11.3, 12.7 Å⁻¹) to obtain the radial distribution function (RDF). The EXAFS spectrum for the first co-ordination shells was isolated by inverse Fourier transform of the RDF over the appropriate region and fitted using the single scattering EXAFS equation. Amplitude and phase functions for fitting Pd-O and Pd-Pd shells were obtained respectively from Pd(acac) and Pd metal foil references.

Pd catalysts were tested for buta-1,3-diene hydrogenation in a laboratory batch reactor at 10 bar, 290K with gas chromatography analysis of products.

RESULTS

a) cobalt catalysts

Reduction of the Co₃O₄ phase under hydrogen proceeds via the formation of CoO to the formation of metallic cobalt [6]. The XRD pattern after reduction at 773K shows the presence of both fcc and hcp forms of cobalt. Comparing the XRD patterns of the Co/SiO₂ and Co/Al₂O₃ catalysts at a 673K (figure 1) shows that the degree of reduction differs for the different supports.

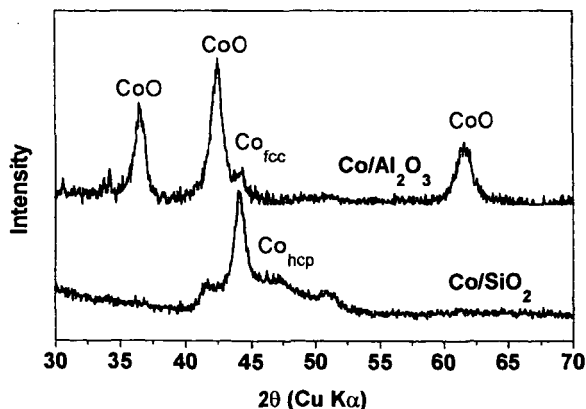


Figure 1 : In-situ XRD patterns of Co/SiO₂ and Co/Al₂O₃ at 673K under hydrogen

The silica supported catalyst is more strongly reduced at 673K than the $\text{Co}/\text{Al}_2\text{O}_3$ sample. This is in agreement with temperature programmed reduction studies showing that Co/SiO_2 is fully reduced at this temperature whereas $\text{Co}/\text{Al}_2\text{O}_3$ shows (as does Co/TiO_2) hydrogen consumption up to much higher temperatures.

The support also has an influence on the relative intensities of the diffraction peaks corresponding to the two forms of metallic cobalt (figure 2). The samples in which the cobalt is reduced only at higher temperatures show an increased proportion of fcc structure compared to hcp cobalt.

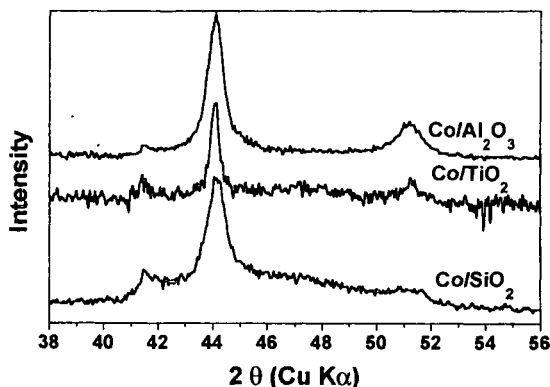


Figure 2 : XRD patterns of the cobalt catalysts reduced at 873 K

Carrying out the Fischer-Tropsch reaction in the XRD cell showed a CO conversion at 50 hrs time on stream of 25% for Co/SiO_2 whereas those of $\text{Co}/\text{Al}_2\text{O}_3$ and Co/TiO_2 were 15% and 14% respectively. On the working hypothesis that the reduction temperature was related to the cobalt microstructure developed, protocols were developed to modify the reduction temperature for a given support. By heating the calcined samples in nitrogen it was possible to stabilise the CoO form on silica at high temperature (823 K). Introducing hydrogen at this temperature provoked the reduction of CoO to metallic cobalt. It was indeed found that reduction at high temperature led to the preferential formation of fcc form. A lowering of the reduction temperature was achieved by adding ruthenium to Co/SiO_2 (impregnation of the calcined sample with ruthenium nitrate in aqueous solution to a loading of 0.3% wt). This sample was found to be fully reduced at 673 K with a majority of hcp cobalt. Figure 3 compares the structures obtained for Co/SiO_2 using these two protocols with that obtained by reduction under hydrogen. Modifying the temperature at which the metallic cobalt is formed clearly leads to controlled variation of the microstructure.

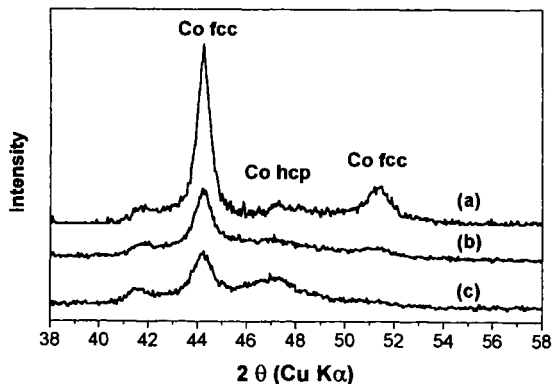


Figure 3 : Comparison of cobalt forms for Co/SiO_2 for (a) high, (b) medium and (c) low temperature reduction protocols.

Activities for the conversion of CO in the Fischer-Tropsch reaction of Co/SiO₂ samples containing different fcc/hcp ratios were significantly different. Promoted Co/SiO₂ (with a high hcp component) showed a two-fold gain in activity compared with Co/SiO₂ whereas the high temperature fcc form showed a two-fold reduction in CO conversion.

b) palladium catalysts

After reduction the sample Pd[NO₂] shows an EXAFS spectrum very similar to Pd metal foil, but of reduced intensity (figure 4). Modelling of the filtered data (inverse Fourier transform window : 1.5 to 3.0 Å) allows the average number of first nearest neighbours to be estimated as 5 +/-1, consistent with the existence of particles less than one nanometer in diameter.

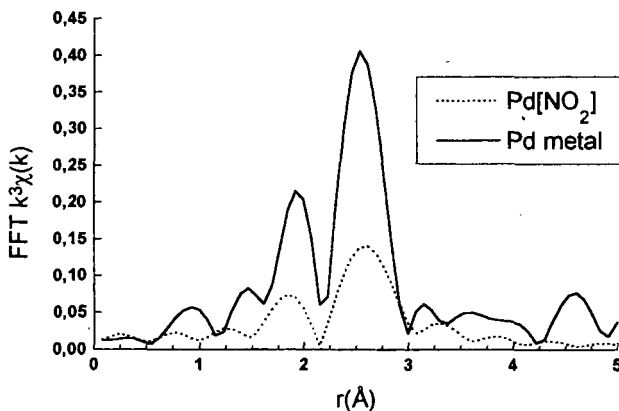


Figure 4 : RDF of the Pd[NO₂] catalyst compared to that of a Pd metal foil

The RDF of the Pd[Acac] sample is compared with that of Pd[NO₂] in figure 5. The Fourier transformed data clearly shows, in addition to Pd-Pd neighbours, a peak at low distances for Pd[Acac]. Modelling of the filtered data (inverse Fourier transform window : 0.95 to 3.0 Å) reveals this peak to be due to oxygen atoms, the average Pd-O co-ordination number being three at a distance of 1.95 Å. Pd-Pd co-ordination is similar so that particle size can be considered practically unchanged.

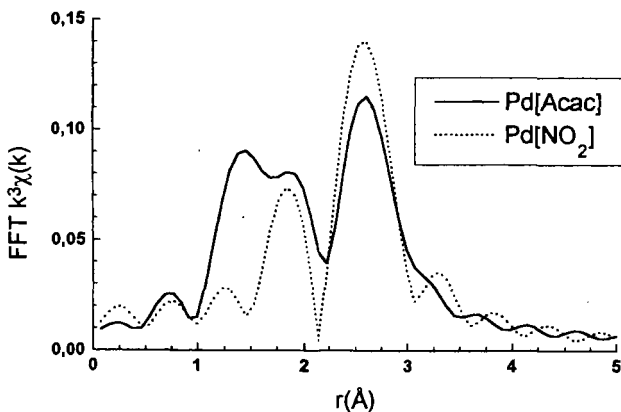


Figure 5 : Comparison of RDFs of the Pd[NO₂] and Pd[Acac] catalysts.

Buta-1,3-diene hydrogenation tests showed that the activity of the Pd[NO₂] catalysts for conversion to butene, 14 mole/min/g(Pd), was over ten times that of the Pd[Acac] catalysts, 1.2 mole/min/g(Pd), with an activity per surface Pd atom close to that obtained by Boitiaux et al. [4] for large palladium particles.

DISCUSSION

In the case of cobalt based Fischer-Tropsch catalysts the support clearly influences both the reducibility of the precursor oxide and the structure of the metal phase obtained after reduction. Our study shows that these effects are linked, and that it is the temperature of reduction that determines the fraction of different cobalt structures in the active catalyst. Modification of the reduction temperature by stabilising the intermediate oxide to high temperatures or by adding a promoter to induce reduction at low temperature enables the microstructure to be controlled. Thus, although it is not yet clear how the various oxide supports influence the temperature of reduction, the parameters controlling the activity of the final catalyst should probably be considered in the light of an oxide-support rather than a metal-support interaction. The catalytic results show that differing ratios of the two cobalt phases, fcc and hcp, lead to differing activities in the conversion of CO. Further work is required to investigate whether the differences can be attributed to intrinsic activities of the two phases or if, as suggested by Srinivisan et al. [9], it is the presence of defects induced by the presence of stacking faults in the cobalt particles that generates the active sites.

The X-ray absorption results for the Pd[NO₂] sample show the palladium in reduced samples to be in an environment close to that of bulk metallic palladium. Although the Pd-Pd co-ordination number is reduced due to the small particle size, no evidence of a well defined particle-support interaction is observed. It is clear on the contrary that the palladium in the Pd[acac] sample is in strong interaction with the support. Comparison of the catalytic results of the two systems clearly demonstrates that for conventional methods of preparation it is the metal-support interaction which leads to a reduction of activity in the case of small particles. The small Pd[NO₂] particles show similar activity to large particles for which the metal-support interaction would be diluted.

CONCLUSIONS

In-situ XRD and EXAFS have allowed the microstructure of catalysts in the active state to be characterised and give an insight into the parameters controlling the activity of the metallic phase. In the case of large cobalt particles, XRD shows differences in microstructure as a function of the support that can be rationalised in terms of reduction temperature. This has allowed protocols to be defined that lead to controlled microstructures whose presence can be directly correlated to activity in Fischer-Tropsch synthesis. EXAFS studies of small palladium particles demonstrate that the activity of hydrogenation catalysts can be clearly linked to the presence or absence of metal-support interaction. Control of this interaction can lead to higher activities for small particles and thus to more efficient catalysts.

ACKNOWLEDGEMENTS

This work was partly supported by a grant from the European Union (contract N° JOF3-CT95-0016). The authors are grateful to D. Bazin and M. Gaillanou (L.U.R.E., Orsay) for assistance in EXAFS and anomalous XRD experiments.

REFERENCES

- 1 C. H. Bartholomew, *Catal. Lett.*, **7**, (1990), 27-52
- 2 S. Bessel, *Appl. Catal.*, **96**, (1993) 253-268
- 3 E. Iglesia, S. L. Soled and R. A. Fiato, *J. Catal.*, **137**, (1992) 212-224
- 4 J. P. Boitiaux, J. Cosyns, E. Robert, *Appl. Catal.*, **345**, (1987) 193-209
- 5 J. C. Bertolini, P. Delichère, B. C. Khandra, J. Massardier, C. Noupa and B. Tardy, *Catal. Lett.*, **6**, (1990) 215-224
- 6 O. Ducreux, J. Lynch, B. Rebours, M. Roy, P. Chaumette, *Studies in Surf. Sci. and Catalysis*, **119**, (1998) p. 125-130
- 7 F. W. Lytle, G.H. Via and J. H. Sinfelt, in *Synchrotron Radiation Research*, eds. H. Winick and S. Doniach, Plenum Press, New York, 1980, 401-424
- 8 A. Michalowicz A., *J. Phys. IV*, **7**, (1997), C2-235-236
- 9 R. Srinivisan, R. J. de Angelis, P. J. Reucroft, A.G. Dhere and J. Bently, *J. Catal.*, **116**, (1989) 144-163

CHARACTERIZATION OF NANOSTRUCTURED ZIRCONIA PREPARED BY HYDROLYSIS AND REVERSE MICELLE SYNTHESIS BY SMALL-ANGLE NEUTRON AND X-RAY SCATTERING

P. Thiagarajan¹, X. Li^{1,4}, K.C. Littrell¹, S. Seifert², R. Scensits³, and C.K. Loong¹.
¹Intense Pulsed Neutron Source, ²Chemistry Division, ³Materials Science Division Argonne National Laboratory, 9700 South Cass Avenue, Argonne, IL 60439,
⁴Chemical Engineering Department, University of Louisville, Louisville, KY 40292.

Keywords: Nanophase Zirconia, Reverse Micelle Synthesis, Small angle neutron and x-ray scattering

ABSTRACT

Low temperature techniques such as hydrolysis and reverse micelle syntheses provide the opportunity to determine the relationship between the structural properties and preparation conditions of zirconia powders as well as to tailor their physicochemical properties. We have performed small-angle neutron and synchrotron x-ray scattering (SANS and SAXS) experiments to study the nucleation and organization of zirconia nanoparticles via different preparation routes. First, the formation of reverse micelles in individual and mixed solutions of $(\text{ZrOCl}_2 + \text{D}_2\text{O})/\text{AOT}/\text{C}_6\text{D}_5\text{CD}_3$, and $(\text{NH}_4\text{OH} + \text{H}_2\text{O})/\text{AOT}/\text{C}_6\text{D}_5\text{CD}_3$ systems at water/AOT molar ratio of 20 was characterized. Second, the aggregation of zirconia gels obtained from the reaction of the reverse micelle solutions after heat treatments was studied. Third, the nanostructure of zirconia powders prepared by the reverse micelle method is compared with the corresponding powders prepared by hydrolysis after different heat treatments.

INTRODUCTION

Zirconia based materials are widely used as catalysts and catalytic supports by the automobile industry for the automobile-exhaust emission control. These materials offer unique combination of properties such as high surface area, good thermal stability and rich site activity. They can be prepared by a variety of novel preparation methods such as hydrolysis, sol-gel and reverse micelle synthesis. We have demonstrated that doping of zirconia with certain rare earth oxides significantly alter its microstructure and enhance its thermal stability¹. Recently, we have also investigated the structural features of a series of AOT/ H_2O /toluene reverse micelle solutions in the presence of reactants for the synthesis of zirconia nanoparticles by SANS².

The nanostructure of the zirconia powder and its thermal stability are closely related to the synthetic conditions used in the solution phase. To gain a better understanding of the structure and function relationship of zirconia we have prepared zirconia by an hydrolysis method at pH = 9.8 and a reverse micelle method in AOT/ H_2O /toluene at water/AOT ratio $w = 20$. The obtained gels were calcined at 580 °C for 2 hours in order to remove the residual hydrocarbons and water. The SEM and TEM images of the calcined zirconia powders prepared by the hydrolysis and reverse micelle methods are shown in Figs. 1A and 1B, respectively. It can be seen that the particle size in the zirconia powder from hydrolysis method is in the micrometer range, while it is in the nanometer range from the reverse micelle synthesis. Thus controlled environment used in the reverse micelle method significantly affects the nanostructure of the particles in the zirconia powder.

While TEM provides direct images of the particles in the zirconia powder, the small angle scattering techniques with either neutrons (SANS) or x-rays (SAXS) can characterize the organization of the fundamental structural units in gels, powders and solutions. The latter techniques have high sensitivity to structural features in the length scale of 1 to 50 nm. Our objectives in the present study are: 1) to obtain a structure of the particles in the solution phases used in the hydrolysis and reverse micelle methods for the zirconia synthesis by using SANS, 2) to compare the structure of the reverse micelles in deuterated toluene from SANS and that in n-heptane from SAXS at $w = 20$, and 3) to investigate the systematic changes in the nanostructure of zirconia powders prepared by the two techniques as a function of heat treatment.

MATERIALS AND METHODS

In the hydrolysis method a zirconium hydroxide gel was prepared by the addition of an aqueous ammonia solution to an aqueous solution of 0.2 M zirconium oxychloride under continuous vigorous stirring. Solutions were prepared at pH = 9.8 and the pH was adjusted by using 25 wt.% NH_4OH (Alfa) stock solution. The precipitate was washed with water and filtered several times until no Cl^- was detected in the filtrate. The gel was dried at 120 °C for 5 hours followed by calcination at 580 °C in the air to obtain the zirconia powder.

Equation 3 has been derived from model for mass-fractal aggregates⁵ of spheres of radius R , given by

$$I(Q; \xi, D_F, R) = I_{0S} \left(1 + \frac{\sin[(D_F - 1) \arctan(Q\xi)]}{(QR)^D \left(\frac{1}{Q^2 \xi^2} + 1 \right)^{\frac{D-1}{2}}} \right) P_{\text{Sphere}}(Q; R) + I_{\text{Background}}, \quad (4)$$

where I_{0S} is the intensity scattered by the fundamental spherical particle extrapolated to $Q = 0$. I_{0A} is related to I_{0S} by the expression

$$I_{0A} = I_{0S} (D_F - 1) \Gamma(D_F - 1) \left(\frac{\xi}{R} \right)^D. \quad (5)$$

This model is a valid approximation when the scattering from the form factor for the fundamental sphere is not visible or, alternately, whenever $\xi \gg R$ and $Q_{\text{max}} R \ll 1$, where Q_{max} is the value of Q at which the power-law scattering fades into the background scattering.

RESULTS AND DISCUSSION

SANS data for the reverse micelles of AOT containing D_2O , $ZrOCl_2$, NH_4OH - D_2O and Zirconia in D-toluene on absolute scale are presented in Fig. 2A. For clarity of presentation the data for the above systems were multiplied by 1, 0.1, 10 and 3, respectively. Similarly scaled SAXS data of AOT containing H_2O , $ZrOCl_2$, NH_4OH and zirconia in n-heptane are in Fig. 2B. The important features in the SANS data are the secondary peaks whose maxima occur at different Q values. In the case SAXS data the secondary peaks are not prominent.

SANS data of the reverse micelles were fitted by using equation 1 to obtain the information on the scattering length density of the core and the results are shown in Table 1. The size of the water core of AOT reverse micelles in D-toluene at $w = 20$ is influenced by its constituents. In the presence of D_2O the core radius is 18 Å with a rms spread of 4 Å, while it decreases to 8 Å in the presence of NH_4OH . The shell thickness remains around 12 Å, except for the micelle with NH_4OH . It is interesting to note that α varies from -1.43 to 0.04 consistent with the composition changes in the core. The effect of the small α values for the NH_4OH and zirconia reverse micelles can be seen in the blurred secondary peaks in the SANS data (Fig. 2A). Another important feature seen for the zirconia containing reverse micelle is the power-law scattering of $Q^{-2.16}$ in the low Q region, implying the presence of vesicles⁶.

SAXS data in Fig. 2B were modeled by using equation 1 to obtain the core radius, shell thickness and α and the results are given in Table 2. SAXS data show that the core radius is larger for the micelle with water, but it becomes smaller for the other cases. The solvent effect is significant on the size of the AOT/water reverse micelles at $w = 20$ as the radius is about 42 Å in n-toluene (SAXS) while it is 30 Å in D-toluene (SANS). Comparison of the SANS data of AOT/water reverse micelles at $w = 20$ in D-toluene and the SAXS data of reverse micelles in n-heptane indicate the strong effect of organic solvent on the reverse micelles size. This is consistent with the fact that the solvent-solute interactions in the aromatic solvents with π electrons will be stronger than that in the aliphatic solvents.

SANS data for the heat-treated zirconia powder samples from the hydrolysis and reverse micelle methods are shown in Figs. 3A and 3B. The presence of peaks in Fig. 3A implies that the zirconia particles are organized at specific distances and the movement of peak positions (Q_{max}) indicates that the particles grow with increasing temperature (Table 3). The approximate particle size ($2\pi/Q_{\text{max}}$) at 300 °C is 60 Å and grows to 423 Å at 800 °C. The power-law slope in the high Q region reaches a value of -4 at 800 °C implying that the surface of the particles became smooth.

SANS data for the zirconia powder prepared from the reverse micelle method are shown in Fig. 3B. This data exhibit power-law scattering Q^{-D} behavior in a wide Q region, but have no peaks. In the case of fractal aggregates the power-law exponent values can be used to identify the mass and surface fractals. For example, mass fractal aggregates have $1 < D < 3$, while the surface fractals will have $3 < D < 4$. The data were fitted by using equation 3 and obtained the mass fractal dimensions that vary in the range of 2.7 to 2.9 and the cut-off lengths vary in the range of 180 to 340 Å (see Table 4). Thus the zirconia from the reverse micelle method would be better for the high temperature applications than that from the hydrolysis method.

The details of the synthesis of zirconia by the reverse micelle method have been presented elsewhere². Briefly, sodium bis(2-ethylhexyl) sulphosuccinate (AOT) was dissolved in toluene to form a 0.1 M solution. Deionized water was then added to form the reverse micelle with [water]/[AOT] molar ratio $w = 20$. To obtain the Zr-containing reverse micelles, appropriate amounts of 0.2 M ZrOCl_2 stock solution corresponding to $w = 20$ was added to the AOT/toluene solution. Similarly, ammonium hydroxide was added to AOT/toluene solution to achieve $w = 20$. All solutions were stirred continuously during the formation of reverse micelles. Subsequently, the Zr- and ammonium-containing solutions of the same w value were mixed and stirred for 20 minutes at room temperature to ensure equilibrium.

SANS experiments were carried out at the time-of-flight small-angle neutron diffractometer (SAND) at the Intense Pulsed Neutron Source of Argonne National Laboratory. This instrument provides a useful range of wave vectors ($Q = 4\pi\sin(\theta)/\lambda$, where θ is half the scattering angle and λ is the neutron wavelength) of $0.0035 - 0.6 \text{ \AA}^{-1}$ in a single measurement. In order to obtain the best contrast for SANS, D_2O (Alfa) and $\text{C}_6\text{D}_5\text{CD}_3$ (Alfa, 98% D-atom) were used. The following four systems, $\text{D}_2\text{O}/\text{AOT}/\text{C}_6\text{D}_5\text{CD}_3$, ZrOCl_2 in $\text{D}_2\text{O}/\text{AOT}/\text{C}_6\text{D}_5\text{CD}_3$, NH_4OH in $\text{AOT}/\text{C}_6\text{D}_5\text{CD}_3$ and ZrOCl_2 reacted with NH_4OH in $\text{AOT}/\text{C}_6\text{D}_5\text{CD}_3$ were considered for the present study. The data were corrected following routine procedures³.

SAXS experiments on $\text{AOT}/\text{H}_2\text{O}/n$ -heptane solutions at $w = 20$ were carried out at the ASAXS instrument on the BESSRC ID-12 beam line at the Advanced Photon Source⁴ also at Argonne National Laboratory. Data were collected using a position sensitive $15 \text{ cm} \times 15 \text{ cm}$ CCD area detector and exposure times for each measurement were 1–2 seconds. A known quantity of a solution was injected into a flow cell using motorized syringes that can position the sample into the 1.5 mm diameter cylindrical capillary tube viewed by the x-ray beam. The sample to detector distance was 0.7 m and the energy of x-ray radiation was set at 13.5 keV .

DATA ANALYSIS

The SAS data from the reverse micelle samples were analyzed by using the core-shell model given in equation 1. In this equation the variables, r , T and α are the core radius, thickness and the ratio of scattering length density difference between the core and shell to that between the shell and the solvent, respectively. The neutron scattering length densities of D_2O , AOT and D-toluene are $6.336 \times 10^{10} \text{ cm}^{-2}$, $0.62 \times 10^{10} \text{ cm}^{-2}$ and $5.644 \times 10^{10} \text{ cm}^{-2}$ respectively. The x-rays are scattered by the electrons and the scattering length densities of H_2O , AOT and n -heptane are $9.36 \times 10^{10} \text{ cm}^{-2}$, $10 \times 10^{10} \text{ cm}^{-2}$ and $6.64 \times 10^{10} \text{ cm}^{-2}$ respectively. The scattered intensity can be expressed as

$$I(Q) = nP(Q)S(Q) \quad (1)$$

where n is the number density of the reverse micelles, $P(Q)$ is the form factor and $S(Q)$ is the inter-particle structure factor which is assumed to be 1 in this case. The form factor $P(Q)$ for a spherical shell with a polydispersity in radius with Shultz distribution is given by

$$P(Q) = \frac{\int_0^{\infty} [\sin(Q(r+T)) - Q(r+T)\cos(Q(r+T)) + \alpha(\sin(Qr) - Qr\cos(Qr))] \left(\frac{r}{r_0}\right)^{z-1} \exp\left(-\frac{zr}{r_0}\right) dr}{\int_0^{\infty} \left[(r+T)^3 + \alpha^2 \left(\frac{r}{r_0}\right)^{z-1} \exp\left(-\frac{zr}{r_0}\right) dr\right]} \quad (2)$$

where

$$\alpha = \frac{\rho_{\text{core}} - \rho_{\text{shell}}}{\rho_{\text{shell}} - \rho_{\text{solvent}}}, \quad \text{and} \quad z = \frac{r_0}{\sigma},$$

where σ is the rms core radius spread.

The SANS from the zirconia powders are fitted by using equation 3 for fractal aggregates⁵.

$$I(Q, \xi, D_f) = I_{0A} \frac{\sin[(D_f - 1)\arctan(Q\xi)]}{(D_f - 1)Q\xi(Q^2\xi^2 + 1)^{\frac{D_f - 1}{2}}} + I_{\text{Background}} \quad (3)$$

where I_{0A} is the overall intensity scattered by the aggregate extrapolated to $Q=0$, D_f is the mass-fractal dimension, ξ is the exponential cutoff length at which the system reaches the macroscopic density, and $I_{\text{Background}}$ is the background intensity.

CONCLUSIONS

SAXS and SANS are quite sensitive for the study of the nanostructure of catalytic systems. The high sensitivity of the scattering techniques can be seen from their ability to provide a number of parameters on the structure and organization of the reverse micelles. We obtained unique information on the water core that provides clues to the enhanced properties of zirconia. Coarsening occurs in zirconia powder prepared by hydrolysis method upon heat treatment, while the particles are uniform in size and do not grow upon heat treatment up to 750 °C.

ACKNOWLEDGEMENTS

This work was performed under the auspices of the Office of Basic Energy Sciences, Division of Chemical and Materials Sciences, U.S. Department of Energy, under contract number W-31-109-ENG-38. We are indebted to Randall Winans, Chemistry Division for his effort in setting up the SAXS instrument at BESSRC. The support of Jennifer Linton, Guy Jennings and Mark Beno at BESSRC and Denis Wozniak at IPNS is appreciated.

REFERENCES

1. Loong, C.K.; Thiyagarajan, P.; Richardson Jr., J.W.; Ozawa, M.; Suzuki, S. J. Catalysis 1997, 171, 498-505.
2. Li, X.; Loong, C.-K.; Thiyagarajan, P.; Lager, G.A.; Miranda, R. J. Appl. Cryst. (In Press).
3. Thiyagarajan, P.; Epperson, J.E.; Crawford, R.K.; Carpenter, J.M.; Klippert, T.E.; Wozniak, D.G. J. Appl. Cryst. 1997, 30, 280-293.
4. Seifert, S.; Winans, R.E.; Tiede, D.M.; Thiyagarajan, P. J. Appl. Cryst. (In Press)
5. Freltoft, T.; Kjems, J.; Sinha, S.K. Phys. Rev. 1986, B33, 269.
6. Ravey, J.C.; Buzier, M. J. Colloid. Interface Sci., 1987, 116, 30.

Table 1
Parameters from the Shultz Polydisperse Shell model fits of SANS of Reverse Micelles of AOT/D₂O in D-Toluene, w = 20.

Core in AOT/ D-Toluene Reverse Micelle	Core radius (Å)	RMS Core Radius Spread (Å)	Shell thickness (Å)	$(\rho_{\text{core}} - \rho_{\text{shell}}) /$ $(\rho_{\text{shell}} - \rho_{\text{solvent}})$ (α)	ρ_{core} (10 ¹⁰ cm ⁻²)
D ₂ O	18.0 ± 0.1	4.0 ± 0.1	12.0 ± 1.0	-1.143	6.36
ZrOCl ₂	10.1 ± 0.7	1.6 ± 0.2	12.0 ± 0.8	-1.019	5.73
NH ₄ OH	8.4 ± 0.4	2.3 ± 0.4	14.1 ± 0.4	-0.051	0.88
ZrO ₂	12.0 ± 2.0	2.6 ± 0.1	11.0 ± 2.0	0.040	0.42

Table 2
Parameters from the Shultz Polydisperse Shell model fits of SAXS of Reverse Micelles of AOT/H₂O in n- heptane, w = 20.

Core in AOT/ n-heptane Reverse Micelle	Core radius (Å)	RMS Core Radius Spread (Å)	Shell thickness (Å)	$(\rho_{\text{core}} - \rho_{\text{shell}}) /$ $(\rho_{\text{shell}} - \rho_{\text{solvent}})$ (α)	ρ_{core} (10 ¹⁰ cm ⁻²)
H ₂ O	30.7 ± 0.01	8.5 ± 0.01	11.3 ± 0.05	-0.328	8.90
ZrOCl ₂	11.0 ± 0.01	3.9 ± 0.01	10.7 ± 0.06	-0.520	8.25
NH ₄ OH	24.4 ± 0.01	7.8 ± 0.01	12.0 ± 0.1	-0.386	8.70
ZrO ₂	27.2 ± 0.01	8.2 ± 0.01	12.0 ± 0.1	-0.375	8.74

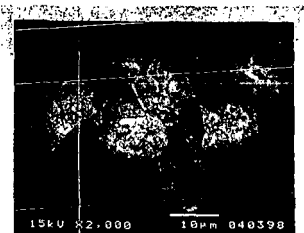
Table 3
Particle size from the SANS data of the zirconia powders prepared by the hydrolysis method upon heat treatment for 2 hours at different temperatures.

Temp. (°C)	Particle Size (Å)
300	60
400	90
500	134
600	203
700	295
800	423

Table 4

Parameters obtained from the Fractal model fit of the SANS data of the zirconia powders prepared using reverse micelle method upon heat treatment for 2 hours at different temperatures.

Temp (°C)	Fractal Dimension	Cutoff Length (Å)
100	2.7	186
200	2.7	197
300	2.7	148
400	2.9	124
550	2.93	223
750	2.9	341



(A)



(B)

Fig. 1. A) STM of calcined Zirconia powder prepared by hydrolysis method B) TEM of calcined zirconia powder prepared by reverse micelle method with H_2O/AOT $w=20$.

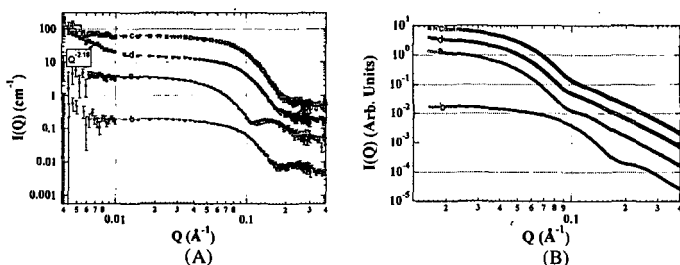


Fig.2 A) SANS of reverse micelle solutions at $w = 20$: (a) $D_2O/AOT/C_6D_5CD_3$, (b) $(ZrOCl_2 + D_2O)/AOT/C_6D_5CD_3$, (c) $(NH_4OH + H_2O)/AOT/C_6D_5CD_3$, and (d) the mixture of (b) and (c). B) SAXS of reverse micelle solutions at water/AOT molar ratio = 20: (a) $H_2O/AOT/C_7H_{16}$, (b) $(ZrOCl_2 + H_2O)/AOT/C_7H_{16}$, (c) $(NH_4OH + H_2O)/AOT/C_7H_{16}$ and (d) mixture of (b) and (c). For clarity, the absolute intensities of data a, b, c and d are multiplied by 1, 0.1, 10 and 3, respectively. Lines are the fits using equation 1 and the results from the fits of SANS and SAXS data are given in Tables 1 and 2, respectively.

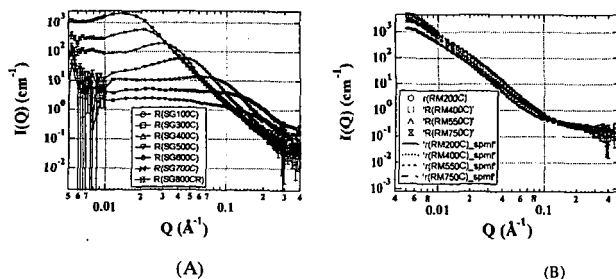


Fig. 3 SANS of ZrO_2 powders prepared by A) hydrolysis and B) reverse micelle synthesis after heat treatment at different temperatures for 2 hours. While the aggregates in ZrO_2 powders prepared by hydrolysis method shows monotonic increase in their size, those in ZrO_2 powders from reverse micelle method seem to be stable up to 750 °C.

APPROACH TO THE IRON-CATALYZED FORMATION PROCESS OF N_2 FROM HETEROCYCLIC NITROGEN IN CARBON BY USE OF XRD AND XPS METHODS

Yasuhiro Ohshima, Ye Wang, Naoto Tsubouchi, and Yasuo Ohtsuka

Research Center for Organic Resources and Materials Chemistry

Institute for Chemical Reaction Science, Tohoku University

Katahira, Aoba-ku, Sendai 980-8577, JAPAN

KEYWORDS: Fuel nitrogen, iron catalyst, X-ray diffraction analysis

ABSTRACTS

PAN-derived carbon as a model of coal char has been heated in high purity He, and the catalysis of N_2 formation by precipitated iron has been investigated by means of TEM, XPS and XRD. Nanoscale iron particles are very active for this reaction at 600 – 1000°C. The XPS and XRD analyses after heat treatment reveal that nitrogen functionality does not change significantly but carbon crystallization takes place via the dissolution of iron into the carbon substrate. The *in situ* XRD measurements during heating show the formation of solid solution of iron and nitrogen (and carbon). The iron-catalyzed conversion of heterocyclic nitrogen to N_2 probably proceeds through formation of the solid solution and subsequent decomposition into N_2 .

INTRODUCTION

The nitrogen present in coal (coal-N) is emitted as NO_x and N_2O during combustion. The NO_x has been implicated in acid rain and photochemical smog. In conventional pulverized coal-fired plants, 75 – 95 % of the NO_x emitted originates from coal-N. The N_2O is known to be involved in the green house effect and the ozone layer depletion. The concentration of N_2O is much higher in fluidized bed combustion that can be operated at lower temperatures (< 1000°C) than in pulverized coal-fired boilers. The N_2O arises from coal-N alone. When coal is fed into a combustion chamber, the devolatilization (pyrolysis) first takes place. In this process, part of coal-N is released as tar-N, and the remainder is retained as char-N, some of the tar-N being subsequently decomposed into HCN and NH_3 [1,2]. All these nitrogen species are the precursors of NO_x and N_2O . If coal-N can be converted efficiently to N_2 upon devolatilization, the emissions of NO_x and N_2O can greatly be reduced during subsequent combustion.

The present authors' group has found that FeOOH precipitated on low rank coals can drastically catalyze conversion of coal-N to N_2 in the fluidized bed pyrolysis at $\geq 750^\circ\text{C}$ [3,4]. We have also shown that Fe-containing minerals in low rank coals, probably as ion-exchanged forms, can also promote N_2 formation in the fixed bed pyrolysis at almost the same temperature range as above [5,6]. Since N_2 formation occurs dominantly after complete release of volatile-N (tar-N, HCN, and NH_3), it is strongly suggested that the iron derived from Fe-containing minerals as well as FeOOH catalyzes conversion of char-N to N_2 . However, the detailed mechanism is not clear. The present work therefore focuses on making clear the Fe-catalyzed formation process of N_2 at solid phase by using PAN-derived carbon as a model of coal char.

EXPERIMENTAL

Pure carbon without any minerals was used in place of coal char in order to avoid their influences on N_2 formation. The carbon was prepared by carbonization of PAN for 30 min at 1000°C, followed by activation in 20 vol% O_2 at 500°C. The C, H and N contents in the carbon with size fraction of 44 – 74 μm were 79.3, 0.4 and 6.8 wt%, respectively, the BET surface area determined by N_2 adsorption being 480 m^2/g . Fine particles of FeOOH were precipitated onto the carbon from an aqueous solution of FeCl₃ by using $\text{Ca}(\text{OH})_2$ [7].

The carbon (180 mg) with or without 1.9 wt% Fe was heated with a fixed-bed quartz reactor in a

stream of high purity He ($> 99.9999\%$) at $10^\circ\text{C}/\text{min}$ up to 1000°C , and N_2 evolved was determined on line at 5 min intervals with a high speed micro GC. Detailed procedures have been described elsewhere [5]. The samples before and after heat treatment were characterized by TEM, XPS and XRD. The *in situ* XRD measurements were also made with Mn-filtered $\text{Fe-K}\alpha$ radiation during heating the Fe-loaded carbon under the same conditions as above.

RESULTS AND DISCUSSION

Formation of N_2 . Figure 1 shows the temperature-programmed profiles for N_2 formation. The iron remarkably promoted conversion to N_2 at $600 - 1000^\circ\text{C}$. The catalytic effect appeared at a lower temperature of around 600°C than observed with low rank coals [3,4], probably because of a lower heating rate in the present work. The rate of N_2 formation reached the maximal value at 800°C and then decreased. The rate at 800°C with $1.9\text{ wt}\%$ Fe was about 10 times that without catalyst. The presence of the iron almost doubled N_2 yield after 60 min soaking at 1000°C , the yield being 32 and 63 % without and with $1.9\text{ wt}\%$ Fe, respectively.

XPS spectra. The N 1s XPS spectra were measured to examine the change in nitrogen functionality upon heat treatment, and least-squares curve fitting of the spectra was performed using Gaussian peak shapes [8]. Pyrrolic-N ($398.7 \pm 0.1\text{ eV}$), and pyridinic-N ($400.3 \pm 0.1\text{ eV}$) were the main nitrogen forms in the original carbon before heat treatment. The ratio was almost unity, which was much lower than that observed for brown coal char after pyrolysis at 900°C [8]. When the carbon with $1.9\text{ wt}\%$ Fe was heated at $600 - 1000^\circ\text{C}$, the distribution of pyrrolic-N, pyridinic-N and quaternary-N ($401.4 \pm 0.1\text{ eV}$) was significantly unchanged. This suggests that N_2 evolves from these species at almost the same rate. On the other hand, the iron precipitated on brown coal is effective for preferential formation of N_2 from pyrrolic-N [8]. The difference may be related with a larger ratio of pyrrolic-N/pyridinic-N in the latter case.

TEM observations. The average size of iron particles at 600°C , that is, before the start of N_2 formation, was as fine as 15 nm. When the iron was precipitated onto PAN-derived carbon without O_2 -activation in the same manner as above, the average particle size was much larger (70 nm), and the iron was less active. The activation increased not only the surface area but also the amount of oxygen functional groups, which lead to the formation of the more highly dispersed iron on the activated carbon. The average size increased from the initial 15 nm to 23 nm after heat treatment at 1000°C . In the size distribution, most of iron particles were initially $\leq 20\text{ nm}$ in size, whereas more than half of them were $\geq 20\text{ nm}$ at 1000°C , and the iron with the size of 40 – 60 nm was also observed. These observations show that iron particles move within the carbon matrix, catalyze N_2 formation, and agglomerate in this process.

XRD measurements. Figure 2 shows the XRD profiles for Fe-bearing samples cooled to room temperature after heat treatment. At 600°C , the small peaks of magnetite (Fe_3O_4) and wustite (Fe_{1-x}O) were observed, which means the transformation of the initial form of FeOOH to these oxide forms. At 1000°C , the oxide species disappeared, and instead the XRD lines of metallic iron ($\alpha\text{-Fe}$) and cementite (Fe_3C) appeared. Not only the reduction to metallic iron but also the reaction of the iron with the carbon substrate took place between 600 and 1000°C . Figure 2 also provides information about carbon structures due to C(002) lines, which can be separated into amorphous and turbostratic carbon, denoted as A- and T-carbon respectively, by deconvolution. As the temperature increased, the proportion of T-carbon increased from 14 to 18 %. On the other hand, no significant change in C(002) lines was observed in the absence of the iron. The formation of cementite and T-carbon indicates that the iron first dissolves in the carbon substrate and subsequently catalyzes crystallization reactions [9]. It can readily be expected that the iron reacts with heterocyclic nitrogen forms in the carbon matrix.

Figure 3 shows the *in situ* XRD profiles during heating the carbon with $1.9\text{ wt}\%$ Fe. At 655°C , metallic iron ($\alpha\text{-Fe}$) was the dominant species, though the small peaks of wustite were also observed. Interestingly, the XRD lines of austenite, solid solution of $\gamma\text{-Fe}$ and nitrogen

(and/or carbon), existed as well. When the temperature was raised to 815 and 1025°C, the XRD intensities of this species increased with a corresponding decrease in the intensity of metallic iron, and austenite was the predominant form in this temperature region. When the sample heated at 1025°C was quenched to room temperature, metallic iron and cementite were formed, in harmony with the XRD profile given in Figure 2.

Mechanism. It should be noted that the catalysis of conversion to N_2 by iron (Figure 1) and the formation of austenite (Figure 3) occur at almost the same temperature range. According to phase diagrams of Fe-N and Fe-C [10], nitrogen can dissolve rapidly into iron at a lower temperature of about 590°C, compared with that (740°C) for carbon. The former temperature corresponded well to the onset of the Fe-catalyzed formation of N_2 . It is thus likely that the austenite observed at < 740°C is the solid solution of Fe and N, and that N_2 formation in this temperature range proceeds through the intermediate. The austenite may be transformed to iron nitrides (Fe_3N), which can readily be decomposed into N_2 because of thermal instability [8]. The austenite formed at $\geq 740^\circ\text{C}$ may be composed of Fe, N and C, and converted to Fe_3N_2C as well as Fe_3N . The decomposition of Fe_3N_2C into N_2 may involve carbon crystallization, that is, the formation of turbostratic carbon (Figure 2). The presence of such crystallized carbon might prevent iron particles from moving within the carbon matrix. As mentioned above, the TEM observations revealed that catalyst agglomeration took place in the process of N_2 formation. The lowering in both mobility and activity of iron particles may be responsible for the decreased rate of N_2 formation observed after 800°C (Figure 1).

CONCLUSIONS

Fine iron particles with the average size of 15 nm promote remarkably N_2 formation from PAN-derived carbon during heating in an inert gas at 600 – 1000°C. Catalyst agglomeration occurs in this process. The XPS spectra show that pyrrolic-N and pyridinic-N are the main forms, and that such nitrogen functionality is significantly unchanged upon heat treatment. The XRD analyses reveal the transformation of amorphous to turbostratic carbon, meaning the dissolution of the iron into the carbon substrate. Furthermore, the *in situ* XRD measurements during heating show the formation of austenite that is solid solution of iron and nitrogen (and carbon). It is likely that iron nanoparticles move in the carbon matrix and react with heterocyclic nitrogen to form the solid solution, which is subsequently decomposed into N_2 .

ACKNOWLEDGMENTS

The present work was supported in part by the Proposal-Based New Industry Creative Type Technical R&D Promotion Program from the New Energy and Industrial Technology Development Organization (NEDO), Japan. The authors acknowledge the assistance of Ms. Hazuki Satake in carrying out experiments.

REFERENCES

- 1 Davidson, R.M. In *Nitrogen in Coal*, IEAPER/08; IEA Coal Research: London, 1994.
- 2 Leppälähti, J.; Koljonen, T. *Fuel Processing Technology* 1995, 43, 1.
- 3 Ohtsuka, Y.; Mori, H.; Watanabe, T.; Asami, K. *Fuel* 1994, 73, 1093.
- 4 Mori, H.; Asami, K.; Ohtsuka, Y. *Energy Fuels* 1996, 10, 1022.
- 5 Wu, Z.; Ohtsuka, Y. *Energy Fuels* 1997, 11, 477.
- 6 Wu, Z.; Ohtsuka, Y. *Energy Fuels* 1997, 11, 902.
- 7 Ohtsuka, Y.; Asami, K. *Catalysis Today* 1997, 39, 111.
- 8 Ohtsuka, Y.; Watanabe, T.; Asami, K.; Mori, H. *Energy Fuels* 1998, 12, 1356.
- 9 Oya, A.; Marsh, H. J. *Mater. Sci.* 1982, 17, 309.
- 10 Massalski, T.B. In *Binary Alloy Phase Diagrams*; Vol. 2; ASM International: Ohio, 1990.

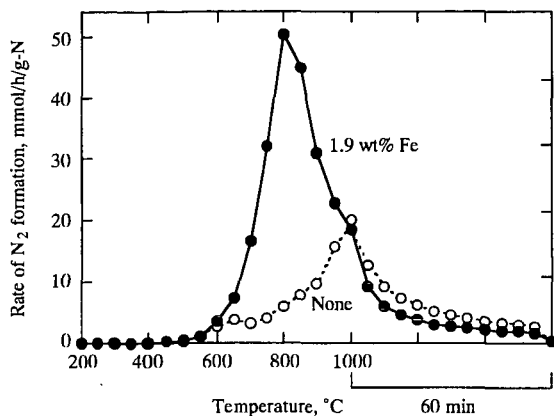


Figure 1 N_2 formation during temperature programmed heat treatment of PAN-derived carbon.

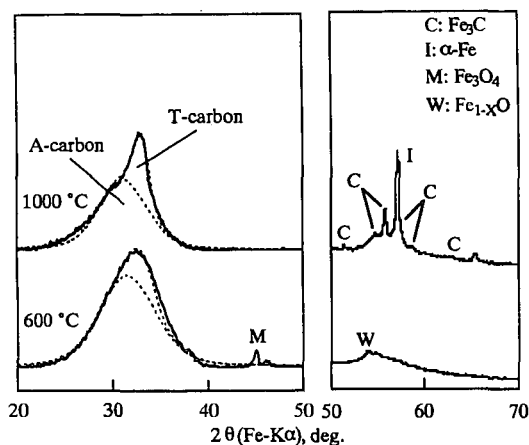


Figure 2 XRD results for Fe-bearing samples cooled to room temperature after heat treatment.

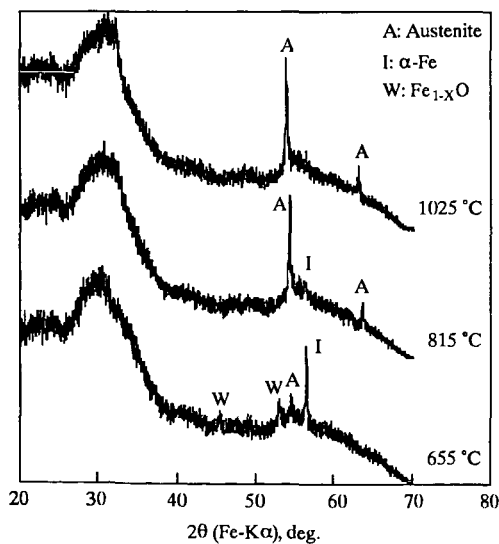


Figure 3 *In situ* XRD profiles during heating of Fe-bearing carbons.

Characterization of Peats by X-ray and NMR Methods

S. R. Kelemen, M. Afeworki and M. L. Gorbaty
Exxon Research and Engineering Company
Annandale, NJ 08801

A. D. Cohen
U. of South Carolina
Dept. of Geological and Environmental Sciences
Columbia, SC 29208

Keywords: Peat, XPS, Solid State ^{13}C NMR

X-ray photoelectron spectroscopy (XPS), X-ray absorption near edge structure (XANES) spectroscopy and solid state CP MAS ^{13}C NMR spectroscopy have proven to be viable non-destructive techniques for quantifying heteroatom functionalities in complex carbonaceous systems. Coals and kerogens have been examined extensively by these techniques. However, much less attention has been given to diagenetic stage precursors of these fossil materials. In this work, a set of eight well-defined peat samples has been examined by X-ray and NMR methods. Oxygen is by far the most abundant heteroatom species in peat derived from lignin and cellulose materials. A combination of XPS and NMR methods has been examined for quantifying organic oxygen species in peat. Total organic oxygen determined by XPS was significantly less than the amount obtained from oxygen determined by difference. XPS and NMR results confirm that carbon bonded to a single oxygen species are the predominant form in all peat samples studied and that multiply bonded carbon oxygen species make up only 25% of the oxygen population in these peat samples. The advantages of a multiple technique approach for quantifying organic oxygen forms in carbonaceous solids is discussed.

I. Introduction

X-ray and NMR are viable non-destructive techniques for quantification of organic nitrogen, sulfur and oxygen species in complex carbonaceous systems. For coal and kerogen, chemistry of heteroatom transformations is important for understanding both geological and utilization processes. Next to carbon and hydrogen, oxygen is usually the most abundant atom in organic sedimentary material. Nevertheless, determining the amount and kinds of organic oxygen species remains a formidable analytical challenge for these materials. Total organic oxygen is usually determined by difference [1]. Other methods involve fast neutron activation analysis for oxygen corrected for inorganic forms or pyrolysis followed by coulometry [1]. Infrared spectroscopy [2-4], solid-state (SS) ^{13}C NMR analysis [5] and X-ray Photoelectron Spectroscopy (XPS) [6-8] have been used to directly gain information about the kinds of organic oxygen species in coal.

Peat is a sedimentary deposit composed primarily of plant derived material and is a precursor of coal. The organic oxygen content exceeds that of coal. The physical and chemical make-up of peat varies widely and differences in organic oxygen functional group distributions are expected [9]. The present work uses a combination of XPS and SS ^{13}C NMR to quantify oxygen species in a set of eight well-defined peat samples.

II. Experimental

A) Samples

The peat samples were obtained from the peat sample bank of the University of South Carolina [9]. The elemental data for the peat samples are shown in Table 1. These peats differ significantly in composition due to the variety of source plants and depositional settings. The fresh starting coal samples were obtained in sealed ampoules from the Argonne Premium Coal Sample Program [10]. Other coal samples were obtained from the Penn State coal sample bank [11]. The elemental data for these coals are included in Table 1.

B) X-ray Photoelectron Spectroscopy

The XPS spectra were obtained with a Vacuum Generators (VG) ESCA Lab system using Al K alpha non-monochromatic radiation and a five channel detection arrangement. The samples were evacuated to remove moisture and ground into fine powders. The powders were mounted on a metallic nub via non-conducting double-sided tape. An energy correction was made to account for sample charging based on the carbon (1s) peak at 284.8 eV. The elemental concentrations are reported relative to carbon on an atomic basis, calculated from XPS spectra based on the area of the characteristic

photoelectron peaks after correcting for atomic sensitivity. The amount of organic oxygen was derived from the total oxygen (1s) signal by taking into account inorganic contributions [8]. The main inorganic elements observed via XPS are found in Table 2. For coal, the amount of each inorganic element determined by XPS may differ from the bulk inorganic elemental composition due to particle size effects and organic encapsulation [8].

The nature of the organic oxygen species present in lignite and lignin were determined by analyzing oxygen's effect on the XPS carbon (1s) signal of adjacent carbon atoms [8]. The level of carboxyl and carbonyl is derived from the curve resolved carbon (1s) spectrum. The amount of oxygen associated with carbon-oxygen single bond species is determined by subtracting the carboxyl and carbonyl oxygen levels from the total amount of organic oxygen. The relative amount of aromatic carbon was determined by the method of Π to Π^* signal intensity [12]. A complete list of XPS data for samples contained in this report is found in Table 2.

Five peaks were used to curve resolve the XPS carbon (1s) signal for peat. These occur at 284.8, 285.3, 286.3, 287.5, and 289.0 (± 0.1) eV. The 284.8 eV peak represents contributions from both aromatic and aliphatic carbon. The 286.3 eV peak (Type I) represents carbon bound to one oxygen by a single bond (e.g., C-O, C-OH etc.). The 287.5 eV peak (Type II) corresponds to carbon bound to oxygen by two oxygen bonds (C=O, O-C-O). The 289.0 eV peak (Type III) corresponds mainly to carbon bound to oxygen by three bonds (O=C-O). The 285.3 peak will have contributions mainly from carbon adjacent to carboxyl carbon (beta peak) and carbon bound to nitrogen (i.e. pyrrole, pyridinic). The 285.3 eV peak is therefore fixed to the sum of the intensity of the 289.0 eV peak and the intensity of carbon adjacent to nitrogen (i.e. twice the nitrogen level). The results shown in Table 3 assume 1) that two oxygens are associated with the Type III carbon (1s) signal and 2) that one oxygen is associated with the Type II carbon (1s) signal. The amount of oxygen associated with the Type I carbon (1s) signal is obtained by subtracting the oxygen associated with the Type II and the III carbon (1s) signal from the amount of total organic oxygen.

C) Solid State ^{13}C NMR Spectroscopy

High-resolution solid-state ^{13}C NMR measurements of peat samples were performed using a Chemagnetics CMX-200 spectrometer operating at a static magnetic field of 4.7 T (50.2 MHz ^{13}C). Peat samples were packed into a 5-mm diameter zirconia rotor and spun at 8-kHz using dry nitrogen gas. Cross-polarization magic-angle spinning (CPMAS) NMR was used to characterize the peat samples. The CPMAS experiments were performed at a ^1H - ^{13}C CP contact time of 3 ms and a pulse repetition delay of 2 seconds. The ^1H and ^{13}C radio-frequency fields for cross-polarization and the proton high power decoupling during data acquisition were at 62.5 kHz. The definition of ^{13}C NMR structural parameters and chemical shift ranges are shown in Table 4. A complete list of structural parameters obtained by solid-state ^{13}C NMR for samples contained in this report is found in Table 5.

III. Results and Discussion

The atomic H/C and O/C ratios are plotted for peat, lignite and coal in Figure 1 (called a Van Krevelan Diagram [13]). The O/C values were obtained from XPS data. All peat samples have higher H/C and O/C values than coal and lignite. These results are in good general agreement with established ordering for these materials [13]. The range of organic oxygen determined by XPS for peat is roughly between 20 and 30 oxygen per 100 carbons, (Table 3). These results are significantly lower than the amount of oxygen determined by difference, (Table 1).

A combination of XPS and SS ^{13}C NMR was used to characterize the peat samples. Figure 2 shows excellent agreement between the percent aromatic carbon determined by XPS and NMR methods. Previously published results for coal and lignite are included for comparison [12]. Not surprisingly, peat has significantly lower levels of aromatic carbon. The close correspondence between the XPS and NMR values for peat indicate that the aromatic carbon level at the surface of finely ground peat is comparable to the bulk.

XPS was used to distinguish the kinds of organic oxygen species present in peat. Table 3 shows the results based on the methodology described in the experimental section. Carboxyl oxygen accounts for roughly 1/3 of the oxygen present in peat. Carbon oxygen single bond species account for roughly half of the oxygen species. For coal, carbonyl is the predominant Type II oxygen form. This situation may be different for peat. Species such as O-C-O (present in cellulose) would contribute to the Type II carbon (1s) signal. The presence of a significant amount of O-C-O species in peat would complicate the interpretation for the amount of oxygen associated with Type II carbon (1s) signal. The C=O values listed in Table 3 therefore represent upper limits.

Table 4 provides the definition of ^{13}C NMR structural parameters based on the carbon species and chemical shift ranges. Table 5 shows results obtained for the different structural parameters as a fraction of the total ^{13}C signal. SS ^{13}C NMR parameters fa^{C} , (carboxyl, carbonyl, amide), fa^{P} (phenolic, phenoxy) and fa^{O} (alcohol, ether) have oxygen associated with them. The range for the percentage of carbon associated with oxygen ($\text{fa}^{\text{C}} + \text{fa}^{\text{P}} + \text{fa}^{\text{O}}$) in peat is 32 to 49. It is not possible to determine the total amount of oxygen relative to carbon from the sum of oxygen related ^{13}C NMR signals (fa^{C} , fa^{P} , fa^{O}) because it is uncertain what oxygen stoichiometry to assign to each oxygen related ^{13}C NMR signal. Nevertheless, a conservative estimate of the amount of oxygen associated with fa^{C} is 1.0 (i.e. carbonyl, amide etc.) and 0.5 for fa^{P} and fa^{O} (i.e., aliphatic ether, methoxy etc.). Undoubtedly other species will have a combined impact on fa^{C} , fa^{P} and fa^{O} . A comparison of the XPS derived total organic oxygen signal and the NMR estimate based on $\text{fa}^{\text{C}} + 0.5(\text{fa}^{\text{P}} + \text{fa}^{\text{O}})$ is shown in Figure 3. The NMR parameter fa^{C} is expected to be related to the amount of oxygen with $\text{O}-\text{C}=\text{O}$ (Type III) determined by XPS. Figure 3 shows a close correspondence for these XPS and NMR parameters with all peat samples. Figure 3 also shows that the amount of oxygen found with Type I plus Type II XPS species is closely related to $0.5(\text{fa}^{\text{P}} + \text{fa}^{\text{O}})$. We would expect this correspondence if most of the oxygen species associated with the XPS Type II carbon (1s) signal are $\text{O}-\text{C}-\text{O}$ species and if ether species predominate in fa^{P} and fa^{O} .

IV. Summary

A self-consistent interpretation of oxygen derived XPS and ^{13}C NMR signals provides insight into the kinds of oxygen species present in peat. Multiply bonded carbon oxygen species make up only 25% of the oxygen population in these peat samples. XPS and NMR results indicate that carbon oxygen single bonded species are the predominant form in all peat samples studied. It is likely $\text{O}-\text{C}-\text{O}$ species and, in general, ether species makeup a large part of the carbon oxygen single bond population.

V. References

- 1) Ehmann, W. D.; Koppenaal, D. W.; Hamrin, C. E.; Jones, W. C.; Prasand, M. N.; Tian, W. Z., *Fuel* **1986**, 65, 1563.
- 2) Kuehn, D. W.; Snyder, R. W.; Davis, A.; Painter, P. C., *Fuel*, **1982**, 61, 682.
- 3) Reisser, B.; Starsinic, M.; Squires, E.; Davis, A.; Painter, P. C., *Fuel*, **1984**, 63, 1253.
- 4) Dyrkacz, G. R.; Bloomquist, C. A.; Solomon, P. R., *Fuel*, **1984**, 63, 536.
- 5) Solum, M. S.; Pugmire, R. J.; Grant, D. M., *Energy and Fuels*, **1989**, 3, 187.
- 6) Clark, D. T.; Wilson, R., *Fuel*, **1983**, 62, 1034.
- 7) Grint, A.; Perry, D. L., *Fuel*, **1983**, 62, 1029.
- 8) Kelemen, S. R.; Kwiatek, P. J., *Energy and Fuels*, **1995**, 9, 841.
- 9) Cohen, A. D.; Rollins, M. S.; Durig, J. R.; Raymond, R. JR., *J. Coal Quality*, **1991**, 10, 145.
- 10) The Users Handbook for the Argonne Premium Coal Sample Program; Vorres, K. S., Ed.; Argonne National Laboratory: Argonne, IL, 1989; ANL-PCSP-89-1; *Energy and Fuels*, **1990**, 4, 420.
- 11) Glick, D. C.; Davis, A., *Org. Geochem.*, **1991**, 17, 421.
- 12) Kelemen, S. R.; Rose, K. D.; Kwiatek, P. J., *Appl. Surf. Sci.*, **1993**, 64, 167.
- 13) Krevelen, D. W. van: Coal: Amsterdam: Elsevier, **1993**, p 181.

Table 1

Sample	(per 100 C) Hydrogen	(per 100 C) Nitrogen	(per 100 C) Sulfur	(per 100 C) Oxygen*
Peat				
Mian. Hem.	117	4.5	0.2	42.1
Me. Sph.	131	0.8	0.1	58.9
Lox. Nym.	130	6.3	0.5	39.1
Lox. Saw.	111	4.8	0.7	40.1
Sh. Rv. Rhiz.	118	3.9	2.8	50.4
Oke. Tax.	121	4.0	0.2	41.0
Oke. Nym.	122	5.3	0.3	39.4
N.C. 1 st Col.	107	1.3	0.1	35.0
Coal/Lignite				
DECS-11 Beulah	73	1.2	0.4	31.0
DECS-25 Post	82	1.2	0.2	17.6
PSOC-1468 Buck Mountain	16	0.8	0.2	0.9

(*) determined by difference

Table 2

Sample	Aromatic Carbon	Nitrogen	Sulfur	Si	Al	Ca
<u>Peat</u>						
Minn. Hem. (Peat) SCSB	26	2.8	0.2	0.5	0.3	--
Me. Sph. (Peat) SCSB	24	1.0	0.1	--	--	--
Lox. Nym. (Peat) SCSB	23	3.9	0.2	--	--	0.7
Lox. Saw. (Peat) SCSB	28	3.2	0.3	--	--	0.7
Sh. Rv. Rhiz. (Peat) SCSB	35	2.3	1.9	3.8	2.9	--
Oke. Tax. (Peat) SCSB	25	2.7	0.1	2.4	--	--
Oke. Nym. (Peat) SCSB	23	4.4	0.1	1.5	--	--
N.C. 1 st Col. (Peat) SCSB	29	1.1	<0.1	--	--	--
<u>Coal/Lignite</u>						
DECS-11 Beulah	55	1.3	0.3	2.4	2.5	1.1
DECS-25 Pust	52	1.3	0.3	3.2	4.1	1.3

Table 3

Sample	Total Organic Oxygen	-O	C=O	O-C=O
Minn. Hem. (Peat) SCSB	24.2	11.3	6.7	6.2
Me. Sph. (Peat) SCSB	22.4	10.7	6.1	5.6
Lox. Nym. (Peat) SCSB	22.2	8.6	6.6	7.0
Lox. Saw. (Peat) SCSB	27.0	9.3	8.3	9.4
Sh. Rv. Rhiz. (Peat) SCSB	24.3	7.3	8.8	8.2
Oke. Tax. (Peat) SCSB	25.6	9.3	6.9	9.4
Oke. Nym. (Peat) SCSB	30.2	14.5	7.9	7.8
N.C. 1 st Col. (Peat) SCSB	21.2	11.1	3.7	6.4

Table 4 - Definition of ¹³C NMR Structural Parameters

	<u>Chemical Shift</u>		
<u>Parameter</u>	<u>Range (ppm)</u>		<u>Carbon Type</u>
fa	90-240		Aromatic/Carboxyl/Carbonyl/Amide
fa'	90-165		Aromatic
faC	165-240		Carboxyl/Carbonyl/Amide
fa ^P	150-165		Phenoxy/Phenolic
faS	135-150		Alkyl-Substituted Aromatic
fa ^B	90-135		Bridgehead Aromatic
fal	0-90		Aliphatic
fa ^H	22-50		Methylene/Methine
fa [*]	0-22 & 50-60		Methyl/Methoxy
fa ^O	50-90		Alcohol/Ether

Table 5

	fa	fa'	faC	fa ^P	fa ^S	fa ^B	fal	fa ^H	fa [*]	fa ^O
Minn. Hem.	0.41	0.35	0.07	0.04	0.06	0.24	0.59	0.19	0.11	0.37
Me. Sph.	0.40	0.33	0.06	0.04	0.04	0.24	0.60	0.18	0.07	0.39
Lox. Nym.	0.35	0.24	0.11	0.03	0.04	0.16	0.65	0.30	0.12	0.30
Lox. Saw.	0.43	0.33	0.10	0.05	0.06	0.22	0.57	0.20	0.11	0.33
Sh. Rv. Rhiz.	0.40	0.33	0.06	0.04	0.06	0.23	0.60	0.18	0.13	0.38
Oke. Tax.	0.38	0.29	0.09	0.04	0.05	0.19	0.62	0.30	0.10	0.28
Oke. Nym.	0.40	0.30	0.10	0.04	0.05	0.21	0.60	0.18	0.11	0.38
N.C. 1 st Col.	0.45	0.36	0.09	0.05	0.07	0.23	0.56	0.33	0.09	0.18

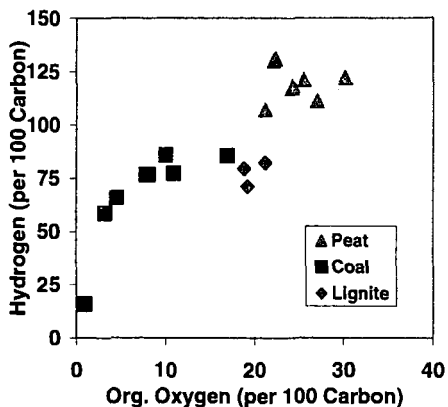


Figure 1 - H/C vs. O/C diagram for peat, and lignite. The O/C values were obtained from XPS data. H/C values are from elemental data. Previously reported results from Argonne Premium Coal are included for reference.

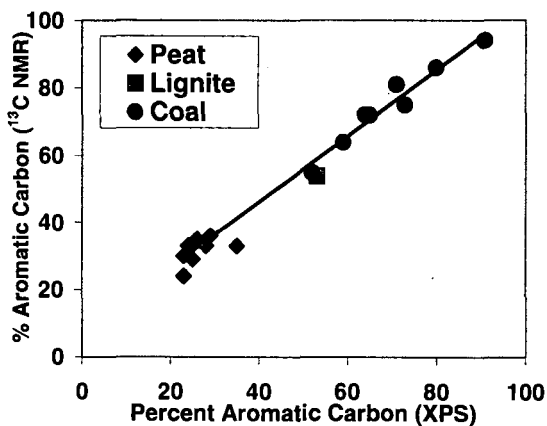


Figure 2 - Comparison of XPS and ^{13}C NMR results for aromatic carbon from peat, coal and lignite. Previously reported results for Argonne Premium Coal [12] are included for reference.

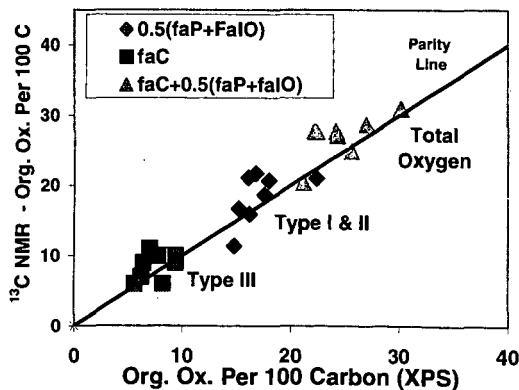


Figure 3 - Comparison of XPS and ^{13}C NMR derived parameters for organic oxygen species in peat.

SULFUR BEHAVIOR IN VARIOUS CHEMICAL TREATMENTS OF COAL

Katsuyasu Sugawara¹⁾, Naoto Tsubouchi¹⁾, Takuo Sugawara¹⁾ and Masayuki Shirai²⁾

1) Faculty of Engineering and Resource Science, Akita University, Akita 010-8502 JAPAN

2) Institute for Chemical Reaction Science, Tohoku University, Sendai 980-8577 JAPAN

KEYWORDS: Coal, organic sulfur, pyrolysis, pretreatment, XANES

INTRODUCTION

Coal is abundant and low-cost energy resource and deserves increasing use in developing countries. Efficient precleaning technology must be developed for the utilization of high-sulfur and low-grade coals. Sulfur is a key component not only for the environmental conservation but also for the development of new coal utilization processes. Incomplete understanding of the behavior of organic sulfur during heat treatment has given rise to a misbelief that organic sulfur in coal cannot be removed by the pretreatments.

Development of surface analyses enables us to know the actual forms of organic sulfur in coal. XANES and XPS have been demonstrated as strong tools to elucidate organic sulfur forms in coal and heavy hydrocarbons.¹⁻⁴

We have demonstrated the dynamic behavior of sulfur forms during pyrolysis in a series of studies on chemical coal cleaning processes.⁵⁻⁷ These studies showed that rapid pyrolysis removed organic sulfur effectively in some types of coal. The release rate as well as the extent of organic sulfur removal increased with the contents of exinite and vitrinite. Part of the organic sulfur exist in a thermally stable form which is difficult to remove from coal by pyrolysis. Thermally stable organic sulfur remaining in the solid should be changed to decomposable forms to achieve efficient desulfurization in the pretreatment process.

In the present study, behavior of sulfur forms has been followed for lignite, subbituminous and bituminous coals in rapid pyrolysis. Chemical pretreatments were carried out to transfer the thermally stable form of reactive species before pyrolysis. Organic sulfur forms were determined by using XANES for coal before and after rapid pyrolysis with chemical pretreatments. Sulfur capture experiment was also conducted for rapid pyrolysis char in a nitrogen stream containing hydrogen sulfide to seek a new application to porous carbon.

EXPERIMENTAL

Table 1 shows proximate, ultimate and sulfur-form analyses for the sample coals, Spanish lignite Mequinenza, Australian subbituminous Muswellbrook, Chinese bituminous Nantong, and Montana subbituminous Rosebud coals. Average particle size of the sample was 0.35 mm.

Two kinds of chemical pretreatments were carried out as follows. The coal samples were immersed in a saturated aqueous solution of potassium hydroxide for 24 h with agitation at room temperature. The wet alkali immersed samples were then heated at 523 K for 4 h in a nitrogen atmosphere after filtration from potassium hydroxide solution. The alkali-treated samples were washed repeatedly with distilled water to reduce the basicity and then dried out at 380 K.⁸

Table 1 Analyses of sample coals

Sample	Ultimate [wt%, daf]					Proximate [wt%, db]		Sulfur form [wt% of total sulfur]		
	C	H	N	S	Diff.	VM	Ash	Pyritic	Sulfate	Organic
Mequinenza	69.3	5.5	1.0	13.6	10.6	48.8	21.4	7	0	93
Muswellbrook	77.5	6.0	2.1	0.8	13.6	41.1	8.3	11	3	86
Nantong	88.9	4.9	0.6	5.0	0.6	17.0	17.3	34	1	65
Rosebud	73.0	4.5	0.9	0.9	20.7	39.8	10.2	32	3	65

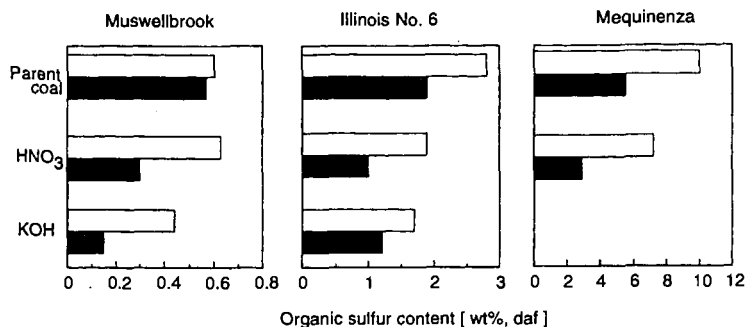


Fig.1 Change in organic sulfur content with various pretreatments
(□, before pyrolysis; ■, after pyrolysis)

Nitric acid pretreatment was also carried out. The sample coals were immersed in nitric acid aqueous solution at a boiling temperature. After filtration and drying, rapid pyrolysis was conducted for the pretreated coals by using a free-fall pyrolyzer. This apparatus enables coal particles to be heated in a nitrogen stream at rates from 10^3 to 10^4 K/s depending on particle density and diameter. The temperature was 1253 K at the isothermal section of the reactor. The details of the apparatus were described elsewhere.⁶

To investigate the effect of macerals on sulfur-form and distribution, the samples were fractionated into three density groups by sink-float in zinc chloride aqueous solution. The separated samples were repeatedly washed to remove zinc chloride, which might catalyze tar decomposition. The absence of zinc chloride in the sample was confirmed by extraction with hydrochloric acid solution.⁹

Sulfur capture behavior was investigated for rapid pyrolysis char in hydrogen sulfide/nitrogen gas mixture at 1073 K in a fixed bed.

Some improvements to ASTM (D2492) were applied to analyzing sulfur forms (pyrite, ferrous sulfide, sulfate and organic sulfur) in parent and chemically pretreated coals, and in rapidly pyrolyzed char. The details of the analytical method were reported previously.¹⁰ Sulfur K-edge XANES was applied to specifying the forms of organic sulfur.¹¹ XANES measurements were carried out at beam line 2A of Photon Factory in the High Energy Accelerator Research Organization. Si(111) monochromators were used to vary the incident X-ray energy. The beam irradiated the samples fixed on a nickel plate under 10^{-3} Pa in a vacuum chamber. Data were recorded in the fluorescence mode in the region of the sulfur K-edge at room temperature. The fluorescence spectra were collected using a scintillation counter. The absolute photon energy was calibrated with the assumption that the giant resonance of K_2SO_4 appears at 2481.7 eV. The third derivatives of XANES spectra from model compounds were used as fingerprints for interpreting sulfur forms in the sample. Pyrite, ferrous sulfide, crystalline sulfur, DL-cystine, thioxane-9-one, s-methyl-L-cysteine, DL-methionone sulfoxide and potassium sulfate were selected as the model compounds.

RESULTS AND DISCUSSION

Figure 1 shows change in organic sulfur content in rapid pyrolysis with the chemical pretreatments. A considerable decrease in organic sulfur was observed for rapid pyrolysis chars of nitric acid or potassium hydroxide pretreated Muswellbrook. Rapid pyrolysis of parent coal did not show appreciable change in organic sulfur. The effect of chemical pretreatments can also be found in the rapid pyrolysis of Illinois No.6 coal. The organic sulfur content decreased to one third of parent coal. While Mequinenza is well known as a lignite containing more than 10 % of organic sulfur, the rapid pyrolysis of this sample shows that about half of organic sulfur decomposes during the treatment. XANES spectra indicate large amount of disulfide in

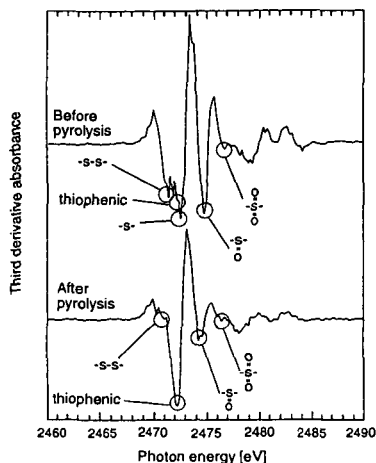


Fig.2 Sulfur K-edge XANES spectra of HNO_3 treated coal before and after pyrolysis.

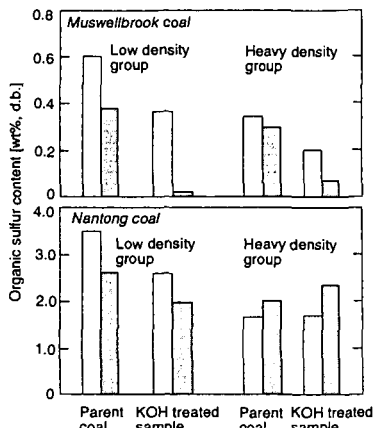


Fig.3 Effect of KOH pretreatment on organic sulfur content before and after pyrolysis for density separated samples.

(□, before pyrolysis; ▨, after pyrolysis)

Mequinenza coal which caused the high extent of organic sulfur removal during rapid pyrolysis. Efficient removal of organic sulfur was obtained for the combined process of rapid pyrolysis with nitric acid pretreatment. Potassium hydroxide pretreatment could not be carried out because lignite was dissolved with alkali solution.

Figure 2 shows third differential curves of XANES spectra for the nitric acid treated Illinois No.6 coal before and after rapid pyrolysis. Strong peaks are observed around 2472 eV for the coal before pyrolysis, which are attributable to disulfide, thiophene and sulfide. A strong peak at 2474.5 eV results from sulfoxide. This peak is larger than that of parent coal. After the rapid pyrolysis of nitric acid treated coal, the peaks of disulfide and sulfide disappear and the sulfoxide peak becomes small.

To investigate the effect of change in the forms and content of organic sulfur with maceral concentration on desulfurization behavior, potassium hydroxide pretreatment and rapid pyrolysis were conducted for the density separated coals of Muswellbrook and Nantong. The samples were separated into three groups (low, medium and heavy density groups): $<1.26 \text{ g/cm}^3$; $1.26\sim1.40 \text{ g/cm}^3$; $>1.40 \text{ g/cm}^3$ for Muswellbrook, and $<1.32 \text{ g/cm}^3$; $1.32\sim1.42 \text{ g/cm}^3$; $>1.42 \text{ g/cm}^3$ for Nantong coals, respectively. Figure 3 indicates change in organic sulfur content with potassium hydroxide pretreatment and rapid pyrolysis for the density separated coals. The clean char less than 0.02 % of organic sulfur was obtained for the potassium hydroxide treated sample of Muswellbrook low density group. While change in organic sulfur content was not appreciable after rapid pyrolysis of heavy density group, potassium hydroxide pretreatment was effective for change of the thermally stable organic sulfur to decomposable forms. For Nantong low density group, some extent of organic sulfur decreased with potassium hydroxide pretreatment and rapid pyrolysis. Organic sulfur content increased after rapid pyrolysis for heavy density group.

Figure 4 shows change in sulfur content of char exposed to a nitrogen stream containing hydrogen sulfide in a fixed bed at 1073 K. The sample char was obtained by rapid pyrolysis of Rosebud coal in a nitrogen stream at 1253 K. Sulfur content increased with hydrogen sulfide concentration and attained to 12 % in nitrogen gas containing 2.91 % of hydrogen sulfide. XANES analysis indicates that adsorbed sulfur formed organic sulfur in the solid phase.

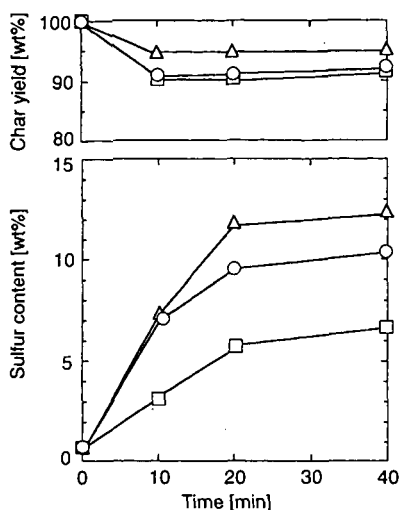


Fig. 4 Sulfur capture by Rosebud char in H₂S/N₂ stream at 1073 K. (Hydrogen sulfide conc.: □, 0.29%; ○, 1.01%; △, 2.91%)

ACKNOWLEDGMENT

The authors are grateful to Mr. Hiroaki Inoue for his assistance. This work was supported in a part by Basic Research Associate for Innovated Coal Utilization Program (NEDO).

REFERENCES

- 1) Kelemen, S. R.; George, G. N.; Gorbaty, M. L. *Fuel* **1990**, 69, 939-944
- 2) Kelemen, S. R.; Gorbaty, M. L.; George, G. N.; Kwiatek, P. J.; Sansone, M. *Fuel* **1991**, 70, 369-402
- 3) Huffman, G. P.; Huggins, F. E.; Mitra, S.; Shah, N.; Pugmire, R. J.; Davis, B.; Lytle, F. W.; Greegon, R. B. *Energy Fuels* **1989**, 3, 200-205
- 4) Huffman, G. P.; Mitra, S.; Huggins, F. E.; Shah, N.; Vaidya, S.; Lu, F. *Energy Fuels* **1991**, 5, 574-581
- 5) Sugawara, K.; Tozuka, Y.; Sugawara, T.; Nishiyama, Y., *Fuel Process. Technol.* **1994**, 37, 73-85
- 6) Sugawara, T.; Sugawara, K.; Nishiyama, Y.; Sholes, M. A. *Fuel* **1991**, 70, 1091-1097
- 7) Sugawara, K.; Gunji, T.; Sugawara, T.; Shirai, M.; Nishiyama, Y. *Energy Fuels*, **1997**, 11, 1272-1277
- 8) Sugawara, K.; Abe, K.; Sugawara, T.; Nishiyama, Y.; Sholes, M. A. *Fuel* **1995**, 74, 1823-1829
- 9) Sugawara, K.; Tozuka, Y.; Kamoshita, T.; Sugawara, T.; Sholes, M. A. *Fuel* **1994**, 73, 1224-1228
- 10) Sugawara, T.; Sugawara, K.; Ohashi, H. *Fuel* **1989**, 68, 1005-1011
- 11) Sugawara, K.; Sugawara, T.; Shirai, M. *Jpn. J. Appl. Phys.* **1999**, 38, 608-611

XAFS STUDY OF SULFUR FORMS IN COALS DURING RAPID PYROLYSIS

Masayuki Shirai¹, Masahiko Arai¹, and Katsuyasu Sugawara²

¹ Institute for Chemical Reaction Science, Tohoku University,
Katahira, Aoba, Sendai, 980-8577, JAPAN

² Faculty of Engineering and Resource Science, Akita University,
1-1 Tegata Gakuen-cho, Akita City, Akita 010-8502, JAPAN

Keywords: Coal, Desulfurization, XAFS

ABSTRACT

Various kinds of coal, having the same average diameter and 89% C daf, were pyrolyzed rapidly in a free-fall reactor at atmospheric pressure under a nitrogen stream at a terminal temperature of 1253 K. The extent of organic sulfur removal in the rapid pyrolysis were different. Sulfur K-edge X-ray absorption near edge structure indicated that the organic sulfur species removed from coals were elemental, disulfide, sulfide and sulfoxide sulfur. The extent of organic sulfur removal in the rapid pyrolysis depended on the coals, because the amount and fraction of the volatile organic sulfur species were different even when the coals have the same carbon content.

1. INTRODUCTION

Sulfur is one of the most troublesome contaminants in coal. Although, present only in low concentrations, sulfur causes problems in every process that uses coal. When released into the atmosphere as SO₂ through combustion, it produces so-called acid rain. Certainly, a better understanding of the nature and distribution of sulfur-bearing minerals, organic sulfur-containing functional groups and their concomitant chemistry is necessary for improving advanced coal preparation processes and the environmental acceptability of coal-derived energy. Sulfur takes on several forms in coal including elemental, mineral and organic. Conventional coal cleaning technologies are grouped into physical and chemical methods. Because physical processes are limited to removal of inorganic constituents, development of an efficient process of organic sulfur removal is an urgent issue for sustainable resource development and environmental conservation. Development of a chemical desulfurization process requires a detailed understanding of organic sulfur forms in coal.¹ X-ray absorption near edge structure (XANES) spectroscopy has been shown to be a powerful method for the direct, nondestructive, and quantitative determination of organic sulfur-containing functional groups forms in coal.²⁻⁴

In the present study, dynamic behaviors of sulfur forms for several coals were followed in rapid pyrolysis. These coals were first served as a lumped sample which had the same average particle diameter without density separation. Then, the same samples were separated into three groups by a sink-float method to investigate effects of particle-density distribution on sulfur forms and their desulfurization behavior in rapid pyrolysis. Organic sulfur forms were determined by using XANES for the density-separated coals before and after pyrolysis.

2. EXPERIMENTAL

The coal samples were used in the experiment as soon as received. Average particle size of the sample was 0.35 mm. The samples were separated into three density groups by a sink-float method in zinc chloride aqueous solution. The absence of zinc chloride in the density-separated sample was confirmed by extraction with 5 M HCl for 2 h.

Rapid pyrolysis experiment was conducted by using a free-fall pyrolyzer. This apparatus enables coal particles to be heated in a nitrogen stream at rates from 10³ to 10⁴ K/s depending on particle density and diameter. Particle residence time is varied by changing the length of the heating section. The temperature was 1253 K at the isothermal section of the reactor.

Sulfur K-edge X-ray absorption near edge structure spectroscopy was applied to specifying the forms of organic sulfur in raw and char. XANES measurements were carried out at beam line 2A of Photon Factory in the National Laboratory for High Energy Physics. Si(111) monochromator was used to vary the incident X-ray energy. The beam irradiated the samples fixed on a nickel plate under 10⁻³ Pa in a vacuum chamber. Data were recorded in the fluorescence and electron yield modes in the region of the S K-edge at room temperature. The absolute photon energy was calibrated with the

assumption that the giant resonance of K_2SO_4 ($S\ 1s \rightarrow t_2$) appears at 2481.7 eV. The third derivatives of XANES spectra from model compounds were used as fingerprints for interpreting sulfur forms in the sample. Ferrous sulfide, pyrite, crystalline sulfur, DL-cysteine, thioxane-9-one, S-methyl-L-cysteine, DL-methionine sulfoxide, and potassium sulfate were selected as the model compounds.

3. RESULTS AND DISCUSSION

Table 1 shows proximate, ultimate, and sulfur-form analyses for the sample coals. Figure 1 shows a correlation between extent of organic sulfur removal and carbon content for Nantong, Yanzhou, and Furong coals being studied in the present work, and for other 13 coals, carbon content ranging from 65 to 90% daf. The extent of organic sulfur removal is defined by

$$\{1 - (\text{organic sulfur in char}) / (\text{organic sulfur in raw coal})\} \times 100 (\%)$$

where ultimate content of organic sulfur in the rapid pyrolyzed char based on coal basis was used as organic sulfur in char in this equation. By considering the thermal stability of thiophenic, and sulfide sulfur, it is plausible that the extent of organic sulfur removal decreases linearly with the increase of carbon content due to the increase of thiophenic sulfur content.

Table 1. Analyses of Sample Coals

sample	ultimate (wt %, daf)					proximate (wt %, db)		sulfur form (wt % of total sulfur)		
	C	H	N	S	diff	VM	ash	pyritic	sulfate	organic
Nantong	88.9	4.9	0.6	5.0	0.6	17.0	17.3	34	1	65
Yanzhou	89.1	5.5	1.1	3.2	1.1	43.2	9.1	38	1	61
Furong	88.9	3.1	0.9	6.6	0.5	10.5	21.6	77	0	23

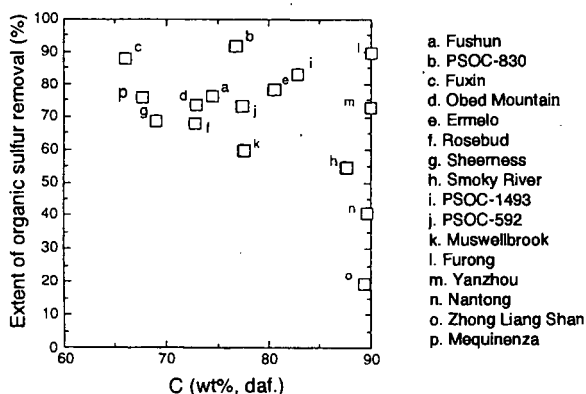


Figure 1. Change in extent of organic sulfur removal from solid phase with carbon content.

An apparent linear correlation, however, cannot be obtained between the extent of organic sulfur removal in rapid pyrolysis and carbon content of raw coals as demonstrated in Figure 1. The large difference from 19% to 89% of the extent of organic sulfur removal was noted for five kinds of high-rank coals containing more than 87% carbon. High-rank Furong coal was desulfurized to 89%, the second highest extent of desulfurization in 16 coals.

Figure 2 shows a relation between yield and density obtained by the sink-float method in zinc chloride aqueous solution. The density distribution differs from coal to coal even through carbon content is the same. The samples were separated into three groups with expected differential concentration of macerals.⁵ The range of each group was altered in three kinds of coal to obtain enough amount of fractionated samples to be supplied for rapid pyrolysis experiments.

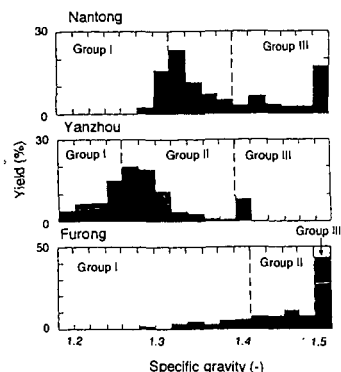


Figure 2. Yield distribution in density separation.

The raw and separated samples, group I, II, and III, were rapid pyrolyzed in a nitrogen stream with the free-fall reactor. Figure 3 represents a relation between the extent of organic sulfur removal and average density. Nantong and Yanzhou coals show linear relationship between the extent of organic sulfur removal and average density of the groups in each coal. This result implies that thermally stable organic sulfur increases with the increase on density. The existence of thermally stable organic sulfur is expected in the group III of Nantong and group II of Furong coals because of smaller extent of organic sulfur removal than volatile yield. Group I of Furong coal showed larger extent of organic sulfur removal than group II as the same tendency as the other coals though volatile yield was independent of average density. Exceptionally, more than 90% of the extent of organic sulfur removal was observed for group III of Furong coal, although the low extent of organic sulfur removal was expected because of high rank coal.

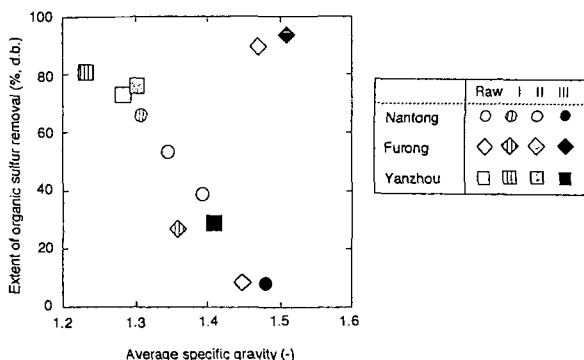


Figure 3. Change in organic sulfur removal with average density.

Figure 4 shows third differential curves of XANES spectra for groups I and III of Nantong coal. Strong peak is observed around 2472 eV for group I, which are attributable to thiophene and sulfide. A strong peak at 2474.5 eV results from sulfoxide. Through group III shows the similar distinct peaks of thiophene and sulfoxide to group I, the sulfide peak dose not appear for group III. It could be estimated that efficient desulfurization in a smaller density group such as group I is related to the presence of sulfide though the absolute amount of each sulfur form should be determined.

Third differential curves of XANES spectra for groups I and III of Furong coal are shown in Figure 5. Thiophene, sulfoxide, and pyritic sulfur are observed for group I as the same as the curves of Nantong, group I. On the other hand, the curves for group III of Furong are very different from that of group I. In addition to the peaks resulting from thiophene, sulfoxide, and sulfate, intensive peaks are observed at 2470.4-2470.8 eV, which are combined peaks attributable to pyritic sulfur and elemental sulfur. Figure 6 represents third differential curves of XANES spectra of rapid pyrolysis chars for group I and III of Furong coal. The curve of char for group I indicates that the sulfoxide peak becomes

smaller after pyrolysis while the peak of thiophenic sulfur remained. A peak at 2468.7 eV resulted from ferrous sulfide produced by reduction of pyrite. The peaks of pyritic sulfur and elemental sulfur disappeared and a large peak of ferrous sulfide at 2468.7 eV newly appeared after pyrolysis for group III. Fulong coal has distinguishing characteristics as high organic sulfur content and removal extent of organic sulfur in larger density group III. XANES analysis, however, indicated that efficient extent of organic sulfur removal might be caused by releasing of elemental sulfur rather than organic sulfur.

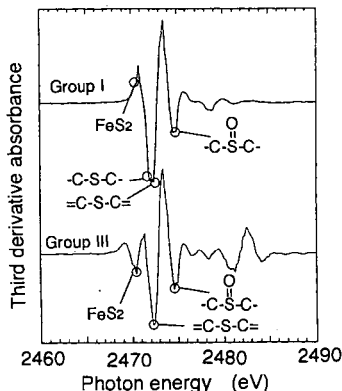


Figure 4. Sulfur K-edge XANES spectra of group I and III for Nantong coal.

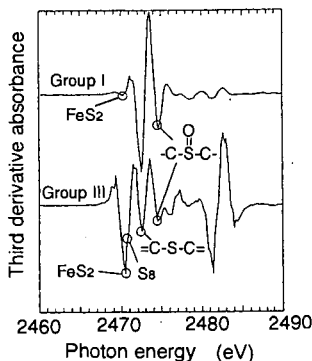


Figure 5. Sulfur K-edge XANES spectra of group I and III for Fulong coal.

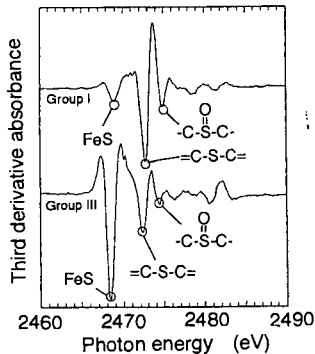


Figure 6. Sulfur K-edge XANES spectra of char for Fulong coal.

4. Conclusion

In a serious on chemical coal cleaning, the desulfurization behavior in rapid pyrolysis was investigated for raw coals and their density-separated samples. The extent of organic sulfur removal shows linear decreasing tendency with the increase of density for each sample coal though the extent of organic sulfur removal was different from coal to coal even with the same carbon content. The high extent of desulfurization was estimated to be caused by elemental sulfur in the large density group of high-rank Fulong coal.

References

- (1) Davidson, R.M. *Fuel* **1994**, 73, 988-1005.
- (2) George, G. N.; Gorbaty, M. L. *J. Am. Chem. Soc.* **1989**, 111, 3182-3186.
- (3) Huffman, G. P.; Huggins, F. E.; Mitra, S.; Shah, N.; Pugmire, R. J.; Davis, B.; Lytle, F. W.; Gregor, R. B. *Energy Fuels* **1989**, 3, 200-205.
- (4) Shirai, M.; Sugawara, K. *Inter. J. Mater. Eng. for Resources*. **1999**, 7, 320-338.
- (5) Sugawara, K.; Tozuka, Y.; Kamoshita, T.; Sugawara, T.; Sholes, M. A. *Fuel* **1994**, 73, 1224-1228.

CHARACTERIZATION OF MICRO-DOMAIN STRUCTURE OF SOLVENT-SWOLLEN COAL BY SMALL ANGLE NEUTRON SCATTERING AND PROTON SPIN DIFFUSION

Koyo NORINAGA¹, Masashi IINO, and George D. CODY¹

*Institute for Chemical Reaction Science, Tohoku University
Katahira, Aoba-ku, Sendai, 980-8577, Japan*

¹*Geophysical Laboratory, Carnegie Institution of Washington
5251 Broad Branch Road, Washington, D. C. 20015*

KEYWORDS: Coal, Swelling, Microphase separation

ABSTRACT

Blind Canyon coal was swollen by deuterated pyridine and was subjected to small angle neutron scattering (SANS) and ¹H NMR relaxation measurements. Based on the transverse relaxation characteristics, it was found that there exist at least two distinct structural regions in the swollen coals. However the measured longitudinal relaxation was best characterized by a single component as spin diffusion is rapid in the swollen coals. The dynamics of spin diffusion were revealed using a partially modified Goldman-Shen pulse sequence and analyzed by a simple mathematical model of a two phase system. The interdomain spacing, d_i , was estimated based on the diffusive path length for each spatial dimension. The d_i value evaluated under one-dimension was 15 nm and agreed with d_i determined by SANS, suggesting that the domain shape is sheet.

INTRODUCTION

The most convincing model of coal structure is that of a cross-linked macromolecular network.¹⁻⁵ The swelling of coal in various solvents has been studied to evaluate the molecular weight between cross-link points.^{2, 4, 8} The Flory-Rehner theory⁹ has been frequently employed to relate the macromolecular network parameters to the degree of swelling in a good solvent. The theory assumes that the deformation is affine, i.e., the primitive chain is deformed in the same way as the macroscopic deformation (swelling) of the sample. Accordingly, the coal must swell uniformly in the segmental scale when we relate the macroscopic swelling to molecular characteristics such as the cross-link density. Based on the ¹H NMR transverse relaxation characteristics, however, it was found that the coal hydrogen in the pyridine-swollen state could be divided into two groups: those with relaxation characteristic of solids and those with relaxation characteristic of liquids.¹⁰⁻¹⁷ Barton et al.¹² reported that up to 60 % of coal's macromolecular structure becomes mobile when immersed in deuteropyridine, while the remaining 40 % remains rigid as detected through ¹H NMR transverse relaxation measurements. Based on this finding, they first established that the swollen coal has a phase separated structure involving a solvent rich phase and an apparently solvent impervious phase.

Recently, Norinaga et al.¹⁸ reported that the scale of the heterogeneity in the swollen coals. They characterized the phase separated structure of solvent swollen coal using its proton spin diffusion property. Five coals of different ranks were swollen by saturation with deuterate pyridine and were subjected to ¹H NMR relaxation measurements. The dynamics of spin diffusion were revealed using a partially modified Goldman-Shen pulse sequence and analyzed by a simple mathematical model of a two phase system. These calculations indicated that the solvent rich phase domains in the swollen coals range in size from several up to 20 nm. These results highlight the current limits in our understanding of the macromolecular structure of coals and place into question the use of affine models of strain for the interpretation of macroscopic swelling measurements. However the results depend on the spatial dimension of domains, i.e., the degree of freedom of the spin diffusion. Hence the information regarding the morphology of the domains is required to evaluate the domain size more precisely.

In the present study, the phase structure of a bituminous coal swollen by deuterate pyridine was characterized. In order to evaluate the morphology of the domains, we employ two different techniques. One is proton spin diffusion and the other is small angle neutron scattering (SANS). SANS gives an information on the average periodicity of the microphase structure, that is, the average distance between the centers of adjacent solvent-impervious domains. It is possible to convert the size of the solvent rich phase into an interdomain spacing using an appropriate domain model. Thus the morphology of the domains can be evaluated by comparing the results of the spin diffusion with those of SANS.

EXPERIMENTAL

Samples. Blind Canyon coal supplied from Argonne Premium Coal Sample suite was used. The elemental composition of the dried Blind Canyon coal (hereafter referred to as BL) was C=80.7 wt %, H=5.8 wt %, N=1.6 wt %, S=0.4 wt %, and O=11.6 wt % on a dry-ash-free basis.¹⁹ Their particle sizes were finer than 150 μ m. 0.3 g of BL was weighed and transferred to an NMR tube with a 10 mm o.d. This tube was charged with per-deutero pyridine (Aldrich, 99.99% atom D), py- d_5 , and sealed under a pressure of less than 2 Pa while frozen in liquid nitrogen. Solvent to coal mass ratio (S/C) ranged from 0.36 to 4.12. BL was exhaustively extracted in pyridine prior to SANS experiments. 0.15 g of sample

was loaded into a suprasil cylindrical cell with 2 mm path length (vol = 0.7 mL). 0.6 mL of deuterated solvent (benzene / pyridine mixed solvent) was introduced to the cell.

SANS. SANS data were measured at the Intense Pulsed Neutron Source of Argonne National Laboratory, using the Small Angle Diffractometer (SAD). This instrument uses pulsed neutrons derived from spallation with wavelengths in the range of 0.1 - 1.4 nm and a fixed sample-to-detector distance of 1.54 m. The scattered neutrons are measured using a 64 x 64 array of position sensitive, gas filled, 20 x 20 cm², proportional counters with the wavelengths measured by time of flight by binning the pulse to 67 constant $\Delta t/t = 0.05$ time channels. The size range in a SANS experiment is constrained by both the geometry of the instrument and the wavelength of the neutrons which determine the working range of momentum transfer Q .

$$Q = 4\pi\lambda^{-1} \sin\theta \quad (1)$$

where θ is half the Bragg scattering angle and λ is the wavelength of the neutrons. Given the characteristics of the SAD at the Intense Pulsed Neutron Source (IPNS), useful SANS data in the Q range of 0.0006-0.025 nm⁻¹ can be obtained in a single measurement. The reduced data for each sample is corrected for the backgrounds from the instrument, the suprasil cell, and the solvent as well as for detector nonlinearity. Data are presented on an absolute scale by using the known scattering cross-section of a silica gel sample.

¹H NMR. NMR measurements were carried out at 303 K using a JEOL Mu-25 NMR spectrometer equipped with a spin locking unit operating at a proton resonance frequency of 25 MHz. The solid-echo pulse sequence, ²⁰ 90°_x- τ -90°_y (90° phase shift) provided an approximation to the complete free induction decay (FID). Typical values for the pulse width, pulse spacing, repetition time and number of scans were 2.0 μ s, 8.0 μ s, 6 s, and 32, respectively. The saturation recovery pulse sequence, 90°_x- τ -90°_x, was used to monitor the recovery of the magnetization with the pulse separation time, τ and provided T_1 . $T_{1\rho}$ was measured using a spin-locking pulse sequence,²¹ that includes a 90°_x pulse followed by a reduced amplitude pulse, phase shifted 90°, and sustained for a variable time, t . The magnetization remaining at time t is monitored by observation of the free induction decay signal. The rotating frame measurements were made in a 6 G radiofrequency field. The spin diffusion was monitored with the Goldman-Shen pulse sequence.²² In order to avoid the dead-time effect after the pulse, the original pulse sequence was modified as 90°_x- τ_0 -90°_x- τ -90°_x- τ_1 -90°_y, according to Tanaka and Nishi.²³

RESULTS AND DISCUSSION

SANS results. The SANS data for a number of solutions of varying benzene to pyridine are presented in Figure 1. These data are presented as the log of the coherent scattering intensity, $I(Q)$, against the log of the momentum vector, Q . It is clear that there are significant changes in coherent scattering with increasing swelling ratio. These changes are relatively large scale. For example in the intermediate Q range around 0.02, $I(Q)$ increases by a factor of five with increased swelling (pyridine concentration in solution). It should be noted that $Q \sim 0.02$ corresponds to a real space length of ~ 16 nm. It is noteworthy that at low Q , the effects of swelling are considerably less, thus the changes in coherent scattering "peak" in the intermediate Q range. Cody et al.²⁴ observed that similar creation of scattering intensity in the intermediate Q range with swelling of the Upper Freeport coal. In that work, they argued that the scattering at low Q was independent of scattering at intermediate Q . Thus, we concluded that the intermediate scattering was the results of an interparticle scattering phenomena as opposed to primary scattering of individual particles. The same interpretation can be applied here since the swelling of this coal is inhomogeneous, i.e., there exist solvent rich and solvent impervious domains as will be demonstrated by the ¹H NMR relaxation characteristics.

¹H NMR results. The FID curves for the swollen BL coal are drawn as a function of decay time in Figure 2. Although the solvent swelling enhances the fraction of slowly decaying components, a portion of the coal hydrogen remains rigid. For a dipole coupled rigid systems such as dry coal, the time decay of the nuclear magnetization can be characterized by a Gaussian function. On the other hand, in a liquid or a liquid-like environment, the magnetization decay is approximately an exponential function. Therefore the observed FID was assumed to be expressed by the following equation and was analyzed numerically by the nonlinear least squares method.

$$I(t) = I_G(0) \exp[-t^2/2T_{2G}^2] + I_{L1}(0) \exp[-t/T_{2L1}] + I_{L2}(0) \exp[-t/T_{2L2}] \quad (2)$$

where $I(t)$ and $I_i(t)$ are the observed intensity at time t , and that attributed to component i , respectively, and T_{2i} is the transverse relaxation time of the i th component. The fractions of hydrogen producing exponential decays, f_{MH} , are plotted against S/C in Figure 3. f_{MH} was increased up to 0.5 with increase in S/C. However, f_{MH} kept almost constant value above S/C=2.24, indicating that there exist the solvent impenetrable regions in the swollen coal even at S/C=4.72. For the swollen coal samples, it is clear that there are domains which do not swell and are not penetrated by solvent as shown schematically in Figure 4. The phase structures of the swollen coal are separated into at least two phase, i.e., solvent rich (SR)

and solvent impervious phase (SI).

To examine whether the spin diffusion process is active or not in the swollen coal samples, proton longitudinal relaxation was measured both in the laboratory and rotating frame. Table 1 lists the result of T_1 and $T_{1\rho}$ measurement for the swollen UF coal. T_1 is composed of one component while $T_{1\rho}$ can be analyzed by the sum of two exponential functions. From these results, one can clearly understand the effect of spin diffusion. T_2 signals are composed of three components without the effect of spin diffusion while $T_{1\rho}$ and T_1 measurements are affected strongly by spin diffusion and the number of the components decreases from $T_{1\rho}$ to T_1 . The existence of at least two time constants for a rotating frame longitudinal relaxation process i.e., $T_{1\rho}$, in a system means that spin-diffusion processes cannot effectively average the different dynamical properties of protons in different spatial domains on the relevant time scale of the specific relaxation process. On the other hand, in the time scale of T_1 measurements, the distinctly separated spin systems were sufficiently averaged by the spin diffusion. The scale of spatial heterogeneities of the swollen coals can be estimated by evaluating the diffusive path length, i.e., the maximum linear scale over which diffusion is effective. The Goldman-Shen pulse sequence was thus employed to monitor the spin diffusion process. The advantage of the Goldman-Shen experiment is that the time for spin diffusion can be arbitrarily varied, and if this time is much less than T_1 , the analysis is straightforward. The Goldman-Shen experiment is a technique to put the separate spin systems at different spin temperatures and then sample them as a function of time so that their approach to equilibrium can be followed. In Figure 5, the recovery factor of the magnetization of SI phase, $R(t)$, is plotted versus square root of time, $\tau^{1/2}$ for the solvent-swollen BL coals. S/C has almost no effects on the observed $R(t)$. The time evolution of $R(t)$ is analyzed by the diffusion equation solved by Cheung and Gerstein²⁵ to get information on the diffusive path length, l . The solid curves in Figure 5 represent the nonlinear least squares fits to the data by using the diffusion equation. The analytical fits give l to be 7, 16, and 25 nm for one, two, and three dimensions, respectively.

Comparison of SANS and ^1H NMR results. To compare the NMR results with SANS, we must convert the spin diffusion path length into an interdomain spacing. The spheres of SI phase are assumed to be covered with a uniform layer of SR phase of thickness l as shown in Figure 6. This model allowed to produce the following two equations,

$$l = r_c - r_{\text{SI}} \quad (3)$$

$$\phi_{\text{SI}} = \phi_c (1 - f_{\text{MH}}) = \left(\frac{r_{\text{SI}}}{r_c} \right)^d \quad (4)$$

where ϕ_{SI} , ϕ_c , and d are volume fractions of SI domains, volume fraction of coal in the swollen coal gel, and spatial dimension of the domain, respectively. In eq 4, we assumed that the hydrogen ratio is identical to the volume ratio. Twice r_c is taken to be equal to the interdomain spacing, d_i . d_i was estimated for each spatial dimension. The d_i evaluated under one-dimension at S/C=4 was approximately 15 nm and agreed with d_i determined by SANS, suggesting that the domain shape is sheet.

ACKNOWLEDGMENT. The authors are grateful to Drs. Tadashi Yoshida and Masahide Sasaki of the Hokkaido National Industrial Research Institute for their useful advice on the NMR measurements. This work was supported in part by a "Research for the Future Project" grant from the Japan Society for the Promotion of Science (JSPS), through the 148th Committee on Coal Utilization Technology.

REFERENCES

- (1) van Krevelen, D. W. *Fuel* **1966**, *45*, 229.
- (2) Green, T.; Kovac, J.; Brenner, D.; Larsen, J. W. In *Coal Structures*; Mayers, R. A., Ed.; Academic Press: New York, 1982.
- (3) Brenner, D. *Fuel* **1985**, *64*, 167.
- (4) Larsen, J. W.; Green, T. K.; Kovac, J. *J. Org. Chem.* **1985**, *50*, 4729.
- (5) Lucht, L. M.; Peppas, N. A. *Fuel* **1987**, *66*, 803.
- (6) Sanada, Y.; Honda, H. *Fuel* **1966**, *45*, 295.
- (7) Kirov, N. Y.; O'Shea, J. M.; Sergeant, G. D. *Fuel* **1968**, *47*, 415.
- (8) Nelson, J. R. *Fuel* **1983**, *62*, 112.
- (9) Flory, P. J. *Principles of Polymer Chemistry*; Cornell University Press: Ithaca: NY 1953.
- (10) Jurkiewicz, A.; Marzec, A.; Idziak, S. *Fuel* **1981**, *60*, 1167.
- (11) Jurkiewicz, A.; Marzec, A.; Pislewski, N. *Fuel* **1982**, *61*, 647.
- (12) Barton, W. A.; Lynch, L. J.; Webster, D. S. *Fuel* **1984**, *63*, 1262.
- (13) Kamiński, B.; Pruski, M.; Gerstein, B. C.; Given, P. H. *Energy Fuels* **1987**, *1*, 45.
- (14) Jurkiewicz, A.; Bronnimann, C. E.; Maciel, G. E. *Fuel* **1990**, *69*, 804.
- (15) Jurkiewicz, A.; Bronnimann, C. E.; Maciel, G. E. High-Resolution ^1H NMR studies of Argonne premium coals. In *Magnetic Resonance in Carbonaceous Solids*; Botto, C. E., Sanada, Y., Eds.; Advances in Chemistry; American Chemical Society: Washington, DC, **1993**, 229, 401.

- (16) Yang, X.; Larsen, J. W.; Silbernagel, B. G. *Energy Fuels* **1993**, *7*, 439.
- (17) Yang, X.; Silbernagel, B. G.; Larsen, J. W. *Energy Fuels* **1994**, *8*, 266.
- (18) Norinaga, K.; Hayashi, J. i.; Chiba, T.; Cody, G. D. *Energy Fuels* **1999**, *in press*.
- (19) Vorres, K. S. *User's Handbook for the Argonne Premium Coal Sample Program*; Argonne National Laboratory: Argonne: IL, 1993.
- (20) Powles, J. G.; Mansfield, P. *Phys. Lett.* **1962**, *2*, 58.
- (21) Hartmann, S. R.; Hahn, E. L. *Phys. Rev.* **1962**, *128*, 2042.
- (22) Goldman, M.; Shen, L. *Phys. Rev.* **1966**, *144*, 321.
- (23) Tanaka, H.; Nishi, T. *Phys. Rev. B* **1986**, *33*, 32.
- (24) Cody, G. D.; Obeng, M.; Thiyagarajan, P. *Energy Fuels* **1997**, *11*, 495.
- (25) Cheung, T. T. P.; Gerstain, B. C. *J. Appl. Phys.* **1981**, *52*(9), 5517.

Table 1 Results of Proton Longitudinal Relaxation Measurements for Blind Canyon Coal Swollen in Deuterated Pyridine.

S/C ^a	$T_{1\rho}$ [ms]		T_1 [ms]
	$T_{1\rho}^b$	$T_{1\rho}^{*c}$	
0	0.7(0.52)	4.8(0.48)	66(1.00)
0.36	-	-	65(1.00)
0.68	1.0(0.52)	5.7(0.48)	108(1.00)
1.03	1.3(0.59)	7.3(0.41)	104(1.00)
1.33	0.8(0.67)	5.3(0.33)	112(1.00)
1.67	1.7(0.62)	12.1(0.38)	128(1.00)
2.24	1.7(0.54)	12.9(0.46)	141(1.00)
2.57	1.8(0.55)	15.8(0.45)	145(1.00)
3.52	1.7(0.54)	16.1(0.46)	130(1.00)
4.72	1.8(0.52)	20.2(0.48)	144(1.00)

Values in parentheses; fraction of each component, ^a Mass ratio of solvent to coal ^b Fast. ^c Slow.

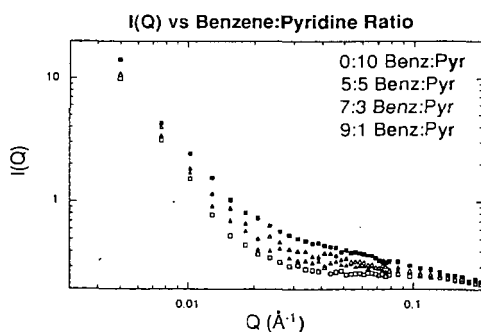


Figure 1 Coherent scattering intensity vs momentum vector for variably swollen BL residues in binary solvent of benzene-pyridine

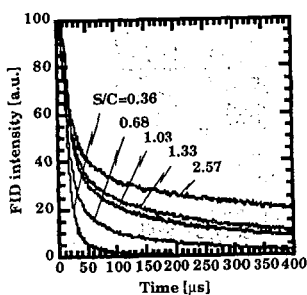


Fig.2 Transverse relaxation signals for pyridine swollen BL coal.

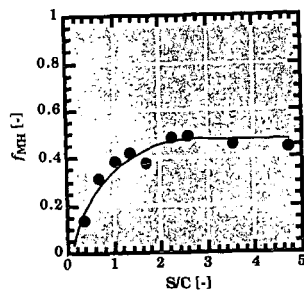


Fig.3 Change in f_{MH} with S/C.

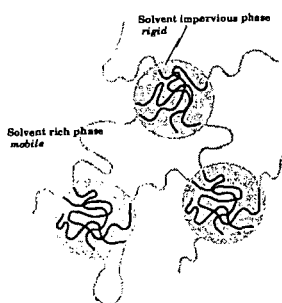


Fig. 4 Conceptual model for microdomain structure of solvent-swollen coal.

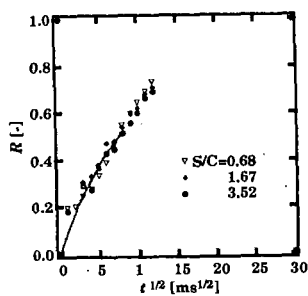


Fig.5 Recovery of proton magnetization in SI phase as a function of $t^{1/2}$ for the solvent-swollen BL coal. Solid lines represent the best fit to the data using a diffusion model.

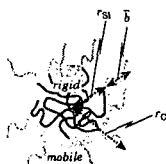


Fig.6 A 3-D domain model used to calculate the interdomain spacing from the spin diffusion distance.

SMALL ANGLE X-RAY SCATTERING STUDY OF COAL SOOT FORMATION

R. E. Winans, J. T. Parker[†], S. Seifert, and T. H. Fletcher[†]

Chemistry Division, Argonne National Laboratory, Argonne, IL 60439

and [†]Chemical Engineering Department, Brigham Young University, Provo, UT 84602

Keywords: soot, SAXS, coal

ABSTRACT

The objective of this study is to examine, by small angle X-ray scattering (SAXS), the formation of soot from individual coal particle combustion in a methane flat flame burner. The SAXS instrument at the Basic Energy Sciences Synchrotron Radiation Center (BESSRC) at the Advanced Photon Source (APS) can be used to observe both the formation of spherules and clusters since it can access length scales of 6-6000 Å. The high X-ray flux enables rapid acquisition of scattering data of various regions of the flame. SAXS data reveal particle size, shape, surface areas, and surface roughness.

INTRODUCTION

Particulate formation in many types of combustion, such as in diesel engines and coal combustion, is a significant problem. For example, in coal combustion, soot formation control is important because of radiation heat transfer effects. The objective of this study is to observe in situ the formation of particles in flames using small angle X-ray scattering (SAXS). As a result of a DOE-BES Facilities Initiative (1), we have developed a high resolution SAXS instrument in the BESSRC-CAT at the Advanced Photon Source (APS). The SAXS facility offers new capabilities for measuring atomic order within disordered media, including combustion particulates, on a length scale of 6-6000 Å. A small research, flat flame burner has been constructed (2). The flux of photons from an undulator at the APS is needed to be able to observe the small number of soot particles in combustion of single coal particles.

We propose to look at the problem of particulate formation in coal combustion from the early growth stages to particulate agglomerate formation, all using SAXS. In an early in situ study (3) using SAXS to probe flames, the author noted that optical techniques had a lower limit of 600 Å while his instrument had an upper limit of 1000 Å. Typically, individual soot particles cluster to sizes starting at ~1000 Å. Optical methods can readily observe the clusters, but not the smaller spherules as they are formed. Our instrument can observe both the formation of spherules and clusters since it can access length scales of 6-6000 Å. SAXS data can reveal particle size, shape, surface areas, surface roughness and can provide information on the internal structure. This method provides complementary data to that obtained by optical methods.

Presently, a number of optical techniques are used to study soot in flames. Recently, Köylü (4) observed that there were large errors in determining soot particle size from light scattering. Also, the determination of properties were suspect due to uncertainties in soot refractive indices. However, thermophoretic sampling compiled with transmission electron spectroscopy (an ex situ method) has provided reliable size and shape information on the soot aggregates (4,5). These data can be used to help interpret the in situ SAXS results. Other optical techniques, such as laser induced fluorescence (6), have been used to analyze the pyrolysis process and especially to look at the polycyclic aromatic hydrocarbons, which are the probable precursors to soot.

A classic paper by Freltoft, Kjems, and Sinha (7) describes how power law correlations of small angle scattering can be used to describe clusters of small particles. A parameter called the fractal dimension (d_f) can be derived from this correlation. This value, d_f , relates how the mass of a cluster changes with a linear dimension. We have used this approach to examine coal derived molecules in pyridine with small angle neutron scattering data (8).

The experiments were conducted using a smaller version of a Hencken flat flame burner using a methane-air flame as the heat source. The coal particles are introduced individually through the center of the burner (5). It can be run fuel rich to observe pyrolysis or fuel lean to combust the coal particles. Other fuels, such as hydrocarbons, have been used with this burner. The burner is mounted on vertical and horizontal translation stages so that different parts of the flame can be probed.

EXPERIMENTAL

The SAXS instrument was constructed at ANL and used on the Basic Energy Sciences Synchrotron Radiation Center CAT undulator beamline ID-12 at the Advanced Photon Source (<http://www.bessrc.aps.anl/>). The SAXS instrument has been designed to minimize parasitic scattering which would interfere with scattering from dilute samples such as soots in flames. An important key to this feature of the instrument is that the beam is defined 20 m from the sample which reduces the problem of scattering from the defining slits. A schematic of the instrument is shown in Scheme 1.

Monochromatic X-rays (8.5 - 23.0 keV) are scattered off the sample and collected on a 9-element mosaic CCD detector (15 x 15 cm) with maximum of 3000 x 3000 pixel resolution with 10 sec exposure times (9). The scattered intensity has been corrected for absorption, the air scattering, and instrument background. The differential scattering cross section has been expressed as a function of the scattering vector Q , which is defined as $Q = (4\pi/\lambda) \sin \theta$, where λ is the wavelength of the X-rays and θ is the scattering half angle. The value of Q is proportional to the inverse of the length scale (\AA^{-1}). The instrument was operated with two different sample-to-detector distances, 68.5 cm to obtain data at $0.04 < Q < 0.7 \text{ \AA}^{-1}$ and 3740 cm to measure at $0.006 < Q < 0.1 \text{ \AA}^{-1}$.

The Argonne Premium Coal Samples (10) used in this study were sized to the range of 45-75 μm . The burner used for these studies was a 1" x 1" axial symmetric flat flame burner produced by Research Technologies. The coal and liquids were fed through a tube centered in the burner and, a 0.25" nitrogen and helium co-flow around the perimeter was used to stabilize the methane/hydrogen flame. The individual coal particles were fed to the flame using a technique which has previously been described (5). Liquid samples were introduced into the flame via a 0.25 μm fused silica tube which protruded 2 mm above the surface of the burner. Samples such as toluene and heptane were flowed into the flame at 0.1 ml using an automated syringe.

The burner was mounted on a x-y translational stage such that the flame could be moved through the X-ray beam both vertically and horizontally.

Small Angle X-ray Scattering

A typical plot of the scattering data for soot formation as a function of distance from the top of the burner of the Illinois No. 6 bituminous coal (APCS 3) is shown in Figure 1. These curves can be analyzed to determine size of features, topology, and changes in total scattering. Power law slope from the data, such as is shown in Figure 1, are used to describe the topology of the system. Finally, the invariant Q_0 is calculated and is proportional to the fluctuation of the electron density in the system. Changes in the invariant are useful in monitoring topological changes in the sample, $Q_0 = \int_0^\infty I(Q) Q^2 dQ$. For example, the invariant goes to zero for a homogeneous system that does not have any concentration fluctuation.

RESULTS AND DISCUSSION

The scattering data were obtained as the burner was moved in 1 mm steps, such that the X-ray beam passed through the flame vertically from the bottom (0 mm) to 40 mm above the bottom. In addition, vertical sets of data were collected as the beam was positioned on center, where the coal particles emerged, and 1 ml increments from the center. The Illinois No. 6 (APCS 3) data from a vertical set at the center of the burner is shown in Figure 1. An initial Guinier analysis of this data suggests that the particle sizes are polydispersed over the section of the flame where soot is observed. Also, there are no systematic changes in the invariant. However, as can be seen in Figure 2, the power law slope is increasing. This suggests that there is a roughening in the soot particle surface. Note the large amount of scatter in the data. This may mean that a wide range of soot particles are observed, or else that there is merely a lot of scatter in the data. With combustion of the coal particles, the scattering decreased rapidly as the X-ray beam is moved away from the center (not shown) and becomes difficult to measure at 3 mm from the center.

Hydrocarbons, such as toluene, gave much better data in this system than coal particles. The flame conditions and the data acquisition parameters are the same in both cases, but apparently a much more stable soot cloud results from the direct infusion of the aromatic hydrocarbon. The power law slope data for the toluene ($Q = 0.016$ to 0.04) is shown in Figure 3. For the first 5-10 mm of the lower part of the flame, the value of $d_p = 2.0$, strongly suggests that larger polycyclic aromatic

expected, the scattering for the combustion of heptane (not shown) was much less than that for toluene.

CONCLUSIONS

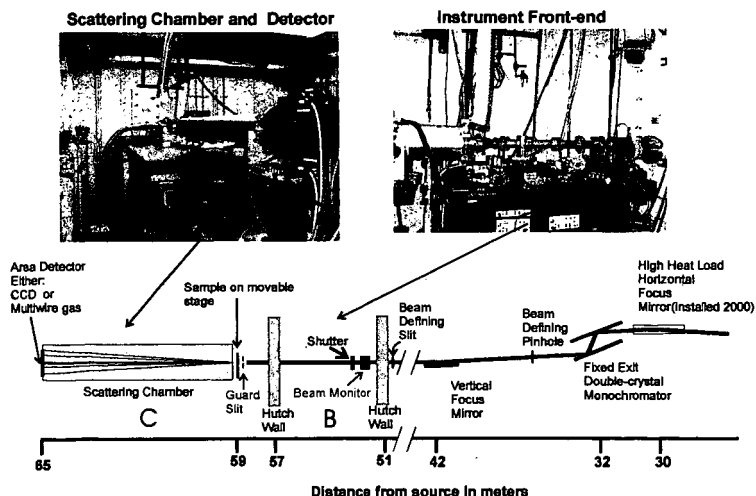
Some of the initial results look promising, but we need a low flame temperature in order to observe the intermediate sized particles. This approach may reduce the polydispersity.

ACKNOWLEDGMENTS

This work was performed under the auspices of the Office of Basic Energy Sciences, Division of Chemical Sciences, U.S. Department of Energy, and use of the Advanced Photon Source was supported by BES-DOE, all under contract number W-31-109-ENG-38. The support of the BESSRC staff is appreciated, especially J. Linton, M. Beno, G. Jennings, and M. Engbretson.

REFERENCES

1. DOE-BES Facilities Initiative entitled "Development of a Facility at APS for Time-Resolved/Anomalous Small Angle X-ray Scattering: Applications in Condensed Matter Research," R. E. Winans, P. Thiyagarajan, R. K. Crawford, K. A. Carrado, and D. M. Tiede.
2. McLean, W. M.; Hardesty, D. R.; and Poll, J. H. *Proc., 18th Symp. (Int'l.) Combust.*, 1213 (1980).
3. England, W. A. *Combust. Sci. and Tech.* **1986**, *46*, 83-93.
4. Köylü, Ü. Ö. *Combustion and Flame* **1996**, *109*, 488-500.
5. Ma, J.; Fletcher, T. H.; Webb, B. W. *Energy Fuels* **1995**, *9*, 802-808.
6. Ragucci, R.; De Joannon, M.; Cavaliere, A. *Proc., 26th Symp. (Int'l.) Combust.*, Vol. 2, 2525-2531 (1996).
7. T. Freltoft, J. K. Kjems, S. K. Sinha, *Phys. Rev. B* **33**, 269-275 (1986).
8. Cody, G. D.; Thiyagarajan, P.; Botto, R. E.; Hunt, J. E.; Winans, R. E. *Energy Fuels* **1994**, *8*, 1370-1378 (1994).
9. Westbrook, E. M.; Naday, I. *Methods Enzymol.* **1997**, *276*, 244-268.
10. Vorres, K. S. *Energy Fuels* **1990**, *4*, 420-426.



Scheme 1. TR/ASAXS Instrument on the APS BESSRC ID-12-B&C Undulator Beamline

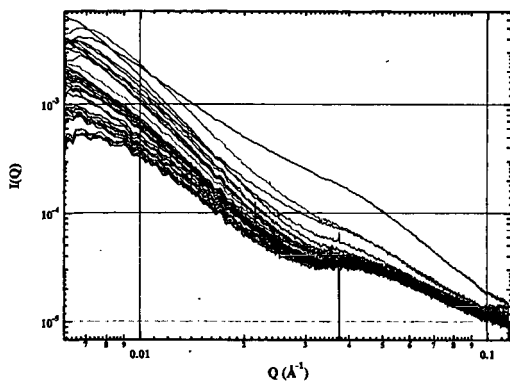


Figure 1. Scattering from Illinois coal (APCS 3) taken at 1 mm intervals from 0 to 40 mm above the top of the burner centered.

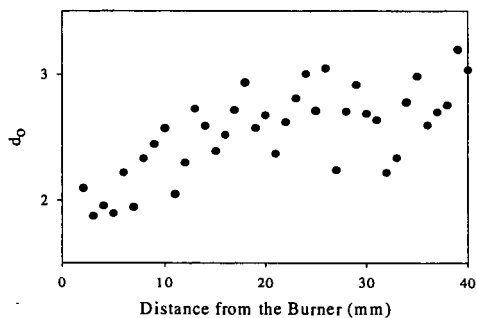


Figure 2. Power law slope from scattering of Illinois coal (APCS 3) soot taken along the centerline at 1 mm intervals from 0 to 40 mm above the top of the burner.

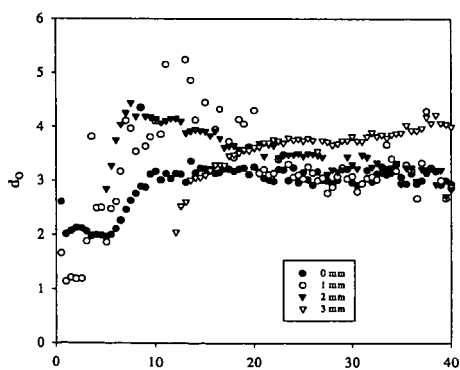


Figure 3. Power law slope from scattering of toluene soot taken at 1 mm intervals from 0 to 40 mm above the top of the burner at 1 mm intervals from the center.

For comparison, the nickel-impregnated coals were also prepared. About 1 g of raw coal was immersed in an aqueous solution containing about 6 or 12 wt % of nickel chloride and the water in this mixture was evaporated at 323 K under vacuum using rotary evaporator. The pH of the solution was controlled by using HCl or NH₃. The impregnated samples are identified using an additional code indicating impregnation (Im) and the pH at the time of impregnation, e.g., 10.51Ni (Im, pH3) for the specimen impregnated with 10.51 wt% nickel from solution of pH 3.

2.2 C1 Gas Analysis. The pyrolysis experiment was carried out in a fixed-bed-type pyrolyzer under helium flow at a heating rate of 5 K/min from 373 to 1173 K, and the evolved C1 gases were analyzed every 6 min by a gas chromatograph attached to the pyrolyzer.

2.3 Infrared Spectroscopy. Coal samples were diluted to 3 wt% by mixing of potassium bromide. Infrared spectra were obtained by diffuse reflectance method using a Perkin-Elmer 1600 Series FT-IR spectrometer.

2.4 XAFS. The details of procedure were described previously.^{8,9} Briefly, data were collected at beam lines BL-7C, -10B, and -12C at the Photon Factory. Data were recorded in the transmission mode in the region of the Ni K edge (8331.7 eV) at room temperature. The transmission spectra were collected using ion chambers that were filled with nitrogen gas. EXAFS oscillation was extracted from the EXAFS raw data by using a cubic spline method and normalized with the edge height. The k^3 -weighted EXAFS spectra were Fourier transformed to R space. The inversely Fourier filtering data were analyzed by a curve-fitting technique on the basis of the single-scattering plane-wave theory. Experimentally determined phase shifts and backscattering amplitudes for Ni-Ni and Ni-O were obtained from EXAFS data for Ni foil (Ni-Ni; coordination number (N) = 12, distance (R) = 2.488 Å) and NiO (Ni-O; N = 6, R = 2.098 Å), respectively.

3. RESULTS AND DISCUSSION

3.1 C1 Gas Evolution. Typical C1 gas evolution profiles are given in Fig. 1. Obviously, the gas evolution was affected by the presence of nickel. The main features in the nickel-exchanged coals can be summarized as follows. The evolved CO gas shown in Figure 1(b) - (d) consisted of two peaks; one at 670 - 770 K and the other at around 920 K. When the nickel content was increased, the former peak shifted to lower temperature by 100 K but was almost the same in height. On the other hand, the latter peak height increased with the nickel contents, notably in the region below 3 wt%. For CO₂ evolution, it was seen that main peak shifted to lower temperature by 20 - 30 K compared to AW coal. The CO₂ evolution in the higher temperature region, above 800 K, was negligibly small for nickel content below 3 wt%, whereas the CO₂ in this region increased with the amount of nickel above 3 wt%. The CH₄ evolved profile had a small decrease in the middle temperature region between 720 and 870 K, possibly due to the nickel catalyzing secondary decomposition.

For nickel-impregnated coals, C1 gas evolution profiles are also shown in Figure 1. When the pH of the solution was low (Fig. 1(e)), C1 gas profile was similar to that of AW coal. On the contrary, C1 gas profile of sample prepared in the high pH of the solution (Fig. 1(f)) was similar to that prepared by ion exchange method.

The total gas evolution versus metal loading is presented in Fig. 2. The filled marks in this figure indicate the gas evolution from the impregnated coal. The effects of metal observed here consist of those metal-catalyzed decomposition of functional groups and the secondary conversion of oxygen containing volatiles into CO and CO₂ catalyzed by metal elements. From this figure, CO yields remarkably increased from 8% to 15% with increasing nickel loadings from 0 to about 3 %, whereas CO₂ yields were almost constant at about 7% in the same region of nickel contents. Above 3wt% of nickel loadings, CO and CO₂ yields gradually increased. It seems that the exchanged nickel below and above about 3 wt% differ somewhat in the way it affects the decomposition, whereas the impregnated nickel behaved quite differently and yielded less gases than the exchanged nickel.

These differences can be ascribed to a different state of nickel species. In the case of ion exchange, nickel ions are associated with carboxyl groups. On the other hand, most of nickel species loaded by impregnation method would form a cluster of the metal salt and, upon decomposition, distribute over the entire coal surface and not limited specifically to functional group sites. Therefore, it is likely that the exchanged nickel ions have a stronger influence than the impregnated species on the decomposition of functional groups in coal.

3.2 States of nickel species after ion exchange. For the nickel-exchanged coals, it is very interesting to change the pyrolysis behavior below and above 3 wt% of nickel loadings. In order to examine the chemical state of the exchanged nickel ions in brown coal, FT-IR measurement was carried out. Figure 3 shows the IR spectra of brown coals with various

exchanged nickel contents. The differences of IR spectra between AW and the nickel-exchanged coal are also shown in this figure. From this figure, it was found that the absorption band of carboxyl groups, which appeared at 1720 cm^{-1} , decreased with increasing nickel contents. On the contrary, the bands of OCO asymmetric stretching (ν_s) at 1550 cm^{-1} and OCO symmetric stretching (ν_s) at $1480 - 1410\text{ cm}^{-1}$ of carboxylate groups increased. It should be noted that the peak position of ν_s band depended on the amount of the exchanged nickel. The peak at 1480 cm^{-1} in low nickel loaded sample was dominant, but in high nickel loaded sample the peak at 1410 cm^{-1} was dominant. This suggests that the chemical state of nickel species differs by the nickel content. According to reference, it was found that this difference of peak position corresponded with the difference of the structure of carboxylate groups; the nickel ions in low loaded sample were associated with carboxyl groups in the form of bidentate-type, while those in high loaded sample were in the form of bridge-type.

3.3 EXAFS. To examine how such differences in the chemical form of nickel species influence on the behavior of nickel species during pyrolysis, EXAFS experiments were carried out. Figure 4 shows the Fourier transforms for EXAFS spectra of the 0.77Ni and 6.4Ni samples pyrolyzed from 373 to 853 K. From Fourier transformed EXAFS spectra of both nickel exchanged coals at 373 K, only Ni-O bond appeared between 1 and 2 Å was observed, indicating that the nickel species were highly dispersed on the brown coal surface independent of nickel loadings. The intensity of Ni-O bond decreased with increasing heat treatment temperature, while new peak around 2.5 Å, which was attributed to Ni-Ni bond, was appeared and its intensity increased. That is, the divalent nickel ions were reduced to the metallic state during pyrolysis. More interestingly, the transition temperature from divalent cations to metal particles depended on the nickel contents. Figure 5 shows the dependence of Ni-Ni coordination numbers on the pyrolysis temperatures. Nickel species in the low loaded sample aggregated to metal particles at 750 K. On the other hand, nickel species aggregated at 650 K in the high loaded sample. The transition temperature for the low loaded sample was 100 K higher than that of the high loaded sample. These transition temperatures corresponded with temperatures of the former CO peak described previously, which appeared at 770 K in the low loaded sample and at 670 K in the high loaded sample. The peak shift at about 100 K suggests that the states of nickel species in coal and their effects are different according to the nickel amounts. We suppose that the metallic nickel particle formation is related to the decomposition of carboxyl groups / CO evolution.

4. CONCLUSIONS

The following conclusions are obtained in this study.

- (1) At the initial stage of pyrolysis, the exchanged nickel influenced on the decomposition of functional groups.
- (2) The chemical structure of nickel carboxylate groups differs by the nickel content; the nickel ions in low loaded sample were associated with carboxyl groups in the form of bidentate-type, while those in high loaded sample were in the form of bridge-type.
- (3) By using XAFS technique, the aggregation temperature of nickel species, which was 750 K at low loaded sample, was observed to have shifted to lower temperature by 100K at high loaded sample.

References

- (1) Otake, Y., and Walker Jr., P. L., *Fuel*, **72** (1993) 139.
- (2) Tyler, R. J., and Schafer, H. N. S., *Fuel*, **59** (1980) 487.
- (3) Franklin, H. D., Peters, W. A., and Howard, J. B., *Fuel*, **61** (1982) 155.
- (4) Schafer, H. N. S., *Fuel*, **58** (1979) 667.
- (5) Schafer, H. N. S., *Fuel*, **58** (1979) 673.
- (6) Murakami, K., Shirato, H., Ozaki, J., and Nishiyama, Y., *Fuel Process. Tech.*, **46** (1996) 183.
- (7) Murakami, K., Ozaki, J., and Nishiyama, Y., *Fuel Process. Tech.*, **43**, (1995) 95.
- (8) Shirai, M., Murakami, K., and Nishiyama, Y., *Energy Fuels*, **11** (1997) 1012.
- (9) Shirai, M., Arai, M., and Murakami, K., *Energy Fuels*, **13** (1999), 465.

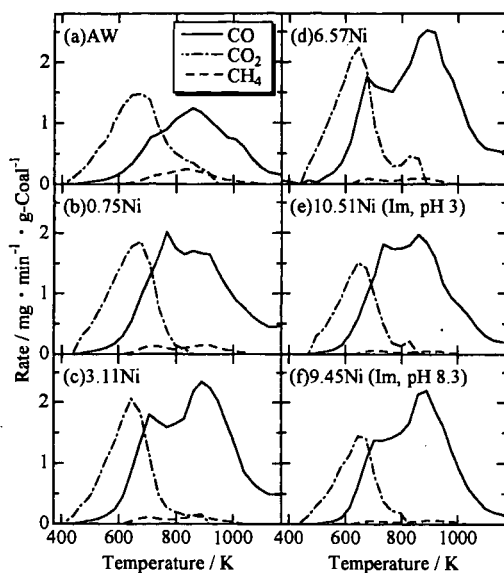


Figure 1. C1 gas evolution profiles of AW, nickel-exchanged coals, and nickel-impregnated coals.

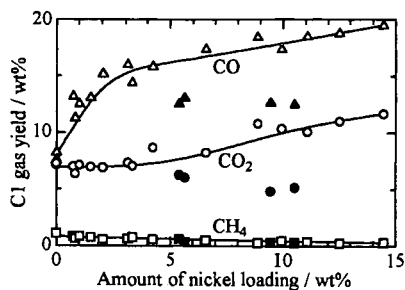


Figure 2. Change of C1 gas yields with the amount of nickel loading. Filled marks indicates impregnated samples.

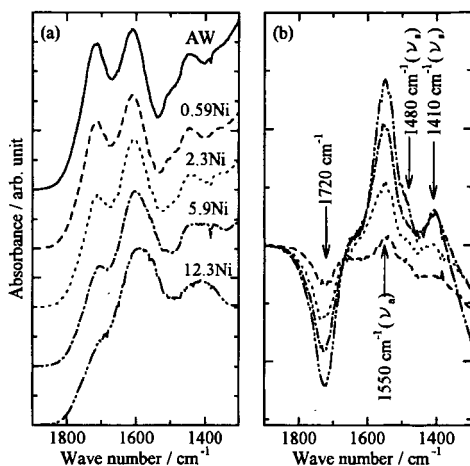


Figure 3. (a) IR spectra and (b) difference spectra of the nickel-exchanged coals.

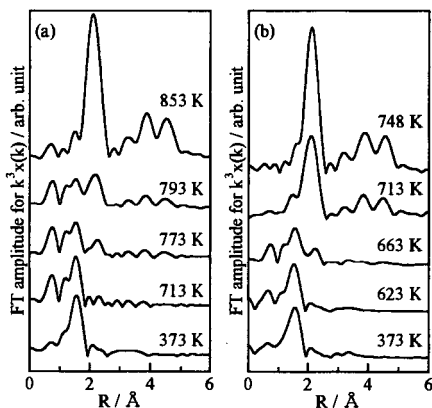


Figure 4. Fourier transforms for EXAFS oscillations of (a) 0.77Ni and (b) 6.4Ni nickel-loaded brown coals treated at several temperatures. These distributions were obtained by the Fourier transforms of the k^3 -weighted EXAFS data.

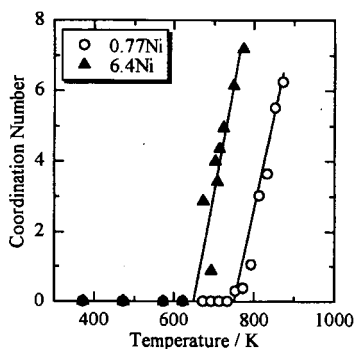


Figure 5: Coordination numbers of Ni-Ni bonds as a function of treatment temperature.

INFLUENCE OF ION-EXCHANGED NICKEL ON PYROLYSIS OF LOY YANG BROWN COAL

Kenji Murakami¹, Kiyoshi Fuda¹, Toshiaki Matsunaga¹, and Masayuki Shirai

¹ Department of Materials-process Engineering & Applied Chemistry for Environments, Faculty of Engineering and Resource Science, Akita University, Akita 010-8502, Japan

² Institute for Chemical Reaction Science, Tohoku University, Aoba-ku, Sendai 980-8577, Japan

Keywords: Pyrolysis, Ion-Exchanged Nickel, XAFS

ABSTRACT

Influence of ion-exchanged nickel on pyrolysis of Loy Yang brown coal was examined, partly using the X-ray absorption fine structure (XAFS) technique. Pyrolysis experiments were carried out up to 1173 K at 5 K/min in helium flow. CO yields remarkably increased from 8% to 15% with increasing nickel loadings from 0 to about 3 %, whereas CO₂ yields were almost constant at about 7% in the same region of nickel contents. Above 3wt% of nickel loadings, CO and CO₂ yields gradually increased. The peak of CO evolution in the acid-washed coal, without any nickel ions, was broad at 870K. On the contrary, the peak of CO was divided into two by the loading of nickel ions. First peak, which appeared at 670-770K, shifted to lower temperature with increasing ion-exchanged nickel, while second peak appeared at about 920K independent of the amount of nickel ions. Further, by using the XAFS technique, it was shown that the nickel species aggregated to metal particles at 750K in the case of low loaded sample and that the aggregation of nickel species shifted to lower temperature by 100K at high loaded sample.

1. INTRODUCTION

The pyrolysis behavior of brown coals and lignites on heat treatment has been studied extensively.¹⁻³ The initial stage of pyrolysis is thought to consist of decomposition of several functional groups. The thermal decomposition of functional groups affects significantly the initial stage of coal liquefaction, gasification, and pyrolysis, where several structural changes take place simultaneously. Particularly, it is very important to understand the effects of the ion-exchanged metal species, which are associated with mainly carboxyl groups, on the decomposition process, since these cations are well known to be good catalysts for coal conversion processes. Schafer investigated the relation between the decomposition of functional groups and the evolved gas during pyrolysis of acid-washed coal and alkali or alkaline earth metal exchanged coals.⁴⁻⁵ He presented that CO and CO₂, which were evolved from the acid-washed coal during heat treatment, originated from phenolic hydroxyl groups and carboxyl groups, respectively. In the case of the cation-exchanged coals, other oxygen-containing groups associated with carboxyl groups yielded CO₂ before the carboxylate groups decomposed into CO₂, that is, the presence of metal cation stabilized carboxylate groups. However, the details of the decomposition process are still not understood.

We reported previously that the temperature of the C1 gas evolution as well as the C1 gas yields during the pyrolysis of the nickel-exchanged coal changed by their loadings.⁶ This result suggests that the catalytic properties depend on the structure of active species during pyrolysis. The purpose of this study is to examine the influence of ion-exchanged nickel on pyrolysis of Loy Yang brown coal, partly using the X-ray absorption fine structure (XAFS) technique, which can provide information on local structure of highly dispersed catalytic species in coal.

2. EXPERIMENTAL

2.1 Sample Preparation. Loy Yang brown coal from Victoria, Australia, was used in this study. Raw coal was ground smaller than a 250 μ m particle size, washed with deionized water, dried at 323 K under vacuum, and stored in a desiccator. The analyses for this coal are as follows: C: 67.6 % (daf), H: 5.2 % (daf), N: 0.8 % (daf), O: 26.4 % (diff), and ash: 0.2 % (dry). Acid-washed coal (AW) was prepared by stirring the raw coal in 0.5 mol/l of hydrochloric acid for 24 h. The concentration of carboxyl groups was 3.7 mmol/g.⁷ About 10 g of the coal sample in 500 ml of an aqueous solution of nickel chloride at a concentration of 0.1 mol/l was stirred, and the pH of the solution was adjusted by adding ammonia or hydrochloric acid. After the pH remained unchanged for 5 h, the exchange reaction was judged to be equilibrium. The extent of exchanged nickel cation was determined by extracting the cation from the sample by hydrochloric acid. The nickel cation-exchanged samples are identified by the amount of loading (wt %), e.g., 0.75Ni for 0.75 wt% nickel-exchanged coal (daf).

WAVELENGTH DISPERSIVE X-RAY FLUORESCENCE SPECTROMETRY AS A TOOL TO STUDY THE EFFECTS OF PYRIDINE ON THE INORGANIC MOIETIES IN THE ARGONNE PREMIUM COALS.

David L. Wertz and Stephen S. DuBose
Department of Chemistry & Biochemistry
University of Southern Mississippi
Hattiesburg, MS 39406 USA
david.wertz@usm.edu

KEYWORDS. Gels, Pyridine, Inorganics

INTRODUCTION. Several manuscripts have appeared within the time frame of the Argonne Premium Coals Sample Program which have addressed the inorganic moieties contained in these coals. At the same time, numerous studies of the effects of liquids on the micro- and macro-level structuring in coals have been undertaken. This group, using x-ray diffraction, helped define the crystalline moieties in the APC's and, using x-ray scattering methods, has been studying the effect(s) of the additions of liquids on the average inter-layer distance for several of the coals. For many of these studies (including ours), pyridine has been of the liquids receiving primary focus - perhaps because of its polarity and its ability to form hydrogen-bonds. In addition, its aromaticity (and thus planarity) offers other possibilities for interactions with the organic moieties in coals. However, these same structural features cause pyridine to be an effective ligand towards metal ions - particularly the soft metal cations found in coals; and a extensive coordination chemistry exists using pyridine as either the solvent, and an inner-coordination sphere ligand, or both. In addition, pyridine has the capability to interact with both "inorganic" and "organic" sulfur. Consequently, the abundances of important inorganic species such as FeS_2 may be effected by the presence of excess pyridine. Presented below are the first results of a study of the gels produced by reacting pyridine with the APC's.

Experimental. 25 Mls of anhydrous pyridine (Aldrich) were added to a 5 grams (-100 mesh) sample of each of the Argonne Premium Coals. Each sample was allowed to equilibrate for 10-14 days. At the end of this period, the gels formed from the coal-pyridine interactions was separated from the remaining liquid by filtration. Each gel was air-dried and then mounted onto a sampleholder. A wavelength dispersive x-ray fluorescence (WDXRF) spectrum was obtained by irradiating each gel with rhodium Xrays (from an end-centered x-ray tube). The secondary Xrays emitted by each gel were focussed onto a graphite monochromator ($d = 3.342 \text{ \AA}$). The WDXRF spectrum was obtained by accumulating intensity data for 4 seconds at angular increments of $\Delta 2\theta = 0.05^\circ$ over the angular range from $2\theta = 8.00^\circ$ to 140.00° . In terms of the wavelength and the energy of the secondary Xrays, this angular region corresponds to:

2θ	λ	E
8.00°	0.47 \AA	26.4 keV
140.00°	6.30 \AA	1.97 keV

For comparison purposes the WDXRF spectrum of each of the APC's was also obtained.

RESULTS. Shown in Figure 1 are the superimposed WDXRF spectra of the eight Argonne Premium Coals. These spectra indicate the advantages of the wavelength dispersive method, good peak resolution and good signal/noise ratio. These spectra indicate that the eight APC's contain many of the same inorganic atoms, but in considerably different proportions. Principal among these are iron, calcium, and sulfur - which represent the major components. In addition, small peaks due to either titanium and/or potassium also appear in at least two of the spectra. These spectra verify the existence of the inorganic moieties previously reported.

The intensity of a specific peak in the WDXRF spectrum of a sample containing many components may be written as:

$$I_A(\lambda_A) = \eta_A \cdot M(\lambda_A) \cdot I^*(\lambda_A) \cdot \exp(-t_s \cdot \{\rho_s \cdot [\mu_s(\lambda_{Rh}) + \mu_A(\lambda_A)]\}). \quad (1)$$

In eq 1, $I_A(\lambda_A)$ is the intensity, typically in counts or counts per second, measured in the WDXRF spectrum and due to ana abundance of η_A of analyte A in the sample S. The efficiency of the spectrometer for detecting Xrays at wavelength λ_A is given by M. $I^*(\lambda_A)$ is the absorption and enhancement-corrected intensity due to 100% analyte A and may frequently be determined by iterative methods. The exponential includes several factors and is typically referred to as the matrix absorption effect(s). Among these factors are the mass absorption coefficients of the sample for the incident Rh Xrays and the mass absorption coefficient for the secondary Xrays

produced by analyte A, the density of the sample (ρ_s) and the thickness of the sample (t_s). Using mixtures of model compounds, the product of $M \cdot I^*$ is being determined for a number of the important analytes in these coals. In addition, the sample thickness is controlled by the opening in the sampleholder. Consequently, for comparisons, several of the parameters noted in eq 1 may be eliminated from further considerations.

Shown below is the WDXRF spectrum of an Argonne Premium coal compared to the WDXRF spectrum of the gel formed when that coal has been treated with pyridine. A summary of the analysis of the intensity under the iron K_α peak, the calcium K_α peak, and the sulfur K_α peak is presented in Table I.

TABLE I. COMPARISON OF PEAK INTENSITIES.

COAL	PEAK INTENSITIES IN COUNTS PER SECOND					
	Fe PEAK @ 1.94 Å		Ca PEAK @ 3.36 Å		S PEAK @ 5.37 Å	
	Coal	Gel	Coal	Gel	Coal	Gel
APC 101	19,083	15,007 -21%	2,181	1,822 -16%	2,005	1,734 -14%
APC 301	33,594	28,227 -16%	4,790	4,302 -10%	5,785	4,553 -21%
APC 401	16,008	10,451 -35%	2,026	1,388 -31%	4,089	2,621 -36%

Comparison show that the peaks intensities for these inorganics parallel their previously reported abundances, verifying the accuracies of the WDXRF method used in these experiments -- at least at a semi-quantitative level.

Peak intensity comparisons also show that in the transformation from the coal to the gel, the intensity of each peak is reduced -- by approximately the same amount. Each intensity reduction indicates that the abundance of each of these key inorganic moieties is also decreased. However, the cause(s) of the reductions in peak intensities has not been established unequivocally. This uncertainty in interpretation of the WDXRF spectra is because of the versatility of pyridine in its reaction(s) with coal. Specifically, it is known that pyridine causes coals to swell, which at the molecular level, is consistent with a change in the density of a powdered sample. The inclusion of pyridine into the organic matrix of the coal to form the gel causes a reduction in the abundances of the inorganic moieties in the coal. Both the change in abundances and the density change will affect the intensity of the analyte in an exponential manner. In addition, pyridine may complex with one (or more) of the inorganic analytes in the coal in such a manner as to be removed from the gel which is formed upon pyridine addition, thus causing a reduction in the abundance of that analyte.

Figure 1. WDXRF spectra of the Argonne Premium Coals.

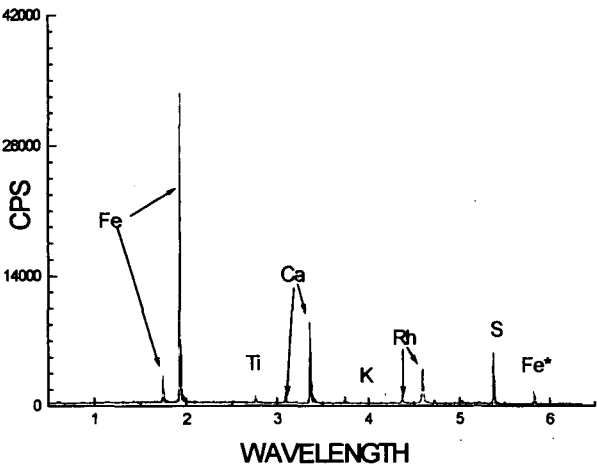


Figure 2. WDXRF spectra of APC 101 and its gel formed with pyridine.

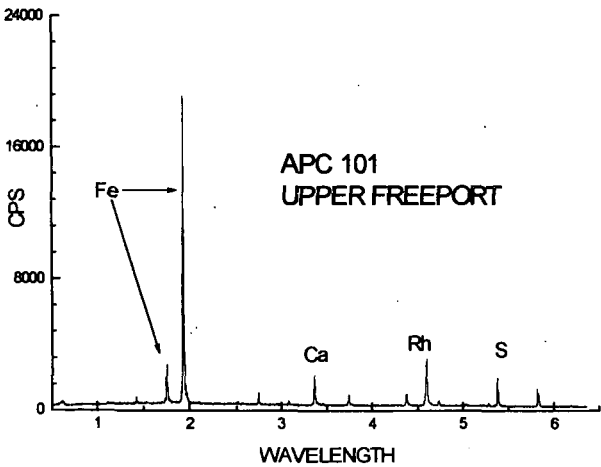


Figure 3. WDXRF spectra of APC 301 and its gel formed with pyridine.

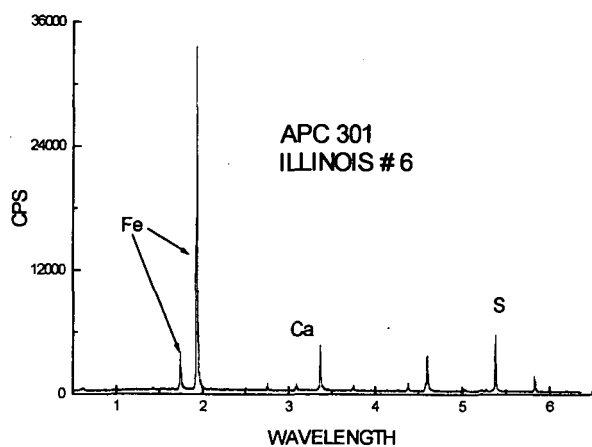
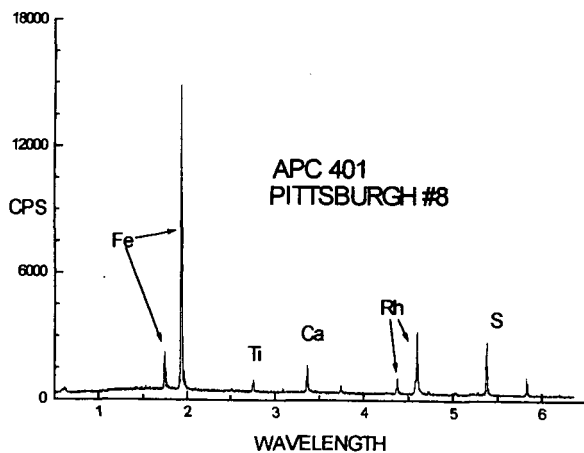


Figure 4. WDXRF spectra of APC 401 and its gel formed with pyridine.



SMALL ANGLE X-RAY SCATTERING STUDIES OF CARBON ANODES USED IN LITHIUM RECHARGEABLE BATTERIES

[†]Giselle Sandf*, [†]Kathleen A. Carrado, [†]Randall E. Winans,
[†]Sönke Seifert, and ^{††}Christopher S. Johnson

Argonne National Laboratory, [†]Chemistry and ^{††}Chemical Technology Divisions,
9700 South Cass Ave., Argonne, IL 60439

ABSTRACT

In our laboratories, disordered carbons with predictable surface area and porosity properties have been prepared using inorganic templates containing well-defined pore sizes. The carbons have been tested in electrochemical cells as anodes in lithium secondary batteries. They deliver high specific capacity and display excellent performance in terms of the number of cycles run. *In situ* small angle X-ray scattering (SAXS) during electrochemical cycling was carried out at the Advanced Photon Source, at ANL. In order to monitor the carbon electrode structural changes upon cycling, an electrochemical cell was specially designed to allow for the application of electrical current and the collection of SAXS data at the same time. Results show that upon cycling the structure of the carbon remains unchanged, which is desirable in reversible systems. The fractal dimension and the invariant do not show significant variation upon cycling the templated carbon electrode. However, large variations were observed for the graphite electrode, indicating changes in the sample topology.

KEYWORDS: SAXS, carbon anodes, lithium secondary batteries

INTRODUCTION

Carbonaceous materials have received considerable interest for use as anodes ever since Sony introduced the lithium-ion battery [1,2]. Carbon containing systems are noted for potential safety and reliability advantages because the carbon anodes are less prone to form dendrites than metallic lithium anodes. Most investigations have utilized carbon materials that are available from existing sources such as natural graphite, cokes, carbon fibers, non-graphitizable carbon, and pyrolytic carbon [3,4]. In these studies, high lithium capacities have been found to be associated with either disorder [5] or the presence of hydrogen [6].

An alternative avenue is the custom synthesis of carbons specifically tailored for use as anodes in lithium-ion batteries. This latter approach provides predictable control over critical properties such as the surface area and the porosity. Previously, Sandf and coworkers employed pillared clays with known interplanar spacing as templates for the synthesis of custom carbon anode materials [7-9]. They have also recently found that carbons with curved lattices can exhibit enhanced lithium capacity over that of graphite [10].

Our latest approach focuses on the use of sepiolite clay to tailor the synthesis of carbonaceous materials. Sepiolite is a phyllosilicate clay insofar as it contains a continuous two-dimensional tetrahedral silicate sheet. However, it differs from other clays in that it lacks a continuous octahedral sheet structure. Instead, its structure can be considered to contain ribbons of 2:1 phyllosilicate structure, with each ribbon linked to the next by inversion of SiO_4 tetrahedra along a set of Si-O-Si bonds. In this framework, rectangular channels run parallel to the x-axis between opposing 2:1 ribbons, which results in a fibrous morphology with channels running parallel to the fiber length. Channels are $3.7 \times 10.6 \text{ \AA}$ in sepiolite (they are $3.7 \times 6.4 \text{ \AA}$ in palygorskite). Individual fibers generally range from about 100 \AA to 4-5 microns in length, $100\text{-}300 \text{ \AA}$ width, and $50\text{-}100 \text{ \AA}$ thickness. Inside the channels are protons, coordinated water, a small number of exchangeable cations, and zeolitic water. There are three sorption sites in sepiolite: (a) oxygen ions on the tetrahedral sheets, (b) a small amount of cation exchange sites ($0.1\text{-}0.15 \text{ meq}/100\text{gm}$), and (c) SiOH groups along the fiber axis. Adsorption is also influenced by the size, shape, and polarity of

the molecules involved. The SiOH groups act as neutral adsorption sites suitable for organic species. These factors are all important to our goal of loading the clay with certain organic monomers that will polymerize on the surface and, following a pyrolysis step, carbonize to a material suitable for use as a carbonaceous anode in secondary lithium batteries.

Our main objective is to synthesize carbon with pores sizes capable of Li^+ diffusion in a rechargeable battery. The carbonaceous materials are derived from ethylene or propylene upon incorporation in the vapor phase in the channels of sepiolite, taking advantage of the Brønsted acidity in the channels to polymerize olefins. In order to monitor the carbon electrode structural changes upon cycling, an electrochemical cell was specially designed to allow for the application of electrical current and the collection of SAXS data at the same time.

EXPERIMENTAL

Details about the synthesis of the carbonaceous materials can be found in reference [11]. In summary, ethylene and propylene (AGA, 99.95%) were loaded and pyrolyzed in the gas phase in one step. A three-zone furnace was used. Quartz boats containing sepiolite were placed within a quartz tube. The temperature of the oven was gradually increased from room temperature (about 5 °C/min) to 700 °C. The oven was then held at that target temperature for 4 hours. The clay from the loaded/pyrolyzed sepiolite sample was removed using HF. It was then rinsed to neutral pH and refluxed with concentrated HCl for 2 hours. The sample was washed with distilled water until the pH was > 5 to ensure that there was no acid left. The resultant carbon was oven dried overnight at 120 °C.

In situ small angle X-ray scattering (SAXS) during electrochemical cycling was carried out at the Advanced Photon Source, (Basic Energy Sciences Synchrotron Research Center CAT), Argonne National Laboratory. Monochromatic X-rays (8.8 keV), are scattered off the sample and collected on a 18 x 18 cm² position sensitive two-dimensional gas detector. The scattered intensity has been corrected for absorption and instrument background. The intensity has been expressed as a function of the scattering vector Q , which is defined as: $Q = (4\pi/\lambda) \sin \theta$, where λ is the wavelength of the X-rays and θ is the scattering half angle. The value of Q is proportional to the inverse of the length scale (\AA^{-1}). The instrument was operated with a sample-to-detector distance of 68.5 cm to obtain data at $0.04 < Q < 0.7 \text{ \AA}^{-1}$. For these studies, a specially designed sample cell was used to record both the electrochemical response and SAXS data at the same time (see figure 1). The carbon sample was mixed with a teflon binder suspension (80/20 % w/w). The sample was oven dried and pressed against a Cu mesh. The electrode was then dried out in a vacuum oven at 80 °C overnight. A piece of lithium foil (0.008"; 0.203 mm from FMC Lithium Division, Gastonia, NC) with the same dimensions as the carbon composite was also pressed against Cu mesh. A propylene membrane (Hoechst-Celanese, Charlotte NC) was used as the separator. The electrodes were held together by using kapton tape along the edges. The electrolyte was 1 M LiPF_6 in a mixture of 50% v/v ethylcarbonate and 50 % v/v diethylcarbonate (Merck, Germany). A control experiment was performed using commercial graphite (Aldrich). The cell was discharged from the open circuit voltage (OCV) to 0 V and back to 2.5 V at a scan rate of 0.1 mV/s using a EG&G 273A potentiostat.

RESULTS AND DISCUSSION

In order to monitor the carbon electrode structural changes upon cycling, an electrochemical cell was specially designed to allow for the application of electrical current and the collection of SAXS data at the same time. The availability of very intense X-rays from synchrotron sources enables the use of SAXS to study the meso and micropore size distributions of many materials. Small-angle scattering from x-rays arises due to the presence of discontinuities in the density of a material. Thus, the particles and pores in the carbons can produce strong small angle scattering signals in a wide momentum-transfer range. The small angle scattering data can be modeled to obtain information on the microstructure of the porous network. In battery applications, if the liquid organic electrolyte penetrates the pores of the carbon anode, it leads to irreversible electrolyte decomposition during the first

electrochemical reaction of lithium with the carbon, and hence a large irreversible capacity. If the pores are small (of the order of 15 Å or less), and the structure remains intact, the liquid electrolyte cannot penetrate, so excellent reversible behavior should be expected.

Figure 2 shows a typical two-dimensional plot of the time-resolved studies of a lithium ion cell made with carbon derived from sepiolite/propylene composite (upper curves) and an electrode made from commercial graphite (bottom curves). A spectrum was taken of the cell at the open circuit voltage (OCV = 2.99 V for the templated carbon and 2.70 V for the graphite electrode) and used as the background correction for the subsequent measurements. Upon application of voltage, a spectrum was taken every 60 mV (every 5 minutes). The results obtained for the templated carbon indicated that during cycling, there are no structural changes upon lithium intercalation as is evidenced by the near overlap of all curves. This means that solvent penetration into the carbon anode, which causes irreversible capacity, is avoided and so excellent reversibility is attained. The results of the control experiment using commercial graphite clearly indicates that there are changes in the structure of graphite and that these changes are not reversible.

These curves can be analyzed to determine size of features, topology, and changes in total scattering. At small Q in the Guinier region, the radius of gyration (R_g), which is related to the size of the scattering features, can be determined. For example, R_g for spheres can be determined from the slope of $I(Q)$ vs Q^2 in a Q region where $R_g Q < 1.0$. Power law slope (fractal dimension) from the data is used to describe the topology of the system. Figure 3 shows the variation of the power law as a function of the applied voltage for both systems. For a layered material such a graphite a fractal dimension close to 2 is typical. When there is no lithium in the graphite lattice (at the OCV voltage), the fractal dimension must be close to the original material. In this case, the fractal dimension corresponded to 2.028, in excellent agreement to the theoretical value. As the voltage decreases, large fluctuations in the power law as a function of voltage are observed. At about 1.2 V, where the intercalation of lithium begins, the value of the power law increases to 2.16, indicating that the layers are expanding. These changes, however, are not reversible since the lattice does not contract to the original position. This is not the case for the templated carbon electrode, where the fractal dimension remains fairly constant throughout the voltage range. Since this is a disordered carbon, it is expected that the power law would be higher than graphite. The initial value corresponded to 2.57 and there are no significant changes throughout the measurement.

The invariant, Q_0 , is proportional to the square of the electron density difference in the system, and is calculated as follows:

$$Q_0 = \int_0^{\infty} I(Q) Q^2 dQ$$

Figure 4 shows a plot of invariant as a function of voltage for both electrodes. As expected, large variations in the electron density occur in the graphite electrode (especially at > 1.2 V) probably due to solvent incorporation upon irreversible lattice expansion, whereas the templated carbon shows variation within the statistical error.

CONCLUSIONS

Based on the electrochemical performance and much higher structural stability compared to graphite, carbon anodes derived from sepiolite as templates are demonstrated as good candidates for lithium ion cells. The synthetic approach described here yielded well defined carbon tubes with little or no graphitic character as evidenced by TEM. The yield of carbon based on the amount of inorganic template is about 25 times higher than our previous synthetic method, which makes it viable for commercial applications.

ACKNOWLEDGMENTS

This work has benefit from the use of the Advance Photon Source at Argonne National Laboratory, and was performed under the auspices of the U.S. Department of Energy, Office of Basic Energy Sciences, Division of Chemical Sciences, under contract number W-31-109-ENG-38.

REFERENCES

- [1] D. Linden (ed.), *Handbook of Batteries*, 2nd edition, p.36, McGraw Hill, New York (1995).
- [2] T. Nagaura and K. Tozawa, *Progress in Batteries and Solar Cells*, **9**, 209 (1990).
- [3] R. Takagi, T. Okubo, K. Sekine, and T. Takamura, *Denki Kagaku*, **65**, 333 (1997).
- [4] H. H. Schönfelder, K. Kitoh, and H. Nemoto, *J. Power Sources*, **68**, 258 (1997).
- [5] Y. Liu, J. S. Xue, T. Zheng, and J. R. Dahn, *Carbon*, **33**, 193 (1996).
- [6] P. Papanek, M. Radosavljevic, and J. Fischer, *Chem. Mater.*, **8**, 1519 (1996).
- [7] G. Sandí, R. E. Winans, and K. A. Carrado, *J. Electrochem. Soc.*, **143**, L95 (1996).
- [8] G. Sandí, K. A. Carrado, R. E. Winans, J. R. Brenner, and G. W. Zajac, *Mater. Res. Soc. Symp. Proc., Macroporous and Microporous Materials*, **431**, 39 (1996).
- [9] G. Sandí, R. E. Winans, K. A. Carrado, C. S. Johnson, and P. Thiyagarajan, *J. New Mat. Electrochem. Systems*, **1**, 83 (1998).
- [10] L. G. Scanlon and G. Sandí, *Journal of Power Sources* **81-82**, 176 (1999).
- [11] G. Sandí, K. A. Carrado, R. E. Winans, C. S. Johnson, and R. Csencsits, *J. Electrochem. Soc.*, **146**, 3644 (1999).

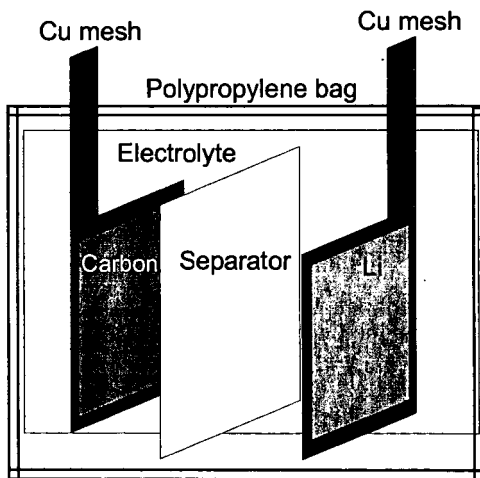


Figure 1: SAXS electrochemical cell for in situ measurements.

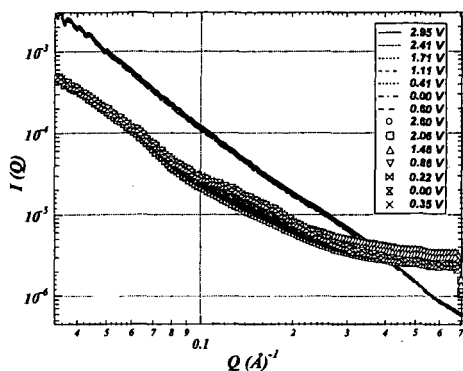


Figure 2: SAXS of electrodes made with templated carbon (upper lines) and commercial graphite (bottom symbols).

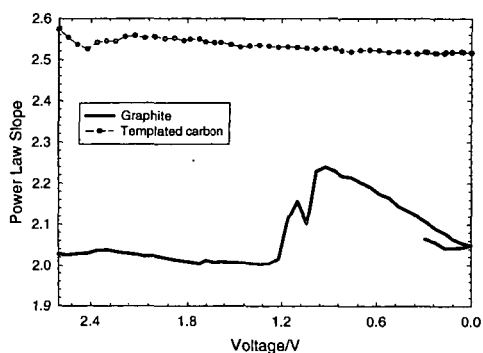


Figure 3: Variation of the power law as a function of discharged voltage of graphite and template electrodes.

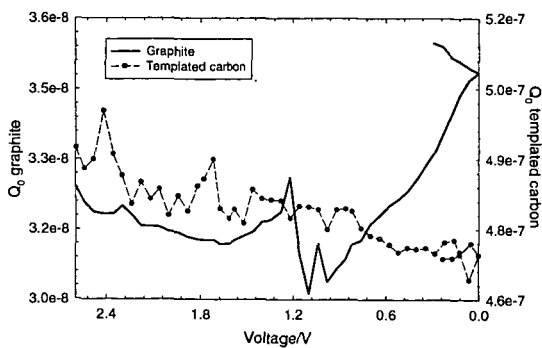


Figure 4: Invariant fluctuations as a function of discharge voltage of graphite and template electrodes.

STIMULI-RESPONSIVE POLYMER-GRAFTED LIPID-BASED COMPLEX FLUIDS AS ORGANIZED MEDIA FOR SUPRAMOLECULAR PHOTOCHEMISTRY

M.A. Firestone¹, D. M. Tiede¹, S. Seifert¹, and P. Thiyagarajan²

¹Chemistry and ²Intense Pulsed Neutron Source Division,
Argonne National Laboratory, Argonne, IL 60439

Keywords: Complex-Fluids, Stimuli-Responsive, Photochemistry

INTRODUCTION

Recent studies involving the use of micelles, reverse micelles, and microemulsions as organized microheterogeneous media for effecting photochemical transformations have led to growing recognition that the nature of the reaction medium (*i.e.*, microenvironment) may strongly influence the course and efficiency of photoinduced electron transfer (1,2). Of particular interest in photochemical energy conversion research is the study of such effects in natural photosynthesis, the process whereby plants and photosynthetic bacteria convert light into chemical energy. The primary process in photosynthesis occurs in transmembrane pigment-protein complexes called reaction centers (RCs), where following the absorption of light, primary charge separation occurs. This electrochemical energy is stored, and the initial charge separation used to drive all subsequent electron and proton transfer reactions in photosynthesis.

The bacterial photosynthetic reaction center provides an excellent protein-pigment complex with which to explore the influence of environment on biological electron transfer, as it is a membrane-associated protein that has been structurally well-characterized and that can be readily isolated from natural photosynthetic membranes and purified (3). One area of current research interest is the determination of the effect of conformational changes in detergent-solubilized RCs on electron transfer (4). In this report, we consider a related issue: the introduction of RCs into biomembrane mimetics and its impact on protein conformation, orientation, and function. As a medium for these studies, we have employed a recently developed a stimulus-responsive complex fluid (smart material) that possesses the ability to respond to an environmental change/external stimulus on a molecular level and amplify it in the form of a macroscopically observable phase/structural change (5). Specifically, this material undergoes a dramatic, thermoreversible phase change from a fluid, micellar phase to a biomembrane-mimetic, lamellar gel phase as the temperature is raised above 16°C. Macroscopically, this phase change manifests itself as a change from a low-viscosity state with no detectable optical birefringence to a high-viscosity (gel) state that shows strong birefringence (*i.e.*, liquid crystal). This complex fluid comprises three organic solids: a zwitterionic surfactant, a phospholipid, and a PEGylated phospholipid that spontaneously self-assembles into a non-covalent aggregate when dispersed in water. The inverted phase behavior (*i.e.*, a fluid phase at a lower temperature than the liquid-crystalline gel phase) of this composition is unique, and allows delicate biological macromolecules (*e.g.*, membrane proteins) to be introduced/dispersed in the complex fluid at low temperature and transferred to the ordered, liquid-crystalline phase by simply warming to room temperature. This material thus offers new opportunities for conducting studies of supramolecular photochemistry, for performing fundamental investigations on proteins such as RCs in native-like environments, and for examining how protein functioning is modulated by the surrounding medium. In addition, this complex fluid offers the potential for harnessing the native functioning of biological molecules for the development of protein-based devices for electro-optic and/or solar energy conversion by spatially organizing them in a synthetic matrix.

EXPERIMENTAL

Preparation of Reaction Centers and Complex Fluids. Membrane-associated, photosynthetic reaction centers (RCs) from the photosynthetic bacterium *Rhodospirillum rubrum* R-26 were isolated and purified using established procedures (6). Briefly, the RCs were extracted from chromatophores with a solution consisting of 0.6% (w/v) LDAO, 100 mM NaCl, and 10 mM Tris at pH 7.8, and partially purified by ammonium sulfate fractionation followed by sucrose density gradient centrifugation. Final purification was achieved on a DEAE Sepharose column by extensive washing with a solution of 0.06% (w/v) LDAO, 60 mM NaCl, and 10mM Tris at pH 7.8. Purified RCs were eluted from the column with 0.06% (w/v) LDAO, 280 mM NaCl, 10 mM Tris pH 7.8. RCs were dialyzed against 100 mM NaCl, 10 mM Tris pH 7.8, 0.1% LDAO prior to introduction into the complex fluid. The complex fluid was prepared by hydration of the organic components, dimyristoylphosphatidylcholine (DMPC), 1,2-dimyristoyl-sn-glycero-3-phosphoethanolamine-N-poly(ethylene glycol) (DMPE-EO₄₅), and lauryldimethylamine-N-oxide (LDAO) using the composition reported previously (5).

Physical Methods. UV-visible-NIR absorption spectra were recorded using a Shimadzu 1601 spectrophotometer at a spectral resolution of 2 nm. Time-resolved spectroscopic measurements were made with a single-beam, pump-probe, diode array instrument following procedures previously

described (7). Synchrotron small angle X-ray scattering (SAXS) measurements were performed either on the BESSRC undulator beamline (12ID) of the Advanced Photon Source (APS) at Argonne National Laboratory or at the Stanford Synchrotron Radiation Laboratory (SSRL, Stanford, CA) on beamline 4-2. The scattering profiles were recorded at APS were made with a mosaic detector composed of 9 CCD chips with an imaging area of 15 x 15 cm, with 1536 x 1536 pixel resolution. The scattering curves collected at SSRL recorded using a linear detector (BioLogic, Grenoble, France). The sample-to-detector distances were set such that the detecting range for momentum transfer was $0.006 < Q < 0.3 \text{ \AA}^{-1}$ at SSRL and $0.008 < Q < 0.8 \text{ \AA}^{-1}$ at APS. Samples were held in 1.5 mm quartz capillaries or in 1 mm pathlength plexiglass cells with quartz coverslips as windows. Data were corrected for background scattering and calibrated based upon the known positions of silver behenate powder Bragg reflections. Small angle neutron scattering was performed on the SAND beamline at the Intense Pulsed Neutron Source (IPNS), at Argonne National Laboratory. The average wavelength of radiation was 1-14 Å and the momentum transfer, Q was 0.0035 - 0.6 Å⁻¹. Samples were held in sealed, 1 mm pathlength quartz cells. Sample temperature was regulated by a water recirculating bath and measured using a calibrated thermocouple. Low temperature measurements were carried out with the sample chamber under a N₂ atmosphere. Samples were prepared with D₂O, thereby eliminating the large incoherent background arising from H₂O and enhancing the contrast between the lipid aggregates and the solvent. Data were collected with the sample-to-detector distance of 1.54 m. Scattered neutrons were measured using a 128 x 128 array of position-sensitive, gas-filled 40 x 40 cm proportional counters, while the wavelengths were measured by time-of-flight. Data were collected for 5-8 h and reduced using standard methods (9).

RESULTS AND DISCUSSION

In our initial investigations, the effect of introducing RCs into the stimuli-responsive complex fluid on the extent of denaturation of the protein and its functional properties were examined. Introduction of the protein (as a solution in its detergent-solubilized state) into the preformed complex fluid produced an optically transparent, deep blue gel at room temperature. Evaluation of the extent of retention of the native structure and photochemical activity of the reconstituted RCs was carried out by two spectroscopic assays. First, the stability of reaction centers within the gel phase of the complex fluid was determined by monitoring the position and relative intensities of the co-factor absorption bands. The photosynthetic reaction center from *Rhodobacter sphaeroides* R26 is a large protein (10⁵ kD) composed of three protein subunits (L, M, H) encasing nine co-factors arranged in *ca.* C₂ symmetry (3) (Figure 1B, C). Two bacteriochlorophyll molecules comprise the special pair that functions as the primary electron donor. On each side of this dimer is a bacteriochlorophyll monomer (Bchl) that, in turn, lies adjacent to a bacteriopheophytin (Bph), followed by a ubiquinone. A non-heme iron separates the primary quinone (Qa) from the terminal acceptor, the secondary quinone (Qb). The room temperature, ground-state absorption spectrum of the reaction center in the near-IR region shows three major absorbance bands, the position and intensities of which are sensitive to the integrity of the co-factors and local protein environment.

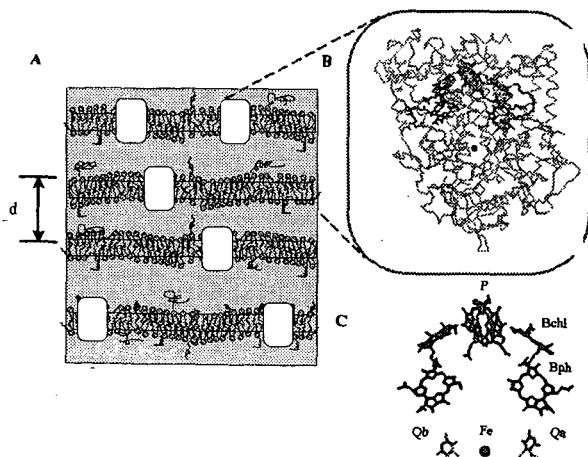


Figure 1. (A). Schematic showing lamellar structure of polymer-grafted lipid-based complex fluid with possible arrangement of reconstituted RCs. (B). The molecular structure of the photosynthetic reaction center (RC) of purple bacteria (*Rhodobacter sphaeroides* R26). (C). Co-factor arrangement of RCs taken from X-ray crystal structure data (3).

These absorption peaks, whose intensities are *ca.* 1:2:1, arise from the bacteriopheophytin (Bph, 755 nm), monomeric bacteriochlorophyll (Bchl, 802 nm), and bacteriochlorophyll dimer (P, 865 nm) cofactors. A comparison of the NIR absorption spectra of reaction centers in their detergent solubilized state and after their reconstitution into the lamellar gel phase of the complex fluid is presented in Figure 2. The close correspondence between the two spectra demonstrates that reaction centers can be successfully incorporated into the complex fluid without loss of structural integrity.

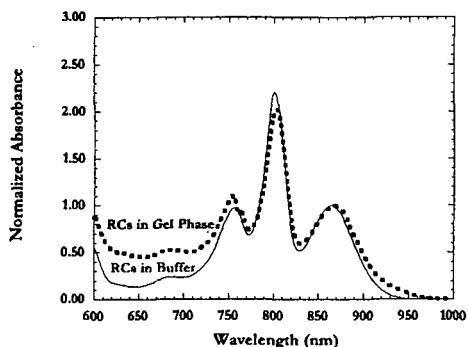
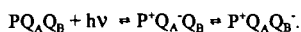


Figure 2. NIR absorption spectra of RCs in 10mM Tris-100mM NaCl-0.01%LDAO-0.01mMEDTA-pH7.8 buffer solution (solid line) and in polymer-grafted membrane-mimetic gel (dashed line).

The second spectroscopic assay involved evaluation of the photosynthetic activity of the RC in the gel phase of the complex fluid. A well-documented, diagnostic assay for reaction center photochemistry is the measurement of the laser flash-induced, transient absorbance decrease and recovery of the 865 nm absorption band of the primary electron donor chlorophyll, P (7). That is, following laser-induced, ps charge separation, the photosynthetic reaction ends with electron transfer between quinone cofactors (accompanied by proton uptake), Q_A and Q_B :



This electron transfer (between quinones) is the final such transfer in the reaction center, and the one that is the most sensitive to perturbation, since Q_B is a readily exchangeable cofactor. The recovery of the ground state P absorption following laser flash excitation has characteristic lifetimes that depend upon the extent of completion of the photochemical sequence. Kinetics for laser flash-induced recovery of the 865 nm band measured both for RCs in the native, detergent-solubilized state and in the gel phase of the complex fluid are shown in Figure 3. Recovery of the 865 nm band in the native RCs was fit as a biexponential function, with 90% of the recovery having a lifetime of 0.9 s, corresponding to recombination from the final $P^+Q_B^-$ state, and the remainder having a lifetime of 60 ms, corresponding to recovery from the $P^+Q_A^-$. In the gel sample, 80% of the recovery was fit with a lifetime of 1.4 s, and the remaining 20% was fit with a 120 ms lifetime. The recovery kinetics indicate that extent of the final $Q_AQ_B^- \rightarrow Q_AQ_B$ electron transfer was diminished only by about 10% in the gel phase. The increase in the recovery times for the $P^+Q_B^-$ and $P^+Q_A^-$ in the gel phase is consistent with previous measurements that showed similar recovery times for RCs in high osmolarity media (7). These results indicate that the polymer-grafted, membrane-mimetic matrix has no adverse impact upon the electron and proton transfer activities of the RC.

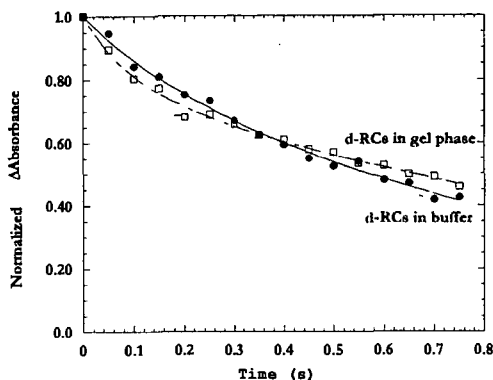


Figure 3. Kinetics for laser-flash induced recovery of the 865 nm band for RCs in 10mM Tris-100mM-NaCl-0.01%LDAO-0.01mMEDTA-pH7.8 buffer solution (solid circles) and in polymer-grafted membrane-mimetic gel (open squares).

To determine the effect of the introduction of RCs on the properties of the complex fluid, the response of the gel phase to addition of the RCs was examined by small angle X-ray diffraction. A typical SAXS pattern recorded for the complex fluid in the gel phase (at room temperature) is presented in Figure 4A. The pattern is dominated by four Bragg peaks of integral order ($Q = 0.041, 0.083, 0.124, 0.164 \text{ \AA}^{-1}$) and is indicative of a lamellar structure, that is, one consisting of alternating layers of water and organic components (Figure 1A). The first order Bragg peak corresponds to a periodicity of 153 Å. The effect of the incorporation of RCs (12 µm) into the gel phase is presented in Figure 4B. The SAXS profile shows the same periodic structure (*i.e.*, lamellar structure) as indicated by the integral order of the four observed Bragg peaks ($Q = 0.035, 0.072, 0.108, 0.144 \text{ \AA}^{-1}$). Some changes in the scattering pattern are apparent, however. First, the position of the first order Bragg peak indicates that the lattice spacing increases from 153 to 180 Å upon protein reconstitution. Second, introduction of RCs, which is believed to occur by insertion into the alkane region of the lipid bilayer, leads to both a reduction in the amplitude and an increase in the breadth of the diffraction peaks, suggesting a loss of spatial coherence and orientational disorder. This finding is consistent with prior work in which hydrophobic, dodecanethiol- derivatized gold nanoparticles, which selectively partition into the alkyl chains of the lipid/surfactant bilayer, were found to produce a similar effect on the observed SAXS profile (10).

Small angle neutron scattering (SANS) has also been used to assess the gels response to RC reconstitution and to obtain information regarding structural organization. Unlike X-ray scattering techniques, SANS permits determination of the structure of the fluid (cold) phase, by selective deuteration to highlight the aqueous channels (8). Previous, neutron scattering results yielded a low-resolution structure of the cold phase as normal hexagonal (5). Preliminary SANS investigations on complex fluid compositions incorporating reaction centers (data not shown) indicate that the cold phase structure changes to a cubic phase upon RC addition. Details of this analysis, along with results of studies employing deuterated reaction centers used to assess reaction center organization within these phases, will be presented in a future report (11).

CONCLUSIONS

The results presented here indicate that introduction of bacterial photosynthetic reaction centers into the polymer-grafted lipid-based complex fluid has no adverse impact on the structural or functional integrity of the protein. Preliminary investigations indicate that RC reconstitution does alter the structural organization of the complex fluid below the phase transition temperature (from a 2-D hexagonal array of prolate micelles to a 3-D cubic structure of micelles). Conversely, this introduction does not appreciably alter the structural properties of the gel phase of the complex fluid. Taken together, these results demonstrate that the complex fluid provides a medium of great potential utility in which to conduct fundamental investigations of protein structure and function.

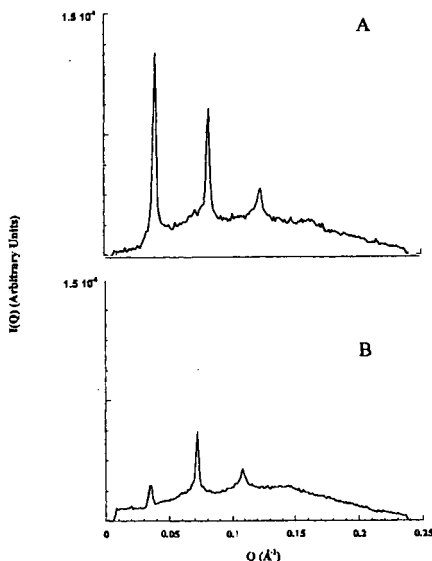


Figure 4. Small angle X-ray scattering profiles of (A) gel phase of the complex fluid, (B) gel phase incorporating 12 μm RCs.

ACKNOWLEDGMENTS

The authors would like to thank Dr. Hiro Tsurata (SSRL) for his help in using the scattering instrument at beamline 4-2 (SSRL). This work was supported by the U. S. Department of Energy, Office of Basic Energy Sciences, Division of Chemical Sciences, under contract W-31-109-Eng-38.

REFERENCES

1. (a) Scaiano, J. C.; Garcia, H. *Acc. Chem. Res.* **1999**, *32*, 783. (b) Willner, I.; Willner, B. *Top. Curr. Chem.* **1991**, *159*. (c) Fox, M. A. *Top. Curr. Chem.* **1991**, *67*.
2. (a) Weidemaier, K.; Tavernier, H. L. Chu, K. T.; Fayer, M. D. *Chem. Phys. Lett.*, **1997**, *276*, 309. (b) Suguru, H.; Datsura, N.; Shin-ichi, S.; Yotaro, M.; Hiroshi, I.; Takahiro, K.; Yoshiteru, S. *Chem. Lett.* **1999**, *3*, 191. (c) Behera, G. B.; Mishra, B. K.; Behera, P. K.; Panda, M. *Adv. Colloid Interface Sci.* **1999**, *82*, 1.
3. Feher, G.; Allen, J. P.; Okamura, M. Y.; Rees, D. C. *Nature*, **1989**, *339*, 111.
4. Utschig, L. M.; Ohigashi, Y.; Tiede, D. M.; Thurnauer, M. C. *Biochemistry* **1998**, *37*, 8278.
5. Firestone, M. A.; Thiagarajan, P.; Tiede, D. M. *Langmuir*, **1998**, *14*(17), 4688.
6. Marone, P. A.; Thiagarajan, P.; Wagner, A. M.; Tiede, D. M. *J. Crystal. Growth*, **1998**, *191*, 811.
7. Tiede, D. M.; Vazquez, J.; Cordova, J.; Marone, P. A. *Biochemistry*, **1996**, *35*, 10763.
8. Firestone, M. A.; Tiede, D. M.; Thiagarajan, P. in *Materials Research Using Cold Neutrons at Pulsed Neutron Sources*; Thiagarajan, P.; Trouw, F.; Marzec, B.; Loon, C.-K., Eds.; World Scientific Publishing Co.: New Jersey, **1999**, 160.
9. Thiagarajan, P.; Epperson, J. E.; Crawford, R. K.; Kippert, T. E.; Wozniak, D. G. *J. Applied Cryst.* **1997**, *30*, 280.
10. Firestone, M. A.; Rajh, T.; Makarova, O. V.; Seifert, S.; Teide, D. M.; Nedeljkovic, J. M. submitted to *Polymer Preprints*.

APPLICATIONS OF X-RAY METHODS TO SPECIATE MANGANESE

PARTICULATES FROM VEHICLES USING MMT FUEL

John G. Reynolds, and Art J. Nelson
Lawrence Livermore National Laboratory
Livermore, CA

J. Roos,
Ethyl Corporation, Richmond, VA

INTRODUCTION

Methylcyclopentadienyl manganese tricarbonyl (MMT) has been used as a fuel additive in both gasoline and diesel fuel [1]. Testing of fuels with this additive has been performed on a variety of makes and models of auto and diesel vehicles. These studies have been conducted with fuel containing MMT at a concentration of 0.03125 gram manganese per gallon. X-ray techniques (such as XAS and XPS) have been applied to samples of particulates collected from these test vehicles and engines to speciate the Mn and other metal compounds found in these exhaust particulates. Mn species such as phosphates, sulfates and oxides have been found in varying concentrations depending upon the make and model, the type of fuel, and the test conditions.

EXPERIMENTAL

Samples and techniques have been described in detail elsewhere [2]. The samples were collected using a Moudi Impactor on vehicles operated over the Urban Dynamometer Driving Schedule using a modification of the dilution tunnel technique described in 40 CFR Part 86. Seven samples were examined taken from five different vehicles: 92BR-TP (1992 Buick Regal Tailpipe), 93FE-TP (1993 Ford Escort tailpipe), 93FE-EO (1993 Ford Escort engine out), 93HC-TP (1993 Honda Civic tailpipe), 93HC-CO (1993 Honda Civic after catalytic converter), 93HC-TP (1993 Toyota Camry tailpipe), 93TCWOC-TP (1993 Toyota Camry without catalytic converter).

RESULTS

The approach for speciation of the Mn components employed the model compound technique. The selection of model compounds was based on knowledge of the behavior of Mn compounds in oxidative environments. The XPS and/or XAS spectra were taken on the samples and compared with spectra taken on the model compounds under the same conditions. Table 1 shows selected Mn, S, P, and O XPS parameters for the model compounds used in this study. Table 2 shows the XPS parameters for the particulate samples.

Table 1. Values of Binding Energies and Auger Parameter (in eV) for Manganese Model Compounds.

Sample	Mn 2p _{3/2}	FWHM ^a	ΔMn 3s	Mn LMM ^b	α ^c	O 1s	S 2p	P 2p
Mn	639.0	1.40	3.4	586.5	-28.1	—	—	—
MnO	640.9	2.34	6.0	582.9	-29.8	529.8	—	—
Mn ₂ O ₃	640.7	2.49	5.8	583.7	-29.2	529.5	—	—
Mn ₂ O ₄	641.0	2.02	5.7	583.6	-29.0	529.5	—	—
MnO ₂	641.7	2.50	4.8	583.8	-28.1	529.3	—	—
MnSO ₄	641.8	2.39	6.3	581.2	-30.6	531.9	168.6	—
MnS	640.4	2.03	5.7	584.4	-28.8	—	160.9	—
MnPO ₄	641.9	2.35	6.3	581.0	-30.7	531.8	—	133.9
Hureaulite ^d	641.5	2.11	6.3	581.3	-30.8	531.1 532.4	—	133.5
Mn ₃ P ₂ O ₇	641.7	2.43	6.3	580.8	-31.1	531.5	—	133.9
Mn ₃ (PO ₄) ₂	641.7	2.04	6.3	581.2	-30.7	531.6	—	133.5

a) Full width half-maximum of Mn 2p_{3/2} peak in eV.

b) Kinetic energy of Mn L_{2,3}M_{2,3}M_{4,5} Auger peak.

c) Auger parameter, α = BE + KE - 1253.6 eV.

d) Mn₃(PO₄)₂[PO₃(OH)]₂ · 4H₂O.

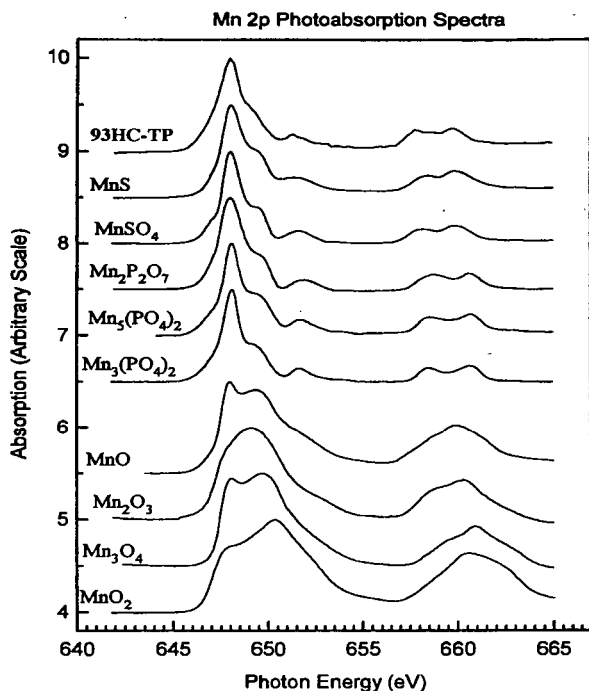


Figure 1. XAS spectra of selected Mn model compounds and the 1993 Honda Civic Tailpipe particulate sample.

Table 2. Binding Energies (in eV) of Major Elements Found in Particulate Emissions Collected on Cu and Au Foils.

Sample	Mn 2p _{1/2}	α^a	C 1s	O 1s	S 2p	P 2p
93HC-TP	641.8		284.5	529.9 531.5 532.8	163.4, 167.9	133.5
93HC-CO	641.7	-31.6	284.3	530.1 531.4 532.2	161.7, 162.9	133.4
92BR-TP	642.0		284.6	530.2 532.2 534.0	163.0, 169.1	133.9
93FE-TP	642.3		284.8	530.9 532.6	161.6, 163.6 166.9, 169.6	133.7
93FE-EO	641.9		284.5	532.2	161.6, 163.1	130.8 133.6
93TC-TP	641.9	-29.9	284.7	532.3	163.2, 169.4	133.6
93TCWOC-TP	642.0	-30.5	284.8	530.6 532.1 533.6	163.2, 168.1	130.7 133.7

a) Auger parameter, $\alpha = BE + KE - 1253.6$ eV.

Comparisons of the model compounds with the auto emission samples show that, in general, the particulates contain Mn phosphates, sulfates, and oxides.

Figure 1 show the XAS L-edge spectra of several Mn model compounds, one of the auto samples. Table 3 shows a summary of the XAS parameters for the model compounds, including energy shift, L_2 Linewidths and Branching ratios. Table 4 shows these parameters determined from the XAS L-edge spectra of the auto samples.

Table 3. Summary of the Mn L-edge Spectral Features for Selected Mn Compounds.

Compound	Mn Valency	$\Delta E(L_3 - L_2)$ (eV)	L_3 Linewidth FWHM (eV)	Branching Ratio $I(L_3)/I(L_3 + L_2)$
MnO ₂	IV	10.1	5.5	0.65
Mn ₂ O ₃	II, III	12.9, 11.5	4.1	0.68
Mn ₂ O ₃	III	11.5	3.9	0.68
MnO	II	12.1	4.0	0.70
Mn ₃ (PO ₄) ₂	II	12.9	1.2	0.85
Hureaulite ^a	II	12.9	1.3	0.83
Mn ₂ P ₂ O ₇	II	12.9	1.5	0.85
MnSO ₄	II	11.9	1.3	0.85
MnS	II	11.9	1.6	0.84

a) Mn₃(PO₄)₂[PO₃(OH)]₂ • 4H₂O.

Table 4. Summary of the Mn L-edge Spectral Features for Particulate Emissions Collected on Cu and Au Foils.

Sample	Estimated Average Mn Valency	$\Delta E(L_3 - L_2)$ (eV)	L_3 Linewidth FWHM (eV)	Branching Ratio $I(L_3)/I(L_3 + L_2)$
93HC-TP	II	11.9	1.7	0.85
92BR-TP	II	11.9	1.6	0.86
93FE-TP	II	11.9	1.8	0.84
93TCWOC-TP	II	11.9	1.5	0.85
93TC-TP	II	11.8	1.6	0.86

In agreement with the results from the XPS analyses, the predominant Mn species found in the particulate samples are Mn phosphates, sulfates, and oxides.

CONCLUSION

The XPS and XAS L-edge characterization of particulate emission samples taken from several automobiles operating with MMT in the fuels and in the UDDS mode show that the predominant Mn species are phosphates, sulfates, and oxides.

ACKNOWLEDGMENT

This work was performed under the auspices of the U.S. Department of Energy by the Lawrence Livermore National Laboratory under contract No. W-7405-ENG-48.

REFERENCES

- [1] J. E. Faggan, J. D. Bailie, E. A. Desmond, D. L. Lenane, SAE Paper 750925, Warrentonville, PA, Society for Automobile Engineering (1975). D. P. Hollrah, and A. M. Burns, *Oil and Gas J.* March 11, 1991, pp 86-90.
- [2] C. Colmenares, S. Deutsch, C. Evans, A. J. Nelson, L. J. Terminello, J. G. Reynolds, J. W. Roos, and I. L. Smith. *Applied Surface Sci.*, 1999, 151, 189-202.

STRUCTURE OF ACTIVATED CARBONS PRODUCED FROM PAPER MILL SLUDGE USING SMALL ANGLE NEUTRON SCATTERING

¹Giselle Sandf*, ²Nasrin R. Khalili, ³Kenneth C. Littrell, and ³P. Thyagarajan

¹Chemistry and ³Intense Pulsed Neutron Source Divisions, Argonne National Laboratory, 9700 South Cass Ave., Argonne, IL 60439; ²Department of Chemical and Environmental Engineering, Illinois Institute of Technology, Chicago, Illinois 60616

ABSTRACT

A novel, cost-effective, and environmentally benign process was developed to produce highly efficient carbon-based adsorbents (CBAs) from paper mill sludge. The production process required chemical activation of sludge using zinc chloride and pyrolysis at 750°C in N₂ gas. The produced CBAs were characterized according to their surface area and pore size distribution using N₂-BET adsorption isotherm data. Further characterization of the surface and pore structure was conducted using small angle neutron scattering (SANS). The structural features analyzed by SANS revealed the dependence of porosity on zinc chloride concentration. The presence of inaccessible pores was also determined by solvent contrast-variation SANS experiments.

KEYWORDS: SANS, carbon-based adsorbents, paper mill sludge, porosity.

INTRODUCTION

A series of novel carbon-based adsorbents (CBAs) have been produced from paper mill sludge. The significant feature of the produced sludge-based activated carbon, that makes it a unique and particularly economical adsorbent/catalyst/catalyst support system, is that waste materials are used for its production. The produced CBAs can be extensively used as adsorbents, catalysts and catalyst supports in a variety of industrial and environmental applications (such as purification processes, recovery of chemical products, and removal of organic and metals). Their adsorption capability and catalytic activity are largely controlled by their surface characteristics [1,2]. For example, carbons used for the adsorption of gases and vapors should have pores with effective radii considerably smaller than 16-20 Å [2], while activated carbons with pore sizes in the range of 20-500 Å have been shown to be significant adsorbents for the removal of coloring impurities from liquid phase systems [3]. The relationship between the surface properties of activated carbon and its effectiveness as an adsorbent or catalyst, emphasizes the importance of developing methodologies by which activated carbon with specified surface properties can be produced.

Analysis of the surface physical properties of the produced carbons initially included determination of the total surface area, extent of microporosity, and characterization of the pore size distribution using nitrogen adsorption isotherms data [2, 3, 4]. While the results of the surface analysis have shown that activation methodology used to produce novel CBAs has a significant impact on the surface structure and performance of the carbons produced, these data alone were not sufficient to draw definite conclusions about the extent of correlation between the carbons' microporous structure and the activation methodologies employed in their production. Therefore, small angle neutron scattering (SANS) was used to supplement existing analysis and provide valuable information about the microscopic structures of the carbons produced, such as produced pore distribution, pore width, pore radii, characteristic lengths, and voids. The SANS data were used to study the surface properties of the carbons at mesoscopic length scales and to characterize their microstructure by determining the sizes and geometries of the component clusters and through solvent contrast variation, the accessibility of their micropores to solvent.

This information is fundamental for the characterization of these carbons and evaluation of the extent of availability of their pores to adsorbates in gas and/or liquid phase environments.

EXPERIMENTAL

The raw paper mill sludge was first dried in an oven at 110°C for 24 hours, then crushed mechanically using a paint-mixing machine. Crushing provided smaller particles with increased surface area and also enabled more efficient chemical activation of the raw material. Samples were sieved after mechanical crushing to obtain particle with sizes smaller than 600 μm . This particle size range was found to be the most suitable for the chemical activation process that was performed using five different ZnCl_2 to dried sludge mass ratios of 0.75, 1.0, 1.5, 2.0, and 2.5 [5]. To ensure a complete reaction between ZnCl_2 and sludge particles, sludge was mixed with zinc chloride at 85°C for 7 hours. After chemical activation, samples were dried in air at 110°C for 24-36 hours. The time required for drying varied depending on the amount of zinc chloride used for the activation process (i.e., higher impregnation ratios required longer drying time). After drying, the sludge was crushed again into a fine powder. Chemically activated samples were exposed to light and humidity (L&H) for about 22 hours to enhance the development of the pore structure during pyrolysis [5].

Pyrolysis of the chemically activated and L&H-treated sludge was carried out in an inert environment (70ml/min flow of nitrogen gas) at 800°C for two hours. Upon completion of the pyrolysis, the sample was removed from the reactor and crushed using a mortar and a pestle. The crushed samples were then cleansed using 500 ml of 1.2 M HCl followed by 500 mL of distilled water to remove excess zinc chloride and residual inorganic matter. After drying in air, the samples were transferred to 20-mL vials for storage prior to conducting the physical activation process. During the physical activation, samples were heated for two hours at 800 °C in a mixture of 75% CO and 25% CO₂. Upon completion of the physical activation, the produced carbons were characterized according to their surface properties by BET and related measurements.

For the SANS measurements, the carbons were ground into a powder. The SANS measurements at the SAND time-of-flight SANS instruments at the Intense Pulsed Neutron Source at Argonne National Laboratory [6] using cylindrical Suprasil sample containers with a neutron optical path length of 1 mm. SAND provides data in a Q range of 0.004 to 0.6 \AA^{-1} in a single measurement. All samples were studied as dry powders. Additionally, a contrast-variation SANS study was performed on the sample treated with the highest zinc chloride ratio by preparing the powdered sample as slurries in mixtures of normal and deuterated toluene with deuterated toluene proportions of 0, 25, 50, 75 and 100 %. In preparing the slurries, the powder was slowly evacuated to avoid air bubble formation prior to adding the solvent. The scattering from an empty cell was used for background correction in these measurements.

RESULTS AND DISCUSSION

The SANS data for the dry powder samples was initially analyzed by using a modified version of the unified Guinier analysis and power law model proposed by Beaucage et al. [7, 8] to fit the full range of the data. As shown in Table 1, the results of this unified fit indicate that at the lowest Q scale, the behavior all of the dry powder carbon samples except the one prepared with a 0.75/1 ZnCl_2 ratio is that of surface-fractal interfaces of large objects. However, the low Q fractal dimension of -4 obtained for the 0.75/1 ZnCl_2 ratio sample is characteristic of a smooth interface. At higher Q and thus shorter length scales, the power law exponents obtained were consistent with those from mass fractal aggregates.

In order to gain a better understanding of the microstructure of these systems, we subtracted the low- Q power law behavior from the measured scattering curves, enhancing the visibility of features at higher Q , and fit the difference data using the model developed by Teixeira [9]. In this model, which describes the scattering from mass fractal aggregates of small, uniform spheres of radius R , the scattered intensity is given by:

$$I(Q; \xi, D_f, R) = I_{OS} \left(1 + \frac{\sin[(D_f - 1)\arctan(Q\xi)]}{(QR)^{D_f} \left(\frac{1}{Q^2 \xi^2} + 1 \right)^{\frac{D_f - 1}{2}}} \right) P_{Sphere}(Q; R) + I_{Background}$$

where D_f is the mass-fractal dimension, ξ is the exponential cutoff length for the aggregate, $I_{Background}$ is the background intensity, and I_{OS} is the intensity scattered by the fundamental sphere extrapolated to $Q=0$. Here,

$$P_{Sphere}(Q, R) = \left[\frac{3(\sin(QR) - QR\cos(QR))}{(QR)^3} \right]^2$$

is the scattering form factor for the fundamental sphere [10].

The data with the low Q power law scattering subtracted is compared with the fit functions in figure 1 and the corresponding fit parameters are given in Table 1. The results of the Teixeira model fits to the data for the samples prepared with the three highest ratios of $ZnCl_2$ indicates that these samples are similar in their microstructure. For these samples, both the fractal dimension and the size of the aggregates as indicated by the exponential cutoff size parameter ξ increase as the $ZnCl_2$ ratio increases. However, the other two samples are significantly different in their microstructure. The sample prepared with a $ZnCl_2$ ratio of 0.75 has a much lower mass fractal dimension and a much larger extent. The sample prepared with a $ZnCl_2$ ratio of 1.0 has a mass fractal dimension close to 1 and is better fit by the form factor for a cylinder [10]. Similar behavior has also been observed in silica systems [11]. The size of the fundamental particle of which these aggregates are composed is found from the fits to be approximately 2 Å and is thus of nearly atomic size.

The same approach was used to analyze the data from the solvent contrast variation study performed using slurries of the sample with a $ZnCl_2$ ratio of 2.5 immersed in different mixtures of toluene and deuterated toluene. The results of the fits are presented in Table 2. The quality of the fits to the data with the low Q power law behavior subtracted is shown in figure 2. The low- Q power law of this sample in 100% D-toluene was that of a mass fractal while all of the other samples had surface-fractal power-laws. Similarly, while the other four samples were well described by the Teixeira mass fractal model at high Q , the data for the sample in 100% deuterated toluene is inconsistent with this model but well described as a polydisperse, nearly hollow shell. The change in the shapes of the scattering curves without loss of intensity at low Q seen in figure 2 for the three samples with the highest concentration of deuterated toluene indicates that the toluene solvent is unable to completely contrast-match the scattering length density of the aggregates. This suggests that the toluene is not able to completely penetrate the micropores in these samples.

CONCLUSIONS

This SANS study has shown that the microscopic structure of these activated carbons prepared from paper-mill sludge is sensitively dependent on the ratio of $ZnCl_2$ used in their preparation. The mass fractal dimensions observed for the samples prepared with higher ratios of $ZnCl_2$ are similar to each other and to the fractal dimension of 2.5 associated with growth by percolation and/or diffusion-limited aggregation. The parallel trends observed in BET analysis and the structural determination by small angle scattering for these samples shows that modifications of the production procedure can significantly and systematically alter the quality and characteristics of the final products. The lower fractal dimensions of the other two samples show that they are lower dimensional structures. The fitted fractal dimension was consistent with the rod-like structure observed for the sample prepared with $ZnCl_2$ /sludge ratio of 1.

The small pore structure of these carbons suggests that they can be used in a variety of gas-phase cleaning applications. Further studies of the catalytic and adsorbate properties of these activated carbons and others similar to them correlated with these studies of their microstructure and mesoscopic surface structure will allow for the production procedure to be systematically tailored to produce activated carbons that are optimized for performance in a variety of applications.

ACKNOWLEDGMENTS

This work has benefitted from the use of the Intense Pulse Neutron Source at Argonne National Laboratory, and was performed under the auspices of the U.S. Department of Energy, Office of Basic Energy Sciences, Division of Chemical Sciences, under contract number W-31-109-ENG-38.

REFERENCES

- [1] Bansal, R. C.; Donnet, J.; Stoeckli, F. *Active Carbon*, NY:New York City, **1988**.
- [2] Boppart, S.; Ingle, L.; Potwora, R. J.; Rester, D. O. *Chemical Processing* **1996**, 79.
- [3] Walker, P. L. *Chemistry and Physics of Carbon*, NY:New York City, **1996**.
- [4] Campbell, M. MS thesis, Illinois Institute of Technology, **1998**.
- [5] Khalili, N. R. IIT Patent #147, **1999**.
- [6] Thiagarajan, P.; Epperson, J. E.; Crawford, R. K.; Carpenter, J. M.; Klippert, T. E.; Wozniak, D. G. *J. Appl. Cryst.* **1997**, 30, 280.
- [7] Beaucage, G. *J. Appl. Cryst.* **1996**, 29, 134.
- [8] Beaucage, G. *J. Appl. Cryst.* **1995**, 26, 717.
- [9] Teixeira, J. J. *J. Appl. Cryst.* **1988**, 21, 781.
- [10] Pedersen, J. S. *Adv. Colloid Interface Sci.*, **1997**, 70, 171.
- [11] Hyeon-Lee, J.; Beaucage, G.; Pratsinis, S. E. *Chem. Mater.* **1997**, 9, 2400.

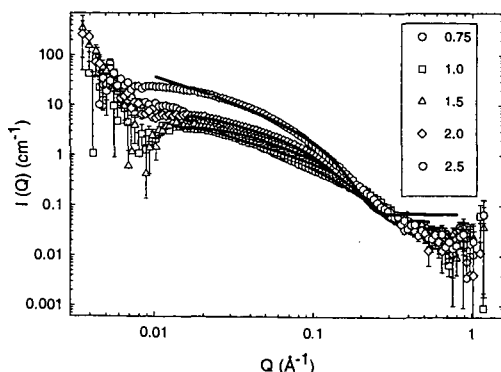


Figure 1: Resulting SANS plots after subtraction of the low Q power law. The solid lines indicate the fit to the Teixeira model.

Table I: Results of the Teixeira sphere mass fractal fit to the samples shown in figure 1.

ZnCl ₂ /sludge ratio	BET surface area (m ² /g)	Low Q Power Law Exponent	High Q Fractal dimension	Cutoff Length ξ (Å)
0.75	895	-4.02 ± 0.04	1.37 ± 0.01	NA (too large)
1.0*	1015	-3.46 ± 0.02	1.19 ± 0.02	67 ± 4
1.5	1067	-3.59 ± 0.01	2.18 ± 0.02	15.6 ± 0.3
2.0	1095	-3.70 ± 0.01	2.36 ± 0.02	17.2 ± 0.2
2.5	1249	-3.52 ± 0.02	2.50 ± 0.01	23.4 ± 0.2

* This data set was better fit by the form factor for a cylinder of radius 7.84 ± 0.09 Å and length 179.6 ± 4.8 Å.

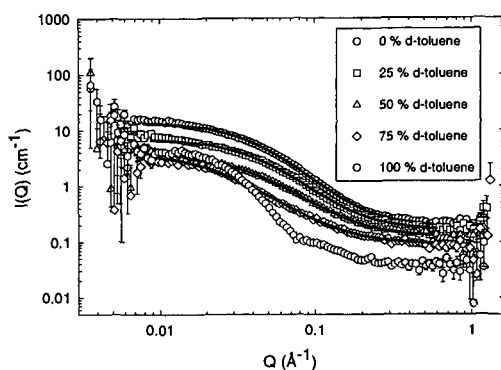


Figure 2: SANS plots of ZnCl₂/sludge ratio of 2.5, immersed in different toluene/d-toluene mixtures.

Table II: Results of the Teixeira sphere mass fractal fit to the samples shown in figure 2.

2.5 ZnCl ₂ /sludge ratio Sample in	Low Q Power Law Exponent	High Q Fractal dimension	Cutoff Length ξ (Å)
0 % d-toluene	-3.64 ± 0.03	2.42 ± 0.01	23.6 ± 0.2
25 % d-toluene	-3.70 ± 0.06	2.35 ± 0.02	22.6 ± 0.4
50 % d-toluene	-3.67 ± 0.11	2.26 ± 0.03	23.1 ± 0.7
75 % d-toluene	-3.29 ± 0.11	2.03 ± 0.04	46.5 ± 2.1
100 % d-toluene	-2.82 ± 0.04	NA	NA

SPECIATION OF NICKEL IN RESIDUAL OIL FLY-ASH BY XAFS SPECTROSCOPY

Frank E. Huggins¹, Gerald P. Huffman¹, Kevin C. Galbreath², Donald L. Toman²,
and John L. Wong³

¹Chemical and Materials Engineering/CFFLS, University of Kentucky, 533 South Limestone Street, Suite 111, Lexington, KY 40506-0043, fhuggins@engr.uky.edu

²Energy & Environmental Research Center, University of North Dakota, P.O. Box 9018, 15 North 23rd Street, Grand Forks, ND 58202-9018

³Department of Chemistry, University of Louisville, 2320 South Brook Street, Louisville, KY 40292

KEYWORDS: Residual oil, nickel speciation, XAFS spectroscopy

ABSTRACT

The US EPA has recently expressed concern about the possible presence of carcinogenic nickel subsulfides (e.g. Ni_3S_2 , etc.) in fly-ash generated and released during combustion of residual oil for power generation. To examine the forms of nickel in residual oil fly-ash samples, we have used a combination of X-ray absorption fine structure (XAFS) spectroscopy, X-ray diffraction, and a sequential extraction-anodic stripping voltammetry (ASV) technique. Differences were found in the nickel speciation between experimental (7 kW) and commercial (400 MW) combustion systems burning similar 0.85 wt% sulfur residual oils. Whereas almost all of the nickel was found to occur as nickel sulfate in the fly-ash from the experimental system, the fly-ash from the commercial system contained significant nickel in the form of a spinel phase, possibly NiFe_2O_4 . No significant evidence was found for the occurrence of any nickel sulfides in any sample, suggesting the cancer risk from Ni in residual oil fly ash is greatly exaggerated.

INTRODUCTION

The combustion of residual (No. 6) fuel oil for steam generation has the potential to release significant quantities of various metals, specifically vanadium, nickel, and chromium, and the semi-metal, arsenic, into the atmosphere [1]. Further, unlike fly-ash products from coal combustion, which contain abundant aluminosilicates that can react with and sequester trace metals in relatively unreactive glassy forms, fly-ash products from residual oil combustion usually do not contain significant quantities of aluminosilicates and the occurrence of these metals in residual-oil fly-ash is principally as oxides or sulfur compounds, either sulfates or sulfides. In particular, there is much concern about the inhalation risk associated with nickel because of the potential for formation of highly carcinogenic nickel subsulfides (Ni_3S_2 , etc.) in the fly-ash or fine particulate matter released during residual oil combustion [1]. Some limited nickel speciation analyses from power plants burning residual oil have reported as much as 26% of the Ni present as nickel subsulfides. However, it is possible that such values arise because of limitations in the indirect method used for speciating the nickel, viz., sequential extraction-anodic stripping voltammetry (ASV).

In this investigation, we have used three complementary methods to examine the nickel speciation in residual oil fly-ash samples produced in laboratory- and commercial utility-scale combustion. These methods are nickel X-ray absorption fine structure (XAFS) spectroscopy, X-ray diffraction (XRD) and the sequential extraction-ASV technique. In addition, samples were measured by XAFS spectroscopy before and after the first step in the sequential-extraction procedure for a more direct comparison with the ASV method.

EXPERIMENTAL

(i) Sample collection

Laboratory fly-ash samples were generated by combustion of a 0.86 wt% sulfur residual oil in a bench-scale down-fired 7 kW combustion unit [2] at an excess O_2 concentration of about 3 mol%. In this unit, a peak temperature of about 1500°C was achieved for about 0.5 s after which the gas-stream was cooled at a rate of 600°C/s before being sampled at a temperature of 300°C. Commercial fly-ash samples were obtained by isokinetic sampling from the stack of a 400 MW boiler using a modified EPA method 17 sampling-train assembly [3]. Samples were collected on two consecutive days: on the first day, a 0.80 wt% sulfur residual oil was burnt; on the second day, a 0.88 wt% S residual oil was burnt. The temperature of sampling was approximately 290°C. Further details of the sampling are given in more detail elsewhere [4].

(ii) Sample analysis methods

Ni K-edge XAFS spectroscopy was carried out at either beam-line IV-3 at the Stanford Synchrotron Radiation Laboratory (SSRL), Stanford University, CA, or at beam-line X-18B at the National Synchrotron Light Source (NSLS), Brookhaven National Laboratory, NY. Similar experimental practice was carried out at both synchrotron sources. Ash samples were suspended in the monochromatic X-ray beam using ultra-thin polypropylene bags. Nickel XAFS spectra were collected from the ash samples in fluorescent mode using either a 13-germanium array detector [5] or a Lytle fluorescence detector [6], depending on the concentration of the nickel. XAFS spectra were typically collected at X-ray energies ranging from about 100 eV below to at least 600 eV above the nickel K absorption edge. A thin nickel metal foil was used as the primary calibration standard; where possible, the foil was run in an absorption experiment after the fluorescence experiment so that it provided a simultaneous calibration. The first major peak in the derivative of the absorption spectrum of the foil was assumed to define the position of the nickel absorption edge at 8,333 eV. In addition, XAFS spectra of a number of standard compounds of nickel were obtained in connection with this work. These spectra were obtained in absorption geometry from thin pellets using ionization detectors.

The XAFS data collected at the synchrotron were returned to the University of Kentucky for analysis. The data were analyzed in the usual fashion [7,8]: after calibration of the energy scale, the spectra were split into separate X-ray absorption near-edge structure (XANES) and extended X-ray absorption fine structure (EXAFS) regions and each region was analyzed separately. The XANES region was used as a fingerprint for identification of the forms of occurrence of nickel in the fly-ash samples. The EXAFS region was mathematically manipulated in the usual manner [7,8] to yield the radial structure function (RSF), which is basically a one-dimensional representation of the local structure around the nickel in the material under investigation.

X-ray diffraction (XRD) was carried out on a Phillips XPert diffractometer system at the University of North Dakota using $\text{Cu K}\alpha$ radiation, a step-size of $0.02^\circ 2\theta$, and a time of 1 s/step. Diffraction patterns were collected over a range of 2θ from 5 to 70° . Samples were ground in an agate mortar and pestle and mounted on quartz plate for the XRD analysis.

Sequential extraction-ASV analysis was performed at the University of Louisville. Although a five-step extraction sequence has been developed for determining nickel speciation in oil fly-ash [9], only the first step, designed to separate soluble nickel compounds from the residual oil fly-ash, was performed in this work. This step involved extracting the ash samples in a 1.0 M sodium acetate - 0.5 M acetic acid solution buffered at pH 5 in an 8 mL centrifuge tube and bubbled with nitrogen for 10 minutes. The capped tube was then sonicated in a water bath for 2 hours at 25°C and centrifuged at 10,000 rpm for 20 minutes. Nickel in the supernatant was quantified by ASV of nickel dimethylglyoxime collected on a hanging Hg drop electrode with a CH-620 electroanalytical system in square-wave voltammetry mode. Nickel concentrations were obtained by the standard additions method. The residue remaining in the centrifuge tube was repeatedly extracted until Ni was not detected in the supernatant. At this point it was assumed that all soluble nickel compounds had been removed from the fly-ash.

RESULTS AND DISCUSSION

(i) XRD Analysis

X-ray diffraction analysis detected abundant amorphous components (glass, unburnt carbon) and anhydrite (CaSO_4) in all three fly-ash samples. In addition, the laboratory fly-ash sample contained gypsum ($\text{CaSO}_4 \cdot 2\text{H}_2\text{O}$) and glauberite, ($\text{Na}_2\text{Ca}(\text{SO}_4)_2$), whereas the commercial fly ash sample collected on the first day of sampling contained hexahydrate ($\text{MgSO}_4 \cdot 6\text{H}_2\text{O}$), periclase (MgO) and tentatively spinel, and that collected on the second day contained sodalite, ($(\text{Na},\text{Ca})_4\text{Al}_6\text{Si}_6\text{O}_{24}(\text{SO}_4,\text{Cl})_{1-2}$), and maghemite, ($\gamma\text{-Fe}_2\text{O}_3$). The magnesium phases are likely to have arisen from reaction and decomposition of brucite ($\text{Mg}(\text{OH})_2$) that was added to the oil to mitigate formation of free H_2SO_4 in the boiler. No nickel phases were specifically identified.

(ii) Acetate Extraction-ASV Analysis

The acetate extraction-ASV analysis divided the nickel into two fractions in each of the fly-ash samples: soluble nickel and insoluble nickel. For the laboratory fly-ash sample, 80% of the nickel was found to be present in soluble forms and the remainder in insoluble forms. For the two commercial fly-ash samples, significantly smaller fractions of the nickel were found to be present in soluble forms: for the Day 1 sample, 51%, and for Day 2 sample, 28%. In addition,

the total nickel concentration was found to be quite different between the laboratory and commercial fly-ash samples, viz., about 0.4 wt % and about 2.0 wt%, respectively.

(iii) XAFS Spectroscopy

The nickel XANES and RSF spectra of the laboratory fly-ash are shown in Figure 1. The RSF exhibits one major peak at a phase-shift uncorrected distance, 1.61 Å, consistent with Ni-O distances, and the overall shape of the XANES spectrum is also consistent with bonding of the nickel to oxygen anions [10]. Based on comparison of the fly-ash XANES and RSF spectra with those of various nickel standard compounds [10], the best match was found to be a hydrated nickel sulfate ($\text{NiSO}_4 \cdot x\text{H}_2\text{O}$). The nickel XAFS data did not change significantly after the acetate extraction process, even though about 80% of the nickel was extracted. This indicates that the nickel is almost entirely present as nickel sulfate. Additionally and most significantly, there is no enhancement of any spectral features that can be attributed to nickel subsulfides, which, if they had been present to any significant extent in the fly-ash, should have been five times more prominent in the spectra of the extracted sample.

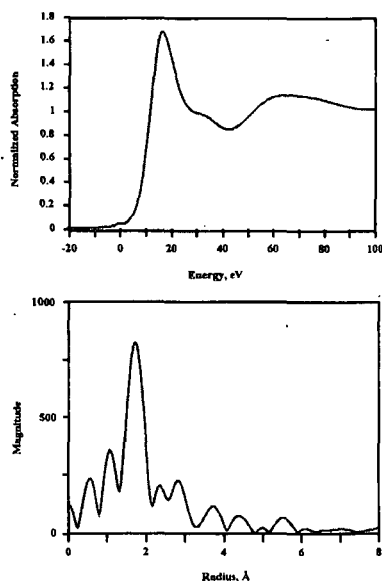


Figure 1: Ni XANES (top) and RSF spectra (bottom) for fly-ash generated in the laboratory from combustion of residual (No. 6) oil. The spectra did not change significantly after the acetate extraction.

The corresponding spectra for the commercial fly-ash sample collected on the first day are shown in Figure 2, both before and after the acetate extraction. Quite similar spectra were

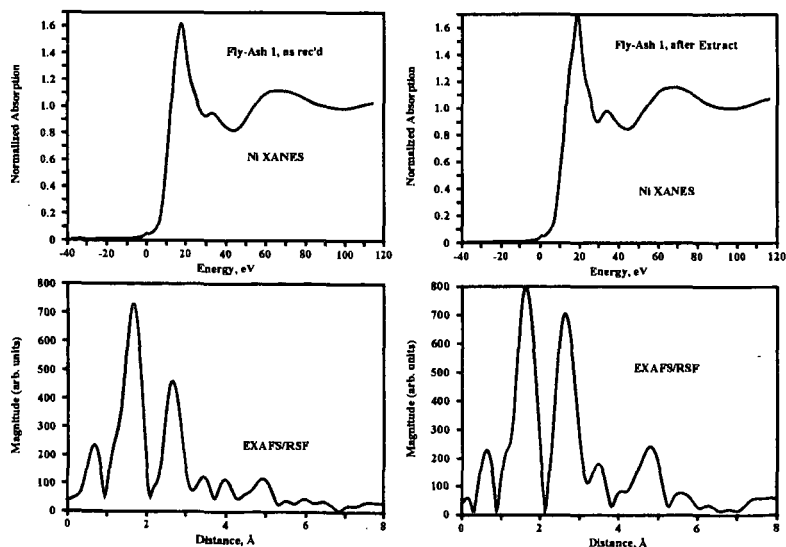


Figure 2: Ni XANES and RSF spectra for the residual oil fly-ash sample collected on day 1 at a commercial power plant, before (left) and after (right) extraction in a sodium acetate/acetic acid solution.

obtained from the fly-ash sample collected on the second day. As can be seen, there are significant differences in comparison with the spectra for the laboratory fly-ash sample and also between the spectra before and after the acetate extraction. In particular, the broad peak in the XANES spectrum at about 30-40 eV is more prominent and there is a second major peak in the

RSF spectrum at about 2.7 Å in the fly-ash samples from the commercial power plant. Both features become even more prominent after the acetate extraction.

Our first attempt at interpretation of the nickel XAFS data for the commercial fly-ash samples was in terms of a mixture of nickel sulfate (NiSO_4) and nickel oxide (NiO). Of the measured standard spectra that we had examined up to that point [10], only NiO had features in its XANES and RSF spectra that were consistent with the enhanced features shown in the corresponding spectra of the commercial fly-ash samples. However, the height ratio of the peaks at 1.6 and 2.7 Å, $A_{1.6}/A_{2.7}$, in the NiO RSF (Figure 3) is much different from that exhibited by the fly-ash and to explain the spectral data on the basis of a mixture of nickel sulfate and nickel oxide we would have to conclude that either (i) the acetate extraction removed only a very small fraction of the nickel as nickel sulfate, contrary to the results from the acetate extraction-ASV data, or (ii) that the reduction in the peak height ratio in the RSF was due to NiO of very small size. Neither of these explanations appeared very satisfactory.

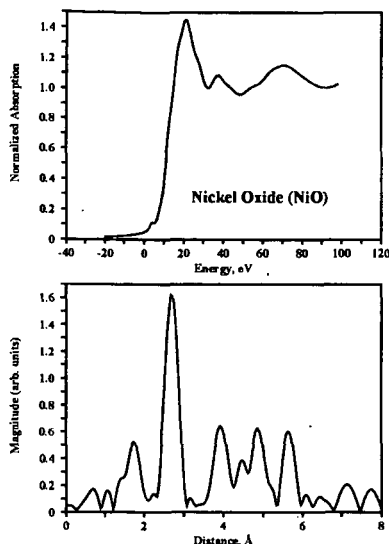


Figure 3: Nickel XANES (top) and RSF (bottom) for nickel oxide (NiO).

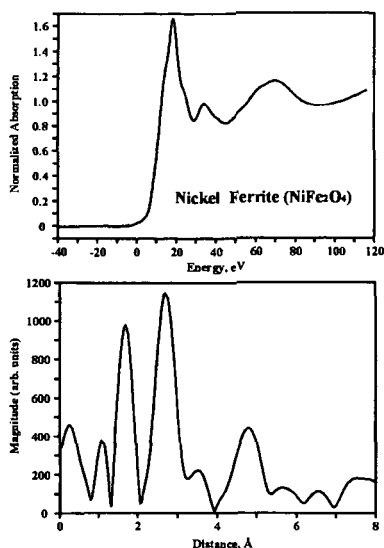


Figure 4: Nickel XANES (top) and RSF (bottom) for synthetic nickel ferrite (NiFe_2O_4).

The XRD patterns for the fly-ash, however, had suggested the possible presence of a spinel phase and nickel is known to enter spinel compounds readily. Hence, the possibility was explored that nickel might be present as a spinel oxide in the fly-ash samples. A sample of the nickel spinel, nickel ferrite (NiFe_2O_4), was synthesized at high temperature at the University of North Dakota by reacting stoichiometric amounts of NiO and $\alpha\text{-Fe}_2\text{O}_3$ at 1600°C and 1400°C for 2 hours and 3 hours, respectively, in air. The purity of the spinel was confirmed using XRD; the measured cell parameter for this cubic material was 8.331 ± 0.006 Å in agreement with the value of 8.339 Å reported in the Powder Diffraction file No. 10-325 for NiFe_2O_4 . The XAFS spectrum was then acquired in absorption geometry from a pressed pellet of the synthesized NiFe_2O_4 diluted in SOMAR mix. The Ni XANES and RSF spectra for the spinel are shown in Figure 4.

Comparison of the spectral data for NiFe_2O_4 with the data for the fly-ash samples provides a much better explanation than that for NiO . Not only is the ratio of the major peaks in the RSF of nickel ferrite much closer to that observed in the spectra of the extracted fly-ash samples, but the presence of a broad peak at about 4.8 Å in the RSF of nickel is also duplicated in the fly-ash spectra, especially those of the extracted samples. It is conceivable that the small differences in the height ratios of the major RSF peaks for the nickel ferrite standard and the extracted samples can be explained by the presence of aluminum or other light element substituting for the ferric iron in the spinel found in the commercial fly-ash. Hence, we do not now have to postulate that the acetate extraction incompletely removed the nickel sulfate, although that certainly remains a possibility, in light of the result obtained for the laboratory fly-ash. Regardless, the XAFS spectra of the extracted residues can be interpreted as arising from a substituted nickel-iron spinel as the predominant nickel-bearing phase.

Although less certain than for the laboratory fly-ash sample, there is no evidence from the XAFS data that there is any significant nickel sulfide species present in either of the commercial fly-ash

samples or their acetate extracts. Simulation of XANES spectra of hypothetical mixtures of the laboratory fly-ash and nickel sulfide (NiS) indicates that it should be possible to recognize a 5-10% occurrence of a nickel sulfide species in a fly-ash sample containing predominantly nickel sulfate species. The fact that spectral features attributable to nickel sulfides are not observed either for the fly-ash samples or their extraction residues indicates that such species are not significant and certainly less than 5% of the total nickel in the fly-ash.

CONCLUSIONS

XAFS spectroscopy, supplemented by results from XRD and acetate extraction-ASV techniques, indicates that hydrated nickel sulfate is the major nickel compound present in laboratory-generated residual oil fly-ash samples, whereas nickel-containing spinel is a significant second component in commercial fly-ash samples obtained from combustion of residual oils of similar sulfur contents. As discussed elsewhere [4], it would appear that the magnesium hydroxide added to the commercial residual oil to prevent formation of free sulfuric acid in the boiler promotes the formation of nickel spinel by providing additional cation species that compete in reacting with the acidic sulfur species. In none of the fly-ash samples was there any evidence for the presence of nickel sulfides. This result suggests that the EPA's estimate of the nickel inhalation cancer risk from residual oil-fired utilities, which is based on the assumption that the nickel species emitted by such utilities have 50% of the cancer potency of nickel subsulfide [1], could be overestimated by as much as a factor of 10.

ACKNOWLEDGEMENTS

This work was jointly sponsored by a consortium consisting of the American Petroleum Institute, Amerada Hess Corporation, Electric Power Research Institute, Florida Power & Light Company, Hawaiian Electric Corporation, and Public Service Electric and Gas Company, and the Center for Air Toxic Metals at the University of North Dakota Energy & Environmental Research Center. The Center for Air Toxic Metals is supported by the U.S. Environmental Protection Agency. Dr. E. Zillioux and co-workers from Florida Power & Light Company are acknowledged for expediting the fly-ash sampling at the 400-MW power plant. The U.S. Department of Energy is acknowledged for its support of the synchrotron facilities at Stanford University, CA, and Brookhaven National Laboratory, NY.

REFERENCES

- [1] Environmental Protection Agency, *Study of Hazardous Air Pollutant Emissions from Electric Utility Steam Generating Units—Final Report to Congress, Volume 1*. EPA Report EPA-453/R-98-004a, February 1998.
- [2] S. Benson, J. Pavlish, C. Zygarlicke, T. Erickson, K. Galbreath, G. Schelkoph, E. O'Leary, R. Timpe, C. Anderson, *Center for Air Toxic Metals Year 2 and 3 Final Technical Report—Section 3.0 Process Impacts on Trace Element Speciation*. Energy & Environmental Research Center Publication 98-EERC-03-03, April 1998, pp. 13-66.
- [3] Environmental Protection Agency, Emission Measurement Technical Information Center, Method 17, *Determination of Particulate Emissions from Stationary Sources (In-Stack Filtration Method)*. <http://www.epa.gov/ttnemc01/promgate/m-17.pdf>, September 1998.
- [4] K. C. Galbreath, D. L. Toman, C. J. Zygarlicke, F. E. Huggins, G. P. Huffman, J. L. Wong, *JAWMA*, submitted October 1999.
- [5] S. P. Cramer, O. Tench, N. Yocum, G. N. George, *Nucl. Instrum. Meth.*, **A266**, 586-591, (1988).
- [6] F. W. Lytle, R. B. Gregor, D. R. Sandstrom, E. C. Marques, J. Wong, C. L. Spiro, G. P. Huffman, F. E. Huggins, *Nucl. Instrum. Meth.*, **226**, 542-548, (1984).
- [7] P. A. Lee, P. H. Citrin, P. Eisenberger, B. M. Kincaid, *Rev. Mod. Phys.*, **53**, 769-808, (1981).
- [8] D. C. Koningsberger, R. Prins, *X-ray Absorption*. J. Wiley & Sons, New York, (1988).
- [9] J. L. Wong, J. Qian, C. H. Chen, *Anal. Chim. Acta*, **349**, 121-129, (1997).
- [10] K. C. Galbreath, D. L. Toman, C. J. Zygarlicke, F. E. Huggins, G. P. Huffman, J. L. Wong, *Energy & Fuels*, **12**, 818-822, (1998).

USING WAVELENGTH DISPERSIVE X-RAY FLUORESCENCE
SPECTROMETRY TO MEASURE CATION SEQUESTRATION
BY WOMBAT TIRE-DERIVED PARTICLES

David L. Wertz, E. Ryan Smith and Ashley D. Trahan

Department of Chemistry and Biochemistry
The University of Southern Mississippi
Hattiesburg, MS 39406-5043, USA

KEYWORDS: Cation sequestration, tire-derived particles

INTRODUCTION: Because wavelength-dispersive x-ray fluorescence (WDXRF) spectrometry may be utilized to examine a variety of condensed phase samples, it has been helpful to this group in our development of a tire processing technique called the WOMBAT -- for analysis of the black graining powder which is one product of the WOMBAT process. This powder, formed by degradation of the styrene-butadiene rubber in the tire, is dispersed in the mixed solvent prior to removal from the WOMBAT reactor and is separated from the mixed solvent by filtration and drying. This tire-derived powder is an important process component.

To a first approximation, the intensity of an analyte peak in the WDXRF spectrum of a multi-component sample is approximately proportional to the abundance of that analyte. This group has used a series of mixtures of solid state materials to approximate the abundances of key analytes (zinc, sulfur, and iron) in tires and in the tire-derived powders that have been produced from chemical degradation of the tires. The WDXRF spectrum of the WOMBAT solid tire-derived solid (TDP) contains a sulfur K_{α} peak which is smaller than the sulfur K_{α} peak (at 5.37 Å) in the untreated tire. The WDXRF spectrum of the black TDP powder is presented in Figure 1. The small zinc K_{α} peak (at 1.44 Å) in the WDXRF spectra of the tire-derived powder, when compared to the corresponding peak in the WDXRF spectrum of the untreated tire, indicates to ca. 95% of the zinc has been removed from the tire during our chemical processing. Using the same analysis procedure, the sulfur abundance is reduced by ca. 35% in the transition from the untreated tire to the TDP. The sulfur reduction produces a material, i.e., the TDP, which is a low polluting solid state fuel. However, the WDXRF spectrum of the TDP contains large iron peaks (K_{α} and K_{β} at 1.77 Å and at 1.94 Å, respectively) that are not present at such intensities in the WDXRF of the untreated SBR from the tire. The intensity of the Fe peaks in the WDXRF spectra of TDP is related to the length of time the TDP is allowed to remain in the reactor. The presence of the large iron peaks is consistent with the following reaction sequences:

- dissolution of iron from the steel belts into the reactor solution, and
- *in vivo* sequestration of the iron from the reaction solution by the TDP.

In order to determine if the TDP produced by the WOMBAT process is effective in sequestering other metal ions from solutions, small aliquots of the TDP have been introduced into aqueous solutions containing selected dissolved metal salts. Our results are presented below.

EXPERIMENTAL PROCEDURE: Five grams of TDP were dispersed into 100 ml of 0.1 molar aqueous solutions containing several reagent metal salts. After allowing the TDP to equilibrate, the TDP was separated from the aqueous solution by filtration, and then dried in a convective oven.

Each dried sample of treated TDP was then split into two parts. Part one was mounted onto a sample holder, and a WDXRF spectrum was obtained. Part two of each treated TDP sample was thoroughly washed with water and then recovered by filtration, dried, and mounted onto a sample holder. A schematic of the process is presented in Figure 2.

A wavelength dispersive x-ray fluorescence (WDXRF) spectrum of each sample was obtained using a Rigaku S-Max spectrometer equipped with an end-centered rhodium x-ray tube to cause elemental excitations and a graphite monochromator to disperse the secondary Xrays emitted by each sample during de-excitation. Each spectrum was obtained by collecting intensities for 4 second intervals between the angles of $2\theta = 8.00^\circ$ and $2\theta = 140.00^\circ$ at increments of $\Delta 2\theta = 0.05^\circ$.

RESULTS: Shown in Figures 3-6 are the WDXRF spectra of the TDP recovered from the

aqueous solution containing Cu^{+2} [Cu-TDP], from the aqueous solution containing Cr^{+3} [Cr-TDP], from the aqueous solution containing Hg^{+2} [Hg-TDP], and from the aqueous solution containing Pb^{+2} [Pb-TDP], respectively. In all of these WDXRF spectra, the zinc peak characteristic of the TDP has become too low to be detected, but the iron peaks are clearly discernible and only slightly less intense than in the WDXRF spectrum of the untreated TDP. The peak(s) due to the metal ions sequestered onto the TDP are labeled in each figure.

Thus, the spectra obtained may be explained in the following manner:

- Large copper peaks, K_{β} at 1.39 Å and K_{α} at 1.54 Å, appear in this WDXRF spectrum.
- The L_{β} and L_{α} peaks due to mercury, at 1.05 Å and at 1.24 Å are quite large in the WDXRF spectrum of this sample.
- The L_{β} and L_{α} peaks for lead, at 0.98 Å and at 1.18 Å, are small but clearly discernible in that WDXRF spectrum.
- The K_{α} peak for chromium, at 2.25 Å, is small but discernible.

Based on qualitative evaluation of the metal ion peaks in these spectra, the spectra was be divided into two groups. In the spectrum of the copper-containing TDP and in the spectrum of the mercury-containing TDP, the analyte peaks are quite large. However, for the spectra of the lead-containing TDP and of the chromium-containing TDP, the analyte peaks are quite small.

In a sample containing several types of atoms, the K_{α} peak intensity for analyte A (at λ_A) is given by:

$$I_A(\lambda_A) = M(\lambda_A) \cdot \eta_A \cdot I_A(\lambda_A) \cdot \exp[-\{\mu_s(\lambda_{Rh}) + \mu_s(\lambda_A)\} \cdot t_s \cdot \rho_s]; \quad (1)$$

where $\mu_s(\lambda_{Rh})$ is the mass absorption coefficient of the sample for the rhodium Xrays, $\mu_s(\lambda_A)$ is the mass absorption of the sample for the secondary Xrays emitted by analyte A contained in the sample of average thickness is t_s and density ρ_s . The abundance of analyte A is given by η_A , and $I_A^*(\lambda_A)$ is the absorption-free intensity for a pure sample of analyte A. $M(\lambda_A)$ described the efficiency of the spectrometer in measuring intensity at wavelength λ_A . For similar samples (P and Q) containing analyte A, a ratio of intensities measured from the WDXRF spectra of sample P and of sample Q may be used to estimate differences in the abundance of analyte A; i.e.,

$$I_{A-P}(\lambda_A) / I_{A-Q}(\lambda_A) \approx \eta_{A-P} / \eta_{A-Q} \quad (2)$$

Shown in Figure 7 are the WDXRF spectra of the Cu-containing TDP before and after the thorough washing with distilled water. The intensity of the copper peaks is decreased by 75-80%. A smaller reduction in peak intensity is noted when the WDXRF spectra of the Hg-containing samples, prior to and after washing with distilled water, are compared (see Figure 8).

The group is attempting to develop methods for utilizing the intensities of the "marker" peaks as the basis for making the matrix absorption effects to the intensities of the analyte peaks, so that the latter may be used to provide realistic measurements of the analytes sequestered onto the WOMBAT TDP.

CONCLUSIONS. The WOMBAT TDP sequesters several metal ions from aqueous solutions. Of these ion, both copper(II) and mercury(II) may be removed from the TDP by washing with distilled water.

REFERENCES.

- Wertz, D. L. et al., *Am. Chem. Soc., Div. Fuel Chem.*, 1999, 44, 998; 1998, 43, 796; 1998, 43, 349; 1997, 42, 741; 1995, 41, 879; 1994, 39, 815.
- Wertz, D. L., Smithhart, C. B., and Wertz, S. L., *Adv. X-Ray Anal*, 1990, 33, 475.
- Wertz, D. L., DuBose, S. B., and Trahan, A. D., *Adv. X-Ray Anal*, 2000, submitted.
- Jenkins, R., "X-Ray Fluorescence Spectrometry", Wiley-Interscience, NY, 1999.

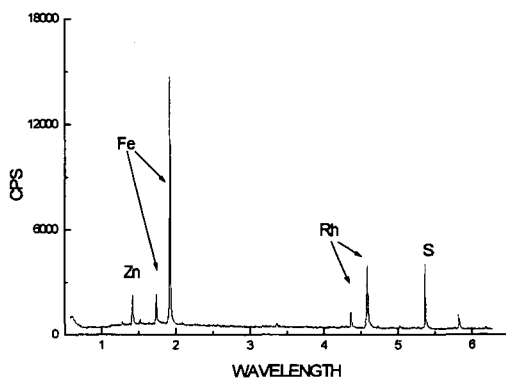


Figure 1. WDXRF spectrum of the WOMBAT TDP.

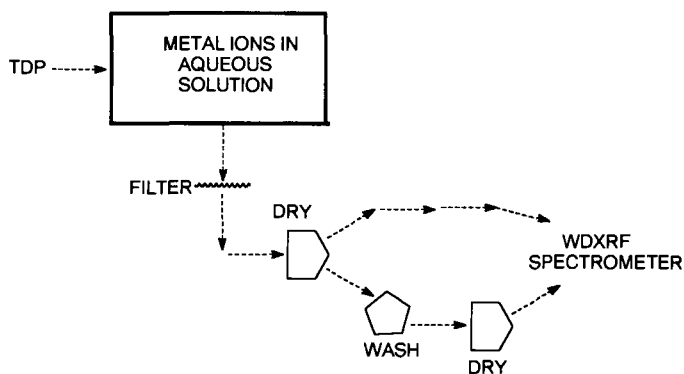


Figure 2. Schematic of the sequestering-washing experiments using WOMBAT TDP.

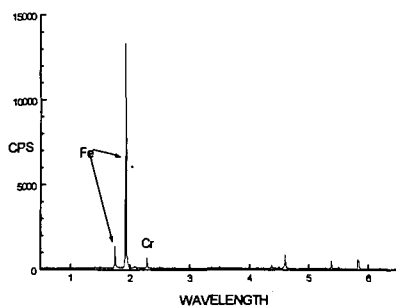


Figure 3. WDXRF spectrum of Cr-TDP.

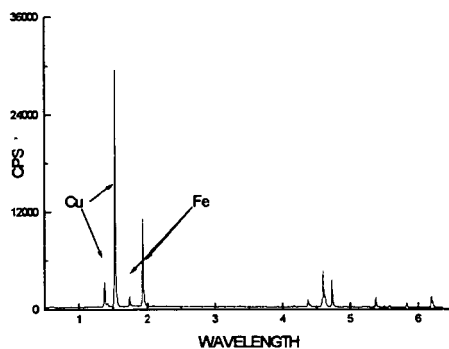


Figure 4. WDXRF spectrum of Cu-TDP.

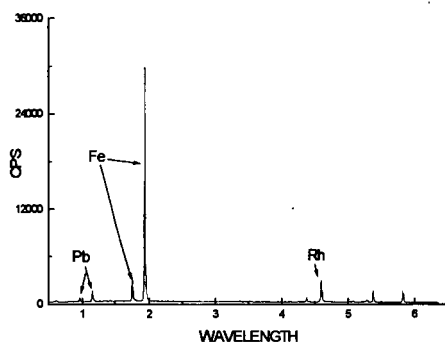


Figure 5. WDXRF spectrum of Pb-TDP.

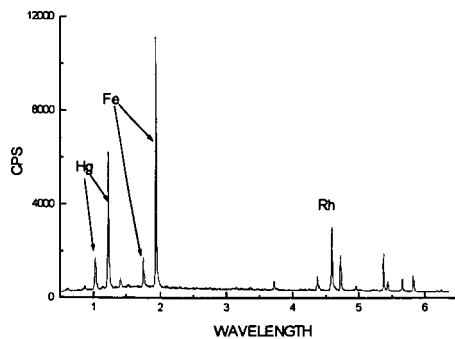


Figure 6. WDXRF spectrum of the Hg-TDP.

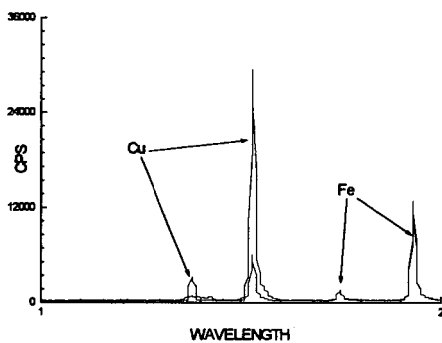


Figure 7. Comparison of the WDXRF spectra of Cu-TDP prior to and after washing with water.

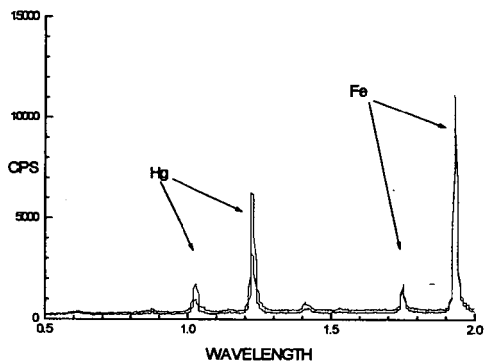


Figure 8. Comparison of the WDXRF spectra of Hg-TDP prior to and after washing with water.